MATHEMATICAL MODELLING OF PREMIXED LAMINAR METHANE-AIR FLAMES

by

KA CHUN KWAN

M. Eng.

Submitted in accordance with
the requirements for the degree of
Doctor of Philosophy

Department of Mechanical Engineering,
University of Leeds.

September 1994

The candidate confirms that the work submitted is his own and that appropriate credit has been given where reference has been made to the work of others.

Abstract

Two mathematical models have been developed to simulate two-dimensional, premixed, laminar, stationary, axisymmetric methane-air flames, and successfully validated with non-intrusive Coherent Anti-Stokes Raman Spectroscopy (CARS) temperature measurements. With the first model, the heat release rate model, volumetric heat release rate was generalised from one-dimensional computations. This approximation greatly simplified the set of governing equations that need to be solved. However, it cannot describe the effects of high stretch rates or of negative stretch rate. The second model made use of a number of reduced chemical kinetic schemes, with realistic elementary reactions. These were drawn from the literature and realistic transport properties have been included. With this model, based on the work of Peters (1985), the effects of stretch are automatically accounted for.

Practical experimental validation was obtained with a multiple slot burner, supplied by the collaborating body, British Gas plc. Temperature fields, obtained with the CARS technique, partially validated the reduced chemical kinetic scheme model. Some uncertainty arose in the prediction of heat loss to the burner tube.

A numerical algorithm based upon the SIMPLE method was employed, with a fully staggered grid. Various discretisation schemes were examined with the heat release model. Based on these tests, the hybrid scheme was selected for use in the reduced model. With this approach, a few reduced kinetic schemes have been selected and implemented. The most successful one was the Peters (1985) scheme. This consisted of 4 global reaction steps with 18 elementary reactions and 7 non-steady chemical species. The scheme has been employed in all the detailed computations in the present study.

With this scheme, two-dimensional field solutions, for methane-air mixtures with equivalence ratios of 0.75, 0.84 and 1.0, with slot widths of 2 mm and 3 mm, and mean inlet velocities ranging from 0.3 m/s to 2.8 m/s have been obtained. Detailed flame structures have been obtained for all these conditions. Under these conditions, a number of parameters, essential in burner design and stability analysis, have been investigated.

These includes flame height, flame thickness, and heat loss to the burner tube. The loss can range between 3% and 32% of the chemical energy in the premixture.

The computations reveal the stretch rates acting on the flame and their effects on the burning velocity. At low flow rates the base of the flame has a negative stretch rate, while the flame tip is positively stretched. These effects are reversed at high flow rates. From the localised relationships between stretch rate and burning velocity, Markstein lengths have been evaluated, for different mixtures and the values compared with those obtained experimentally by other researchers. In general, there was good agreement despite the large scatter in the experimental values. The results further showed that the effects of the two components of flame stretch, namely flame curvature and aerodynamic straining, on burning velocities were very different. It seems appropriate to introduce two Markstein lengths to correlate burning velocity and the two components of stretch and these have been evaluated. Aerodynamic straining has a significantly larger effect on burning velocity than has flame curvature.

Acknowledgments

I wish to express my deepest appreciation to my supervisors, Prof. D. Bradley and Dr. P. H. Gaskell for their invaluable guidance, advice and encouragement throughout the course of this research work. The supervision of Dr. A. K. C. Lau during the first year of this work deserves special mention.

The support, guidance and interest of Dr. S. Hasko and Dr. M. Davies of British Gas plc. throughout the duration of the research is gratefully acknowledged. The financial support from the Science and Engineering Research Council and British Gas plc. is gratefully acknowledged. Without their support, the present work would not have been possible.

I would also like to express my thanks to Dr. M. Scott and the technical staff of the thermodynamics laboratory for their contribution to the experimental programme. Many thanks are also due to Dr. X. Gu for his helpful advice and discussion in relation to the numerical technique.

I would also like to express my graditudes to all my friends, especially, those who spent so many "overnights" with me. A special thanks to my parents, brother and sister for their continuous supports and encouragement.

Contents

List of Tables

List of Figures

Nomenclature

Symbols which are frequently used in the text are listed below. Other locally employed notations are defined as and when required.

A	surface area of a flame
A_{ij}^{*}	ratio of reduced integrals
C_i	concentration of species i
C_p	specific heat at constant pressure
D_{ii}	self diffusion coefficient
D_{ij}	multi-component diffusion coefficient
E	activation energy
$(eps)_{ij}$	Lennard-Jones (12 : 6) potential parameter; single suffix denotes pure component
g	gravitational constant
h_i	specific enthalpy of species i
K	equilibrium constant
k_B	Boltzmann constant
k_i	reaction rate coefficient of ith elementary reaction
$\mathcal{L}$	single Markstein length
$\mathcal{L}_c$	Markstein length for curvature stretch
Le	Lewis number
$\mathcal{L}_a$	Markstein length for aerodynamic straining
m_i	molecular mass of species i
n	normal vector
p	pressure
q	volumetric heat release
R	radius of curvature
S	flame stretch rate

$(si)_{ij}$	Lennard-Jones (12 : 6) potential parameter; single suffix denotes pure component
T	temperature (K)
T^*	reduced temperature
u	velocity in horizontal direction
u_i	diffusion velocity of species i in horizontal direction
u_l	unstretched laminar burning velocity
u_n	stretched laminar burning velocity
v	velocity in vertical direction
v_m	mean velocity in vertical direction
V	fluid velocity
v_i	diffusion velocity of species i in vertical direction
W_i	molecular weight of species i
w_i	reaction rates of the ith elementary reaction
$\dot{w}_i$	chemical production rate of species i
X_i	mole fraction of species i
x	horizontal co-ordinate
y	vertical co-ordinate
Y_i	mass fraction of species i

Greek letters

β	Zeldovich number
δ	flame thickness
δ_{ij}	Kronecker delta (= 0 for $i \neq j$; = 1 for $i = j$)
θ	reaction progress variable
$\Omega_{ij}^{(1,1)^*}$	reduced collision integral
ρ	density
ϕ	equivalence ratio
λ	thermal conductivity

μ	viscosity

Subscipts

i, j, k	chemical species i, j, k (1, 2, ... N)
e, w, n, s	east-, west-, north, south-face of the control volume, respectively
P, E, W, N, S	centre of the control volume and the surrouding nodes in the east, west, north and south, respectively
EE, WW, NN, SS	remote nodes lying beyond east, west, north and south nodes, respectively
u	unburnt gas quantity
b	burnt gas quantity

CHAPTER ONE
Introduction

1.1 Mathematical Models of Laminar Flame Combustion

Laminar premixed flames are important in a number of contexts. First, the structure of such flames is of fundamental importance, in that it reveals the complex interplay of chemical kinetics, diffusion, conduction and the flow field. Second, such flames are of practical importance, particularly in domestic and commercial heating. Third, even in turbulent combustion, turbulent flames are often modelled as an array of laminar flames (Bradley *et al.* 1992). Clearly, the structure of laminar premixed flames is important.

The structure has been studied in many experiments since the Burke-Schumann theory (1928) of the laminar diffusion flame. This predated, by ten years, the Zeldovich and Frank-Kamenetskii (1938a, 1938b) theory of premixed burning, which provided the first satisfactory analysis of the laminar burning velocity, controlled by chemical reaction rates. Subsequent developments in chemical kinetics and computers have enabled computed solutions of mathematical models to yield premixed laminar flame structures and burning velocities. Solutions were first obtained by Spalding (1956), followed by Adams and Cook (1960). Further one-dimensional structures with complete chemical kinetics were revealed, for hydrogen flames, by Dixon-Lewis and Williams (1963), and, for methane flames, by Smoot *et al.* (1976). Methane flames were subsequently studied in a one-dimensional planar configuration by Dixon-Lewis (1981). As the importance of flame stretch became clear, the influence of this was embodied in computational studies. One-dimensional stretched counter flow diffusion flames were studied by Peters and Warnatz (1982), Dixon-Lewis *et al.* (1984), Kee *et al.* (1988) and Dixon-Lewis (1990).

Details of stretched two-dimensional axisymmetric diffusion flames were computed by Smooke *et al.* (1989, 1990), Prasad and Price (1992) and Coelho and Pereira (1993).

In laminar flamelet modelling of turbulent combustion, the turbulent flame is conceived as an array of laminar flamelets which retain the internal structure of the corresponding laminar flame (Bray 1979). With this concept, the complex chemistry and molecular transport properties are decoupled from the modelling of the turbulent flow field. Necessary laminar flame data can be obtained from either experimental or computational studies. Various models based on this concept have been developed by a number of researchers for turbulent premixed and non-premixed flames (Bray 1980, 1990; Bray *et al.* 1981, 1985; Peters 1984, 1986; Bradley *et al.* 1987, 1990 and Abd. Al-Masseeh *et al.* 1990, 1991). The practical motivation for the development of mathematical models of combustion is the improvement in efficiency and the minimisation of noxious emissions. Because of the extensive reserves of natural gas, largely methane, particular importance is attached to the combustion of that gas.

The theoretical study of combustion process is difficult, primarily because of the large number of chemical species. For matrix based numerical solution methods, such as Newton's method, the cost of computation varies with the square of the number of species. For field by field solution methods, the variation is linear with the number of species, though the number of iterations for convergence becomes so large that the algorithm is less efficient than the matrix based one. More importantly, however, since post-processing via first order sensitivity analysis is essential in any flame study, a Jacobian matrix will have to be formed ultimately, even if field by field-solution-methods are employed.

For methane-air oxidation, about 100 elementary reactions are generally thought to be involved in the C_2-chain (Peters and Kee 1987) and the number of identified possibly relevant reactions approaches 200 (Peters and Williams 1987). Numerical solution for the simplest two-dimensional geometry requires the most powerful computers available (Smooke *et al* 1989, 1990, Prasad and Price 1992). Implementation of such reaction schemes for complex geometries or for turbulent flames would be computationally prohibitive. Therefore, in some instances, quite empirically, a one-step reaction has been

employed. Some overall aspects of the flame propagation may be accounted for with such a model, but details of the interactions between fluid mechanics and chemistry are certainly not. In fact, it has never been demonstrated that a complex reaction scheme for hydrocarbon flames can be reduced in a systematic way to a one-step model for any equivalence ratio, pressure, or temperature.

Nevertheless, by using the laminar flamelet approach, a one-dimensional, laminar flame can yield a heat release profile, for use in turbulent flow computations. A similar approach is described in Chapter 3, not, in this case, for turbulent flames but for a two-dimensional laminar flame. However, this model became inadequate as flame stretch became significant. A better strategy appeared to be to reduce the computational effort by using a reduced reaction scheme, with a smaller number of reactions. By assuming some of the intermediate species to be in a steady state and some of the equations to be equilibrated, some of the highly non-linear differential equations for these species are replaced by algebraic ones.

With recent advances in such schemes, it is now possible to implement them in multi-dimensional combustion models (Coelho and Pereira 1993). Encouraged by these developments, and the lack of any previous attention to multi-dimensional premixed laminar methane-air flames, the initial objective of the present study was to develop a two-dimensional mathematical model with a reduced chemical scheme. A slot-burner geometry was chosen, not only because of its practical importance, but also because of its capability of revealing fundamental properties of premixed laminar flames. In particular, the effects of stretch on the burning velocity of the methane-air mixture have been investigated. With the vast number of reduced kinetic schemes that have become available over the past ten years, it was impossible to test them all. Schemes for methane-air mixtures are briefly reviewed in Chapter 3. A few representative schemes then are selected for closer examination, and these are described in Chapter 3.

1.2 Two-dimensional Premixed Flames

Because of the greater computational demands, there has been less work on two than on one-dimensional flames. Most such work has been confined to pseudo-two-

dimensional flat flames, to study the effect of the aerodynamic strain rate on the burning velocity and the volumetric heat release rate. The present study of a two-dimensional flame on a slot burner was in collaboration with the British Gas plc. Gas Research Centre at Loughborough, from which the burner was provided. Practical reasons for the study were, first, to develop the appropriate two-dimensional methodology for the computation of the reacting flow field above the burner and, second, to study the factors influencing flame lift off, flash back, and instability.

It was recognised that it would be necessary to reduce the computational time and storage by recourse to simplification of the flame reactions. Two strategies were adopted. That adopted initially, used the volumetric heat release rate, as a key coupling parameter, expressed as a function of the reaction progress variable, based on temperature. The volumetric heat release rate through the flame was found from one-dimensional, planar flame, computations. This strategy was computationally very efficient, as the volumetric heat release was computed separately. However, it was found that the effects of stretch, which are significant in the slot burner flames, were more difficult to implement than originally anticipated, due mainly to the lack of computational and experimental data on negative stretch such as that occurs at the flame tip.

Thus, a second strategy was adopted. With this, following Peters (1985), a "complete" chemical kinetic scheme, with a large number of chemical species, was systematically reduced to a "reduced" scheme, with less species. It is worth noting that the number of elementary reactions is less important, as the size of the species conservation equation set depends only upon the number of active species. This strategy proved to be computationally efficient, and since realistic chemical kinetics and transport coefficients were included, the effects of stretch were well accounted for. These two strategies are now briefly described, while the conservation equations and evaluation of transport properties are presented in Chapter 3.

1.3 Chemical Heat Release Rate

Before the advent of high speed digital computers and complex chemical kinetic models, the chemical heat release rate had to be evaluated without detailed chemical kinetics. The heat release rate appeared in the classical theory of burning velocity (Zeldovich and Frank-Kamenetskii 1938a, 1938b), which relates the laminar burning velocity to the area under the heat release rate versus temperature profile. In 1957, Spalding presented one of the most refined analytical generalisations of this approach. The chemical heat release was based upon a single-step reaction scheme. Recently, the Leeds Group has used heat release versus temperature profiles in flamelet mathematical modelling of turbulent combustion (Bradley *et al.* 1988, 1990, Bradley and Lau 1990).

1.4 Reduced Chemical Reaction Schemes

1.4.1 Overall strategy

While the general idea of reducing complex kinetic schemes by the introduction of steady state assumptions has long been known to chemists (von Karman and Penner, 1954), it has been applied to hydrocarbon flames only recently (Peters 1985). Subsequently, numerous schemes have been proposed. Here, "reduction" is not synonymous with "simplification" of the chemistry, but is rather a rational reduction in the complexity of the mathematical form necessary to describe the chemical transformations.

The idea of mechanism reduction was introduced at the beginning of the century through application of the pseudo-steady state approximation to reactive intermediates. This led to analytical solutions of non-linear reaction systems, that otherwise could not be solved (Hill 1977). A rigorous mathematical formulation to transform chemical species into a few dynamically equivalents was begun in the 1960s (Wei and Prater 1962, Wei and Kuo 1969 and Kuo and Wei 1969).

A systematic approach has been developed by Peters and Kee (1987) for the construction of reduced combustion mechanisms. First, the species to be eliminated, or assumed to be in a steady state, were identified by examining the relative importance of

the intermediate species with the help of sensitivity analysis. Second, those to be eliminated were removed systematically from the starting mechanism. Third, the concentrations of the steady state species were estimated by application of the steady state or partial equilibrium approximations. Other systematic approaches for developing reduced mechanisms have been proposed by Lam and Goussis (1988) and by Maas and Pope (1992). A comprehensive review has been presented by Frenklach (1991).

A starting mechanism is considered as an already simplified version of a "complete mechanism". For example, to describe premixed methane oxidation, Peters (1985) chose a starting mechanism with the C_1-chain only, neglecting the C_2 and higher carbon chains, which are not important for lean mixtures. Steady state and partial equilibrium assumptions then were made and the basic characteristics of these will now be briefly described.

1.4.2 Steady state approximation

The steady state assumption assumes that during the major part of the reaction, the concentrations and the rates of change of all intermediate species are constant and small. Consider the rate law for the intermediate species B in the following consecutive reaction:

$$\mathrm{A} \xrightarrow{k_a} \mathrm{B} \xrightarrow{k_b} \mathrm{C}\,, \tag{1.1}$$

where the rates of formation are given in terms of the reaction rates k_a, k_b and species concentrations C_A, C_B and C_C:

$$\frac{dC_\mathrm{A}}{dt} = -k_a C_\mathrm{A}\,, \tag{1.2}$$

$$\frac{dC_\mathrm{B}}{dt} = k_a C_\mathrm{A} - k_b C_\mathrm{B}\,, \tag{1.3}$$

$$\frac{dC_\mathrm{C}}{dt} = k_b C_\mathrm{B}\,. \tag{1.4}$$

With the steady state approximation, the net rate of formation of the intermediate species B is approximately zero. Thus,

$$\frac{dC_B}{dt} \approx 0 . \tag{1.5}$$

Substituting into Eq. 1.3 gives,

$$k_a C_A - k_b C_B = 0 . \tag{1.6}$$

The concentration of intermediate species B now can be expressed in terms of the reaction rates k_a, k_b and the concentration of A:

$$C_B = \frac{k_a C_A}{k_b} . \tag{1.7}$$

1.4.3 Partial equilibrium approximation

Consider a sequence of consecutive reactions in which the intermediate species B reaches an equilibrium with the reactants, A and D:

$$A + D \underset{k'_a}{\overset{k_a}{\rightleftarrows}} B \xrightarrow{k_b} C . \tag{1.8}$$

This scheme involves a partial equilibrium, which arises because the rates of formation of the intermediate species B (k_a) and of its decay back into reactants (k'_a) are much faster than the rate of formation of product C (k_b). With A, B and D in equilibrium, then:

$$\frac{k_a}{k'_a} = \frac{C_B}{C_A C_D} , \tag{1.9}$$

and the concentration of the intermediate species B can be expressed in terms of the ratio of reaction rates k_a and k'_a, essentially an equilibrium constant:

$$C_B = \frac{k_a}{k'_a} C_A C_D . \tag{1.10}$$

The rate of reaction of B to form C is very slow relative to the other rates.

1.5 Burning Velocity and Flame Stretch

1.5.1 Burning velocity

The burning velocity is a useful practical combustion parameter characterising the overall reaction rate of a premixed flame. It is generally regarded as a fundamental constant, depending only on the initial temperature, pressure, stretch rate and composition of the mixture. If the coupling between the chemical kinetics and molecular transport properties is known in detail, it will be possible to calculate the burning velocity because it represents the eigenvalue of the time-independent, one-dimensional flame equations (Fristrom and Westenberg 1965). Unfortunately, the combustion kinetics for most hydrocarbon mixtures is not known with sufficient certainty to determine burning velocities accurately from first principles and experimental support is usually necessary.

The apparent simplicity of the theoretical definition of burning velocity belies the experimental difficulties in measuring it. To have any physical significance, such a definition can only refer to a large, flat flame isolated from all heat sinks. In practice, a flame holder acts as a heat sink, the curvature of the flame causes variations in velocity across the flame and a confining vessel causes aerodynamic interactions, all of which are difficult to correct. Although a one-dimensional, stretch-free, flame can be modelled on a computer, in practice all flames are two or three-dimensional and flame stretch is important. It is not surprising, therefore, that wide discrepancies exist in the published data on burning velocities. Andrews and Bradley (1972) have published a critical review of the experimental methods for measuring burning velocity and derived correction factors to compensate for errors inherent in the different techniques, but did not consider the influence of flame stretch.

Historically, the first recorded estimate of a burning rate of a flame appears to have been made by Sir Humphrey Davy who in 1815 published his work on the development of the safety lamp of miners. Since then, there have been considerable disagreements on the definition and values of burning velocity. The problem of determining the propagation velocity of a deflagration wave was first studied by Mallard and LeChatelier (1883), who considered heat loss to be of predominant importance and the chemical

reaction rate to be secondary. Through the use of simplified theoretical models of the wave, Mallard's student Taffanel (1913a) and, later but independently Daniell (1930), appear to have been the first investigators to demonstrate that the burning velocity is proportional to the square root of the reaction rate and to the square root of the ratio of the thermal conductivity to the specific heat at constant pressure.

1.5.2 Flame stretch

Historically, the concept of flame stretch was first introduced by Karlovitz (Karlovitz *et al.* 1953) to describe flame extinction in velocity gradients. It was subsequently adopted by Lewis and von Elbe (1961) to explain and quantify the various phenomena associated with flame stabilisation. The flame curvature aspects of stretch also formed the basis for the study of flame front instability by Markstein (1964). In the past fifteen years or so, significant advances have been made in our understanding of flame stretch and its influence on the flame structure. These include a fundamental generalisation of the definition of stretch, mathematically rigorous analyses of the structure and propagation of stretched flames, experimental and numerical verification and quantification of predicted properties via model flames, and re-interpretation of certain flame phenomena. Recent reviews (Matalon and Matkowsky 1983, Law 1984, Peters 1984, Williams 1985, Clavin 1985) have summarised these.

A flame is stretched when it experiences a continual change in its frontal area. To define stretch, an arbitrary surface such as an isotherm must first be identified. General definitions of stretch at any point on this surface have been provided by various researchers (Phillips 1972, Matalon 1983, Chung and Law 1984, Clavin and Joulin 1989, Candel and Poinsot 1990, Bradley *et al.* 1992). The stretch rate, S, of a surface of area A is:

$$S = \frac{1}{A}\frac{dA}{dt} \tag{1.11}$$

where t denote time, and the evaluation of S is discussed in Chapter 2.

1.5.3 The Markstein relation

A length $\mathcal{L}$ was introduced by Markstein (1951), to characterise the physical effects of stretch. His phenomenological relation between the stretched burning velocity u_n, the unstretched laminar burning velocity u_l and the mean radius of curvature, R (R is defined to be positive when the front is concave towards the unburned gases), of the flame front was:

$$u_l - u_n = u_n (\mathcal{L} / R), \tag{1.12}$$

where $\mathcal{L}$ is a length which became known as the "Markstein length". In his paper, Markstein (1951) anticipated that $\mathcal{L}$ would be of the order of magnitude of the flame thickness δ, and be dependent upon the chemical kinetics and transport properties of the reactive mixture, including those of the reactive species. Of particular importance is the Lewis number, which is defined as the ratio of mass to heat diffusivities:

$$Le = \frac{\lambda}{\rho_u C_p D}, \tag{1.13}$$

where D is the diffusion coefficient of the deficient species in the premixture and λ is the thermal conductivity, ρ_u is the density of the unburned mixture and C_p is the specific heat at constant pressure. The first study of the coupling of diffusion and hydrodynamics was by Markstein, whose review paper of 1964 is seminal. It involved phenomenological considerations, but inevitably not all his assumptions were correct.

Through activation energy asymptotic analysis, Clavin (1985) derived an analytical expression for the Markstein length, $\mathcal{L}$, for a single-step, two reactant mixture:

$$\mathcal{L} = \frac{1}{\gamma} \ln\left(\frac{1}{1-\gamma}\right) + \frac{\beta}{2} (Le - 1) \frac{1-\gamma}{\gamma} \int_0^{\frac{\gamma}{1-\gamma}} \frac{\ln (1 + x)}{x} dx, \tag{1.14}$$

where x is a dummy variable of integration. This expresses the influence of expansion (density ratio, $\gamma = 1 - \rho_b/\rho_u$), activation energy ($\beta$, Zeldovich number) and Lewis number, Le, on Markstein length. The Zeldovich number for an activation energy, E, is defined as:

$$\beta = \frac{E\,(T_b - T_u)}{R\,T_b^2}\,, \tag{1.15}$$

in which T_u is the initial, and T_b is the adiabatic temperature.

Linan and Clavin (1987) extended the restrictive one-step reaction model to one containing a multi-step reaction scheme, representative of a halogen - hydrogen reaction. Their results illustrated the influence of the chemical kinetics of each reaction and also the Lewis number of the intermediate radicals upon the overall Markstein number. Two years later, Clavin and Joulin (1989) suggested the burning velocity to be a function of flame shape, flow field, time-dependence and mixture composition. By involving appropriate assumptions, they obtained phenomenologically the following correlation:

$$u_l - u_n = \mathcal{L}_1\, u_n \left(\frac{1}{R_1} + \frac{1}{R_2} \right) + \mathcal{L}_2\, n.\nabla V.n + \mathcal{L}_3\, div\, V + \mathcal{L}_4\, \frac{d\,Log\,p}{d\,t}\,. \tag{1.16}$$

Here coefficients $\mathcal{L}_1 \ldots \mathcal{L}_4$ are different Markstein lengths and p is pressure. V is the fluid velocity and n, the normal vector of the flame surface.

Along with the laminar burning velocity u_l, the Markstein lengths are physico-chemical properties of the mixture. They are configuration-independent through the variations in pressure. For flame propagation at constant pressure, the last two terms disappear, but in confined combustion such as that occurs in internal combustion engine, they may be important.

At present, theoretical values of $\mathcal{L}_3$ and $\mathcal{L}_4$ have not been obtained. Attention has been restricted to flames propagating in constant-density, constant-pressure mixtures. Evaluations of $\mathcal{L}_1$ and $\mathcal{L}_2$ for realistic, flame models have only been possible for some particular cases (Linan and Clavin 1987), mainly because the chemical kinetics are too complex. Theoretical values of the Markstein lengths $\mathcal{L}_i$ have been provided by simple, analytically tractable models. Even though the values have been generalised to account for two-step or few-step chemical schemes (Clavin 1985), most of them have been derived by asymptotic methods that assume combustion can be modelled by a one-step

overall reaction of the Arrhenius type and that the Zeldovich number is large. The values obtained in this way give only one Markstein length $\mathcal{L}$ (Markstein 1964), i.e. $\mathcal{L}_1 = \mathcal{L}_2 = \mathcal{L}$.

In summary, an expression relating the unstretched u_l and stretched u_n values of the burning velocity to the shape of the flame front and the flow ahead of it with Markstein lengths have been derived phenomenologically. Analytical and experimental evaluations of the different Markstein lengths are, at present, not possible. Numerical evaluations are however, currently being obtained at Leeds by Gu (1994).

In the present study, burning velocity, flow fields, heat release rate contours and isotherms were obtained with a reduced reaction scheme for the two-dimensional slot burner premixed flame. From these, components of flame stretch and the corresponding Markstein lengths are evaluated. Highly curved flame surfaces have been studied at high flow rates, to give a range of stretch rates, typically between -15000 s^{-1} and 1000 s^{-1}.

1.6 Experimental Validation

In experiments on the slot burner the introduction of a solid probe could locally disturb the flow and introduce errors. Non-intrusive techniques range from Laser Doppler Velocimetry (LDV) for velocity validation, Laser Induced Florescence (LIF) for chemical species validation, to Coherent Anti-Stokes Raman Spectroscopy (CARS) for temperature validation. LDV was employed by workers in a consortium of which British Gas was a member. Because of the expertise at Leeds on the CARS technique it was decided to employ this. Temperature measurement by thermocouples would introduce too much disturbance, particularly in the regions of high curvature. Furthermore, they have limited spatial resolution, melt at high temperatures, and their accuracy is dependent upon correction terms to account for radiation and conduction losses (Bradley *et al.* 1989).

On the slot burner the finite CARS measuring volume could lie along an isotherm. On the other hand, while being non-intrusive and free from thermal inertia problems, CARS measurement techniques are expensive and require considerable skill to implement. Fortunately, Dr. M. Scott possesses such skill and this work was done in

collaboration with him. Details of the burner and the temperature measurement are presented in Chapter 6.

1.7 Outline of Present Work

The governing equations for two-dimensional laminar flame propagation and flame stretch are presented in Chapter 2. The difficulties in obtaining the source term for the energy equation are discussed, and the species conservation equations are presented. Evaluations of the detailed transport properties necessary for solving the equations also are described.

The source term problem highlighted in Chapter 2 is dealt with in Chapter 3. Two different approaches were adopted. First, the volumetric heat release, was obtained by the same flamelet approach as has been used by Bradley *et al.* (1990). However, because limitations of this approach were revealed, encouraged by increasing computer capacity and the development of reduced kinetic schemes, a second approach adopted a four-step reduced mechanism.

Chapter 4 reviews the associated numerical methods. The SIMPLE algorithm is reviewed to then provide the basic numerical procedure for both the heat release and reduced reaction models. Some common discretisation schemes including the non-diffusive, boundedness-preserving scheme (CCCT) of Gaskell and Lau (1988) are presented. These schemes were applied to the heat release model and, ultimately, the hybrid scheme was selected, for its simplicity and accuracy, for the reduced model.

Chapter 5 presents the numerical results and compares the four models used in the present study. The one-dimensional model of Dixon-Lewis (1981) with a "complete" chemical mechanism is described, followed by some computational results. Next, details of the simple two-dimensional heat release model and its limitations are discussed. Following that, a model with the reduced chemical kinetic schemes of Peters (1985), referred to as the P1 scheme, is presented, together with computational results. Experimental validation of the reduced model is described in Chapter 6, in which numerical results are compared with those measured by CARS thermometry.

The burning velocity and flame stretch results from the reduced model are analysed in Chapter 7. The Markstein correlation of burning velocity and flame stretch is considered. The possibility of multiple Markstein lengths is found to be appropriate to explain the computed results. Three sets of Markstein lengths are suggested. Practical conclusions, concerning burner operation, as well as aspects of the modelling approach are presented in Chapter 8. Suggestions for future work also appear.

CHAPTER TWO
Governing Equations for Combustion Modelling

2.1 Introduction

Chemical reaction imposes exacting demands for flow field computations. Solutions are required not only for the conservation equations for global mass, momentum and energy, but also for a set of highly non-linear, coupled, species conservation equations. This chapter presents the set of required equations in steady state, two-dimensional, elliptic flows. Accurate expressions for the calculation of transport properties, based on molecular collision theories, are described. Approximated expressions for viscosity and thermal conductivity also are described. These were necessary with the heat-release model. A number of mathematical expressions for evaluating flame stretch are presented. The conservation equations for a premixed laminar flame are well documented in many text books (Kuo 1986, Williams 1985). Those presented here are based on that of Williams (1985).

2.2 Conservation Equations

2.2.1 Mass conservation

The global conservation of mass for a compressible mixture in steady state, two-dimensional, rectangular co-ordinates (x and y denote the horizontal and vertical co-ordinates, respectively) is:

$$\frac{\partial}{\partial x}(\rho u) + \frac{\partial}{\partial y}(\rho v) = 0 , \qquad (2.1)$$

where u and v are velocities in the horizontal and vertical directions, respectively. The equation of continuity for the mass fraction of species i, Y_i, in rectangular co-ordinates is:

$$\frac{\partial}{\partial x}(u\,\rho\,Y_i) + \frac{\partial}{\partial y}(v\,\rho\,Y_i) + \frac{\partial}{\partial x}(\rho\,Y_i\,u_i) + \frac{\partial}{\partial y}(\rho\,Y_i\,v_i) = \dot{w}_i \qquad (2.2)$$

$$i = 1, 2, \ldots\ldots N.$$

where u_i and v_i are diffusion velocities, in horizontal and vertical directions respectively, the calculation of these velocities is discussed in Section 2.3.3. The chemical production rate of species i, $\dot{w}_i$, in units of kg/m^3/s, is calculated from the elementary reaction rates. Its evaluation is discussed in detail in Chapter 3, illustrated with examples of a few kinetically reduced schemes.

2.2.2 Conservation of momentum

For a viscid Newtonian fluid with density ρ and viscosity μ, the Navier-Stokes equations are:

x-component,

$$\frac{\partial}{\partial x}(\rho\,u\,u) + \frac{\partial}{\partial y}(\rho\,u\,v) = -\frac{\partial p}{\partial x} + \frac{\partial}{\partial x}\left(\mu\frac{\partial u}{\partial x}\right) + \frac{\partial}{\partial y}\left(\mu\frac{\partial u}{\partial y}\right), \qquad (2.3)$$

y-component,

$$\frac{\partial}{\partial x}(\rho\,u\,v) + \frac{\partial}{\partial y}(\rho\,v\,v) = -\frac{\partial p}{\partial y} + \frac{\partial}{\partial x}\left(\mu\frac{\partial v}{\partial x}\right) + \frac{\partial}{\partial y}\left(\mu\frac{\partial v}{\partial y}\right) + \rho g, \qquad (2.4)$$

where g is the gravitational constant.

2.2.3 Conservation of energy

All species in the mixture are assumed to follow the perfect-gas law. Radiation and viscous dissipation are assumed to be negligible. The energy equation is then:

$$C_p \frac{\partial}{\partial x}(u\rho T) + C_p \frac{\partial}{\partial y}(v\rho T) - \frac{\partial}{\partial x}\left(\lambda \frac{\partial T}{\partial x}\right) - \frac{\partial}{\partial y}\left(\lambda \frac{\partial T}{\partial y}\right)$$

$$= u\frac{\partial p}{\partial x} + v\frac{\partial p}{\partial y} + \frac{\partial}{\partial x}\left(\rho \sum_{i=1}^{N} Y_i u_i h_i\right) + \frac{\partial}{\partial y}\left(\rho \sum_{i=1}^{N} Y_i v_i h_i\right) - \sum_{i=1}^{N} h_i W_i \dot{w}_i, \quad (2.5)$$

where T is temperature, h_i and W_i are the specific enthalpy in a mole basis and the molecular weight of the species i, respectively.

2.2.4 Auxiliary equations

In addition to the above conservation equations, several further relationships are required in order to close the system of equations.

1. For an ideal gas, equation of state:

$$p = \rho R T \sum_{i=1}^{N} \frac{Y_i}{W_i}, \quad (2.6)$$

where R is the molar gas constant.

2. Rather than set up a species continuity equation for all N components of the reacting system, the physical nature of the problem is preserved against numerical rounding errors by replacing one of the equations by:

$$\sum_{i=1}^{N} Y_i = 1. \quad (2.7)$$

In the present work, Y_{N_2} is obtained via,

$$Y_{N_2} = 1 - \sum_{\substack{i=1 \\ i \neq N_2}}^{N} Y_i, \quad (2.8)$$

and N_2 does not require a conservation equation.

3. In an N-component system, mass and mole fractions, Y_i and X_i, for a species i are related by:

$$Y_i = \frac{W_i X_i}{\sum_{j=1}^{N} (W_j X_j)}, \tag{2.9}$$

$$X_i = \frac{(Y_i / W_i)}{\sum_{j=1}^{N} (Y_j / W_j)}, \tag{2.10}$$

2.3 Transport Properties

The classical Chapman - Enskog procedure for obtaining the fundamental transport relationships satisfactory has been described by many authors (Hirschfelder *et al.* 1954, Chapman and Cowling 1970, Dixon-Lewis 1984). The procedure is very precise but very expensive to compute. Thus, for general modelling of reactive flows, a simplified version of the procedure is usually adopted. Details of the simplifying procedure presented here have been described by Dixon-Lewis (1984) and the procedure is claimed to give good approximations to values obtained with the more comprehensive one. All expressions described here are adopted in the reduced model. However, even this simplified procedure is expensive for computations and requires information on each individual species.

2.3.1 Binary diffusion coefficients

A number of parameters were evaluated in order to calculate the binary diffusion coefficients. First, it is necessary to obtain the reduced temperature T^*. This is given by:

$$T^* = k_B T / (eps)_{ij}, \tag{2.11}$$

where k_B is the Boltzmann constant. The Lennard-Jones (12 : 6) potential parameters for nonpolar molecules are $(eps)_{ij}$, and $(si)_{ij}$. Here, subscripts i and j signify a mixture of species

i and j, and a single suffix denotes a pure component. A list of values of $(eps)_i/k_B$ and $(si)_i$ for relevant species is given in Table 2.1. The combining rules for a mixture are given by:

$$(eps)_{ij} = \sqrt{(eps)_i \times (eps)_j}, \tag{2.12}$$

$$(si)_{ij} = \frac{1}{2}\left[(si)_i + (si)_j \right]. \tag{2.13}$$

Table 2.1

Lennard-Jones (12:6) potential parameters (Svehla, 1962) for various species.

Species	$(eps)/k_B$(K)	(si) (nm)
H[a]	37.0	0.2070
O	106.7	0.3050
OH	79.8	0.3147
N_2	71.4	0.3798
O_2	106.7	0.3467
H_2	59.7	0.2827
CO	91.7	0.3690
CO_2	195.2	0.3941
H_2O	260.0	0.2800
CH_2O	312.0	0.3758
CHO	187.0	0.3465
HO_2	168.0	0.3068
CH_4	148.6	0.3758
CH_3	312.0	0.3644

[a] This combination of parameters for atomic hydrogen uses $(eps)_H/k_B$ from Svehla (1962).

For the present computations, the reduced collision integrals $\Omega_{ij}^{(1,1)*}$ and the ratio of the collision integrals A_{ij}^*, defined by Eq. 2.14, required for computation of binary diffusion coefficients, are obtained from the appropriate polynomial coefficients, given in Table 2.2, for a fourth-order fit of $\Omega_{ij}^{(1,1)*}$ and a second order fit of A_{ij}^* over limited ranges of T^*.

$$A_{ij}^* = \frac{\Omega_{ij}^{(2,2)*}}{\Omega_{ij}^{(1,1)*}}. \tag{2.14}$$

Table 2.2

Coefficients of fourth-order polynomial fits of reduced collision integrals $\Omega_{ij}^{(1,1)*}$ and $A_{H_2O}^*$ and second-order fits of A_{ij}^* (Dixon-Lewis, 1984). Integrals $\Omega_{ij}^{(1,1)*}$, A_{ij}^* and $A_{H_2O}^*$ are expressed in the form $I(T^*) = a_0 + a_1 T^* + a_2 T^{*2} + a_3 T^{*3} + a_4 T^{*4}$.

I	T^*	a_0	a_1	a_2	a_3	a_4
$\Omega_{ij}^{(1,1)*}$	<5.0	2.3527333	-1.3589968	5.2202460E-1	-9.4262883E-2	6.4354629E-3
	5.0-10.0	1.2660308	-1.6441443E-1	2.2945928E-2	-1.6324168E-3	4.5833672E-5
	>10.0	0.85263337	-1.3552911E-2	2.6162080E-4	-2.4647654E-6	8.6538568E-9
A_{ij}^*	<5.0	1.1077725	-9.4802344E-3	1.6918277E-3		
	5.0-10.0	1.0871429	3.1964282E-3	-8.9285689E-5		
	>10.0	1.1059000	6.5136364E-4	-3.4090910E-6		
[a] $A_{H_2O}^*$	5.0-10.0	1.0764205	4.6037515E-2	-1.3506975E-2	1.5404522E-3	-6.0887567E-5
	>10.0	1.1141689	4.8711959E-4	-4.4570091E-6	9.9643413E-9	6.8639118E-11

[a] Table of coefficients of $A_{H_2O}^*$ is for $(eps)_{H_2O}$ = 260.0 K, and $(si)_{H_2O}$ = 0.28 nm.

For the self-diffusion coefficient of non-polar gases, the approximation of Monchick *et al.* (1965), obtained from experimental viscosity data, was used:

$$D_{ii} = 9.84708 \times 10^{-5} \frac{T A_{ii}^* \mu_i}{p m_i}, \qquad (2.15)$$

where m_i is the molecular mass. Units are : D, m²/s; μ, kg/m/s; and p, atm. For species containing one polar component, namely water, a large correction factor is needed to account for resonant collisions and the expression is:

$$D'_{pp} = \frac{D_{pp}}{1+\delta_{pp}}, \qquad (2.16)$$

where D_{pp} is the ordinary self-diffusion coefficient for the polar species and D'_{pp} is the corrected self-diffusion coefficient. The correction factor, δ_{pp}, is evaluated using the

method given by Mason and Monchick (1962). For water, $\delta_{pp} = 2958/T^{1.5}$. The approximated binary diffusion coefficient D_{ij}, between the species i and j, is given by

$$D_{ij} = 1.858\times10^{-3}\ T\frac{\sqrt{T/M_{ij}}}{p(si)_{ij}^2\Omega_{ij}^{(1,1)^*}T^*}, \qquad (2.17)$$

where the reduced mass M_{ij} is given in terms of molecular masses, m_i and m_j, of the species i and j:

$$M_{ij} = \frac{m_i m_j}{m_i + m_j}. \qquad (2.18)$$

2.3.2 Diffusion velocities

These are derived from the binary diffusion coefficients. The diffusion velocities of the species i, in the horizontal, u_i, and vertical, v_i, directions were approximated by the expressions:

$$u_i = -\frac{1-Y_i}{X_i\sum_{\substack{j=1\\ j\neq i}}^{N}\frac{X_j}{D_{ij}}}\frac{\partial X_i}{\partial x}, \qquad i = 1, 2, ..., N, \qquad (2.19)$$

$$v_i = -\frac{1-Y_i}{X_i\sum_{\substack{j=1\\ j\neq i}}^{N}\frac{X_j}{D_{ij}}}\frac{\partial X_i}{\partial y}, \qquad i = 1, 2, ..., N. \qquad (2.20)$$

For a reacting system with N species, there are N equations in each direction and N diffusion velocities. However, for mass conservation, it is further required that,

$$\sum_{i=1}^{N} (Y_i u_i) + \sum_{i=1}^{N} (Y_i v_i) = 0 . \qquad (2.21)$$

This requirement may not be satisfied, as there are N variables to satisfy $N + 1$ equations and error may result. Coffee and Heimerl (1981) introduced the correction terms u_c and v_c to account for the lack of mass conservation in the horizontal and vertical directions, respectively. The corrected diffusion velocities u_i^* and v_i^*, in the horizontal and vertical directions respectively, were given by:

$$u_i^* = u_i + u_c,$$

$$v_i^* = v_i + v_c. \qquad (2.22)$$

The method is efficient with moderate accuracy and is widely used in flame computations, including the CHEMKIN data base (Kee *et al.* 1985).

In 1981, Oran and Boris proposed a more accurate formulation, with Eqs. 2.19 and 2.20 as the first term in a more precise series solution for the diffusion velocity. The remaining terms, obtained by assuming all the velocities to be independent, but subjected to the constraint of Eq. 2.21, lead to the series:

$$u_i = - \frac{1-Y_i}{X_i \sum_{\substack{j=1 \\ j\neq i}}^{N} \frac{X_j}{D_{ij}}} \sum_{j=1}^{N} \left(\delta_{ij} + A_{ij} + \sum_{k=1}^{N} A_{ik} A_{kj} + \cdots \right) \frac{\partial X_j}{\partial x} , \qquad (2.23)$$

$$v_i = - \frac{1-Y_i}{X_i \sum_{\substack{j=1 \\ j\neq i}}^{N} \frac{X_j}{D_{ij}}} \sum_{j=1}^{N} \left(\delta_{ij} + A_{ij} + \sum_{k=1}^{N} A_{ik} A_{kj} + \cdots \right) \frac{\partial X_j}{\partial y} , \qquad (2.24)$$

where

$$A_{ij} = Y_i \delta_{ij} + \frac{X_i \left(1 - Y_j \right)}{D_{ij} \sum_{\substack{i=1 \\ i\neq j}}^{N} \frac{X_i}{D_{ij}}} \left(1 - \delta_{ij} \right) , \qquad (2.25)$$

and δ_{ij} is the Kronecker delta ($\delta_{ij} = 0$ for $i \neq j$; and $\delta_{ij} = 1$ for $i = j$). Evaluation using all three terms given in the series gives results accurate to a few percent, while reducing the number of computer operations from approximately N^3 to N^2. The method is computationally efficient and was employed for the reduced model computations reported in Chapter 5.

2.3.3 Viscosity

For a pure gas, the viscosity of a species i, was found from the expression given by Dixon-Lewis (1984):

$$\mu_i = 266.93 \times 10^{-7} \frac{\sqrt{m_i T}}{(si)_i^2 \Omega_{ii}^{(2,2)^*} T^*}. \tag{2.26}$$

For water, the expression proposed by Shifrin (1959) was employed:

$$\mu_{H_2O} = 4.07 \times 10^{-7}\ T - 3.07 \times 10^{-5}. \tag{2.27}$$

From these, the viscosity of the multi-component mixtures was found from the formulation of Buddenberg and Wilke (1949):

$$\mu = \sum_{i=1}^{N} \frac{\mu_i}{1 + 1.385 \dfrac{\mu_i RT}{X_i P W_i} \displaystyle\sum_{\substack{j=1, \\ j \neq i}}^{N} \frac{X_j}{D_{ij}}}. \tag{2.28}$$

2.3.4 Thermal conductivity

For a pure monatomic gas (hydrogen atoms), the thermal conductivity for the species i, λ_i, was given by (Dixon-Lewis, 1984):

$$\lambda_i = \frac{15}{4} \frac{R \mu_i}{W_i}. \tag{2.29}$$

For polyatomic gases, the modified Eucken correction (Dixon-Lewis, 1984) was employed,

$$\lambda_i = \frac{15}{4}\frac{R\mu_i}{W_i} + \frac{\rho D_{ii}}{\mu_i}\left(C_{v_i} - 1.5R\right), \tag{2.30}$$

in which C_{v_i} is the molar specific heat of species *i*. From these the conductivity of the multicomponent mixtures was found from the expression of Coffee and Heimerl (1981):

$$\lambda_{mix} = 0.5\left[\sum_{i=1}^{N} X_i\lambda_i + \left(\sum_{i=1}^{N}\frac{X_i}{\lambda_i}\right)^{-1}\right]. \tag{2.31}$$

2.3.5 Other properties

The specific heat and enthalpy of formation were calculated with NASA polynomials (William and Gardiner 1984) of the following form:

$$C_p / R = a_1 + a_2T + a_3T^2 + a_4T^3 + a_5T^4, \tag{2.32}$$

$$H^\circ / RT = a_1 + a_2T/2 + a_3T^2/3 + a_4T^3/4 + a_5T^4/5 + a_6/T, \tag{2.33}$$

where a_1, a_2 .....a_6 are best fit coefficients. For the present computations, those given by William and Gardiner (1984) were used.

2.3.6 Further approximation

The heat release rate model, avoids designation of individual species concentrations and the viscosity of the mixture in the Navier-Stokes equations was assumed to be a function of temperature and initial mixture composition only. It was correlated with temperature by the following expression, proposed and fitted to experimental data by Watson (1972). This expression also was employed by Draper (1977) for the modelling of a jet stirred combustor:

$$\mu = \frac{f}{1 + \frac{\phi}{c_1}\left(1 + \sqrt{\frac{c_2 f}{g}}\right)^2} + \frac{g}{1 + \frac{c_3}{\phi}\left(1 + \sqrt{\frac{c_4 g}{f}}\right)^2}, \tag{2.34}$$

where

$$f = \frac{\sqrt{T}}{c_1 + \frac{c_2}{T} + \frac{c_3}{T^2} + \frac{c_4}{T^3} + \frac{c_5}{T^4}},$$

$$g = \frac{\sqrt{T}}{c_1 + \frac{c_2}{T} + \frac{c_3}{T^2} + \frac{c_4}{T^3} + \frac{c_5}{T^4}}. \qquad (2.35)$$

The equivalence ratio is ϕ and c_1,.....c_5 are numerical constants, for which the values given by Watson (1972) were used.

2.4 Mathematical Formulation of Flame Stretch

2.4.1 Review of general expressions

Numerous expressions exist for flame stretch evaluations, a simple one is (Bradley *et al.* 1992):

$$\frac{1}{A}\frac{dA}{dt} = \left(\frac{v_1}{R} + \nabla_t \underline{v} \right) + \frac{u_n}{R}, \qquad (2.36)$$

in which R is the total radius of flame curvature, v_1 is the fluid velocity component normal to the flame and $\nabla_t \underline{v}$ denotes the fluid velocity gradient along the flame surface. This has been applied to a variety of laminar flame configurations by Bradley *et al.* (1992). However, for the present two-dimensional curved flames, this expression is inconvenient and a number of more general expressions now are reviewed and a more convenient one selected.

Stretch is defined as the fractional rate of change of flame area. This generalises the concept of stretch originally introduced by Karlovitz *et al.* (1953) to explain and correlate flame quenching mechanisms and describe turbulent flame structures. Expressions for stretch in terms of the local characteristics of the flow and the flame have been established

by Phillips (1972), Buckmaster (1979), Matalon (1983), Chung and Law (1984) and Candel and Poinsot (1990).

Phillips analysed the stretch of a moving interface. This was based on a Cartesian reference system and the stretch was deduced by examining the change of area of a small surface element (Fig. 2.1). The area is calculated after a time interval, δt, and the stretch rate, $(1/A)dA/dt$, is obtained as δt tends to zero. An expression is derived of the form (notation has been altered for consistency):

$$\frac{1}{A}\frac{dA}{dt} = \underset{(1)}{-(\nu_i \nu_j + \eta_i \eta_j)\frac{\partial V}{\partial x}} + \underset{(2)}{u_n(\nu_i \nu_j + \eta_i \eta_j)\frac{\partial n_i}{\partial x}}, \qquad (2.37)$$

where ν_i and η_i are components of two orthogonal unit vectors belonging to the local tangent plane, and n is the normal vector of the flame surface. The first term on the right represents the strain acting in the tangent plane, while the second describes curvature effects. With a similar reference system and approach, (Fig. 2.1), Matalon (1983) derived an alternative mathematical expression in a more compact form for flame stretch:

$$\frac{1}{A}\frac{dA}{dt} = \underset{(1)}{-\nabla \times (V \times n).n} + \underset{(2)}{(u_n + V.n)\nabla.n}, \qquad (2.38)$$

where the first term represents flame straining and the second flame curvature.

In an attempt to provide a unified view of the different expressions for flame stretch, Candel and Poinsot (1990), unlike previous research workers, deduced the following flame stretch expression from a general transport theorem which considered a surface moving in space with an arbitrary velocity (Fig. 2.2):

$$\frac{1}{A}\frac{dA}{dt} = -nn : \nabla V + \nabla.V + u_n \nabla.n\,. \qquad (2.39)$$

They showed that their expression for stretch is mathematically identical to those of Phillips (1972) and Matalon (1983), as was also the way in which they had grouped the

strain and curvature terms. As a result of this review, it was decided that Matalon's Eq 2.38 was the most suitable for application in the present context. It is simple and each component readily can be evaluated.

2.4.2 Stretch expression for the present geometry

Consider the general expression for flame stretch as given in Eq. 2.38. For a two-dimensional, steady state flow field, the expression reduces to (Appendix A):

$$\frac{1}{A}\frac{dA}{dt} = \left(1 - n_i^2\right)\frac{\partial u}{\partial x} - n_i n_j\left(\frac{\partial u}{\partial y} + \frac{\partial v}{\partial x}\right) + \left(1 - n_j^2\right)\frac{\partial v}{\partial y} + u_n\left(\frac{\partial n_i}{\partial x} + \frac{\partial n_j}{\partial y}\right). \tag{2.40}$$

For a steady state two-dimensional curved flame with two-dimensional flow field as shown in Fig. 2.3, the normal unit vector and velocity vector are given by:

$$n = \left(-\sin\alpha\, i - \cos\alpha\, j\right), \tag{2.41}$$

$$V = \left(u\, i + v j\right). \tag{2.42}$$

Thus, Eq. 2.40 reduces to (Appendix A),

$$\frac{1}{A}\frac{dA}{dt} = \cos^2\alpha\,\frac{\partial u}{\partial x} - \sin\alpha\cos\alpha\left(\frac{\partial u}{\partial y} + \frac{\partial v}{\partial x}\right) + \sin^2\alpha\,\frac{\partial v}{\partial y} + u_n\left(\sin\alpha\,\frac{\partial \alpha}{\partial y} - \cos\alpha\,\frac{\partial \alpha}{\partial x}\right), \tag{2.43}$$

with unidirectional shear flow, $V = u\,(y)\,i$, Eq. 2.43 becomes:

$$\frac{1}{A}\frac{dA}{dt} = -\sin\alpha\cos\alpha\,\frac{\partial u}{\partial y} + u_n\,\frac{\partial \alpha}{\partial x}, \tag{2.44}$$

which is identical to the expression of Matalon (1983) and is the one used in the present study.

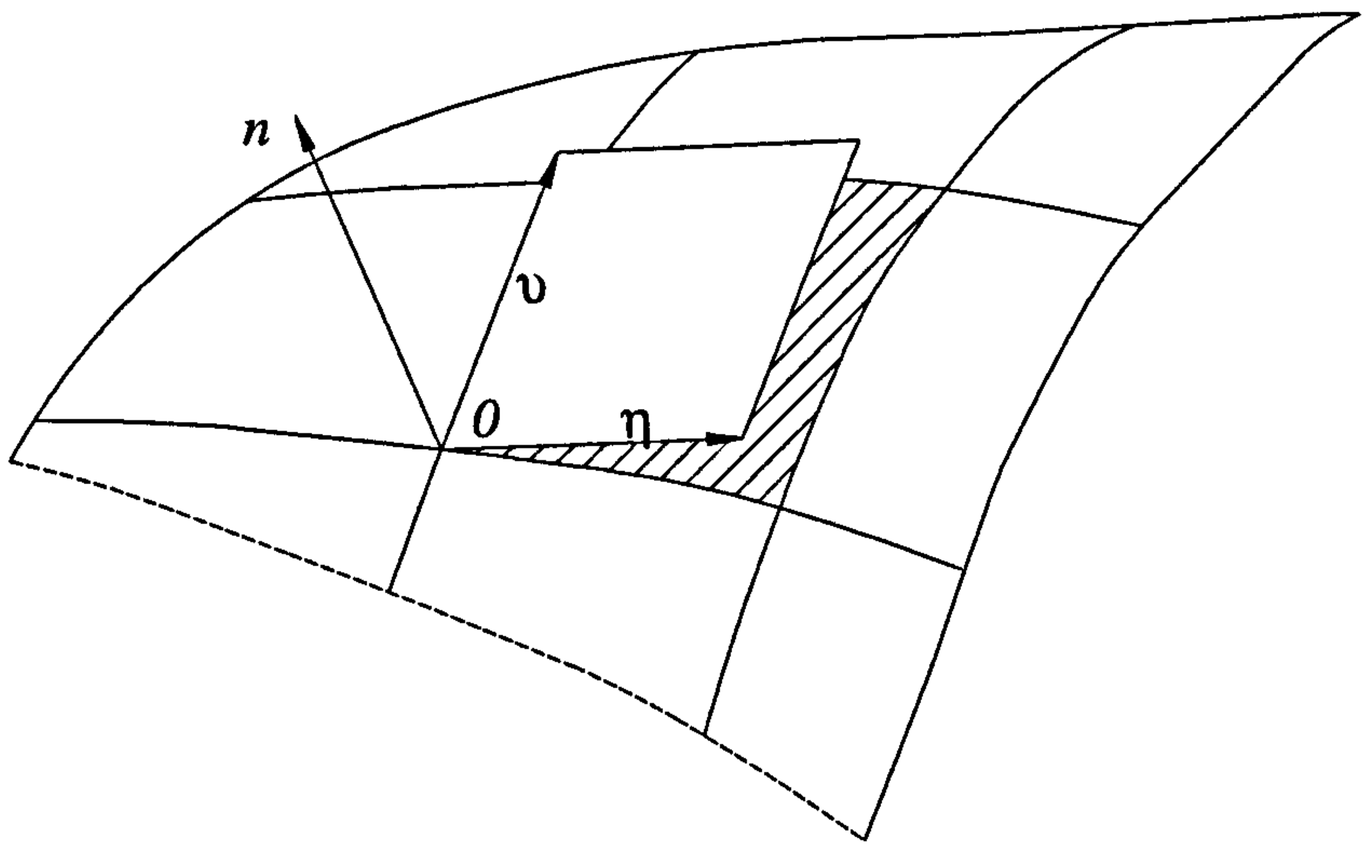

Fig. 2.1 Schematic representation of an element on the flame surface

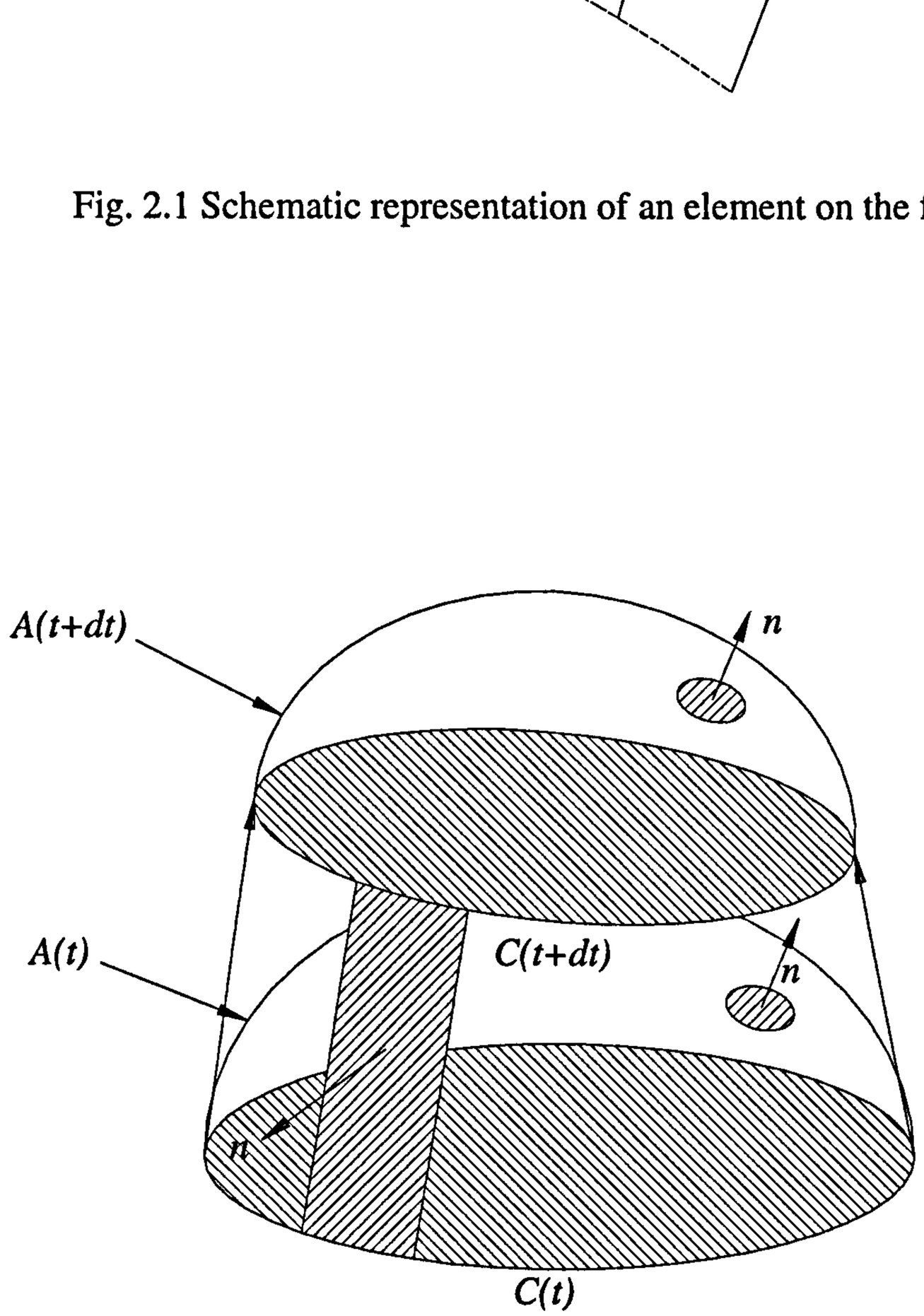

Fig. 2.2 Schematic representation of the front at two time instants t and $t + dt$.

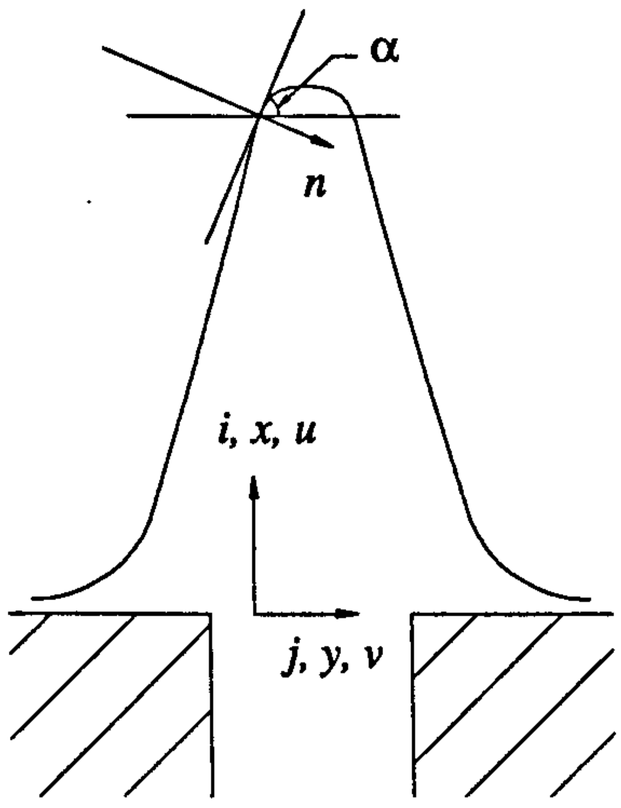

Fig. 2.3 Nomenclature for stationary two-dimensional flame

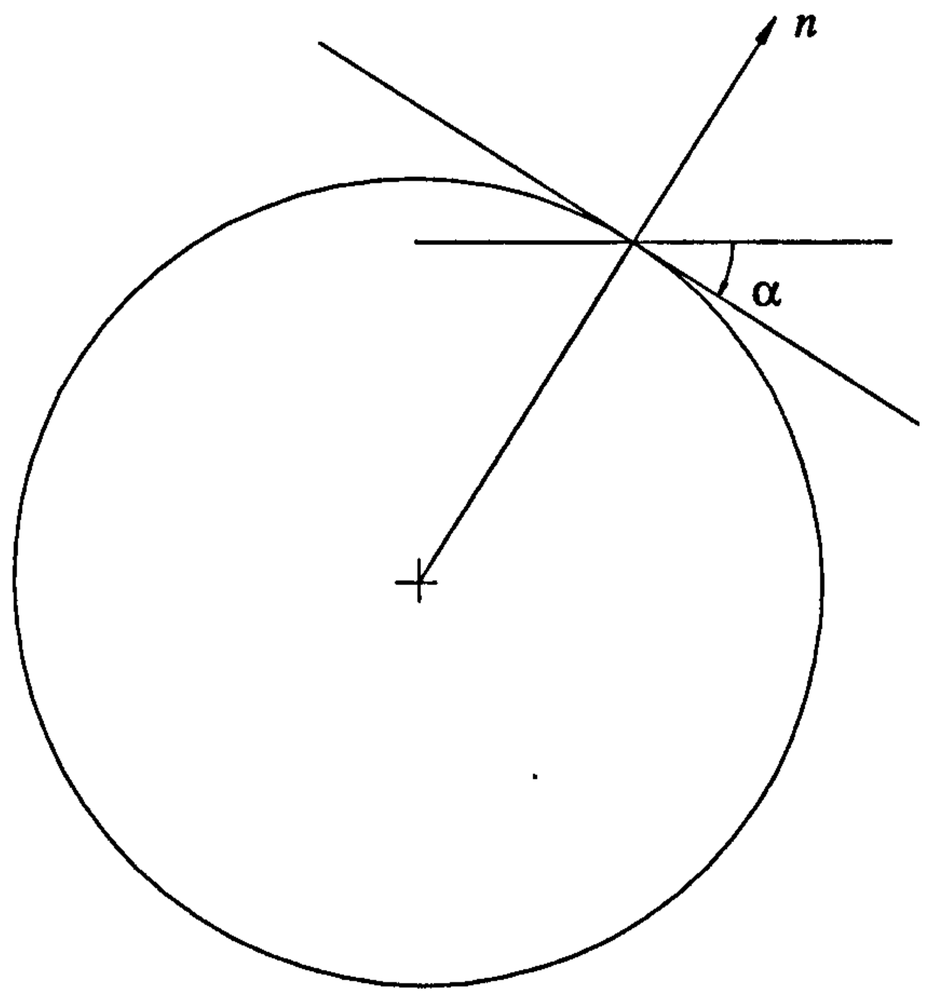

Fig. 2.4 Nomenclature for expanding cylindrical and spherical flames

CHAPTER THREE
Formulation of Chemical Reaction Rates

3.1 Introduction

This Chapter concentrates on the evaluation of the chemical source terms. Three approaches have been adopted. First, the "full" chemical reaction scheme of Dixon-Lewis is presented. The scheme has been used for numerous one-dimensional flame computations, sometimes with strain. In particular, it has been employed to obtain volumetric heat release rate correlations. However, the chemical scheme becomes very expensive, and even prohibitive, when used in two-dimensional flame computations. A number of reduced chemical kinetic schemes, which are computationally much more economic, are reviewed, and schemes appropriate for the current computations are identified. All of these schemes involve the same four global reactions. Three of the reduced schemes, namely, the P1 scheme (Peters 1985), the PW scheme (Peters and Williams 1987), and the MP scheme (Mauss and Peters 1993), are considered in more detail. All three schemes were employed in subsequent computations, but the P1 scheme was responsible for all of the results.

Finally, the simplified approach, originally contemplated, but subsequently abandoned, is presented. In this the volumetric heat release is expressed as a function of the reaction progress variable, based on temperature. In principle, account can be taken of the effects of positive flame stretch and the volumetric heat release rate through the flame found from what is mathematically a one-dimensional flame solution (Section 3.4).

3.2 The "Full" Reaction Scheme

A variety of "full" reaction mechanisms exists (Dixon-Lewis *et al.* 1984, Warnatz 1984). The one presented here is that employed by Dixon-Lewis (1984) in numerous flame computations. It consisted of 53 elementary reactions, involving a total of 18 chemical species, and has been used to obtain the heat release rate correlation in Section 3.4. The reactions and rate parameters are given in Table 3.1.

Table 3.1

Parameters for forward rate coefficients and independent equilibrium constants used in methane-air flame mechanism (Dixon-Lewis 1984). Rate coefficients are expressed as $\kappa = AT^{B}\exp(-C/T)$ and equilibrium constants as $K = DT^{E}\exp(-F/T) = \kappa_{forward}/\kappa_{reverse}$, both in cm mole s units

No.	Reaction	A	B	C (K)	D	E	F (K)
1	$OH+H_2 \Leftrightarrow H_2O+H$	1.17E9	1.3	1825	0.21	0	-7640
2	$H+O_2 \Leftrightarrow OH+O$	1.42E14	0	8250	300.0	-0.372	8565
3	$O+H_2 \Leftrightarrow OH+H$	1.8E10	1.0	4480	2.27	0	938
4[a]	$H+O_2+H_2 \Leftrightarrow HO_2+H_2$	1.03E18	-0.72	0	0.745	0	-23380
7	$H+HO_2 \Leftrightarrow OH+OH$	1.4E14	0	540			
7[a]	$H+HO_2 \Leftrightarrow O+H_2O$	1.0E13	0	540			
12	$H+HO_2 \Leftrightarrow H_2+O_2$	1.25E13	0	0			
13	$OH+HO_2 \Leftrightarrow H_2O+O_2$	7.5E12	0	0			
14[b]	$O+HO_2 \Leftrightarrow OH+O_2$	1.4E13	0	540			
		1.25E12	0	0			
15	$H+H+H_2 \Leftrightarrow H_2+H_2$	9.2E16	-0.6	0			
	$H+H+N_2 \Leftrightarrow H_2+N_2$	1.0E18	-1.0	0			
	$H+H+O_2 \Leftrightarrow H_2+O_2$	1.0E18	-1.0	0			
	$H+H+H_2O \Leftrightarrow H_2+H_2O$	6.0E19	-1.25	0			
	$H+H+CO \Leftrightarrow H_2+CO$	1.0E18	-1.0	0			
	$H+H+CO_2 \Leftrightarrow H_2+CO_2$	5.49E20	-2.0	0			
	$H+H+CH_4 \Leftrightarrow H_2+CH_2$	5.49E20	-2.0	0			
16	$H+OH+M \Leftrightarrow H_2O+M$						
	$M=H_2,O_2,N_2,CO,CO_2,CH_4$	1.6E22	-2.0				
	$M=H_2O$	8.0E22	-2.0	0			
17	$H+O+M \Leftrightarrow OH+M$						
	$M=H_2,O_2,N_2,CO,CO_2,CH_4$	6.2E16	-0.6	0			
	$M=H_2O$	3.1E17	-0.6	0			
18	$OH+OH \Leftrightarrow O+H_2O$	5.75E12	0	390			
21	$OH+CO \Leftrightarrow CO_2+H$	1.5E7	1.3	-385	3.82E-7	1.19	-13067
22[a]	$O+CO+H_2 \Leftrightarrow CO_2+H_2$	5.4E15	0	2300			
23[a]	$H+CO+H_2 \Leftrightarrow CHO+H_2$	5.0E14	0	755	1.7	0	-7080
24	$CHO+O_2 \Leftrightarrow HO_2+CO$	2.5E12	0	0			
25	$CHO+H \Leftrightarrow H_2+CO$	4.0E13	0	0			
26	$CHO+OH \Leftrightarrow H_2O+CO$	5.0E12	0	0			
27	$CHO+O \Leftrightarrow OH+CO$	1.0E13	0	0			
28	$CH_4+H \Leftrightarrow CH_3+H_2$	1.24E14	0	6000	29.3	0	3550
29	$CH_4+OH \Leftrightarrow CH_3+H_2O$	2.2E13	0	2500			
30	$CH_4+O \Leftrightarrow CH_3+OH$	1.9E14	0	5900			

Table 3.1 (continued)

No.	Reaction	A	B	C (K)	D	E	F (K)
31	$CH_3+O \Leftrightarrow CH_2O+H$	1.8E14	0	240	0.072	0	-35100
32	$CH_2O+H \Leftrightarrow CHO+H_2$	1.0E7	2.0	1000	10.6	0	-7778
33	$CH_2O+OH \Leftrightarrow CHO+H_2O$	5.5E13	0	600			
34	$CH_2O+O \Leftrightarrow CHO+OH$	6.0E13	0	1960			
39	$CH_3+CHO \Leftrightarrow CH_4+CO$	1.0E12	0	0			
40	$CH_3+HO_2 \Leftrightarrow CH_4+O_2$	2.0E12	0	0			
41	$CH_3+HO_2 \Leftrightarrow CH_3O+OH$	2.0E13	0	0			
42	$CH_3O+H \Leftrightarrow CH_2O+H_2$	5.0E13	0	0			
43	$CH_3O+OH \Leftrightarrow CH_2O+H_2O$	2.5E13	0	0			
44	$CH_3O+O \Leftrightarrow CH_2O+OH$	2.5E13	0	0			
45[c]	$CH_3+CH_3 \Leftrightarrow C_2H_6$	2.8E14	-0.4	0	5.33E-7	0	-43880
46	$C_2H_6+H \Leftrightarrow C_2H_5+H_2$	5.5E2	3.5	2620	21.7	0	-1140
47	$C_2H_6+OH \Leftrightarrow C_2H_5+H_2O$	6.3E6	2.0	3250			
48	$C_2H_6+O \Leftrightarrow C_2H_5+OH$	3.0E7	2.0	2570			
49	$C_2H_5+O_2 \Leftrightarrow C_2H_4+HO_2$	2.0E13	0	2510			
50	$C_2H_5+H \Leftrightarrow CH_3+CH_3$	4.8E13	0	0			
51	$C_2H_5+O \Leftrightarrow CH_3+CH_2O$	5.0E13	0	0			
52	$C_2H_4+O \Leftrightarrow CH_3+CHO$	2.0E13	0	1300			
53	$C_2H_4+OH \Leftrightarrow CH_3+CH_2O$	4.0E13	0	760	1.9	0	-7910

[a] Except for H_2O in reaction (23), Chaperon efficiencies relative to H_2 = 1.0 are 0.44, 0.35, 6.5, 0.74, and 1.47 for N_2, O_2, H_2O, CO, and CO_2 respectively. In reaction (23), H_2O was assigned an efficiency of 1.0.

[b] $\kappa_{14} = \kappa_{14a} + \kappa_{14b}$.

[c] This is the high pressure value κ_x, and must be multiplied by an RRKM factor. RRKM factors were calculated using the method and data given by Troe.

3.3 The Reduced Four Step Chemical Kinetic Schemes

Those mechanisms that have four global reaction steps, generally known as reduced four-step mechanisms, are becoming popular for numerical calculations. All of the schemes described consist of seven major (or active) species, namely, CH_4, O_2, CO_2, H_2O, CO, H and H_2, and have the same global reaction steps listed below:

$$CH_4 + 2H + H_2O = CO + 4H_2, \qquad \text{(I)}$$

$$CO + H_2O = CO_2 + H_2, \qquad \text{(II)}$$

$$H + H + M = H_2 + M, \qquad \text{(III)}$$

$$O_2 + 3H_2 = 2H + 2H_2O. \qquad \text{(IV)} \qquad (3.1)$$

Further reduction to three global steps is possible (Peters and Williams 1987, Seshadri and Peters 1988 and Mauss and Peters 1993). However, such three-step

schemes generally have been designed for high pressure combustion and have had but limited success. Nevertheless, they are relatively simple to implement and ideal for asymptotic analysis where simplicity is preferred over accuracy (Seshadri and Peters 1988). While all aspects of reduced kinetic mechanisms for methane-air flame have been summarised by Smooke (1991), Peters and Rogg (1993) provide current information on reduced mechanisms for a variety of mixtures. A survey of four-step reduced mechanisms for methane oxidation is summarised in Table 3.2.

In 1985, Peters proposed a detailed systematic procedure for the reduction of a "complete" methane-air reaction mechanism. The proposed procedure was applied to the "short mechanism" of Miller *et al.* (1984), containing about 40 reactions, and led to a four-step reaction mechanism. This mechanism, referred to as the P1 scheme, is discussed in more detail in Section 3.3.1.1.

In 1987, Peters and Kee applied it to a one-dimensional, stretched, stagnation point, diffusion flame, and gave detailed procedures for the numerical calculations. A stretch rate of 450 s^{-1} for flame extinction was reported. Later in the same year, Peters and Williams (1987) introduced another reduced chemical scheme (PW). This scheme, reduced systematically from a C_1-chain mechanism, consisted of 31 reversible elementary-steps. It included a pressure dependent elementary reaction and was suitable for high pressure conditions. More details of this PW scheme are given in Section 3.3.1.2. With a starting mechanism of 22 reversible elementary reactions involving only the C_1-chains, Seshadri and Peters (1988) derived a three-step chemical kinetic mechanism, (SP) and analysed the asymptotic structure of a counter flow methane-air diffusion flame. Two years later, Seshadri and Peters (1990) proposed another four-step mechanism, (SP1), reduced from a starting mechanism with elementary reactions identical to those of Peters and Williams (1987), but with different rate constants. With this SP1 scheme, the authors extended the previous analysis of Peters and Williams on the structure of premixed methane-air flames, in which a reduced three-step chemical kinetic mechanism had been used. The burning velocity was calculated for a stoichiometric methane-air flame for values of initial pressure between 1 and 80 atm. At

Table 3.2 A review of reduced kinetic schemes for methane-air flames

Year	Authors	Code	Starting Mechanisms		Reduced Mechanisms			
			Number of Reactions[1]	Reference	Number of Reactions	Number of Steady Species	Test Case[2]	Burning velocity (cm/s)[3]
1985	Peters	P1	40	Miller *et al.* 1984	18	2	Premixed Planar (A & C)	40.44
1986	Paczko *et al.*	PLP	46	Paczko *et al.*1986	46	16	Premixed Planar (C)	37.3
1987	Peters & Kee	PK[4]	40	Miller *et al.* 1984	18	2	Stagnation Diffusion (C)	------
1987	Peters & Williams	PW	31	Peters & Williams 1987	31	7	Premixed Planar (A)	(35.8 - 49.9)
		PW1	22	Peters & Williams 1987	10	2	-------	------
1988	Seshadri & Peters	SP[5]	22	Seshadri & Peters 1988	10	2	Diffusion (A)	------
1990	Seshadri & Peters	SP1	25	Seshadri & Peters 1990	21	5	Premixed Planar (A)	(35)
1990	Bilger *et al.*	BSK	51	Bilger *et al.* 1990	26	9	Counterflow Diffusion (C)	------
1991	Peters	P2	25	Smooke & Giovangigli 1991	17	6	Premixed Planar (C)	37.9
1993	Mauss & Peters	MP	40	Peters 1993	33	9	Premixed Planar (C)	36
		MP1	61	Peters 1993	52	15	Premixed Planar (C)	41

Note :

[1] Forward and backward elementary reactions counts as a single reaction.

[2] A denote Asymptotic analysis, C denote Computational analysis.

[3] Values for stoichiometric mixtures are quoted. Bracketed values were analytically calculated.

[4] This scheme is identical to the P1 scheme.

[5] This scheme is identical to the PW1 scheme.

atmospheric pressure, this burning velocity was 35 cm/s. It decreased with increasing pressure, in agreement with experiments.

Later in the same year, Bilger *et al.* (1990) proposed a four-step reduced mechanism, (BSK). This scheme was derived from a 58-step mechanism, which was a development of the "short" mechanism of Miller *et al.* (1984), with many of the updated features of the mechanism of Glarborg *et al.* (1986). The authors of the BSK scheme claimed it was an improvement on the P1 scheme, due largely to replacement of the partial equilibrium assumption for O atoms by a steady state approximation. This resulted in different O atom concentrations on the rich side of the diffusion flame.

Peters (1993) has summarised the schemes for various hydrocarbon flames. A detailed kinetic mechanism, with 82 elementary reactions, was suggested as providing a common basis for hydrogen and hydrocarbons, up to the C_3-chain. Numerical procedures for solutions of one-dimensional, unstretched, premixed flames and counterflow diffusion flames also were included. In a separate chapter, by comparing burning velocity values over a range of equivalence ratios from 0.375 to 1.5, Mauss and Peters demonstrated that, while burning velocities computed with the C_1 and C_2 chains starting mechanisms were very similar for lean mixtures, values computed with the C_1 mechanism, for rich mixtures, were lower than those with the C_2 mechanism, which were in good agreement with experiments. From these C_1 and C_2 chains starting mechanisms, they derived two reduced mechanisms, referred to here as the MP and MP1 schemes, respectively. With the MP scheme, the starting 40 elementary reactions were reduced to 33 reactions, with 9 steady state species. A burning velocity of 36 cm/s, for stoichiometric methane-air, was reported. The MP1 scheme contains 52 elementary reactions and was reduced from the original 61 reactions, with 15 steady species. With this a burning velocity of 41 cm/s was computed for stoichiometric methane-air. The MP scheme is presented and discussed in Section 3.3.1.3.

From the survey, it is clear that in the early P1 and PK reaction schemes, most minor species, apart from O and OH, were neglected by application of partial equilibrium assumptions. Steady state assumptions were applied to O and OH. In schemes

developed subsequently (PLP, PW, SP, SP1, BSK, P2, MP and MP1 in Table 3.2), more elementary reactions were considered. Steady state assumptions were applied to most minor species, enabling their concentrations to be expressed in terms of other species concentrations and reaction rates. The presence of more minor steady state species resulted in a more realistic, but more complicated scheme.

Theoretically, the computational effort depends on the number of principal species, and the introduction of more steady state species resulted in only a marginal increase in CPU time. However, in the present study, numerical experiments with the P1, PW and MP schemes applied to the two-dimensional flame showed that, while the CPU times for each iteration were very similar, numerical solutions with the PW and MP schemes required much smaller relaxation factors and many more iterations for convergence. This is probably because of the complex relationships introduced with the additional steady state species in the more recent schemes. As pointed out by Peters (1985), "although there are enough equations for these (other minor) species, the nonlinearity of the algebraic equations would complicate the numerical solution considerably". It is, therefore, not surprising that Coelho and Pereira (1993) preferred the earlier P1 scheme for their two-dimensional flame modelling.

In 1990, when compared their reduced scheme to the P1 scheme, Bilger *et al.* concluded that "with due attention to detail both formulations (P1 and BSK schemes) are equivalent, and the choice is a mater of emphasis. In premixed flames the Peters formulation probably reflects the physics better". Since the present study deals with premixed flames only, for the sake of simplicity and rate of convergence, the P1 scheme is employed in all of the analyses.

3.3.1 Formulation of the reduced schemes

The definition of a "reduced" mechanism must start with a "complete" mechanism. Unlike some earlier approaches (Westbrook and Dryer, 1981, Reitz and Bracco, 1983 and Coffee *et al.* 1983), which involved the adjustment of rate coefficients and reaction orders to fit results of experiments or of computations with more complete chemistry,

the schemes considered here take listed rate coefficients directly from a "complete" scheme. Consequently, the developed reduced mechanism contains many of the features of the complete kinetic scheme. Most of the elementary reactions comprised in the three reduced mechanisms, namely, the P1, PW and MP schemes, are presented in Table 3.3. The numbering of the elementary reactions in the original scheme by Peters (1993) has been altered for convenience.

Table 3.3

Recommended rate coefficients from Peters (1993): $k = BT^n\exp(-E/RT)$, B in moles, cm, sec, E in kJ/mole

	Reaction	B	n	E
1	$CH_4 + H \rightarrow CH_3 + H_2$	2.20E4	3.00	36.60
1b	$CH_3 + H_2 \rightarrow CH_4 + H$	8.39E2	3.00	34.56
2	$CH_4 + OH \rightarrow CH_3 + H_2O$	1.60E6	2.10	10.30
2b	$CH_3 + H_2O \rightarrow CH_4 + OH$	2.63E5	2.10	70.92
3	$CH_3 + O \rightarrow CH_2O + H$	7.00E13	0.00	0.00
4	$CH_2O + H \rightarrow CHO + H_2$	2.50E13	0.00	16.70
5	$CH_2O + OH \rightarrow CHO + H_2O$	3.00E13	0.00	5.00
6	$CHO + H \rightarrow CO + H_2$	2.00E14	0.00	0.00
7	$CHO + M \rightarrow CO + H + M$	7.10E14	0.00	70.30
7b	$CO + H + M \rightarrow CHO + M$	1.14E15	0.00	9.97
8	$CHO + O_2 \rightarrow CO + HO_2$	3.00E12	0.00	0.00
9	$CO + OH \rightarrow CO_2 + H$	4.40E6	1.50	-3.10
9b	$CO_2 + H \rightarrow CO + OH$	4.96E8	1.50	89.76
10	$O_2 + H \rightarrow OH + O$	2.00E14	0.00	70.30
10b	$OH + O \rightarrow O_2 + H$	1.57E13	0.00	3.52
11	$H_2 + O \rightarrow OH + H$	5.06E4	2.67	26.30
11b	$OH + H \rightarrow H_2 + O$	2.22E4	2.67	18.29
12	$H_2 + OH \rightarrow H_2O + H$	1.00E8	1.60	13.80
12b	$H_2O + H \rightarrow H_2 + OH$	4.31E8	1.60	76.46
13	$OH + OH \rightarrow H_2O + O$	1.50E9	1.14	0.42
13b	$H_2O + O \rightarrow OH + OH$	1.47E10	1.14	71.09
14	$O_2 + H + M \rightarrow HO_2 + M$	2.30E18	-0.80	0.00
14b	$HO_2 + M \rightarrow O_2 + H + M$	3.19E18	-0.80	195.39
15	$OH + H + M \rightarrow H_2O + M$	2.20E22	-2.00	0.00

Table 3.3 (Continued)

No.	Reaction		*B*	*n*	*E*
16	$HO_2 + H \rightarrow OH + OH$		1.50E14	0.00	4.20
17	$HO_2 + H \rightarrow H_2 + O_2$		2.50E13	0.00	2.90
18	$HO_2 + OH \rightarrow H_2O + O_2$		6.00E13	0.00	0.00
19	$HO_2 + H \rightarrow H_2O + O$		3.00E13	0.00	7.20
20	$CH + O_2 \rightarrow CHO + O$		3.00E13	0.00	0.00
21	$CHO + OH \rightarrow CO + H_2O$		1.00E14	0.00	0.00
22	$CH_2 + H \rightarrow CH + H_2$		8.40E9	1.50	1.40
22b	$CH + H_2 \rightarrow CH_2 + H$		5.83E9	1.50	13.08
23	$CH_2 + O_2 \rightarrow CO + OH + H$		6.50E12	0.00	6.30
24	$CH_2 + O_2 \rightarrow CO_2 + H + H$		6.50E12	0.00	6.30
25	$CH_3 + H \rightarrow CH_2 + H_2$		1.80E14	0.00	63.00
25b	$CH_2 + H_2 \rightarrow CH_3 + H$		3.68E13	0.00	44.30
26	$CH_3 + H \rightarrow CH_4$	k_∞	2.11E14	0.00	0.00
		k_0	6.26E23	-1.80	0.00
27	$HO_2 + O \rightarrow OH + O_2$		1.80E13	0.00	-1.70
28	$HO_2 + HO_2 \rightarrow H_2O_2 + O_2$		2.50E11	0.00	-5.20
29	$OH + OH + M \rightarrow H_2O_2 + M$		3.25E22	-2.00	0.00
29b	$H_2O_2 + M \rightarrow OH + OH + M$		1.69E24	-2.00	202.29
30	$H_2O_2 + H \rightarrow H_2O + OH$		1.00E13	0.00	15.00
31	$H_2O_2 + OH \rightarrow H_2O + HO_2$		5.40E12	0.00	4.20
31b	$H_2O + HO_2 \rightarrow H_2O_2 + OH$		1.80E13	0.00	134.75
32	$H + H + M \rightarrow H_2 + M$		1.80E18	-1.00	0.00
33	$O + O + M \rightarrow O_2 + M$		2.90E17	-1.00	0.00
34	$CO_2 + CH \rightarrow CHO + CO$		3.40E12	0.00	2.90
35	$CH_2 + O \rightarrow CO + H + H$		8.00E13	0.00	0.00
36	$CH_2O + O \rightarrow CHO + OH$		3.50E13	0.00	14.60
37	$CH_2O + M \rightarrow CHO + H + M$		1.40E17	0.00	320.00
38	$CH_3 + CH_3 \rightarrow C_2H_6$	k_∞	3.61E13	0.00	0.00
		k_0	1.27E41	-7.00	11.56
39	$CH_3 + O_2 \rightarrow CH_2O + OH$		3.40E11	0.00	37.40
40	$CH_4 + O \rightarrow CH_3 + OH$		1.20E7	2.10	31.90

3.3.1.1 The P1 scheme

By examining numerical solutions of methane-air flames with a numerical code provided by Warnatz (1981), Peters (1985) proposed the retention of the 18 major-steps by which the methane is oxidised in Miller's "short" scheme (Miller *et al.* 1984). These are the elementary reactions 1 to 18, in Table 3.3. In these reactions, the methane oxidation starts with the break up of fuel molecules mainly through reactions 1 and 2. Formaldehyde CH_2O is formed via reaction 3, and reacts with H and OH to form CHO by reactions 4 and 5. In reactions 6 to 8, the CHO radical is converted into CO, which is then oxidised in reaction 9. Next, the consumption of oxygen and the formation of radicals is attributed to the reactions of the hydrogen-oxygen system in reactions 10 to 13. Finally, chain breaking occurs mainly through the three-body reactions 14 and 15. Reaction 14 is followed by reactions 16 to 18. This mechanism is completed in the sense that there is a path from the reactants CH_4 and O_2 to the products CO_2 and H_2O.

With the numerical code provided by Warnatz (1981), Peters (1985) demonstrated that some of the intermediate species were present in only very small concentrations, as their production was much less than their consumption rate. Others, such as H, may have a high diffusion rate and hence a large influence on the global reactions, even though their concentration is small. Table 3.4 shows the maximum intermediate species mole fractions, obtained from the calculation with a large mechanism for diffusion flame by Miller *et al.* (1984), and their values when appropriately weighted with their diffusion rates. This enabled identification of some of the species for which the steady state assumption would be justified.

Table 3.4

Maximum Mole fractions of intermediate species in a Methane-Air Flame ($x10^{-2}$) (Miller et al, 1984)

	H	OH	O	H_2	CO	CH_3	CH_2O	CHO	HO_2
Original	0.429	0.629	0.314	3.23	4.71	0.325	0.050	0.0008	0.003
Weighted	1.626	0.724	0.368	8.815	4.17	0.389	0.059	0.0008	0.003

This assumption was applied to those species whose weighted mole fraction was smaller than 0.01 (Peters 1985). Hence, the intermediate species OH, O, HO_2, CH_3, CH_2O, CHO were assumed to be in a "steady state". On the basis of these six "steady state" conditions, Peters eliminated six elementary reactions, namely, reactions 3, 4, 7, 11, 12 and 17 in Table 3.3. In addition, the reactions 5, 13 and 18, which have the same effect as the corresponding parallel reactions 4, 12 and 17, also were eliminated.

Partial equilibrium assumptions, applied to reactions 11, 12 and 13, enabled concentrations of the two intermediate species, OH and O not included in the global reactions (Eq. 3.1), to be expressed explicitly in terms of other species concentrations and rate constants. With reaction 12 equilibrated:

$$C_{OH} = \frac{C_H C_{H_2O}}{C_{H_2} K_{12}} . \tag{3.2}$$

With reaction 11 equilibrated:

$$C_O = \frac{C_H C_{OH}}{C_{H_2} K_{11}} = \frac{C_H^2 C_{H_2O}}{C_{H_2}^2 K_{11} K_{12}} . \tag{3.3}$$

Here C_i denotes the concentration of species i and K_{11} and K_{12} are equilibrium constants applied to the elementary reactions 11 and 12. These values are given by Peters (1985):

$$K_{12} = 0.2657 \times T^{-0.0247} \exp^{\frac{15083}{RT}} , \tag{3.4}$$

where T is the temperature (K) and R the universal gas constant = 1.986. Further application of partial equilibrium assumption to reaction 10 yields the relation:

$$K_{IV} = K_{10} K_{11} K_{12}^2 , \tag{3.5}$$

and Peters (1985) gives:

$$K_{IV} = 11.283 \times T^{-0.2484} \exp^{\frac{11400}{RT}} . \tag{3.6}$$

Now:

$$K_{II} = \frac{K_9}{K_{12}}, \tag{3.7}$$

and Peters (1985) gives:

$$K_{II} = 3.828 \times 10^{-5}\, T^{0.8139}\, \exp^{\frac{9839}{RT}}. \tag{3.8}$$

Note that although the equilibrium constant K_{11} appears in Eqs. 3.3 and 3.5, its evaluation is not required, as it is computationally eliminated if K_{IV} is given. For the 7 main species, the concentration of species *i* is given by:

$$C_i = \frac{\rho Y_i}{W_i}, \tag{3.9}$$

and the molar concentration:

$$C_M = \sum_{i=1}^{n} z_i C_i, \tag{3.10}$$

where the third-body efficiencies z_i are listed in Table 3.5.

Table 3.5

Third-body efficiencies for calculation of molar density (Peters 1985).

Species	H	H_2	O_2	H_2O	CO	CO_2	CH_4	N_2
z_i	1.0	1.0	0.4	6.5	0.75	1.5	6.54	0.4

By introducing steady state and partial equilibrium assumptions, the reaction rates, $w_1, w_2 \ldots\ldots w_{16}$ of the *i*th elementary reaction are obtained by Peters:

$$w_1 = k_1\, C_{CH_4}\, C_H,$$

$$w_2 = \frac{k_2\, C_{H_2O}}{K_{12}\, C_{H_2}}\, C_{CH_4}\, C_H,$$

$$w_6 = \frac{k_1 + k_2[C_{H_2O}/(C_{H_2} K_{12})]}{k_6 C_H + k_7 C_M + k_8 C_{O_2}}\, k_6\, C_{CH_4}\, C_H^2,$$

$$w_8 = \frac{k_1 + k_2[C_{H_2O}/(C_{H_2} K_{12})]}{k_6 C_H + k_7 C_M + k_8 C_{O_2}}\, k_8\, C_{O_2}\, C_{CH_4}\, C_H,$$

$$w_9 = \frac{k_9}{K_{12}} C_H \left(\frac{C_{CO} C_{H_2O}}{C_{H_2}} - \frac{C_{CO_2}}{K_{II}} \right),$$

$$w_{10} = k_{10} C_H \left(C_{O_2} - \frac{C_H^2 C_{H_2O}^2}{C_{H_2}^3 K_{II}} \right),$$

$$w_{14} = k_{14} C_H C_{O_2} C_M ,$$

$$w_{15} = \frac{k_{15} C_{H_2O}}{K_{12} C_{H_2}} C_H^2 C_M ,$$

$$w_{16} = w_{14} \frac{k_{16}}{k_{16} + k_{17} + k_{18}[C_{H_2O} / (K_{12} C_{H_2})]} . \qquad (3.11)$$

Peters expressed the reaction rates of the four global reaction-steps (*I* to *IV*), w_I.....w_{IV} in terms of the rates of elementary reactions by the following expressions:

$$w_I = w_1 + w_2,$$

$$w_{II} = w_9,$$

$$w_{III} = w_6 + w_8 + w_{14} + w_{15},$$

$$w_{IV} = w_{10} + w_{16}, \qquad (3.12)$$

With these global reaction-step rates, the production rates for the different species become:

$$\dot{w}_H = -2w_I - 2w_{III} + 2w_{IV}$$

$$\dot{w}_{H_2} = 4w_I + w_{II} + w_{III} - 3w_{IV}$$

$$\dot{w}_{O_2} = -w_{IV}$$

$$\dot{w}_{H_2O} = -w_I - w_{II} + 2w_{IV}$$

$$\dot{w}_{CO} = w_I - w_{II}$$

$$\dot{w}_{CO_2} = -w_{II}$$

$$\dot{w}_{CH_4} = -w_I \qquad (3.13)$$

All equations presented in this section (Eqs. 3.2 to 3.10) are necessary for the implementation of this scheme and they were all employed for this reduced model. With this scheme, Peters computed a burning velocity of 45.65 cm/s for a one-dimensional planar stoichiometric methane-air flame, somewhat larger than the value of 40.07 cm/s

obtained with the starting mechanism. Peters tested the influence of the number of elementary reactions on burning velocity, and suggested that a burning velocity of 40.44 cm/s could be achieved by eliminating some of the elementary reactions. These were, however, not eliminated in the present computations. Peters proposed this scheme for multi-dimensional flame computations.

3.3.1.2 The PW scheme

Instead of neglecting some of the elementary reactions in the starting mechanism (Miller *et al.* 1984) as in earlier scheme (P1), Peters and Williams (1987) later used all of the 31 elementary reactions in their starting mechanism. The necessity of solving for species additional to the seven major species mentioned earlier was avoided by introducing further steady state assumptions, from which the additional species concentrations were expressed explicitly in terms of the other species concentrations and reaction rates.

This PW scheme employs the elementary reactions 1 to 26 in Table 3.3, with both forward and backward rate coefficients, but omitting reaction 15 and the backward reactions 14b and 25b. On the other hand, 6 further reactions, 41 to 46, are included, as listed in Table 3.6.

Table 3.6

Recommended Rate Coefficients from Peters and Williams (1987): $k = BT^n \exp(-E/RT)$, B in moles, cm, sec, E in kJ/mole

No.	Reaction	B	n	E
41	$CH_3 + OH \rightarrow CH_2O + 2H$	9.00E14	0.00	64.80
42	$CH_3 + OH \rightarrow CH_2O + H_2$	8.00E12	0.00	0.00
43	$CH_3 + OH \rightarrow CH_2 + H_2O$	1.50E13	0.00	20.93
44	$CH_2 + OH \rightarrow CH_2O + H$	2.50E13	0.00	0.00
45	$CH_2 + OH \rightarrow CH + H_2O$	4.50E13	0.00	12.56
46	$CH + OH \rightarrow CHO + H$	3.00E13	0.00	0.00

Further, some of the reaction rate coefficients are different from those presented by Peters (1993) and given in Table 3.3. The new values are given in Table 3.7.

Table 3.7

A comparison of rate coefficients in P1 and PW scheme.

No.	Reaction		PW scheme			MP scheme		
			B	*n*	*E*	*B*	*n*	*E*
1b	$CH_3 + H_2 \rightarrow CH_4 + H$		8.83E2	3.00	33.53	8.39E2	3.00	34.56
10b	$OH + O \rightarrow O_2 + H$		1.40E13	0.00	3.20	1.57E13	0.00	3.52
11	$H_2 + O \rightarrow OH + H$		1.50E7	2.00	31.60	5.06E4	2.67	26.30
11b	$OH + H \rightarrow H_2 + O$		6.73E6	2.00	22.35	2.22E4	2.67	18.29
12b	$H_2O + H \rightarrow H_2 + OH$		4.62E8	1.60	77.50	4.31E8	1.60	76.46
22	$CH_2 + H \rightarrow CH + H_2$		4.00E13	0.00	0.00	8.40E9	1.50	1.40
22b	$CH + H_2 \rightarrow CH_2 + H$		2.79E13	0.00	12.61	5.83E9	1.50	13.08
26	$CH_3 + H \rightarrow CH_4$	$k_{\infty 26}$	6.00E16	-1.00	0.00	2.11E14	0.00	0.00

With regard to reaction 26, Eq. 3.10 in Warnatz (1984), is used by Peters and Williams (1987) to approximate the rate coefficient at low pressure. From the rate coefficient at high pressure, $k_{\infty 26}$, in the PW scheme, k_{26} is given by:

$$k_{26} = \frac{k_{\infty 26}}{1 + \dfrac{21.5 \times 10^{10}\ T^3}{p^{0\,6}}} \tag{3.14}$$

where p is in atm and T in K. The partial equilibrium Eqs. 3.2 and 3.3 again apply. The equilibrium constants K_{12}, K_{IV} and K_{II} in Eqs. 3.4, 3.6 and 3.8, are modified by Peters and Williams (1987), and K_{11} also is introduced:

$$\begin{aligned} K_{11} &= 2.23\ \exp^{-1112/T}, \\ K_{12} &= 0.216\ \exp^{7658/T}, \\ K_{II} &= 0.035\ \exp^{3652/T}, \\ K_{IV} &= 1.48\ \exp^{6133/T}. \end{aligned} \tag{3.15}$$

Further, steady state assumptions for O, OH, CH_3, CH_2, CH, CHO and HO_2 are invoked. The involvement of more chemical species in this scheme necessitates the

assumption of additional species being under steady state conditions, if the number of major species in the global reactions is to remain at seven. The expressions needed to find the concentrations of additional intermediates, which did not appear in the previous (P1) scheme, given by Peters and Williams (1987) are:

$$C_{CH_3} = \frac{(k_1 C_H + k_2 C_{OH}) C_{CH_4}}{k_3 C_O + k_{1b} C_{H_2} + (k_{41} + k_{42} + k_{43}) C_{OH} + (k_{26} + k_{25}) C_H}, \quad (3.16)$$

$$C_{CH_2} = \frac{(k_{25} C_H + k_{43} C_{OH}) C_{CH_3}}{(k_{24} + k_{23}) C_{O_2} + k_{22} (1 - Z) C_H + [k_{44} + k_{45} (1 - Z)] C_{OH}}, \quad (3.17)$$

where

$$Z \equiv \frac{k_{22b} C_{H_2}}{k_{22b} C_{H_2} + k_{20} C_{O_2} + k_{46} C_{OH}},$$

$$C_{CH} = \frac{(k_{22} C_H + k_{45} C_{OH}) C_{CH_2}}{k_{22b} C_{H_2} + k_{20} C_{O_2} + k_{46} C_{OH}}, \quad (3.18)$$

$$C_{CHO} = \frac{w_3 + w_{41} + w_{42} + w_{20} + w_{44} + w_{46}}{k_6 C_H + k_{21} C_{OH} + k_8 C_{O_2} + k_7 C_M}, \quad (3.19)$$

$$C_{HO_2} = \frac{(k_{14} C_M C_H + k_8 C_{CHO}) C_{O_2}}{(k_{16} + k_{17} + k_{19}) C_H + k_{18} C_{OH}}. \quad (3.20)$$

The species production rates are expressed in terms of rates of the four global reaction-steps in the same way as in the P1 scheme (Eq. 3.9), whereas the rates of global reaction steps are modified as follows:

$$w_I = w_1 - w_{1b} + w_2 - w_{26},$$

$$w_{II} = w_1 - w_{1b} + w_{25} + w_{43} - w_{44} - w_{45},$$

$$w_{III} = w_{14} - w_{41} + w_{26} + w_6 + w_{21} + w_8,$$

$$w_{IV} = w_{10} - w_{10b} + w_{16} + w_{19} + w_{25} + w_{43} - w_{44} - w_{46}, \qquad (3.21)$$

in which $w_1, w_2 \ldots\ldots w_{46}$ are rates of the ith elementary reaction.

All the equations presented (Eqs. 3.14 to 3.21), together with the Eqs. 3.2, 3.3, 3.5, 3.7, 3.9 and 3.10 are required for implementation of this scheme and were adopted in the reduced model. With this scheme, Peters and Williams (1987) investigated the influence of the various elementary reactions on burning velocity. For a premixed planar stoichiometric methane-air flame, they calculated asymptotically a range of burning velocities between 35.8 cm/s and 49.9 cm/s, by removing some of the elementary reactions. In addition, burning velocities at higher pressures (up to 20 atm.) also were reported. Further reduction to a mechanism consisting of but three global reaction steps also was presented, together with an asymptotic analysis of the methane-air flame structure. An expression for burning velocity was presented.

3.3.1.3 The MP scheme

The MP scheme (Mauss and Peters 1993), with the C_1-chain only, comprises all the reactions 1 to 40 in Table 3.3. At the cost of increasing complexity, it can be extended to include up to the C_3-chain, as concentrations of additional species must be calculated via further steady state assumptions if the total number of species equations is to remain at seven. Although the C_2-chain has a significant influence in rich methane flames computations, it has been shown to have a negligible effect in lean to stoichiometric flames (Mauss and Peters 1993). Only the latter are considered in the current study.

No partial equilibrium assumptions are made in this scheme, and all minor species concentrations are obtained by application of steady state assumptions, including those of OH and O, which had been obtained formerly by partial equilibrium assumptions in the previous schemes. The concentrations of steady state species OH, O, CH_3O, CH_2O, CHO, HO_2 and H_2O_2 are given by:

$$C_{OH} = \frac{-b + \sqrt{b^2 - 4ac}}{2a}, \tag{3.22}$$

where $a = 2\,(k_{13} + k_{29}\,C_M)$

$$b = k_{10b}\,C_O + k_{11b}\,C_H + k_{12}\,C_{H_2} + k_{18}\,C_{HO_2} + k_{31}\,C_{H_2O_2} + k_{15}\,C_H\,C_M + k_9\,C_{CO} + k_{21}\,C_{CHO} + k_5\,C_{CH_2O} + k_2\,C_{CH_4}$$

$$c = -\,(w_{10} + w_{11} + w_{12b} + 2\,(w_{13b} + w_{16} + w_{29b}) + w_{27} + w_{30} + w_{31b} + w_{9b} + w_{23} + w_{36} + w_{39} + w_{40} + w_{2b})$$

$$C_O = \frac{w_{10} + w_{11b} + w_{13} + w_{19} + w_{20}}{k_{10b}\,C_{OH} + k_{11}\,C_{H_2} + k_{13b}\,C_{H_2O} + k_{27}\,C_{HO_2} + k_{35}\,C_{CH_2} + k_{36}\,C_{CH_2O} + k_3\,C_{CH_3} + k_{40}\,C_{CH_4}}, \tag{3.23}$$

$$C_{CH_3} = \frac{w_{25b} + w_1 + w_{40} + w_2}{(k_{25} + k_{26})\,C_H + k_3\,C_O + k_{39}\,C_{O_2} + k_{1b}\,C_{H_2} + k_{2b}\,C_{H_2O}}, \tag{3.24}$$

$$C_{CH_2} = \frac{w_{25}}{k_{22}\,C_H + k_{35}\,C_O + (k_{23} + k_{24})\,C_{CO_2} + k_{25b}\,C_{H_2} - \dfrac{k_{22b}\,C_{H_2}\,k_{22}\,C_H}{k_{20}\,C_{O_2} + k_{34}\,C_{CO_2} + k_{22b}\,C_{H_2}}}, \tag{3.25}$$

$$C_{CH_2} = \frac{C_{CH_2}\,k_{22}\,C_H}{k_{20}\,C_{O_2} + k_{34}\,C_{CO_2} + k_{22b}\,C_{H_2}}, \tag{3.26}$$

$$C_{CH_2O} = \frac{w_3 + w_{39}}{k_4\,C_H + k_{36}\,C_O + k_5\,C_{OH} + k_{37}\,C_M}, \tag{3.27}$$

$$C_{CHO} = \frac{w_{20} + w_{34} + w_{7b} + w_4 + w_{36} + w_5 + w_{37}}{k_6\,C_H + k_{21}\,C_{OH} + k_8\,C_{O_2} + k_7\,C_M}, \tag{3.28}$$

Similar to C_{OH}, C_{HO_2} is also in quadratic form:

$$C_{HO_2} = \frac{-b + \sqrt{b^2 - 4ac}}{2a}, \tag{3.29}$$

where $$a = k_{28}\left(2 - \frac{k_{31}\,C_{OH}}{k_{29b}\,C_M + k_{30}\,C_H + k_{31}\,C_{OH}}\right),$$

$$b = k_{14b}\,C_M + (k_{16} + k_{17} + k_{19})\,C_H + k_{18}\,C_{OH} + k_{27}\,C_O + k_{31b}\,C_{H_2O} - \frac{k_{31}\,C_{OH}\,k_{31b}\,C_{H_2O}}{k_{29b}\,C_M + k_{30}\,C_H + k_{31}\,C_{OH}},$$

$$c = -\left(w_{14} + w_8 + \frac{k_{31}\,C_{OH}\,w_{29}}{k_{29b}\,C_M + k_{30}\,C_H + k_{31}\,C_{OH}}\right),$$

$$C_{H_2O_2} = \frac{w_{29} + w_{31b}}{k_{29b}\,C_M + k_{30}\,C_H + k_{31}\,C_{OH}} \quad . \tag{3.30}$$

The concentrations of these species must be solved iteratively as a result of the inter-dependent nature of the expressions. The rate constants are taken from Peters (1993) and are given in Table 3.3. The molar concentration C_M, is given by Eq. 3.10. The modified rates of the global reaction-steps are:

$$w_{\mathrm{I}} = w_1 + w_{40} + w_2 - w_{26}$$

$$w_{\mathrm{II}} = w_9 - w_{34} + w_{24}$$

$$w_{\mathrm{III}} = w_{14} - w_{28} + w_{30} + w_{31} + w_{32} + w_{15} + w_6 + w_{21} + w_8 - w_{37} + w_{26}$$

$$w_{\mathrm{IV}} = w_{10} + w_{16} + w_{19} + w_{28} - w_{31} - w_{34} - w_{35} + w_{25} + w_{38} + w_{39} \tag{3.31}$$

Here, the rate coefficients of elementary reactions 26 and 38 are calculated as a function of temperature and pressure in the form:

$$k = \frac{F\,k_\infty\,k_0\,C_M}{k_\infty + k_0\,C_M} \tag{3.32}$$

where k_0 and k_∞ are rate coefficients under zero and infinite pressure respectively, and F is approximated by:

$$\log_{10} F = \frac{\log_{10} F_c}{1 + \left(\frac{\log_{10} (k_0 C_M / k_\infty)}{0.75 - 1.27 \log_{10} F_c} \right)^2} \quad . \tag{3.33}$$

For reactions 26, F_c is calculated from:

$$F_c = 0.577 \exp^{-\frac{T}{2370}} , \tag{3.34}$$

whilst in reaction 38, it is calculated from:

$$F_c = 0.38 \exp^{-\frac{T}{73}} + 0.62 \exp^{-\frac{T}{1180}} . \tag{3.35}$$

With the rates of global reaction steps w_I, w_{II}, w_{III} and w_{IV}, the species production rates are calculated in the same way as was described for the P1 scheme (Eq. 3.9).

3.4 The Heat-Release Formulation

The heat release formulation expresses the volumetric rate of heat release for a laminar flame as a function of temperature and flame stretch rate. Such data comprise what became known as the "strained flame library". They were provided at Leeds by Dixon-Lewis and were used in flamelet mathematical modeling of turbulent combustion (Bradley *et al.* 1988, 1990, Bradley and Lau 1990). This approach eliminates the highly non-linear species equations from the set of governing equations for the flow field. By using the chemical heat release source term $\sum_{i=1}^{N} h_i W_i \dot{w}_i$ in the energy equation, computational power is released for computations in the complex flow field. Heat release rates can be stored in a "look-up" table. For further computational economy, Bradley *et al.* (1990) adopted an *ad hoc* approximate form for the laminar heat release rate:

$$q = q_{\max} \frac{(a+b)^{(a+b)}}{a^a b^b} \theta^a (1-\theta)^b \quad . \tag{3.36}$$

Here $q_{\max}$ is the computed maximum heat release rate in the laminar premixed flame for the particular mixture, whilst a and b are functions of equivalence ratio only.

Values are optimised to give the best possible curve fit to the computed profile of laminar heat release rate against the reaction progress variable θ. Here θ is defined as :

$$\theta = \frac{T - T_u}{T_b - T_u} \tag{3.37}$$

in which T is the temperature of the gas (K), T_u that of the cold reactants, and T_b - T_u represents the maximum temperature rise with T_b the adiabatic gas temperature.

With volumetric heat release rates obtained from the one-dimensional computations of Dixon-Lewis using the scheme of Dixon-Lewis and Islam (1983), the normalised heat releases (q/q_{max}) are correlated with the reaction progress variable θ (Fig. 3.1). The computed values of heat release are shown by crossed points, and the best fit curves of Eq. 3.36 are represented by solid curves. The constants a and b in Eq. 3.36 have been optimised by Bradley *et al.* (1990). The agreement between each of the two profiles is satisfactory, bearing in mind the uncertainties in the values of the different rate constants. A similar degree of agreement was achieved for other equivalence ratios.

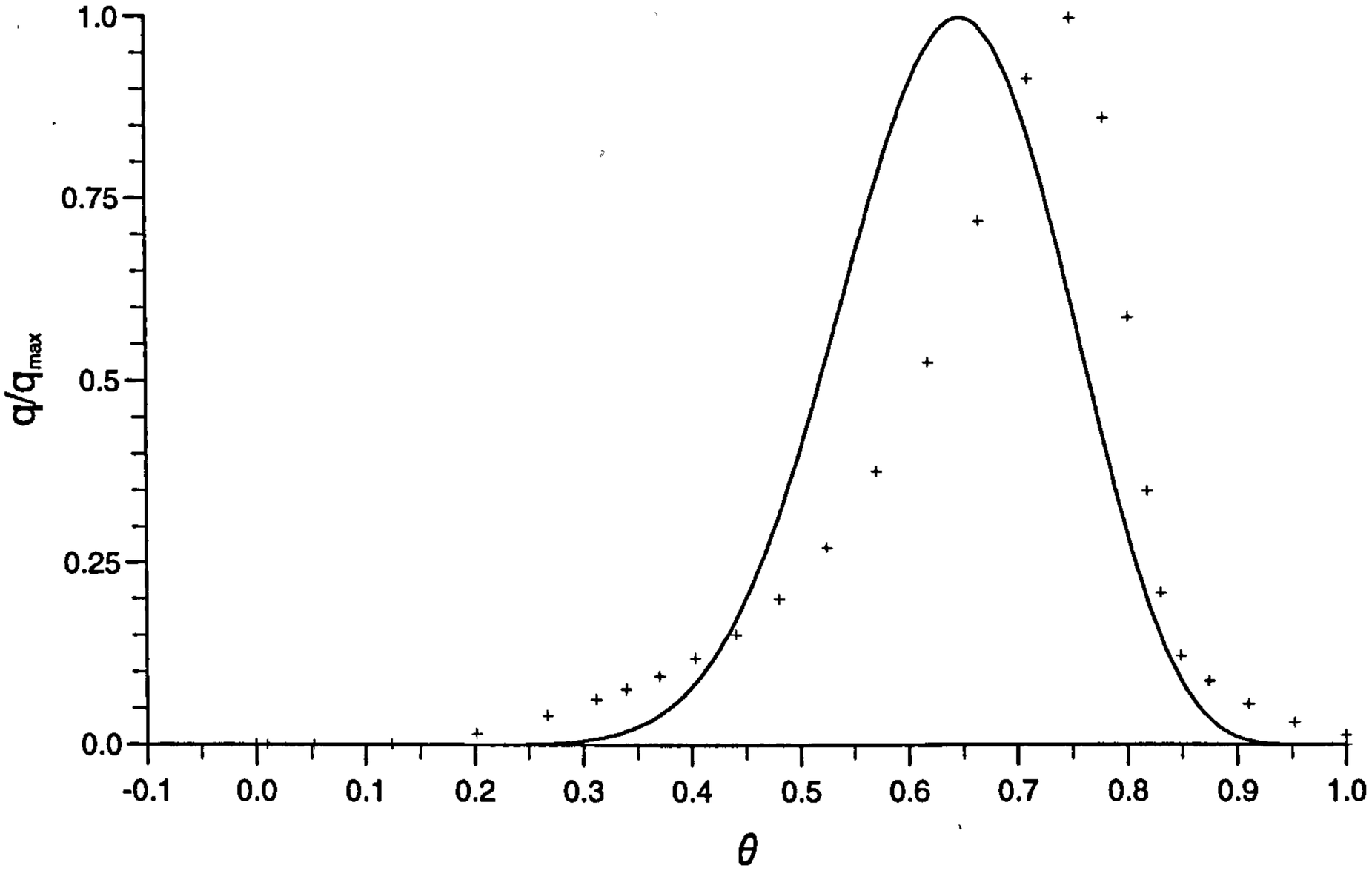

(a)

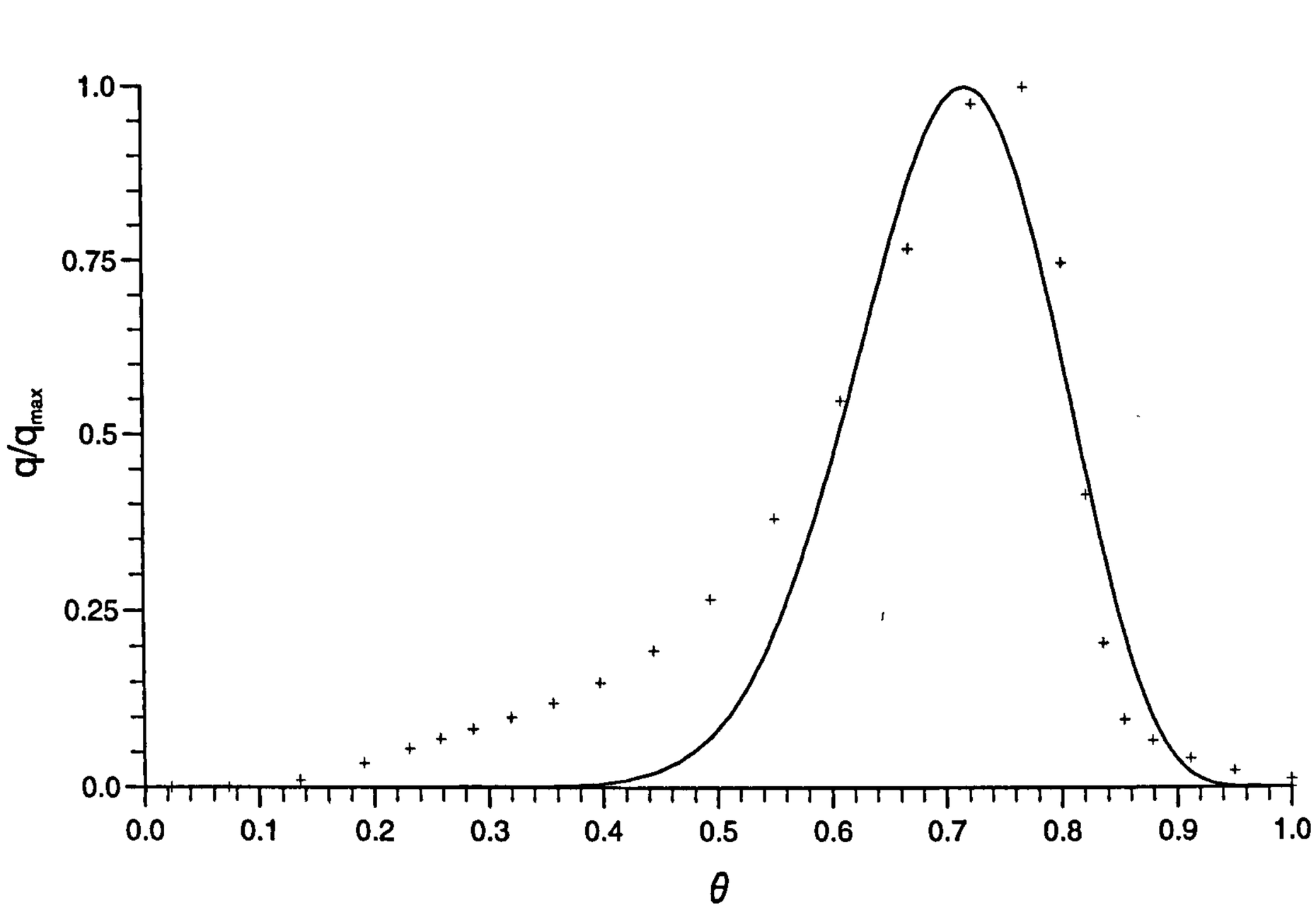

(b)

Fig. 3.1 Computed (cross points) and approximated (full line) heat release rate profile.
(a) $\phi = 0.84$, $T_b = 2050$ K, $q_{max} = 3.4$ GW/m^3, a= 13, b=7.
(b) $\phi = 1.0$, $T_b = 2210$ K, $q_{max} = 4.4$ GW/m^3, a= 18, b=7.

CHAPTER FOUR
Computational Algorithm and Numerical Techniques

4.1 Introduction

The simulation of combustion problems, involving heat/mass transfer phenomena, requires the solution of the Navier-Stokes equations, as well as conservation equations for mass, energy and chemical species. These equations, introduced in Chapter 2, are seen to be highly non-linear and strongly coupled. Analytical solutions to them are impossible to find for all but the simplest of problems; numerical techniques invariably have to be adopted in which a discrete approximation to the continuum problem is made. Generally, one could expect the accuracy of such a numerical approximation to increase in relation to the number of grid nodes, N, employed, with the continuum solution approached as $N \rightarrow \infty$. In practice, however, the size of N is restricted by the memory capacity of the computing platform at hand.

Discretisation of the governing conservation equations poses serious practical difficulties in relation to accuracy, boundedness, numerical stability and conservation, particularly when the first order derivatives associated with convective transport are approximated. These issues and a number of common differencing schemes for the treatment of convective transport are reviewed here. Similarly, the problem of coupling pressure with velocity is raised, and the idea of employing a staggered grid arrangement to prevent spurious pressure oscillations is outlined.

In this chapter, a numerical strategy is developed for the solution of steady state, two-dimensional, reactive, elliptic flows, restricted, for the sake of simplicity, to laminar flow in Cartesian coordinates. The strategy is based on the work of Patankar and

Spalding (1972) and Patankar (1980). Firstly, discretisation of a general transport equation is discussed. The resulting numerical/analogue may be thought of has a balance between competing physical effects: diffusion, convection and source terms. Next, some fundamental aspects under lining the numerical analysis are outlined before a number of common discretisation schemes for approximating convective transport are reviewed. Following this, the algorithm employed to solve the resulting algebraic system is described.

4.2 Discretisation of the Governing Equations

For a given partial differential equation, a discrete analogue can be formulated in a number of ways. These involve either Taylor-series expansions, in which derivatives in the differential equation are approximated via a truncated Taylor series; a variational formulation based on the calculus of variations; the method of weighted residuals which is described in detail by Finlayson (1972), or a control-volume formulation which may be thought of as a variant of the method of weighted residuals.

With a control-volume method, the solution domain is sub-divided into a number of non-overlapping control volumes, each surrounding a single grid point. The differential equation is integrated over each control volume, and piecewise profiles expressing the variation of ϕ, which represents, not only of velocities, but temperature and concentrations of species, between grid points are used to evaluate the required integrals. The result is a discrete equation relating values of ϕ at neighbouring points.

The most attractive feature of the control volume formulation is that the resulting solution embodies the feature that the integral conservation of quantities such as mass, momentum, and energy is exactly satisfied over each and all control volumes and hence over the entire solution domain. This characteristic feature is true for any number of grid points, not just in a limiting sense when the number of grid points becomes large.

4.2.1 General transport equation

The governing equations for the two-dimensional combustion system described in Chapter 2 can be recasted in the form of a general transport equation, which for steady state flow, in Cartesian coordinate, becomes:

$$\frac{\partial}{\partial x}(\rho u \phi) + \frac{\partial}{\partial y}(\rho v \phi) - \frac{\partial}{\partial x}\left(\mu_{\phi x}\frac{\partial \phi}{\partial x}\right) - \frac{\partial}{\partial y}\left(\mu_{\phi y}\frac{\partial \phi}{\partial y}\right) = S_{\phi}, \tag{4.1}$$

where $\mu_{\phi x}$ and $\mu_{\phi y}$ are corresponding transport coefficients for ϕ; S_{ϕ} is a source term.

4.2.2 Grid arrangement

At the outset the solution domain has to be partitioned to produce an appropriate computational grid system. The most commonly adopted approach, and the one used here, is to employ a staggered grid arrangement (Harlow and Welch 1965) for the solution of the dependent variables - that is, the variables are stored at different locations, see Fig. 4.1. The velocities, u and v, are positioned mid-way between two adjacent scalar grid nodes with the result that they are at the correct location for evaluating the convective fluxes for a scalar control volume. More important, is the strong coupling which results between the velocity and pressure fields (Patankar 1980), see Section 4.6.

It is perhaps worth noting that the use of non-staggered, or collocated, grid systems has gained in popularity in recent years. This is due in the main to advances in multi-grid convergence acceleration (Gaskell and Wright 1988) and grid refinement techniques and the increasing desire to solve complex flow problems involving irregular solution domain (Rhie and Chow 1983). However, such an approach can give rise to spurious pressure oscillations unless a corrective measure such as the one proposed by Rhie and Chow (1983) is employed to suppress them. It was decided that there was no particular merit in proceeding in this way for the problems under investigation here.

4.2.3 Discretisation procedure

A discrete form of the transport equation Eq. 4.1 is derived by first integrating the equation over a macro-control volume surrounding the nodal point P (Fig. 4.1),

$$\left.\begin{aligned}
&\int_s^n \int_w^e \left[\frac{\partial}{\partial x}(\rho u \phi) + \frac{\partial}{\partial y}(\rho v \phi)\right] dx\, dy && \Big\} \text{Convective term}\\
&-\int_s^n \int_w^e \left[\frac{\partial}{\partial x}\left(\mu_{\phi x}\frac{\partial \phi}{\partial x}\right) + \frac{\partial}{\partial y}\left(\mu_{\phi y}\frac{\partial \phi}{\partial y}\right)\right] dx\, dy && \Big\} \text{Diffussive term}\\
&= \int_s^n \int_w^e S_\phi\, dx\, dy && \Big\} \text{Source term,}
\end{aligned}\right. \qquad (4.2)$$

where n, s, e and w refer to the location of the space average of any quantity prevailing over the faces of the control volume. By applying the Mean-value Theorem, Eq. 4.2 reduces to,

$$\left.\begin{aligned}
&\left[(\rho u\phi)_e - (\rho u\phi)_w\right]\delta y + \left[(\rho v\phi)_n - (\rho v\phi)_s\right]\delta x && \Big\} \text{Convective term}\\
&-\left[\left(\mu_{\phi x}\frac{\partial \phi}{\partial x}\right)_e - \left(\mu_{\phi x}\frac{\partial \phi}{\partial x}\right)_w\right]\delta y - \left[\left(\mu_{\phi y}\frac{\partial \phi}{\partial y}\right)_n - \left(\mu_{\phi y}\frac{\partial \phi}{\partial y}\right)_s\right]\delta x && \Big\} \text{Diffussive term}\\
&= \int_s^n \int_w^e S_\phi\, dx\, dy && \Big\} \text{Source term.}
\end{aligned}\right. \qquad (4.3)$$

Eq. 4.3 expresses the balance between the net influx of the flow property under consideration through the volume surface, the property's volumetric rate of accumulation and its volumetric rate of generation. To proceed further with this equation, requires the imposition of a number of assumptions.

4.2.3.1 Source term

The source term, S_ϕ, is taken to be uniform over the cell volume, with the following linearised form, (Patankar 1980),

$$\int_s^n \int_w^e S_\phi\, dx\, dy = S_S + S_P\, \phi_P, \qquad (4.4)$$

in which S_ϕ is approximated by central differencing; S_P is required to be negative to avoid numerical instabilities and physically unrealistic solutions.

4.2.3.2 Convective fluxes

For the convection terms, the face values, ϕ_s, ϕ_n, ϕ_w and ϕ_e are approximated as

$$\begin{aligned}
\phi_w &= \beta_w^{WW}\phi_{WW} + \beta_w^{W}\phi_W + \beta_w^{P}\phi_P + \beta_w^{E}\phi_E, \\
\phi_e &= \beta_e^{W}\phi_W + \beta_e^{P}\phi_P + \beta_e^{E}\phi_E + \beta_e^{EE}\phi_{EE}, \\
\phi_s &= \beta_s^{SS}\phi_{SS} + \beta_s^{S}\phi_S + \beta_s^{P}\phi_P + \beta_s^{N}\phi_N, \\
\phi_n &= \beta_n^{S}\phi_S + \beta_n^{P}\phi_P + \beta_n^{N}\phi_N + \beta_n^{NN}\phi_{NN}.
\end{aligned} \tag{4.5}$$

where the βs represent weighting factors whose value depends on the approximation scheme selected (Section 4.4).

The formulation adopted for the convective term is perhaps the most problematic and in recent years various methods of approximation have appeared in the literature, upwind differencing (Gentry *et al.* 1966), hybrid differencing (Spalding 1972), QUICK differencing (Leonard 1979), etc. -some more successful than others. More about this later.

4.2.3.3 Diffusive fluxes

The diffusive fluxes are, in common with most other authors, approximated by the Central Differencing Scheme (CDS) such that the diffusion terms are written as:

$$\begin{aligned}
\left(\mu\frac{\partial\phi}{\partial x}\right)_e &= \frac{\mu_e}{\delta x_e}(\phi_E - \phi_P), \\
\left(\mu\frac{\partial\phi}{\partial x}\right)_w &= \frac{\mu_w}{\delta x_w}(\phi_W - \phi_P), \\
\left(\mu\frac{\partial\phi}{\partial y}\right)_n &= \frac{\mu_n}{\delta y_n}(\phi_N - \phi_P), \\
\left(\mu\frac{\partial\phi}{\partial y}\right)_s &= \frac{\mu_s}{\delta y_s}(\phi_S - \phi_P).
\end{aligned} \tag{4.6}$$

4.2.3.4 Discretise form of the general transport equation

By substituting Eqs. 4.4 - 4.6 into Eq. 4.3, a discretised form of the general transport equation is obtained. For convenience, this equation is expressed as:

$$\left(\sum A_i - S_P\right)\phi_P = \sum A_i\,\phi_i + S_S, \tag{4.7}$$

where $i = EE, WW, NN, SS, E, W, N, S$ and

$$
\begin{aligned}
A_E &= D_e - C_e \beta_e^E + C_w \beta_w^E, \\
A_W &= D_w + C_w \beta_w^W - C_e \beta_e^W, \\
A_N &= D_n - C_n \beta_n^N + C_s \beta_s^N, \\
A_S &= D_s + C_s \beta_s^S - C_n \beta_n^S, \\
A_{EE} &= - C_e \beta_e^{EE}, \\
A_{WW} &= - C_w \beta_w^{WW}, \\
A_{NN} &= - C_n \beta_n^{NN}, \\
A_{SS} &= - C_s \beta_s^{SS},
\end{aligned}
\tag{4.8}
$$

with

$$
\begin{aligned}
D_e &= \delta y \frac{\mu_{\phi x}}{(\delta x)_e}, & C_e &= \delta y (\rho u)_e, \\
D_w &= \delta y \frac{\mu_{\phi x}}{(\delta x)_w}, & C_w &= \delta y (\rho u)_w, \\
D_n &= \delta x \frac{\mu_{\phi y}}{(\delta y)_n}, & C_n &= \delta x (\rho v)_n, \\
D_s &= \delta x \frac{\mu_{\phi y}}{(\delta y)_s}, & C_s &= \delta x (\rho v)_s.
\end{aligned}
\tag{4.9}
$$

4.3 Numerical Analysis

The general finite difference equation (Eq. 4.7) shows the importance of the transport coefficients, (As), through their direct link to the dependent variable. These coefficients not only determine the accuracy of the solution, but also, through the form of the matrix system, strongly influence numerical stability, rate of convergence and the choice of matrix solver. These transport coefficients are determined by the way in which the convective and diffusive fluxes are discretised. However, before dealing with the issue of discretisation more closely, it is useful to consider some important facets of numerical analysis.

4.3.1 Accuracy

The classical definition of the accuracy of a finite difference equation is usually given in terms of the leading truncation error (TE) term of a Taylor series expansion. A

differential operator can be written as a difference operator plus higher order terms (HOT). The absolute value of the HOT is defined as the truncation error (often the lowest order of the HOT is said to be the TE). For the one-dimensional case, the Taylor series expansion for ϕ about x is given by,

$$\phi\,(x+h) = \phi(x) + h\phi'(x) + \frac{h^2}{2}\phi''(x) + \frac{h^3}{6}\phi'''(x) + \ldots\ldots \tag{4.10}$$

Here and in later sections, discussion is centred around a uniform mesh of spacing h. For example, for central differencing, it can be shown that,

$$\left(\frac{\partial\phi}{\partial x}\right)_{\bullet} = \frac{\phi_E - \phi_P}{h} - \left(\frac{h^3}{24}\left(\frac{\partial^3\phi}{\partial x^3}\right)_{\bullet} + \ldots\ldots\right). \tag{4.11}$$

Therefore, the CDS is said to have a truncation error of order two and to be second order accurate.

4.3.2 Convective stability

Convective stability (Leonard 1980) is defined as the sensitivity of the convective influx into a control volume centred at P, to the change in ϕ_P, namely $\partial C_{IF} / \partial \phi_P$. Here, C_{IF} $(= (\rho\phi)_w - (\rho\phi)_{\bullet})$ is the convective influx. There are three possibilities:

$$\frac{\partial C_{IF}}{\partial \phi_P} = \begin{cases} < 0 \ \textit{stable sensitivity}, \\ = 0 \ \textit{neutral sensitivity}, \\ > 0 \ \textit{unstable sensitivity}. \end{cases} \tag{4.12}$$

Physically, convection is associated with the transport of fluid properties from upstream to downstream. In order to achieve convective stability, some form of upwind-biased procedure for approximating the convective flux is essential (Leonard 1979a and 1980). Any numerical approximation to convection that is not upwind-biased will lack convective stability and its associated coefficient matrix will be numerically unstable. The analogous case of diffusive stability yields coefficients that are always negative and hence stable if central differencing is adopted.

4.3.3 Boundedness

For a purely convection-diffusion problem, in which the source term S_ϕ is zero, the general finite difference equation (Eq. 4.7) reduces to,

$$\sum A_i \phi_P = \sum A_i \phi_i , \qquad i = EE, WW, NN, SS, E, W, N, S. \tag{4.13}$$

Physical considerations lead to the conclusion that the solution of Eq. 4.7 must be bounded by its boundary values. This is so if and only if ϕ_P, within any control volume, is bounded by the neighbouring ϕ_i, i.e.

$$\text{min. } \phi_i \le \phi_p \le \text{max. } \phi_i \tag{4.14}$$

A sufficient (but not necessary) condition to ensure this boundedness property is to have a diagonally dominant matrix. The condition for diagonally dominance is (Patankar 1980),

$$\left|\sum A_i\right| \ge \sum |A_i| . \tag{4.15}$$

To satisfy Eq. 4.15,

$$\left|\sum A_i\right| \ge |A_i| , \tag{4.16}$$

all the coefficients of A must have the same sign.

4.3.4 Convective boundedness criterion

In order to simplify the discussion of boundedness, it is instructive and indeed useful to introduce a normalised upwind biased dependent variable $\hat{\phi}$ (Leonard 1979b) so that for $u_w > 0$:

$$\hat{\phi} = \frac{\phi - \phi_{WW}}{\phi_P - \phi_{WW}} \tag{4.17}$$

Here, $\hat{\phi}$ indicates the degree of upwind bias inherent in any normalised finite difference approximation to the face value $\hat{\phi}_w$, Gaskell and Lau (1988a) took this idea a crucial stage further and formulated a rigorous convection boundedness criterion (CBC) for implicit steady state flow calculations. This criterion can be expressed as

$$\begin{cases} 1 < \hat{\phi}_w \leq \hat{\phi}_W, & \hat{\phi}_W > 1, \\ \hat{\phi}_W < \hat{\phi}_w \leq 1, & \hat{\phi}_w > 1, \\ \hat{\phi}_W \leq \hat{\phi}_w < 0, & \hat{\phi}_w > 1, \end{cases} \tag{4.18}$$

and is illustrated in terms of the shaded area in Fig. 4.1. These three constraints are both necessary and sufficient to ensure computed boundedness.

4.4 Discretisation of Convection Transport Terms

A number of discretisation schemes commonly used in CFD are now reviewed, selected on the basis of boundedness, convective stability, conservation and accuracy. Discretisation schemes, such as the semi-analytic (exponential and power-law schemes, Patankar 1980, Wong and Raithby 1979), spline methods and others are not considered here.

The accuracy with which convection is approximated, plays a crucial role in the overall predictive performance of any fluid-flow algorithm. All convection schemes introduce solution errors due to the truncated, approximate nature of the interpolation polynomials on which they are based. These errors may be diffusive or dispersive, the former arising from even, and the latter from odd truncation error terms. Diffusive errors tend to smear gradients while dispersive ones introduce oscillations due to a spatial separation of the Fourier components. In non-linear conditions, dispersion leads to aliasing errors reflecting an exchange of energy between the interacting Fourier modes. Diffusion tends to enhance stability but misrepresents the effects of physical diffusivity, while dispersive oscillation may easily result in an unbounded growth of error and instability. As the order of a scheme is increased, the leading truncation error changes alternatively between odd and even but the influence of both tends to diminish. However, it should be noted that, dispersive errors, even when minor, can quickly lead, via aliasing, to instability if the level of diffusive attenuation is too weak.

4.4.1 The central differencing scheme

As we saw in subsection 4.3.1, the CDS is second order accurate such that a face value, ϕ_w, which lies between two ϕ_P and ϕ_W, is approximated as:

$$\phi_w = \frac{\phi_W + \phi_P}{2}. \tag{4.19}$$

The factor 1/2 arises from the assumption of the interfaces being midway between ϕ_W and ϕ_P ; other interpolation factors would have appeared for differently located interfaces. Thus, the transport coefficients in the discrete form of Eq. 4.8 become:

$$\begin{aligned} A_E &= D_e - 0.5C_e, \\ A_W &= D_w + 0.5C_w, \\ A_N &= D_n - 0.5C_n, \\ A_S &= D_s + 0.5C_s, \\ A_{EE} &= A_{WW} = A_{NN} = A_{SS} = 0. \end{aligned} \tag{4.20}$$

Although it is second order accurate, it has only neutral convective stability. Furthermore, in convection dominated problems, the matrix system does not satisfy the boundedness requirement whenever the absolute value of the local Peclet number, *Pe*, is greater than 2. Solutions may contain unphysical oscillations and even diverge.

4.4.2 The upwind differencing scheme

A remedy for the problems of the CDS is the Upwind Differencing Scheme (UDS) first put forward by Courant *et al.* (1952) and subsequently re-discovered by Gentry *et al.* (1966). With UDS the convection term is calculated with:

$$\begin{aligned} \phi_w &= \phi_W, \quad \text{if } u_w > 0, \\ \phi_w &= \phi_P, \quad \text{if } u_w < 0, \end{aligned} \tag{4.21}$$

and, the coefficients in Eq. 4.8 become:

$$\begin{aligned} A_E &= D_e + max(-C_e, 0), \\ A_W &= D_w + max(C_w, 0), \\ A_N &= D_n + max(-C_n, 0), \\ A_S &= D_s + max(C_s, 0), \\ A_{EE} &= A_{WW} = A_{NN} = A_{SS} = 0. \end{aligned} \tag{4.22}$$

It is unconditionally bounded with stable convective sensitivity. Although the UDS ensures a diagonally dominant matrix system, the first order truncation error results in

very low accuracy through the presence of artificial numerical diffusion. This numerical diffusion dominates physical diffusion when the absolute value of the local Peclet number, *Pe*, is greater than 2.

4.4.3 The hybrid scheme

A slightly better scheme is hybrid differencing, proposed by Spalding (1972). The name hybrid is indicative of a combination of the CDS and UDS. The scheme is identical to the CDS for the Peclet-number range $-2 \le Pe \le 2$, while outside this range, it reduced to the UDS, i.e.

$$\phi_w = \begin{cases} \frac{1}{2}(\phi_W + \phi_P), & if\ |Pe| < 2, \\ \phi_W, & if\ u_w > 0\ and\ |Pe| > 2, \\ \phi_P, & if\ u_w < 0\ and\ |Pe| > 2. \end{cases} \tag{4.23}$$

and the coefficients in Eq. 4.8 are given by:

$$\begin{aligned} A_E &= D_e + max\,(-0.5C_e\,,\ C_e\,,\ 0), \\ A_W &= D_w + max\,(0.5C_w\,,\ C_w\,,\ 0), \\ A_N &= D_n + max\,(-0.5C_n\,,\ C_n\,,\ 0), \\ A_S &= D_s + max\,(0.5C_s\,,\ C_s\,,\ 0), \\ A_{EE} &= A_{WW} = A_{NN} = A_{SS} = 0. \end{aligned} \tag{4.24}$$

4.4.4 The QUICK scheme

Besides the eradication or reduction of numerical diffusion, accurate results with low mesh density and low computing cost can be achieved with higher order discretisation schemes (Gaskell and Lau 1986), which embody more nodal point values than first and second order schemes such as UDS and CDS. One such scheme is Quadratic Upstream Interpolation for Convective Kinematics (QUICK) originally proposed by Leonard (1979). This scheme approximates the face value by quadratic interpolation between immediately adjacent nodal values and the next nearest upstream one. It is third order accurate and takes the form:

$$\phi_w = \frac{3}{8}\phi_P + \frac{6}{8}\phi_W - \frac{1}{8}\phi_{WW}, \qquad (u_w > 0). \tag{4.25}$$

The transport coefficients for implementation of the QUICK scheme are:

$$\begin{aligned}
A_E &= D_e - 6C_e/8 - min\,(C_w\,,\ -3C_e)/8,\\
A_W &= D_w + 6C_w/8 + max\,(C_e\,,\ -3C_w)/8,\\
A_N &= D_n - 6C_n/8 - min\,(C_s\,,\ -3C_n)/8,\\
A_S &= D_s + 6C_s/8 + max\,(C_n\,,\ -3C_s)/8,\\
A_{EE} &= max\,(C_e\,,\ 0)/8,\\
A_{WW} &= -max\,(C_w\,,\ 0)/8,\\
A_{NN} &= max\,(C_n\,,\ 0)/8,\\
A_{SS} &= -max\,(C_s\,,\ 0)/8.
\end{aligned} \tag{4.26}$$

The convective stability of QUICK is enhanced by the upwind bias and first order numerical diffusion is totally absent. However, this scheme is not unconditionally bounded. In parts of the solution domain where ϕ and u_i are smoothly varying functions, QUICK handles Eq. 4.1 quite adequately and in laminar flow calculations, boundedness does not appear to be a problem as long as the matrix system is stable.

4.4.5 The CCCT scheme

By employing the physically realistic constraints of the CBC, Gaskell and Lau (1988) proposed a new generic convective transport approximation called Curvature Compensated Convective Transport (CCCT) which is essentially third-order accurate in the regions of the solution domain where the concept of order is meaningful, preserves the boundedness of solutions and satisfies convective stability. Above all this scheme is easy to implement with relatively low computational cost. The face value at w is given by:

$$\phi_w = \left(\frac{3}{8} + 2\alpha\right)\phi_P + \left(\frac{6}{8} - \alpha\right)\phi_W - \left(\frac{1}{8} + \alpha\right)\phi_{WW}, \tag{4.27}$$

in which

$$\alpha = \frac{\hat{\phi}_w - \frac{3}{8}\left(\hat{\phi}_W + 1\right)}{2\hat{\phi}_W - 1}. \tag{4.28}$$

CCCT is an implicit approximation scheme in which α is evaluated iteratively from:

$$\hat{\phi}_w = \begin{cases} 3\hat{\phi}_W & \text{and } \alpha \in (0,\ 3/8] \quad \text{if } \hat{\phi}_W \in [0,\ 1/6) \\ \frac{3}{8}\left(2\hat{\phi}_W + 1\right) & \text{and } \alpha = 0 \quad \text{if } \hat{\phi}_W \in [1/6,\ 5/6] \\ 1 & \text{and } \alpha \in [-1/8,\ 0) \quad \text{if } \hat{\phi}_W \in (5/6,\ 1] \\ \hat{\phi}_W & \text{and } \alpha \in [-1/8,\ 3/8) \quad \text{otherwise} \end{cases} \tag{4.29}$$

The construction of the transport coefficients when programming this scheme is similar to that for QUICK, except that the parameter α in these coefficients and the calculation of α may involve processes spanning the control volumes; where ϕ_W adopts an 'old' value in the previous iteration, ϕ_w is determined in terms of 'old' values via Eq. 4.29.

The distinction of the CCCT scheme lies in its inherent capability to capture sharp gradients in circumstances where QUICK and other higher order schemes fail. Several of the other schemes described above can be generated via Eq. 4.27 if α is given a fixed value. For example, CCCT reduces to the QUICK scheme when the value of α is set equal to zero.

4.5 Method of Solution

Having discretised the governing transport equations, there remains the task of solving sets of quasi-linear algebraic equations of the form:

$$A_P\phi_P = \sum A_i\phi_i + S_S \tag{4.30}$$

where $A_P = \sum A_i - S_P$ and $i = EE,\ WW,\ NN,\ SS,\ E,\ W,\ N,$ and S.

Many methods exist for solving large systems of linear algebraic equations and these can be catalogued as being either direct or indirect iterative methods. The use of direct methods is not appropriate in the present context. This is because for two-dimensional problems, direct methods are much more time consuming and require more storage than iterative ones. Further, for the non-linear problems considered here, the use of a direct method is not economical since the equations have to be solved repeatedly with updated coefficients.

The iterative methods start from a guessed field for the dependent variables and use the algebraic equations to obtain an improved field. Successive repetitions of the algorithm finally lead to a solution that is sufficiently close to the correct solution of the problem. Iterative methods are especially attractive for handling nonlinearities, since, coefficient values can be updated before the field solution fully converges.

There are many iterative methods for solving algebraic equations. Two of the most common, are point-by-point and line-by-line methods. In general point-by-point methods have a very slow convergence rate, particularly when a large number of grid points are involved. This is because boundary information is transmitted at the rate of one grid interval per iteration only. Although this can be overcome to some extent by adopting a variable sweeping procedure and multi-gridding, Wright (1989). Hence, an efficient line-by-line method, which recommended by Patankar (1980), is employed for the present study.

The standard line-by-line iterative method used in the present study, takes the form of a 'Penta-Diagonal-Matrix-Algorithm' (PDMA) for coefficient matrices including 5 coefficients, reducing to the well known 'Tri-Diagonal-Matrix-Algorithm' (TDMA) when only 3 coefficients are included. Clearly the TDMA is associated with the use of low order convective transport approximations such as the hybrid scheme, while the additional nodal points introduced by the QUICK and CCCT schemes require the PDMA. That is not to say, however, that TDMA could not be used in such cases also. For instance, Han *et al* (1981) suggested dumping nodal values other than those at the *E*, *W*, *N*, *S* and *P* locations into the source term S_s of Eq. 4.30. This special treatment is not necessary when a PDMA is used. Only the PDMA is described below as the TDMA is essentially the same but with nodal values other than those at the *E*, *W*, *N*, *S* and *P* locations equal to zero.

4.5.1 PDMA formulation

If the north-south values of the independent variable along and east-west line are fixed at their previous iterative values, then the matrix system (Eq. 4.30) can be written along an east-west grid line as,

$$-A_{EE}\phi_{EE} - A_E\phi_E + A_P\phi_P - A_W\phi_W - A_{WW}\phi_{WW} = \sum A_i \phi_i^* + S_s. \quad (4.31)$$

where $i = N, S, NN$ and SS.

Applying Eq. 4.31 to all nodal points along the grid line gives,

$$\begin{bmatrix} \cdot & \cdot & \cdot & 0 & 0 & 0 & 0 & 0 & 0 \\ \cdot & \cdot & \cdot & \cdot & 0 & 0 & 0 & 0 & 0 \\ \cdot & \cdot & \cdot & \cdot & \cdot & 0 & 0 & 0 & 0 \\ 0 & \cdot & \cdot & \cdot & \cdot & \cdot & 0 & 0 & 0 \\ 0 & 0 & l_k & m_k & n_k & o_k & p_k & 0 & 0 \\ 0 & 0 & 0 & \cdot & \cdot & \cdot & \cdot & \cdot & 0 \\ 0 & 0 & 0 & 0 & \cdot & \cdot & \cdot & \cdot & \cdot \\ 0 & 0 & 0 & 0 & 0 & \cdot & \cdot & \cdot & \cdot \\ 0 & 0 & 0 & 0 & 0 & 0 & \cdot & \cdot & \cdot \end{bmatrix} \begin{bmatrix} \cdot \\ \cdot \\ (\phi_{EE})_k \\ (\phi_E)_k \\ (\phi_P)_k \\ (\phi_W)_k \\ (\phi_{WW})_k \\ \cdot \\ \cdot \end{bmatrix} = \begin{bmatrix} \cdot \\ \cdot \\ \cdot \\ \cdot \\ \sum(A_i\phi_i)_k + (S_s)_k \\ \cdot \\ \cdot \\ \cdot \\ \cdot \end{bmatrix}, \quad (4.32)$$

where $l = -(A_{WW})$, $m = -(A_W)$, $n = (A_P)$, $o = -(A_E)$, $p = -(A_{EE})$, subscript k indicates the location of the kth nodal point. For convenience, Eq. 4.32 can be considered as:

$$[A]\ [\phi] = [R]. \quad (4.33)$$

With LU decomposition, the matrix $[A]$ can be written as:

$$[A] = [L]\ [U] \quad (4.34)$$

where,

$$[L] = \begin{bmatrix} \gamma_1 & 0 & 0 & 0 & 0 & 0 \\ \iota_2 & \gamma_2 & 0 & 0 & 0 & 0 \\ \nu_3 & \iota_3 & \gamma_3 & 0 & 0 & 0 \\ 0 & \cdot & \cdot & \cdot & 0 & 0 \\ 0 & 0 & \cdot & \cdot & \cdot & 0 \\ 0 & 0 & 0 & \cdot & \cdot & \cdot \end{bmatrix} \quad (4.35)$$

$$[U] = \begin{bmatrix} 1 & \delta_1 & \omega_1 & 0 & 0 & 0 \\ 0 & 1 & \delta_2 & \omega_2 & 0 & 0 \\ 0 & 0 & \cdot & \cdot & \cdot & 0 \\ 0 & 0 & 0 & \cdot & \cdot & \cdot \\ 0 & 0 & 0 & 0 & \cdot & \cdot \\ 0 & 0 & 0 & 0 & 0 & \cdot \end{bmatrix} \quad (4.36)$$

The coefficients ν, ι, γ, δ and ω in the two matrices $[L]$ $[U]$ can be found by multiplying them together and equating coefficients through Eq. 4.34. After some algebraic manipulation, this gives,

$$\begin{aligned} \nu_k &= -(A_{WW})_k \\ \iota_k &= -(A_W)_k - \nu_k \delta_{k-2} \\ \gamma_k &= (A_P)_k - \nu_k \omega_{k-2} \\ \delta_k &= \frac{-(A_E)_k - \beta_k \omega_{k-2}}{\gamma_k} \\ \omega_k &= -\frac{(A_{EE})_k}{\gamma_k}. \end{aligned} \quad (4.37)$$

Thus, the decomposition of $[A]$ into the product of the upper and lower triangular matrices $[L]$ and $[U]$ is achieved via Eq. 4.37.

We now write Eq. 4.33 as:

$$[L]\,[U]\,[\phi] = [R], \quad (4.38)$$

or

$$[L]\,[Y] = [R], \quad (4.39)$$

with

$$[Y] = [U]\,[\phi]. \quad (4.40)$$

The $[Y]$ vector can be found quite easily using forward substitution.

$$y_k = \frac{r_k - \iota_k y_{k-1} - \nu_k y_{k-2}}{\gamma_k}, \quad (4.41)$$

and the vector $[\phi]$ follows from backward substitution,

$$(\phi_P)_k = y_k - \delta_k (\phi_P)_{k+1} - \omega_k (\phi_P)_{k+2}, \quad (4.42)$$

where the rs and ys are the elements of the matrix in $[R]$ and $[Y]$.

For a solution over the whole domain the above procedure is applied to each of the east-west grids in turn, using the most recent values from the previous grid line. After one such sweep the procedure is repeated along north-south grid lines with east-west values fixed.

This double sweep procedure can be repeated any number of times to achieve a desired level of accuracy for the solution of the dependent variable. Usually a single double-sweep is preferred for each dependent variable, except that is for pressure correction equalisation, which requires two double-sweeps.

4.5.2 Nonlinearity and under-relaxation

In the iterative solution of the algebraic equations, a process which speeds up or slows down the changes in the values of the dependent variable, from iteration to iteration, is referred to as over-relaxation or under-relaxation, respectively. Under-relaxation is commonly used for line-by-line method, and is a very useful device for non-linear problems. It is often employed to avoid divergence in the iterative solution of strongly non-linear equations such as the species equation in the present equation set.

To improve convergence rate and avoid divergence, a relaxation factor λ is introduced. Eq. 4.7 becomes:

$$\frac{A_P}{\lambda}\phi_P = \sum A_i\phi_i + S_S + \frac{1-\lambda}{\lambda} A_P \phi_P^*, \tag{4.43}$$

with

$$A_P = \sum A_i - S_P, \quad i = EE, WW, NN, SS, E, W, N, S. \tag{4.44}$$

The superscript * denotes the value at the previous iteration. A value of λ between zero and unity or greater than unity is equivalent to under-relaxation or over-relaxation, respectively. When the iterations converge, ϕ becomes equal to ϕ^*. Eq. 4.43 ensures that the converged values of ϕ satisfy the original Eq. 4.7.

4.6 Coupling of Pressure and Velocity

In previous sections, the procedure for solving a general transport equation for ϕ in the presence of a given flow field is formulated. However, the flow field, in general, can not be specified *a priori* and must be calculated from the appropriate governing equations. The velocity components are governed by the momentum equations in which part of the source term is formed by a pressure gradient. The pressure field is not known before hand and is individually specified via the continuity equation. Hence, the pressure field must be chosen in such a way that the solution of the momentum equations yields a velocity field which also satisfies the continuity constraint.

The classical way to eliminate this difficulty is to use a vorticity streamfunction formulation; whereby the explicit appearance of the pressure gradient is eliminated from the transport equations (Roache 1972, Gosman *et al.* 1969). The shortcomings of this approach are the difficulty of specifying the boundary conditions for the vorticity, and extension of the method to three dimensions for which a streamfunction does not exist.

In recent years, most Computational Fluid Dynamists have employed a primitive variable formulation, in which the velocity components, together with the pressure (or pressure correction), are solved via their own transport equation. Of these, the Semi-Implicit Pressure-Linked Equation (SIMPLE) algorithm, attributed to Patankar and Spalding (1972), represents a remarkably successful solution procedure for achieving this goal. This algorithm was used in the present work and for the sake of completeness, is reviewed briefly below.

4.6.1 Formulation

Applications of the general finite difference equation (Eq. 4.7) to the velocity, u, for a control volume at e (Fig. 4.1), gives:

$$A_P^u u_e = \left(\sum A_i^u u_i \right)_e + S_e^u + a_w \left(p_P - p_e \right), \tag{4.45}$$

where S^u is a source term (other than pressure) in the equation and a_e is the face area, of the control volume, at location e. Equations similar to Eq. 4.45 can be constructed for

the other velocity components at w, n, and s and at all other such nodes covering the solution domain.

For the control volume centred at P (Fig. 4.1), the finite difference equations for the continuity equation can be written as:

$$C_e - C_w + C_n - C_s = 0. \tag{4.46}$$

Since the pressure field is in general unknown, a pressure distribution p^* is assumed, which, when substituted into Eq. 4.45, yields the corresponding approximate velocity field u^*,

$$A_P^u u_e^* = \left(\sum A_i^u u_i^* \right)_e + S_e^u + a_e \left(P_P^* - P_E^* \right). \tag{4.47}$$

The velocity and pressure will need to be corrected with u' and p' accordingly,

$$u = u' + u^*, \tag{4.48}$$

$$p = p' + p^*. \tag{4.49}$$

Subtracting Eq. 4.47 from Eq. 4.45 gives:

$$A_P^u u_e' = \left(\sum A_i^u u_i' \right)_e + a_e \left(P_P' - P_E' \right). \tag{4.50}$$

The velocity correction can not be computed with Eq. 4.50 as a pressure correction is not known. The SIMPLE algorithm overcomes this problem by neglecting the first term on the right hand side of Eq. 4.50 to give the following simplified expression:

$$u_e' = d_e \left(P_P' - P_E' \right), \tag{4.51}$$

where,

$$d_e = \frac{a_e}{A_P^u}. \tag{4.52}$$

Eq. 4.51 can be rewritten (at location e) as:

$$u_e = u_e^* + d_e \left(P_P' - P_E' \right). \tag{4.53}$$

By introducing Eq. 4.53 and analogous expression for u_w, v_n, v_s into Eq. 4.45, we have:

$$A_P p'_P = \sum A_i p'_i + b, \qquad i = E, W, N, S, \tag{4.54}$$

in which:

$$\begin{aligned} A_P &= \sum A_i, \quad i = E, W, N, S, \\ A_E &= \delta y \, \rho_e \, d_e, \\ A_W &= \delta y \, \rho_w \, d_w, \\ A_N &= \delta x \, \rho_n \, d_n, \\ A_S &= \delta x \, \rho_s \, d_s, \\ b &= C^*_e - C^*_w + C^*_n - C^*_s. \end{aligned} \tag{4.55}$$

The solution of p' from Eq. 4.54 updates the velocity and pressure through Eqs. 4.53 and 4.49 respectively. This procedure must be repeated until a converged solution is obtained. To correct the error introduced when neglecting the term in Eq. 4.50, Patankar (1980) suggested using a under-relaxation factor, α_p, when the pressure is updated; i.e. Eq. 4.49 is replaced by:

$$P = \alpha_p p' + p^*, \tag{4.56}$$

and Eq. 4.52 by

$$d_e = \frac{a_e}{A^u_P / \alpha}. \tag{4.57}$$

where α is the relaxation factor for the velocity.

However, Gaskell and Lau (1986) pointed out that the smaller coefficients of the p' matrix, which are responsible for the magnitude of p', are due to the under-relaxation of the velocity. They suggested that Eq. 4.52 should be used rather than Eq. 4.57 and in this case the pressure must be updated by over-relaxing to accelerate the overall convergence. This approach is adopted in the subsequent computations.

4.7 Programs Description

The programs used to solve the problems investigated in subsequent chapters embody the numerical algorithm and procedures outlined above. They are designed to simulate general two-dimensional laminar flow problems, with or without chemical kinetic reactions. The programs have been written in standard FORTRAN, and can be compiled with a standard FORTRAN compiler. They are designed to run on main frame computers. Although they can be easily modified to run on a personal computer (PC), their performance will be severely limited by the capability of the PC and its compiler. The programs are divided into Subroutines and as far as possible, each one is structured independently such that any change in one subroutine does not have any coupling effect on the other subroutines. Fig. 4.2 illustrates the full operation of the computer program.

4.7.1 Data input

For convenience and flexibility, most of the controlling parameters are stored in a data file. The data file is read when the program is executed. Therefore, without any knowledge of the program, the following conditions can be altered in the data file.

1. Grid refinement,
2. Different grid distributions,
3. Change of inlet conditions,
4. Change of geometry,
5. Different numerical schemes,
6. Different relaxation factors,
7. Different convergent criterion,
8. Change of mixture strength.

Thus, it is very convenient to investigate the effects of various attributes mentioned above. A controlling parameter is incorporated in the data file so that the user can chose to use previous results.

4.7.2 Output of results

Two forms of output are incorporated in the code. Firstly, the maximum and averaged residuals for each variable are displayed on screen at selected intervals, so that the user can monitor the convergence performance of each variable and take appropriate action, such as increasing the relaxation factor for slowly converging variables or reduce the relaxation factor for diverging variables, or terminate the program completely. Secondly, the converged or intermediate solutions are written to two files. With one in a compact form for further computations, and the other in a form that can be read by other software such as UNIRAS for producing graphical output.

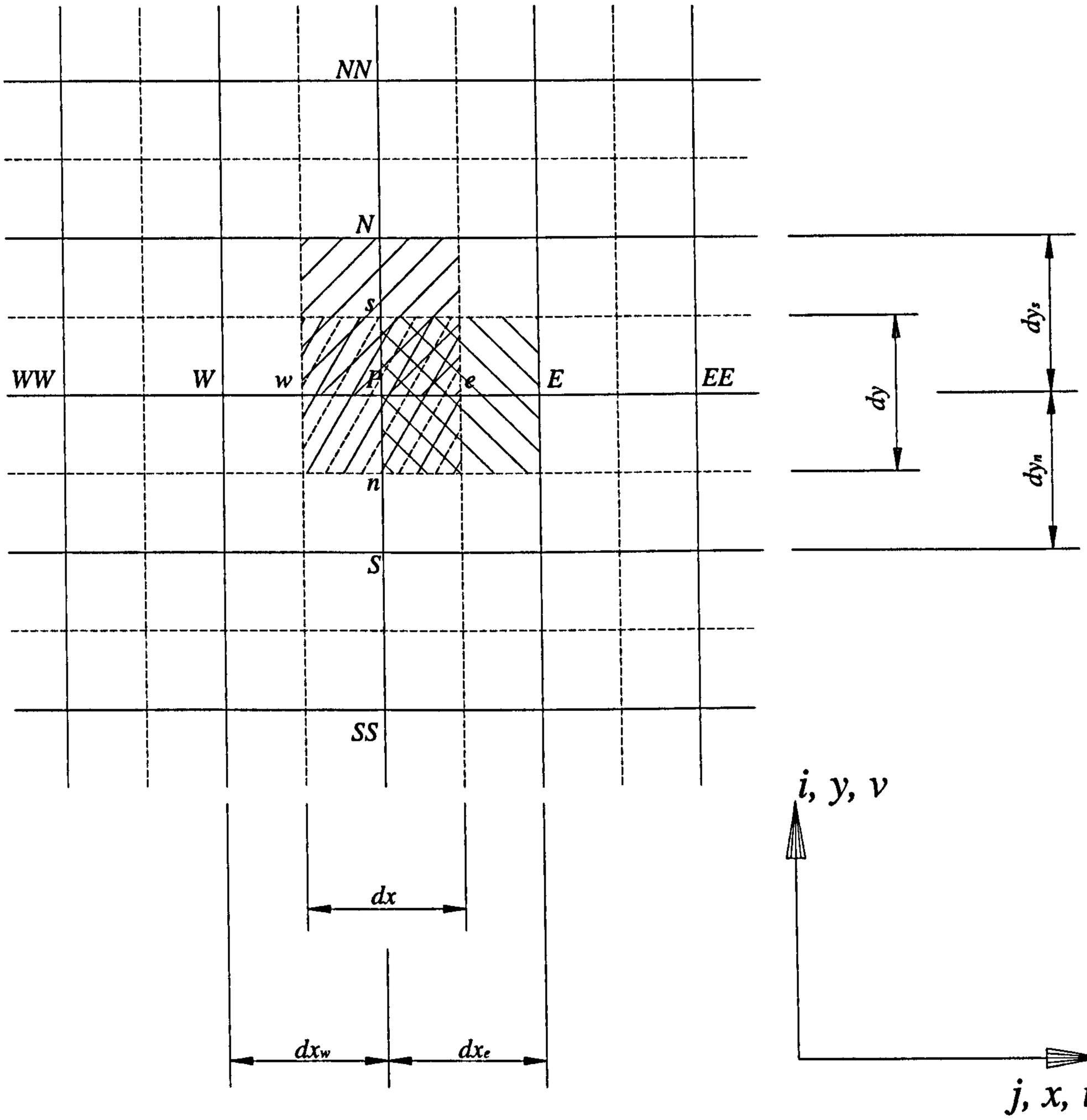

Position of control volumes for :

Fig. 4.1 The staggered grid arrangement

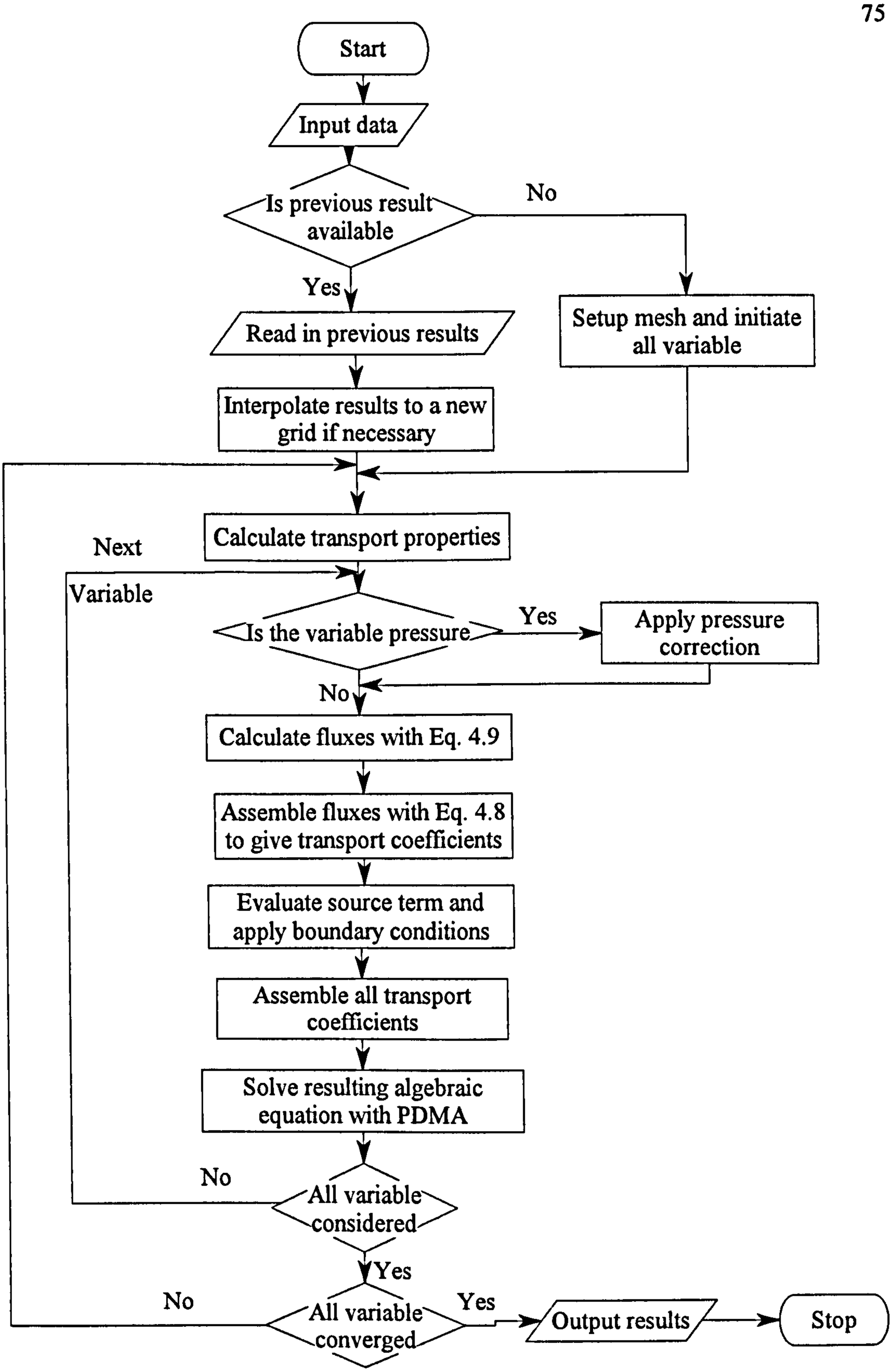

Fig. 4.2 Programme flow chart

CHAPTER FIVE
Laminar Flame Models

5.1 Introduction

This chapter describes the results of computations, using the mathematical models of Chapter 3. Results with the one-dimensional complete reaction scheme of Dixon-Lewis (1981) are described first. These are used in the subsequent heat release model. In this model, the volumetric heat release rates derived from the one-dimensional model are expressed as a function of the fractional temperature increase. The volumetric heat release rate through the flame is found from the one-dimensional flame solution. Application of this approach to two-dimensional field modelling involves expressing the volumetric heat release source term as a function of temperature, and solving a set of but four conservation equations (global mass, energy and momentum in both vertical and horizontal directions). Such an approach avoids the necessity of solving separate chemical species conservation equations. It assumes that the heat release rate is a function of flame temperature only. The third, reduced reaction scheme, model was employed first with the PW scheme described in Chapter 3, followed by the P1 and MP schemes. These schemes couple realistic chemical kinetics with the aerodynamic field and allow for the effects of stretch and preferential diffusion. Unfortunately, computations with the PW and MP scheme were not successful and the presented results of the current work were obtained with the P1 scheme only.

5.2 Planar One-dimensional Flame Model

This model applies a "full" kinetic mechanism to a stationary, planar, one-dimensional flame. The code has been developed over many years by Dixon-Lewis (1981) and has been validated at atmospheric pressure in terms of burning velocities and

gas temperatures. It has been further confirmed in terms of predicted concentrations of CO and H_2 (Dixon-Lewis and Islam 1983).

The model was taken directly from Dixon-Lewis without modification. The results obtained were used to validate the P1 scheme, and generate initial estimates for the reduced model. With this model, when starting a flame computation, a very coarse mesh with as few as six points was used. After a solution had been obtained, extra mesh points were added in regions where the solution or its gradient changes rapidly. The initial guess for the next stage of the computation was obtained by interpolation of the coarse mesh solution. Such use of "adaptive gridding" optimised the computer resources. Thirty-three grid points were eventually placed adaptively in two stages throughout the flame. Detailed transport properties were evaluated as described in Section 3.4.

5.2.1 Boundary conditions

The following boundary conditions were applied.

Unburned Boundary:

$$T_u = 290 \text{ K},$$

$$p_u = 1 \text{ atm.},$$

$$X_i = X_{i_u}, \; i = 1, 2, \ldots\ldots N \tag{5.1}$$

Species CH_4, O_2 and N_2 were in initial mole fractions corresponding to the equivalence ratio. All other species had zero mole fraction (in computations, a very small number was attributed to avoid division by zero).

Burned Boundary:

$$\frac{\partial T}{\partial x} = 0 , \tag{5.2}$$

$$\frac{\partial X_i}{\partial x} = 0, \; i = 1, 2, \ldots\ldots N. \tag{5.3}$$

5.2.2 Results

Three methane-air flames, with initial equivalence ratios of 0.75, 0.84 and 1.0, yielded burning velocities of 0.25, 0.32 and 0.46 m/s, respectively. The computations were on a SUN SPARC II workstation, on which a fully converged solution was obtained in one hour. Results in the form of mole fractions and volumetric heat release rates plotted against temperature, are presented in Figs. 5.1 to 5.3.

From the computed results, it can be seen that, Figs. 5.1 to 5.3, with increasing equivalence ratio, the concentrations of CO, H and O_2 increase at the burnt side. Thus, as far as pollutant formation is concerned, there is a good reason for using lean mixtures. It can be seen from these figures that, the heat release rate and maximum temperature are reduced for a lean mixture.

5.3 The Heat Release Model

The heat release model was initially developed, without consideration of stretch effects, by adopting the procedures described in Chapter 3. However, the curved flame tip is subjected to high stretch rates (Lewis and von Elbe 1964), and it was hoped to include such effects in the heat release model, for which volumetric heat release rates, q, through the flame had been computed for a range of flame stretch rates by Dixon-Lewis (Dixon-Lewis 1988, Bradley and Lau 1990, Bradley *et al.* 1990). It was planned that, in further developments, the flame stretch would be evaluated at each grid node, and revised values of q would be not only appropriate to the temperature, but also the stretch rate.

Initially, this approach seemed efficient and attractive. However, difficulties in its implementation emerged. For example, for the stagnation plane flow configuration used to create the flame stretch, two types of opposed flows are possible. In one fresh mixture and hot products (unburnt-to-burnt) counter flow, whilst in the other both the opposed flows are of fresh mixture (back-to-back). The volumetric heat release rate q profile, not surprisingly, is different under these two configurations (Dixon-Lewis 1990, Bradley and Lau 1990). In addition, within a two-dimensional curved flame, there are both curvature and aerodynamic contributions to the flame stretch and it is impossible, a

priori, to decide which predominates. A further factor is that although the flame is positively stretched near the base, it is negatively stretched near the tip and few data are currently available on the behaviour of volumetric heat release under negative stretch. For these reasons, the implementation of the stretched flame heat-release model eventually was abandoned and preference was given to the reduced four step chemical scheme of Peters (1985). Nevertheless, in the following subsection, the unstretched heat release model is described, and grid dependence tests are conducted to determine the minimum grid size required for such model.

5.3.1 Boundary conditions

Equations 2.1 and 2.3 to 2.5, together with the approximation in Eq. 3.36, were solved with the following boundary conditions (Fig. 5.4):

Inlet ($y = 0$):

$0 < x < x_I$

$$u = 0, \tag{5.4}$$

$$T = 290 \text{ K}, \tag{5.5}$$

$$v = 1.5\, v_m \left(1 - \left(\frac{x}{x_I}\right)^2\right) \tag{5.6}$$

$x_I < x < x_O$

$$u,\ v \text{ and } \frac{\partial T}{\partial y} \text{ all zero}, \tag{5.7}$$

Outer zone ($x = x_O$):

$$u,\ \frac{\partial v}{\partial x} \text{ and } \frac{\partial T}{\partial x} \text{ all zero}, \tag{5.8}$$

Exit ($y \rightarrow \infty$):

$$u,\ \frac{\partial v}{\partial y} \text{ and } \frac{\partial T}{\partial y} \text{ all zero}, \tag{5.9}$$

Axis of symmetry ($x = 0$):

$$u\,,\ \frac{\partial v}{\partial x} \text{ and } \frac{\partial T}{\partial x} \text{ all zero,} \tag{5.10}$$

where v_m is the mean inlet velocity, x_I and x_O represent the inner and outer horizontal coordinates of the slot (Fig. 5.4a). Atmospheric pressure was assumed over the solution domain.

5.3.2 Grid arrangements

It was desirable to position the maximum number of grid nodes in the reaction zone, while achieving grid independent solutions. Advanced techniques such as adaptive and multi-level grid dialogue were considered, but because they would have taken too long to implement, they were discarded and a conventional, non-uniform, rectangular grid was used. With such a grid, some grid nodes were inevitably "wasted" by being located inefficiently; not least because the flame surface of a slot burner is curved whilst the grid system is rectangular.

To minimise wastage, it is necessary to identify the minimum size of the rectangular domain that contains the flow field of interest. The width of this domain depends on the slot width, whilst the height of the domain is set by the flame height. An uniform grid initially was employed to obtain a converged solution, from which the flame height, defined here as 1 mm above the position of the maximum heat release, could be estimated. Vertically, the grid points were so arranged that 70% of them were equally distributed within the flame height, and the rest distributed according to:

$$y(j) = h_f \exp^{\frac{1}{a}(j-h)^{1.5}} \tag{5.11}$$

where $a = \dfrac{(0.3 \times n)^{1.5}}{\ln (h_{max}/h_f)}$

$y(j)$ = horizontal position of the jth grid point

h_f = flame height = $y(ia)$ + 1 mm

n = number of nodes in vertical direction

h_{max} = height of the solution domain above burner.

and the hth grid point corresponds to the vertical position of the maximum heat release.

A number of computer experiments showed that it was necessary for h_{max} to be at least 4 times the flame height for values of velocities and temperature to stabilise. This condition was imposed for all the computations. The grid distribution described by Eq. 5.11 provides a gradual increase in grid spacing above the flame height. A rapid change could de-stabilise convergence. Horizontally, the grid points were so divided that 60% of them were equally distributed within the outlet opening, and the rest equally divided along the slot surface (Fig. 5.5).

5.3.3 Convergence criteria

The convergence criterion and tolerance were:

$$\frac{\sum_{all\ nodes} \left| \frac{\phi_{new} - \phi_{old}}{\phi_{new}} \right|}{Number\ of\ nodes} < 5 \times 10^{-6} \qquad (5.12)$$

where ϕ is the variable concerned. In addition, the downstream velocities and flame height, were monitored so as not to change by more than 5% over 200 iterations. It was necessary for pressure to be over relaxed and Eq. 4.54 had to be solved twice in each iteration (Section 4.6). The relaxation factors employed are presented in Table 5.1.

Table 5.1

Relaxation factors for the 4 primary variables.

Variable	u	v	p	T
Relaxation factor	0.6	0.5	1.2	0.8

They were obtained by trial and error. Initially, a relaxation factor of 0.5 was used for all variables. After a number of iterations, this value was reduced in steps of 0.1 for those equations that diverged, and increased in steps of 0.1 for those that converged.

This process was repeated until all the equations were converging at the maximum rate. Although different mixtures and flow conditions might result in different optimum relaxation factors, there was insufficient time to study this in detail. Convergence was achieved with these relaxation factors for all computations with the heat release rate model.

5.3.4 Grid dependence tests

For a typical flow problem with N grid points, it is generally believed that the required CPU time for obtaining a solution is proportional to N^2. It is therefore essential to use the minimum possible number of grid points commensurate with accuracy. Too coarse a grid can not only produce inconsistent results, but also can lead to problems of convergence.

These objectives led to a series of tests on five different mesh sizes: 40 × 20, 60 × 30, 80 × 40, 100 × 50 and 120 × 60 (number of grid points in the vertical × number in the horizontal directions), with the three commonly used discretisation schemes that have been presented in Chapter 4 : hybrid, QUICK, and CCCT. The grid nodes are non-uniformly distributed, according to the procedure discussed in Section 5.3.2. A typical operating condition of $\phi = 0.84$ and $v_m = 1.0$ m/s was used. Such computations typically required a few hours to half a day of CPU time, the former for the coarsest grid with the hybrid scheme, the latter for the finest grid with the CCCT scheme, on the Computationally Intensive Facility (CIF). This is a 4D/380 system of Silicon Graphics and comprises 8 IP7 processors of 33 MHz processing speed.

Computed heat release rates, temperatures, vertical and horizontal velocities are compared with the different grids vertically along the symmetry axis ($x = 0$), and horizontally at a height of 3.0 mm above burner ($y = 3.0$ mm) in Figs 5.6 to 5.11. Along the axis (Figs 5.6 - 5.8), with all three schemes, as expected, the differences become smaller as the mesh is refined, but are significant with the coarsest mesh. In particular, there is a difference of 0.5 mm in the vertical position of the maximum heat release. This represents a 10% difference in flame height between the coarsest and the finest grid. Similarly, while the shapes of the profiles are very similar, the vertical and horizontal

velocities computed with the coarsest grid show substantial differences in the positions of the maximum velocities. Also, the differences in peak horizontal velocities are over 0.3 m/s, i.e. 150 % difference. Clearly, the results from the coarsest grid (40 × 20) are unacceptable, even though the magnitude of the horizontal velocity is much less than that of the vertical velocity and its contribution to the flow field is small. With regard to temperature, although the maximum values are very similar, the positions of maximum gradient are significantly different (about 0.5 mm in terms of vertical distance). Thus, it can be concluded that, in the vertical direction, at least 60 grid points are required, and 80 grid points are recommended for a flame which is approximately 5.5 mm high. This represents 8 to 10 grid points per 1 mm through the reaction zone.

Much better agreements are obtained in the horizontal direction for almost all but the coarsest grid (Figs. 5.9 - 5.11). Apart from this grid (40 × 20), all other grids provided very good agreements, irrespective of the numerical scheme employed. This indicates that a minimum of 30 grid points are required in the horizontal direction.

Following these conclusions, results are compared, for the different numerical schemes, on a grid of 80 × 40, in Figs. 5.12 and 5.13. Good agreements are observed between the three schemes examined, for all parameters considered. It can be concluded that, with a sufficiently fine grid, there are insignificant differences between the three schemes. However, the hybrid scheme was found to be the easiest to implement and was subsequently employed for the reduced model as well.

5.4 The Reduced P1 Scheme

5.4.1 Introduction

Initially, the PW scheme was used, but yielded high burning velocities for a stoichiometric mixture at a typical average inlet flow velocity of 1 m/s. "Flash back", in which the flame surface propagates upstream when the gas velocity is lower than the burning velocity, was observed, suggesting an excessive burning velocity. A high burning velocity was in evidence in the asymptotic analysis of Peters and Williams (1987), which yielded a value of burning velocity as high as 0.499 m/s. Such an

excessively high value was further confirmed in a recent study of one-dimensional modelling by Dr. Gu, at Leeds (Gu 1994), who computed a burning velocity of 0.63 m/s for a stationary spherical flame with this scheme. He believed that the pressure dependent rate coefficients associated with reaction 26 in Eq. 3.14 may have contributed to such a high value.

Having failed to obtain realistic solutions with this scheme, the alternative P1 scheme was considered. In this scheme, the pressure dependent reaction is eliminated, and there are only 12 elementary reactions, compared with 31 in the PW scheme. Two steady state species are invoked and the scheme is much easier to implement (Section 3.3.1.1). This scheme has been applied successfully to a two-dimensional axisymmetric methane-air diffusion flame by Coelho and Pereira (1993). Species profiles, obtained in the present work, were in good agreement with those computed by the complete scheme of Dixon-Lewis (1983). All of the computations were performed with the P1 scheme, computed results of which are presented in Section 5.5.

The MP scheme was proposed in 1993, in the final stages of the present work. It includes more steady state species and more elementary reactions than the previous mechanisms. Numerical convergence was much slower than with the P1 scheme. It has not been possible to reduce the residuals to levels that satisfy the convergence criterion. Computations were for a stoichiometric mixture with a 2 mm slot width and a mean inlet velocity of 0.5 m/s. Starting values were those obtained with the P1 scheme at the same conditions. Some 300,000 iterations have been performed, over a period of 3 months, yet the residuals, defined in Eq. 5.18, oscillated between the orders of 10^{-1} and 10^{-2}. Adjustment of the relaxation factors and grid size offered only partial improvement. Due to time limitations, computations with this scheme were suspended.

Computations with the P1 scheme were initially on the CIF, and were subsequently transferred to the CIF3. This is a Challenge/XL from Silicon Graphics and comprises 8 IP19 processors of 150 MHz processing speed each. Typically, for a 60 × 40 grid, with optimal relaxation factors, starting with a good initial estimate, 7 days of continuous running, some 30,000 iterations, were required to obtain a converged solution with the CIF. This was reduced to 3 days with the CIF3. Unfortunately, adjustments of the

relaxation factors were frequently required and, typically, 3 weeks were required to obtain a set of solutions on the CIF. This was reduced to about 2 weeks on the CIF3. This lengthy processing time allowed of but a few parametric studies. It was decided to give priority to flame stability investigations at very low and very high flow rates. This is not to say parameters such as mixture preheat and heat loss to burner are not important. Two mixtures of equivalence ratios 0.84 and 1.0 with 2 mm (x_I = 2 mm, x_O = 4 mm) and 3 mm (x_I = 3 mm, x_O = 6 mm) slot widths (Fig. 5.4a), conditions proposed by the collaborating body, were initially considered. A lean mixture of equivalence ratio 0.75 on a 2 mm slot width was later added, as it was thought that the onset of instability could be more quickly achieved with a lean mixture.

With the current computations, once the field solutions had converged on a coarse grid, approximately 5,000 further iterations, 6 hours of CPU time, were required to obtain a converged solution on the next finest grid. Four stages with grid sizes of 60 × 40, 90 × 70, 110 × 110 and 140 × 140 were typically adopted to achieve the finest grid for burning velocity and stretch analysis. Solutions were examined every 5,000 iterations and convergence every 200 iterations.

Since the PW scheme produced unrealistic burning velocities and the MP scheme failed to converge, results from the P1 scheme only are presented. Comparisons of this P1 scheme were made with the "full" scheme of Dixon-Lewis (Section 5.2).

5.4.2 Grid arrangements

The distribution of grid points was very similar to that employed in the heat release model as described in Section 5.3.2. However, regarding minimum grid size, the coarsest grid employed was subjected to two further constraints. First, a minimum grid size of 40 × 40 was required for all computations. Second, as concluded from the grid dependence test performed with the heat release model and verified by a number of computer experiments with the present reduced model, it was necessary to have at least 10 grid points per 1 mm over the reaction zone in order to obtain a consistent solution. Thus, for flames higher than 2.8 mm, it would be necessary to employ more than 40 grid points in the vertical direction to accommodate this flame height. For computation of

the general characteristics, such as flame height, maximum heat release rate and heat loss to burner, the coarsest grid to satisfy the above conditions was used. The grid was refined to 140 × 140 for stretch computations.

5.4.3 Boundary conditions

The governing flow equations are Eqs. 2.1 and 2.3 to 2.5. These are solved with the boundary conditions Eqs. 5.4 to 5.10. However, the boundary condition described by Eq. 5.6 is modified to:

Inlet ($y = 0$):

Outer Zone ($x_I > x > x_O$):

$$u \text{ and } v \text{ are zero}$$

$$T = 290 \text{ K} \tag{5.13}$$

Additional boundary conditions are required for the chemical species equations (Eq. 2.2) considered:

Axis of Symmetry ($x = 0$):

$$\frac{\partial Y_i}{\partial x} = 0, \; i = 1, 2, \ldots\ldots N, \tag{5.14}$$

Exit ($y \rightarrow \infty$):

$$\frac{\partial Y_i}{\partial y} = 0, \; i = 1, 2, \ldots\ldots N, \tag{5.15}$$

Inlet ($y = 0$):

$0 < x < x_I$

$$Y_i = Y_{i_o}, \; i = 1, 2, \ldots\ldots N,$$

$x_I < x < x_O$

$$\frac{\partial Y_i}{\partial y} = 0, \; i = 1, 2, \ldots\ldots N, \tag{5.16}$$

Outer Zone ($x = x_O$):

$$\frac{\partial Y_i}{\partial x} = 0, \; i = 1, 2, \ldots\ldots N, \tag{5.17}$$

where Y_{i_o} is the initial mass fraction of the species i, corresponding to the equivalence ratio.

5.4.5 Convergence criteria

The convergence criterion and tolerance were:

$$\frac{\sum_{all\ nodes}\left|\frac{\phi_{new}-\phi_{old}}{\phi_{new}}\right|}{Number\ of\ nodes} < 5\times10^{-4} \tag{5.18}$$

As before, the downstream velocities were monitored so as not to change by more than 5% over 200 iterations. Among the primary variables, the concentration of H generally had the largest residual and was the slowest to converge. This was probably a result of its small magnitude and high diffusion rate. In practice, a relatively small relaxation factor was used and it was expedient to solve the species equation for H twice in each iteration. Typical relaxation factors are presented in Table 5.2.

Table 5.2

Relaxation factors for the 11 primary variables.

Variable	H	H_2	O_2	CO	CO_2	CH_4	H_2O	*u*	*v*	*p*	T
Relaxation factor	0.1	0.5	0.5	0.2	0.5	0.2	0.5	0.6	0.5	1.2	0.8

They were obtained by the procedure described in Section 5.3.3. The relaxation factors for *u*, *v*, *p* and T are the same as those in the heat release model (Section 5.3.3). During the present study, unless the equations became unstable, these values of relaxation factors were maintained for all conditions.

5.4.6 Starting estimates

Because the governing equations are highly non-linear, their solution required a good starting estimate. This was generated in two stages. First, for the given equivalence ratio, solutions for species concentrations and temperature were obtained from the one-dimensional model as described in Section 5.2. Next, two-dimensional velocity and temperature fields were obtained from the heat release model (Section 5.3), for the same equivalence ratio and given inlet velocity. The two-dimensional flow and

temperature fields from the heat release model, provided initial estimates in the reduced model, whilst species mass fractions from the one-dimensional model solutions were interpolated in relation to the temperature field. Properties such as density, viscosity, conductivity and diffusion coefficient were computed, based on temperature and species mass fractions, according to the procedures outlined in Chapter 2. With these starting estimates, solutions of the reduced model were obtained on the coarsest grid, as discussed in Section 5.4.2. These values were then interpolated onto a finer grid. This procedure was repeated if further grid refinement was required.

This procedure was proved to be successful only when the flow rate was low. It was not so successful at moderate flows (>0.6 m/s). This may be explained by stretch effects, that were not accounted for in the heat release model, but become significant at high flow rates (Chapter 7). For moderate to high flow rates, an alternative procedure therefore was employed. First, a converged solution was obtained with a low flow rate (0.4 m/s). This solution become a starting estimate and the flow rate was increased by a small increment (typically, 0.2 m/s in terms of mean inlet velocity). After about 5,000 iterations, the results were interpolated to a new grid to accommodate the increase in flame height. More grid points might be required to satisfy the 10 grid points per mm criterion (Section 5.4.2). When the solution had fully converged, the procedure was repeated, treating the solution for the increased flow rate as a starting estimate. This procedure, though very time consuming, was found to be necessary to obtain a solution at moderate and high flow rates.

5.4.7 Grid dependence test

To establish grid independence, three different mesh sizes were tested : 70 × 40, 90 × 70 and 140 × 140 (number of grid points in the vertical × number in the horizontal directions), with the hybrid numerical scheme. The test used the P1 scheme and a typical operating condition of ϕ = 1.0 and v_m = 1.0 m/s. Computed heat release rates, temperatures, and species mole fractions are compared with the different grids vertically along the symmetry axis (x = 0) and horizontally at a height of 2 mm above burner (y = 2.0 mm) as shown in Figs. 5.14 to 5.19. For heat release, temperature and all the species

mole fractions considered, good agreements were observed in both vertical and horizontal direction. Clearly, a grid of 70 × 40 is sufficient for a flame of approximately 4.5 mm height.

5.4.8 Validation of the P1 scheme with a "full" scheme

The four-step mechanism is only valid if the results obtained with it conform to those from a complete reaction mechanism or from experiment. In order to attempt some validation of the reduced scheme, the predicted species mole fractions in stretch free regions were compared with those from the "complete scheme" of Dixon-Lewis (Section 5.2) in a one-dimensional flame.

Stretch-free results from the reduced P1 scheme, were obtained as follows:

1. A number of isotherms were identified within the solution domain for the two-dimensional slot burner flame (Fig. 5.11).
2. Stretch was computed along the isotherms (the computation of stretch is described in Chapter 7).
3. Species mole fractions were found in the regions of zero stretch. These were considered to be the stretch-free values at the given temperatures.

Procedures 2 and 3 were repeated for all the isotherms. Results for equivalence ratios of 0.75, 0.84 and 1.0 are presented in Figs. 5.1 - 5.3. The reduced mechanism results are for an inlet velocity of 1.0 m/s, slot width of 3 mm and 140 × 140 grid. The isotherm interval is 50 K. Temperature and species mole fractions were interpolated linearly between adjacent grid nodes. The profiles reveal fair agreement between the two schemes for all three equivalence ratios. With regard to minor species, the reduced P1 scheme over predicts the H_2 mole fraction near stoichiometry.

5.5 Results and Discussion

5.5.1 Field results

Flow field solutions for equivalence ratios of 0.75, 0.84 and 1.0 and inlet mean velocities from 0.4 up to 2.8 m/s were computed. A full list of conditions computed and

values of flame thickness, flame height, flame lift off height, and heat loss to burner base are tabulated in Appendix B. Some of these results are shown graphically in Figs. 5.20 to 5.28. All of the results computed in the course of the present work are presented in a separate Report (Kwan 1994).

A good understanding of the flame structure and flow field is obtained from the contours of volumetric heat release rate, temperature and species mole fractions over the solution domain. Two conditions are considered here: one with an equivalence ratio of 0.84 and mean inlet velocity of 1.4 m/s, another with a stoichiometric mixture and mean inlet velocity of 1.8 m/s. Both conditions are with 3 mm slot width, and are so selected that they have similar flame shape.

Figure 5.20 shows the isotherms in spatial co-ordinates. There are high temperature gradients, for both mixtures, directly above the burner inlet and along the solid surface, leading to significant heat transfer to the burner tube. The temperature rises from 450K to 1950K in about 1.3 mm for the stoichiometric mixture while this length increases to 2.3 mm for the weaker one. This is approximately 8.5 mm above the inlet for both mixtures. This is just below the position of maximum heat release rate (~ 9.5 mm and 9 mm for the stoichiometric and lean mixture, respectively) as shown in Fig. 5.21. The larger separation of the positions of maximum temperature gradient and maximum heat release with the stoichiometric mixture is probably explained by the higher inlet velocity.

The velocity fields are shown in Fig. 5.5. Significant increases in velocity, approximately perpendicular to the temperature isotherms, are observed in the vicinity of the 600 K isotherm. There is no suggestion of any recirculation. Rapid methane and oxygen consumption in the region of the high temperature gradient and heat release rate can be seen in Figs. 5.22 and 5.23. Oxygen consumption rate was faster with the stoichiometric mixture, for which methane consumption rate was slower. Methane and oxygen consumption is followed by relatively large concentrations of CO, H_2, H_2O, CO_2 and H (Figs. 5.24 - 5.28).

Appreciation of flame structures near the instability limits is gained from the illustrations in Figs. 5.29 and 5.30. The two cases considered are both with a

stoichiometric mixture and a 3 mm slot width, but for two extreme inlet velocities, namely, 0.4 m/s and 2.75 m/s. These two velocities represents the lowest and highest velocities obtained in the present study, for which a convergence of numerical solution was achieved. At the low flow rate, Fig. 5.29 illustrates the fairly constant thickness of the heat release zone when and the flame is close to the burner tube with a lift off height of about 0.4 mm. This small lift results in substantial heat flux to the burner surface. This has a peak value of about 320 W/m^2 at the centre of the solid surface. Integration of this flux across the solid surface yields the total heat loss, which in this case represents 32% of the total energy input. This large heat loss is evidenced also by a computed downstream temperature of about 1900 K, about 300 K less than the adiabatic temperature. The stretch rate evaluated at the cold isotherm of 300 K (Fig. 5.29), by the procedure described in Chapter 2, is negative at the base and positive at the tip, but with relatively small numerical values. A substantial increase of gas velocity is observed in the heat release zone.

At high flow rates, the picture is markedly different (Fig. 5.30). The thickness of the heat release zone is fairly constant along the flank of the flame where the stretch rate is relatively small, but becomes significantly thinner at both the tip and base. Here there are very high negative and positive stretch rates, of about -19000 s^{-1} and 2000 s^{-1}, respectively. The heat release rate at the tip is greater than else where, although this cannot be seen in the diagram due to spatial resolution. It would appear that negative stretch focuses heat release there. The lift off height is significantly increased to about 2.6 mm. This results in a reduced heat flux to the burner surface of about 170 W/m^2. Integration of this energy flux profile across the surface gives a heat loss of about 3% of the total energy input. The down stream temperature is approximately 30 K below the adiabatic value of 2200 K.

5.5.2 Flame thickness

In addition to burning velocity, flame thickness is an important parameters in characterising combustion. Physically, the thickness can be considered as a zone of

substantial heat release but its formal definition has yet to be agreed. There are three common definitions of flame thickness illustrated by Fig. 5.31.

1. Zeldovich introduced the "characteristic thickness" in 1944, defined as:

$$\Delta_z = \lambda/(c_p \rho_u u_l) \tag{5.19}$$

2. Gaydon and Wolfhard (1953) define the flame thickness as the thickness between 1% rise of the initial temperature and the maximum temperature gradient. This corresponds to approximately 4.6 times that defined by Zeldovich.

$$\Delta_{GW} \approx 4.6\, \Delta_Z \tag{5.20}$$

3. Spalding (1955) defined the flame thickness as the ratio of maximum temperature rise and maximum temperature gradient.

$$\Delta_s = \frac{T_b - T_u}{(dT/dx)_{max}} \tag{5.21}$$

The Zeldovich expression gives a constant thickness for a given mixture and initial temperature, irrespective of flow conditions is inappropriate. Apart from Spalding's definition, for comparison purpose, a flame thickness can also be considered as the distance for which heat release is above certain rate H_{thick}. In the present analysis, H_{thick} is taken to be 2 GW/m³ per unit depth. Thus, the flame thickness Δ_H is given by

$$\Delta_H = x_{H2} - x_{H1} \tag{5.22}$$

where x_{H1} and x_{H2} are positions where the heat release H_{thick}=2 GW/m³.

Figures 5.32 to 5.34 show the variation of flame thickness with flow rates for equivalence ratios 0.75, 0.84 and 1.0, with both 2 mm and 3 mm slot widths, with 2 mm and 3 mm slot wall thicknesses, respectively. Flame thickness was calculated at the axis of symmetry from Eqs. (5.21) and (5.22). For the three mixtures and the two geometries considered, though with some scatter, flame thicknesses calculated by both methods increases monotonically with flow rate for a given mixture and burner. Thus, as the flow rate increases, the heat release zone is extended whereas the temperature gradient

flattens. It is observed that, compared to the flame thickness obtained with Eq. 5.22, values obtained with Eq. 5.21 overpredict the flame thickness for lean mixtures of ϕ = 0.75 and $\phi = 0.84$.

5.5.3 Flame height

The flame height is an important parameter, as it ultimately dictates the combustion chamber size. For a diffusion flame, the end of the flame can be defined as that point on the flame axis where the fuel and oxidant are in stoichiometric proportions. For a premixed flame, it might be defined by the point where the heat release rate is a maximum. For the present axisymmetric flame, the flame height is defined as the distance, along the axis of symmetry ($x = 0$), between the burner outlet and the flame tip position, where the heat release rate is a maximum (Fig. 5.35). The position of this maximum value is considered as the flame tip.

Values of flame height for various mixtures and flow conditions are presented in Figs. 5.36 to 5.38. For all the conditions considered, there is a linear relationships between flame height and flow rate for a given burner geometry and mixture. This also was observed with the heat-release rate model. However, while the heat-release rate model underpredicted the height for lean mixtures (ϕ = 0.75, 0.84) it was overpredicted for a stoichiometric mixture.

With both the heat release rate model and the reduced P1 scheme, the gradients of the flame height against flow rate curves, for both 2 mm and 3 mm geometries, are very similar for a given mixture, suggesting that a flame height can be marginally reduced, for a given mixture and flow rate, by increasing the slot width. This is illustrated, for example, with a flow rate of 4×10^{-3} m^2/s per unit depth. With the reduced model, a reduction of 0.5 mm and 0.6 mm, (about 10%) in flame height, can be achieved by switching from a 2 mm to 3 mm slot width for mixtures of equivalence ratio of 0.84 and 1.0, respectively. For the three mixtures considered, the gradients of flame height against flow rate are 2.5 s/m, 2.3 s/m and 1.8 s/m for equivalence ratios of 0.75, 0.84 and 1.0 respectively. From Figs. 5.36 to 5.38, it also is observed that, for a given flow rate, with the three mixtures concerned, flame height reduces with increase in ϕ.

5.5.4 Flame stability

At very low flow rates, heat loss to the burner can be excessive and the flame quenched. On the other hand, the flame can be thermally stable at flow velocities less than the burning velocity of the mixture and the flame propagate upstream - the condition of flash back. The computational studies showed flash back to occur with all three mixtures, at mean inlet velocities of 0.3 m/s, 0.34 m/s and 0.40 m/s for equivalence ratios of 0.75, 0.84 and 1.0 respectively. Computations were performed over 0.02 m/s flow velocity increments.

At very high flow rates, the flame can either blow off, when the flame base is severely positively stretched and the flame is quenched, or the flame tip can open as more oxygen is diffused towards the tip due to preferential diffusion and the mixture becomes too lean to burn. It was highly desirable to perform computer experiments to investigate these phenomena, but unfortunately, it was impossible to obtain solutions at the requisite high flow rates, due to diverging numerical instabilities. It is possible that the numerical instability is due to a physical one. Maximum mean inlet velocities, with converged solutions, were 2 m/s, 2.1 m/s and 2.75 m/s for mixtures with equivalence ratios of 0.75, 0.84 and 1.0, respectively. Just beyond these values instabilities developed computationally. In reality the flames blow off at inlet velocities of 3.2, 4.7 and 5.6 respectively.

The lift off height of a flame is defined as the minimum distance between the burner surface and the base of the flame where the heat release rate is 2 GW/m^3 (Fig. 5.35). The lift off heights at various flow rates are illustrated in Figs. 5.39 to 5.41. Despite some scatter a general increase of lift off height with flow rate is observed.

5.5.5 Heat loss to burner tube

The heat loss to the burner is a very important parameter in burner design. From the efficiency point of view, it is desirable to have minimal heat loss to the burner tube. Too high a temperature at the tube will give rise to flash back, discussed in 5.5.4. The temperature at the base can be controlled, to some extent, by selecting a material with appropriate thermal properties. The heat flux is given by

$$\dot{q}_{loss} = \lambda\left(\frac{\partial T}{\partial y}\right) \tag{5.23}$$

where $\dot{q}_{loss}$ is the heat flux to the solid surface ($y = 0$). The temperature gradient $\partial T/\partial y$ was obtained from the boundary grid points at the surface and the adjacent one directly above it. Thermal conductivity was evaluated from Eq. 2.31. Figures 5.42 to 5.44 showed the variation of heat flux across the surface with mean inlet velocities of 0.4, 1.0 and 1.6 m/s, (only half of the slot is shown, as it is symmetrical) and equivalence ratios of 0.75, 0.84 and 1.0, respectively. In every case there is an increase in heat flux from the edge towards the middle of the solid wall. This is explained by the heat removed from near the edge by the flow of fresh mixture. In addition, the flame typically sits somewhere between the edge and the middle of the solid wall, with less heat release directly above the edge of the slot. A boundary condition of 290 K was applied to the solid surface and the inlet mixture temperature was also 290 K. With practical burners, the surface temperature at the middle of the solid wall may be higher due to the high heat flux there. This higher temperature might reduce the temperature gradient and hence heat flux.

It was also observed that, the maximum heat flux, at the middle of the solid wall, increased with the equivalence ratio, for a given flow rate. This is explained by the corresponding relatively larger heat releases and higher temperatures. For a given mixture, the heat flux increased with decreasing flow rate. This is to be expected since with a low flow rate, the flame was short and close to the top of the burner. The shorter lift off height associated with a low flow rate encouraged heat transfer to the slot surface.

By integrating the heat flux along the width of the solid surface, the rate of heat loss, $\dot{Q}_{loss}$, in W/m², to the slot was evaluated. Figure 5.45 gives the total heat loss in watts for a 1 meter deep slot over the width between limit slot edges. For a given burner geometry and flow rate, the richer the mixture the greater the heat loss. For a given flow rate and mixture, the 2 mm burner geometry gives the lower heat loss. This is because the mass flux is higher with this burner, resulting in a higher flame and lift off height.

These reduce the temperature gradient and hence the heat loss. As expected from the Figs. 5.38 to 5.40, heat losses are generally lower for a higher flow rate.

It is interesting to note that, with the burner surface maintained at 290 K, over 650 W of heat energy is lost in 1 meter depth over the width between edges, for a stoichiometric mixture at a flow rate of 0.8×10^{-3} m³/s. This heat loss reduced to about 230 W for a lean mixture of $\phi = 0.75$ at the higher flow rate of 4.0×10^{-3} m³/s.

The rate of supply energy of the fresh mixture $\dot{q}_{IN}$ flowing into the slot per unit depth is given by:

$$\dot{Q}_{IN} = v_m \, t \, \rho_{CH_4} \, \Delta_H \, Y_{CH_4} \tag{5.24}$$

where v_m is the mean inlet velocity, t is the width of the slot opening, and the heat of reaction, Δ_H, is taken from Heywood (1988) as 50.0 MJ/kg. The width of the slot opening, in both cases, is equal to the width between limit slot edges. The percentage heat loss is the heat loss divided by the heat input $(\dot{Q}_{loss}/\dot{Q}_{IN}) \times 100$, evaluated over a slot of unit depth.

For a range of flow rates, Figs. 5.46 to 5.48 demonstrate that, substantial reduction of heat loss can be achieved by selecting a higher flow rate for the burner. Further, for a given mixture and flow rate, the 2 mm burner is more efficient than the 3 mm one. Surprisingly, these figures demonstrate that, over 30% heat loss is possible with a stoichiometric mixture at the low flow rate of 0.8×10^{-3} m³/s. However, the experiments showed that in practice the burner tube temperature were typically 60 degrees above the 290 K temperature used in the computations (Chapter 6). The increased slot temperature would inevitably reduce the temperature gradient, resulting a reduction in total heat loss and percentage heat loss. Nevertheless, these results (Figs. 5.46 to 5.48) demonstrate that heat losses can be substantial.

For all the mixtures considered (ϕ = 0.75, 0.84 and 1.0), Fig. 5.45 shows a decrease of heat loss to the burner base with increasing flow rates. This is a result of the increase in lift off height with flow rate. The changes are more rapid for the 2 mm burner than for the 3 mm burner, and more rapid for $\phi = 1.0$ than for $\phi = 0.84$.

5.6 Conclusions

From these computations, the following conclusions can be made:

1. Flame heights predicted by the heat release model, considering the simplifications made, were in good agreement with the reduced model.
2. Although recently developed, more complex, reduced mechanisms (PW and MP schemes) offered a possibility for improved accuracy over previous scheme (P1), application of them, to two-dimensional flames, was far more difficult than anticipated.
3. With the reduced model, a very close starting estimate is required, particularly when the flow rate is high.
4. As much as 32% heat loss was predicted for a low flow rate and a stoichiometric mixture.

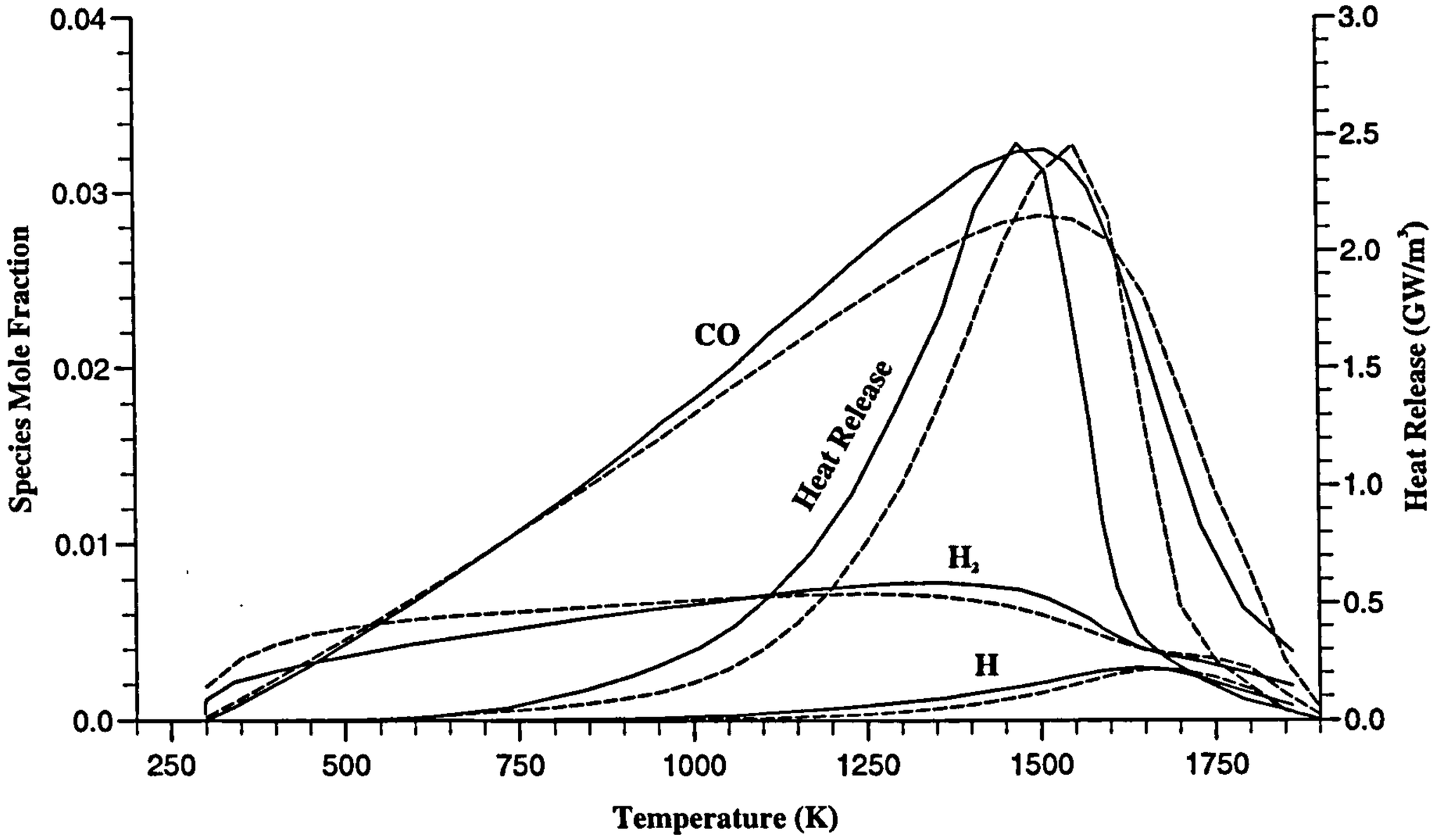

(a)

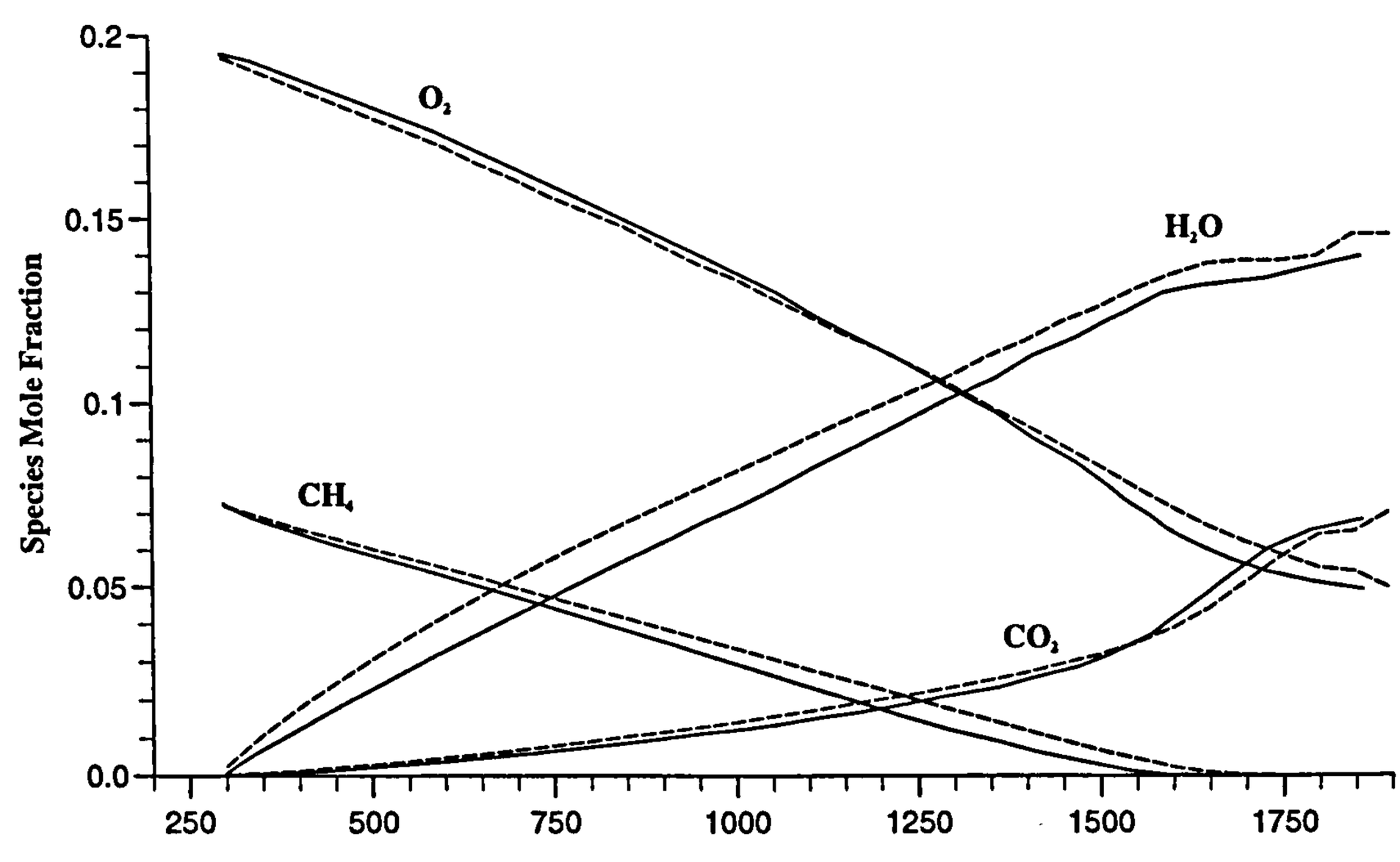

(b)

Fig. 5.1 Comparisons of reduced (dashed line) and complete (full line) schemes in terms of (a) heat release rates and minor species concentration and (b) major species concentration for $\phi = 0.75$, flat flame.

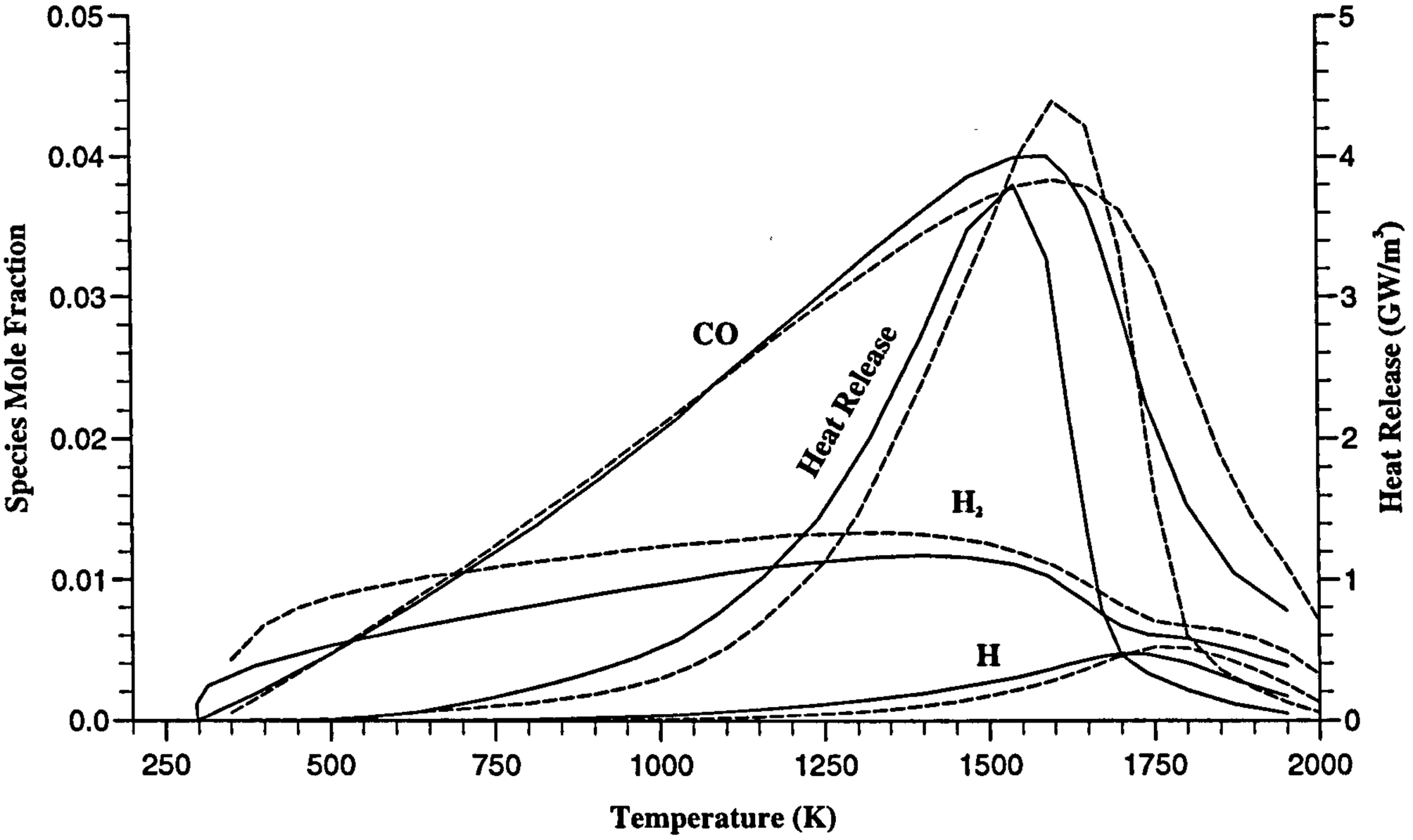

(a)

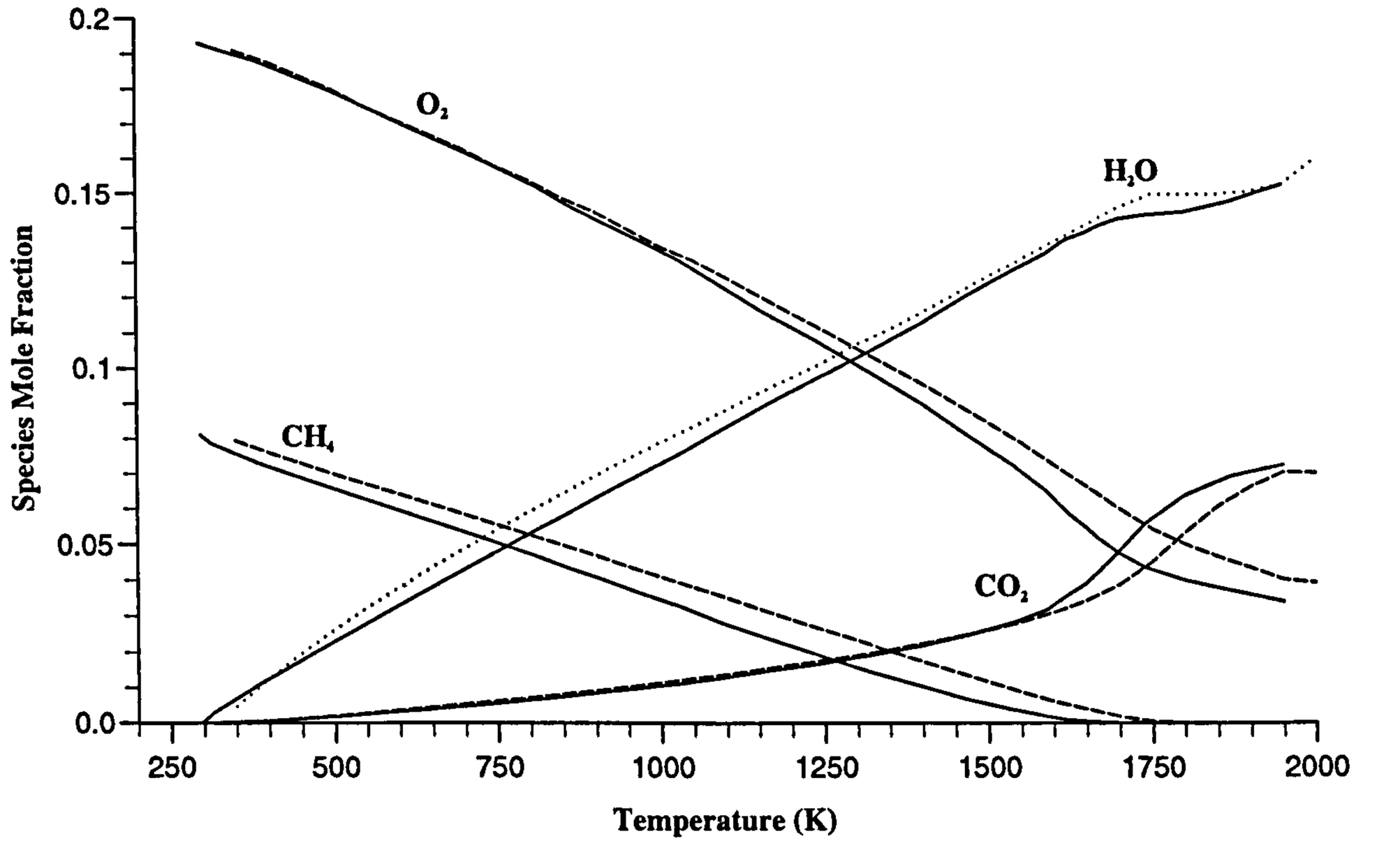

(b)

Fig. 5.2 Comparisons of reduced (dashed line) and complete (full line) schemes in terms of (a) heat release rates and minor species concentration and (b) major species concentration for $\phi = 0.84$, flat flame.

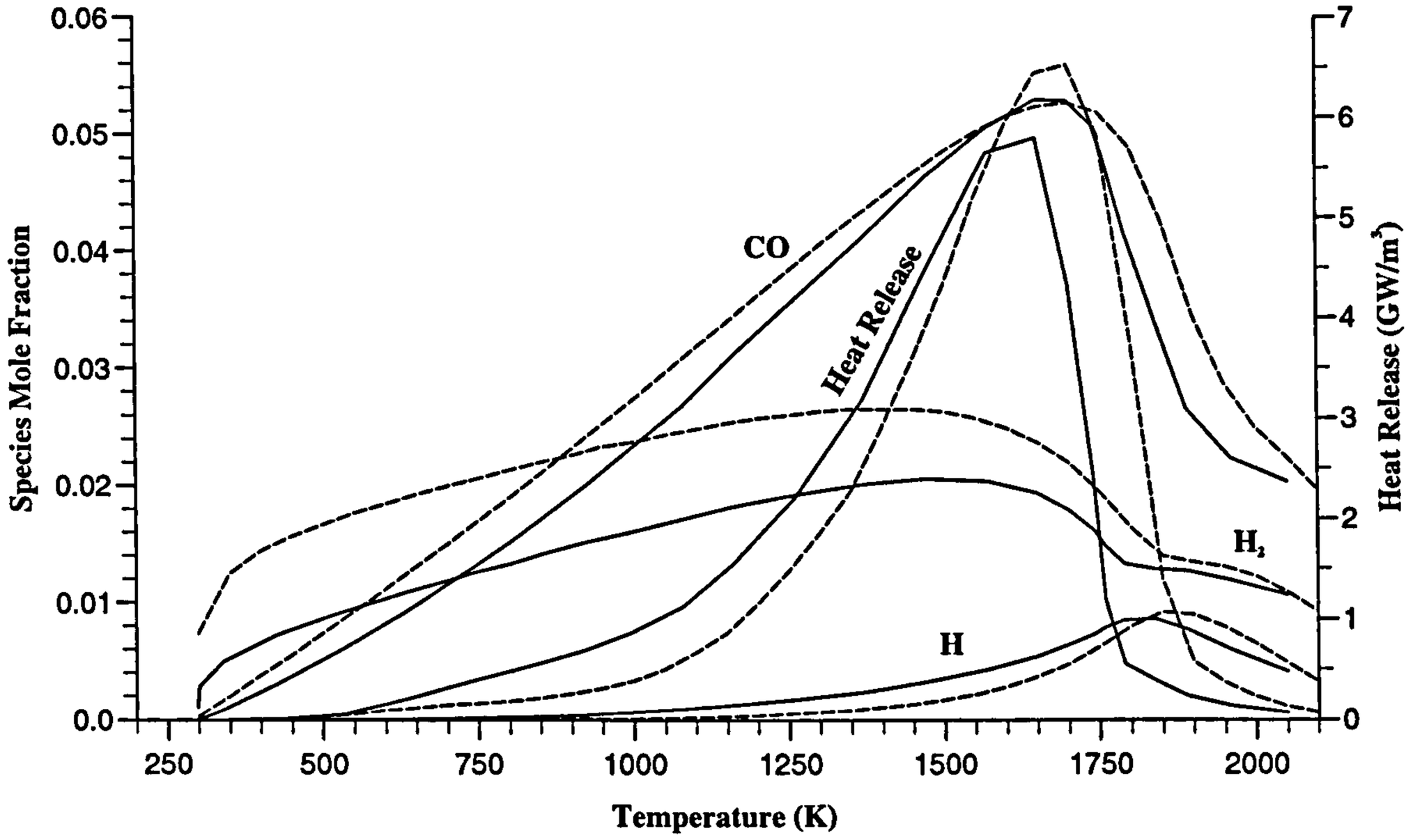

(a)

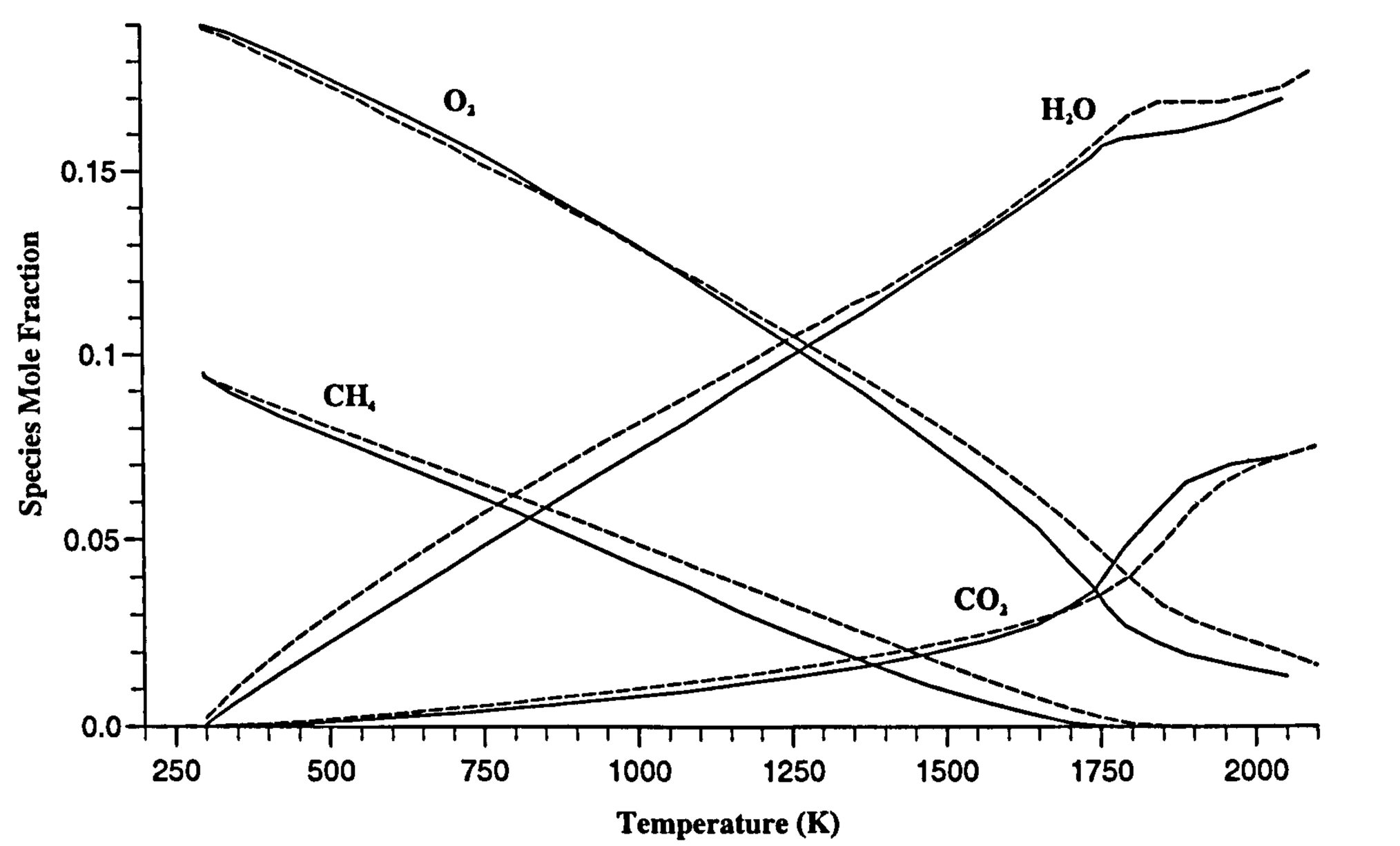

(b)

Fig. 5.3 Comparisons of reduced (dashed line) and complete (full line) schemes in terms of (a) heat release rates and minor species concentration and (b) major species concentration for $\phi = 1.0$, flat flame.

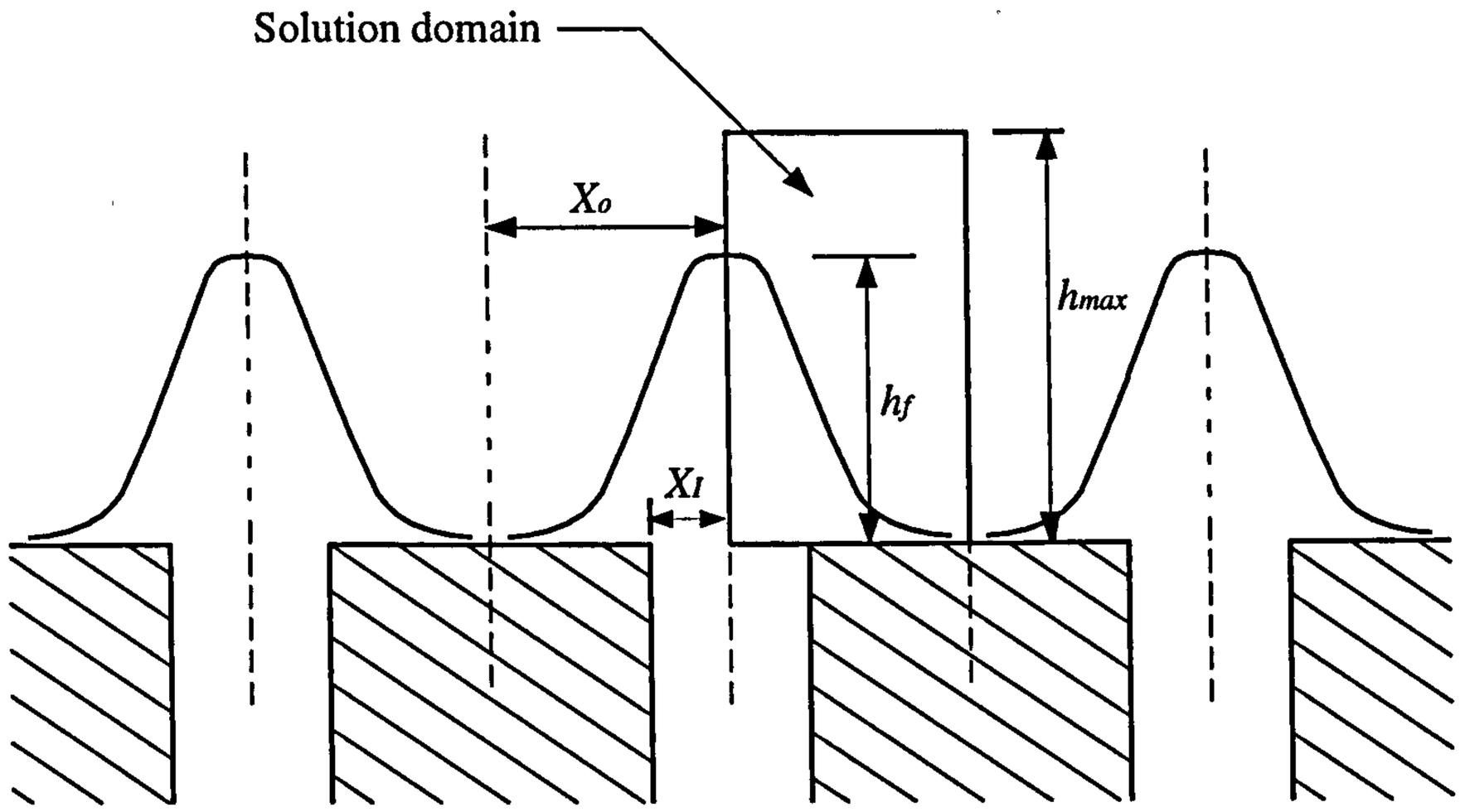

Fig. 5.4a Solution domain in the axisymmetric multi slot burner.

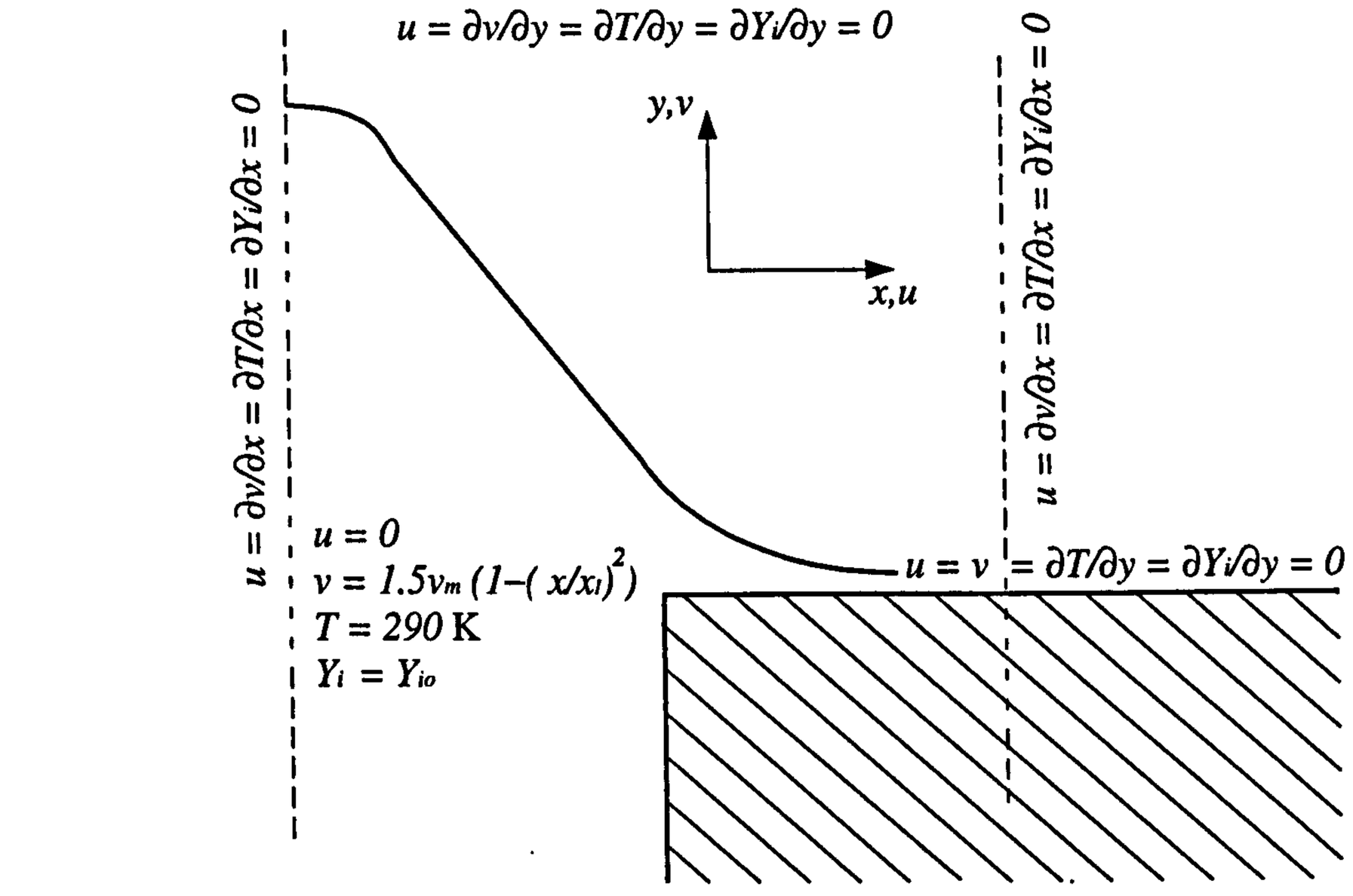

Fig. 5.4b Notation and boundary conditions adopted with the two-dimensional models.

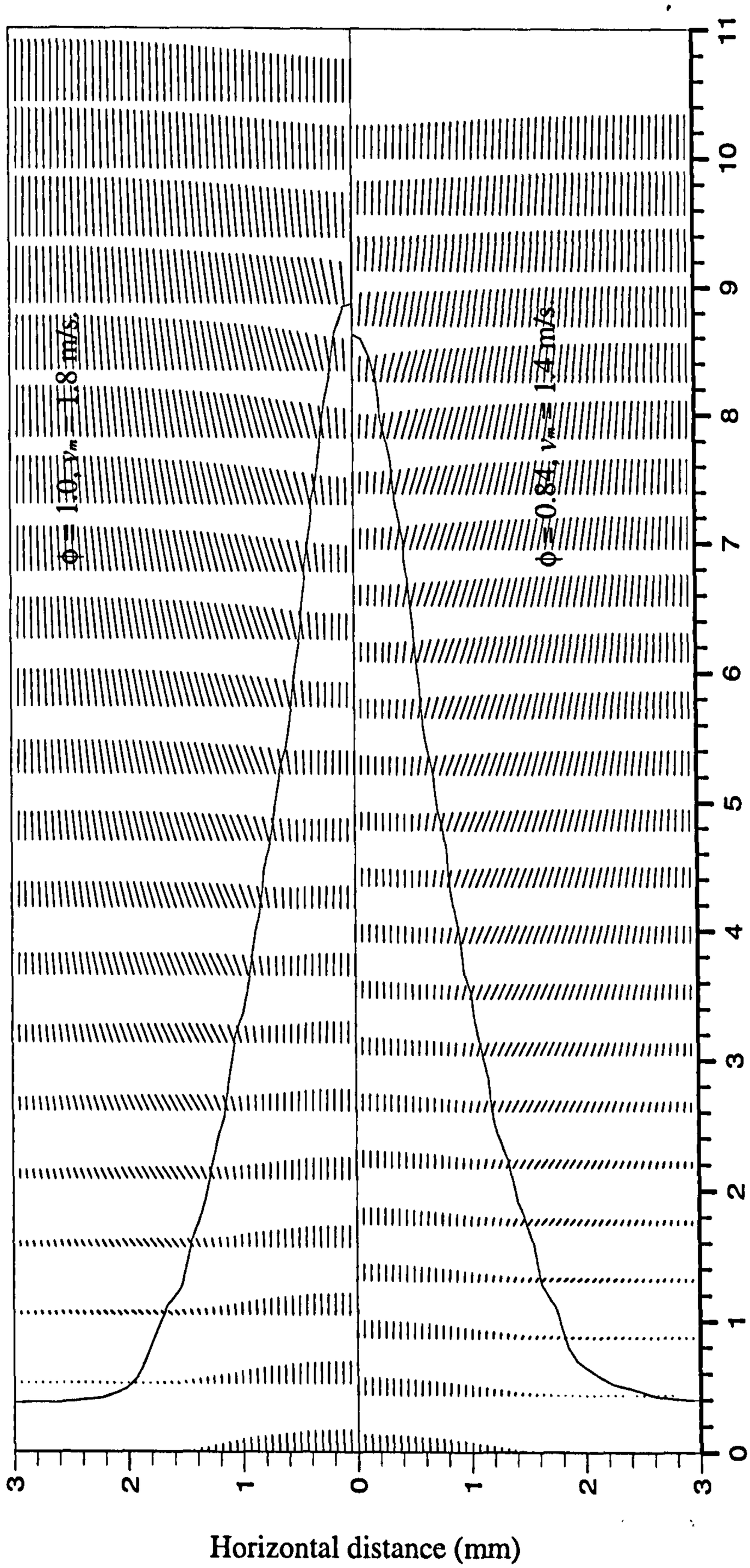

Fig. 5.5 Computed velocity field and the 600 K isotherm for the two axisymmetric slot burner flames.

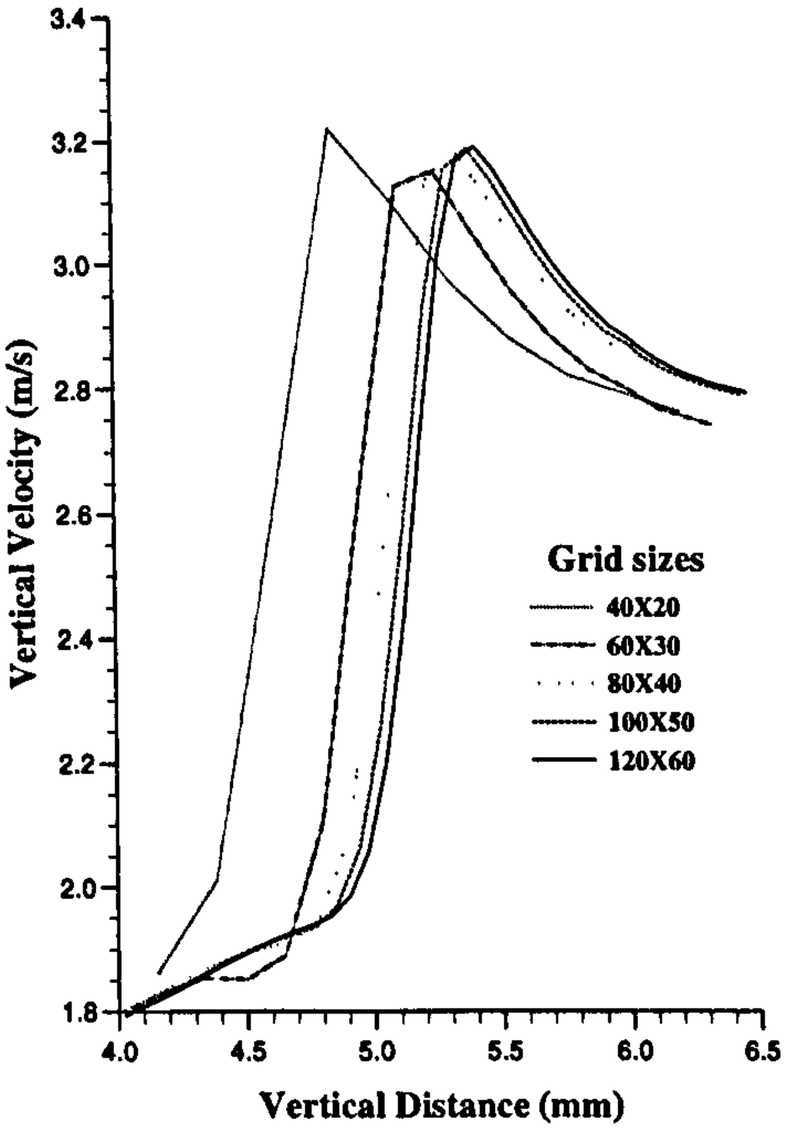

(a)

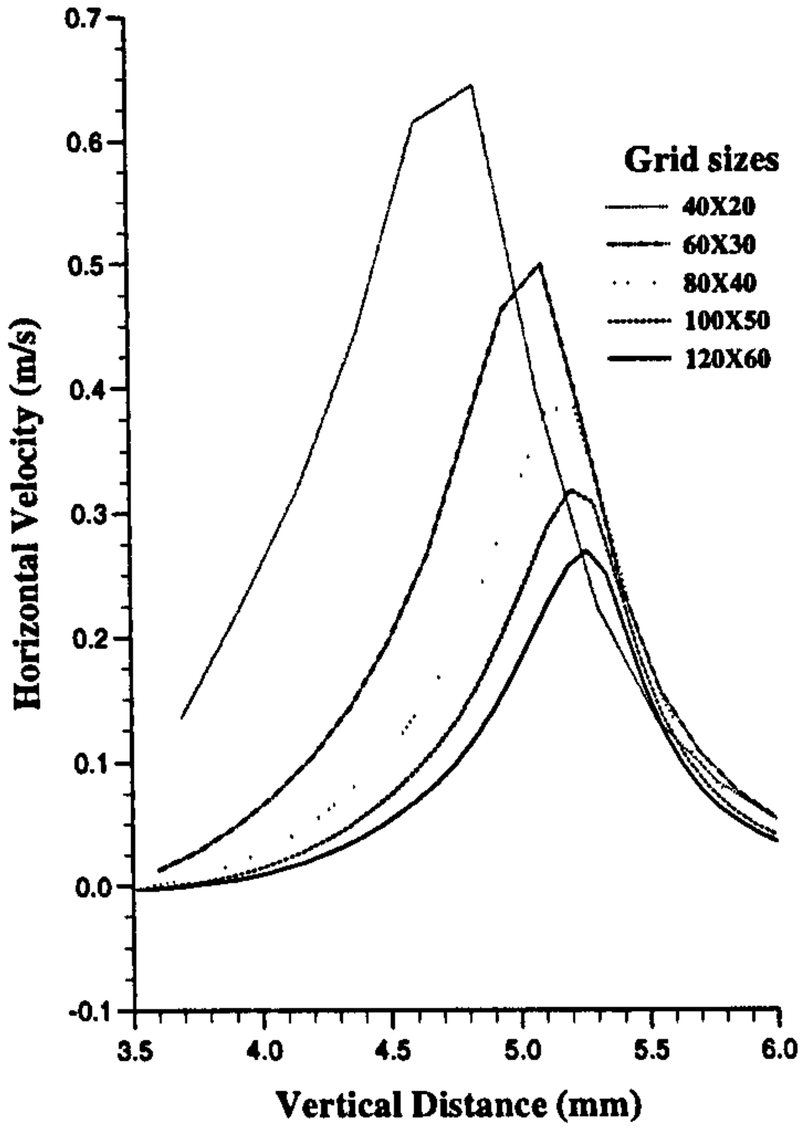

(b)

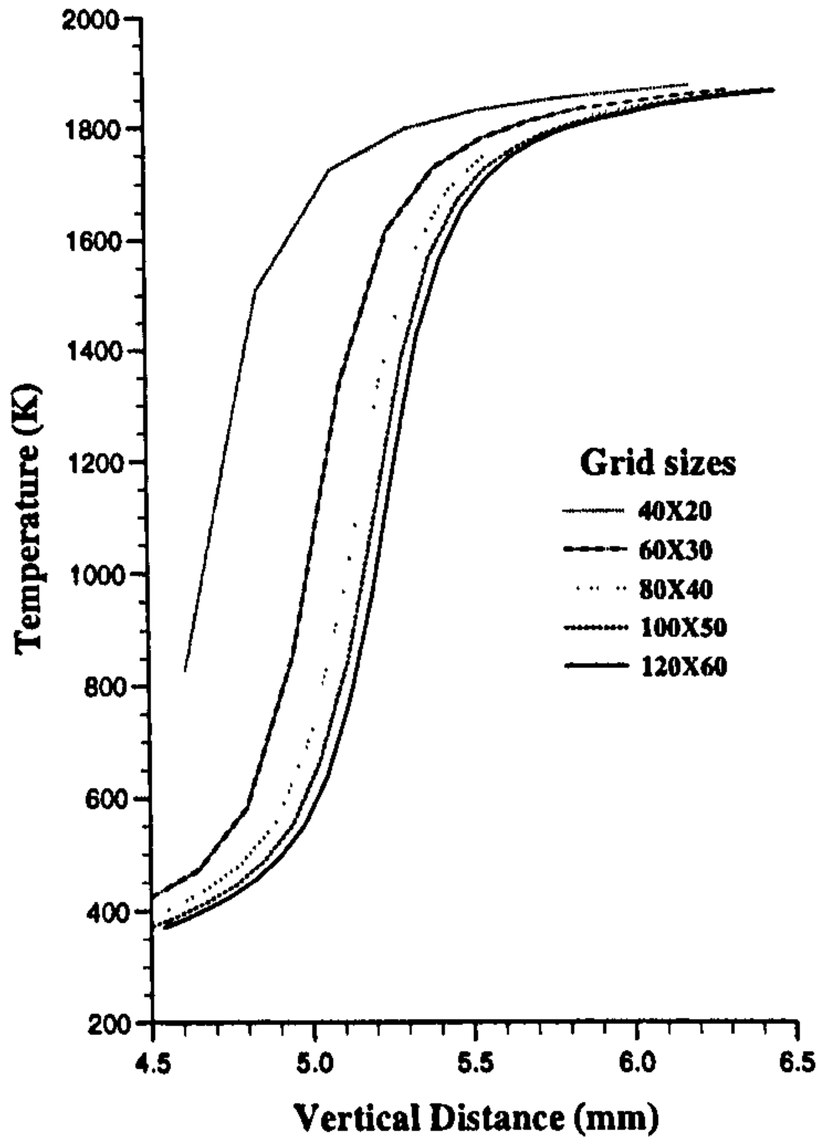

(c)

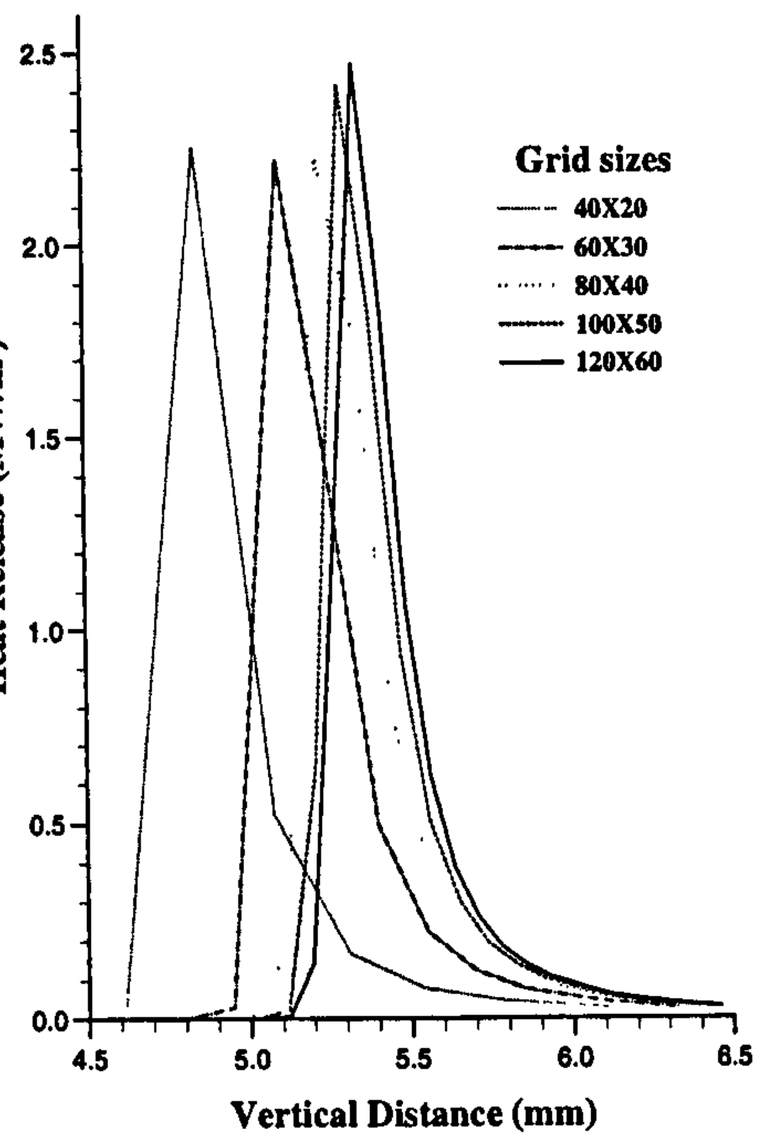

(d)

Fig. 5.6 Computed results with CCCT scheme, along the symmetry axis for grid sizes of 40 x 20, 60 x 30, 80 x 40, 100 x 50 and 120 x 60.

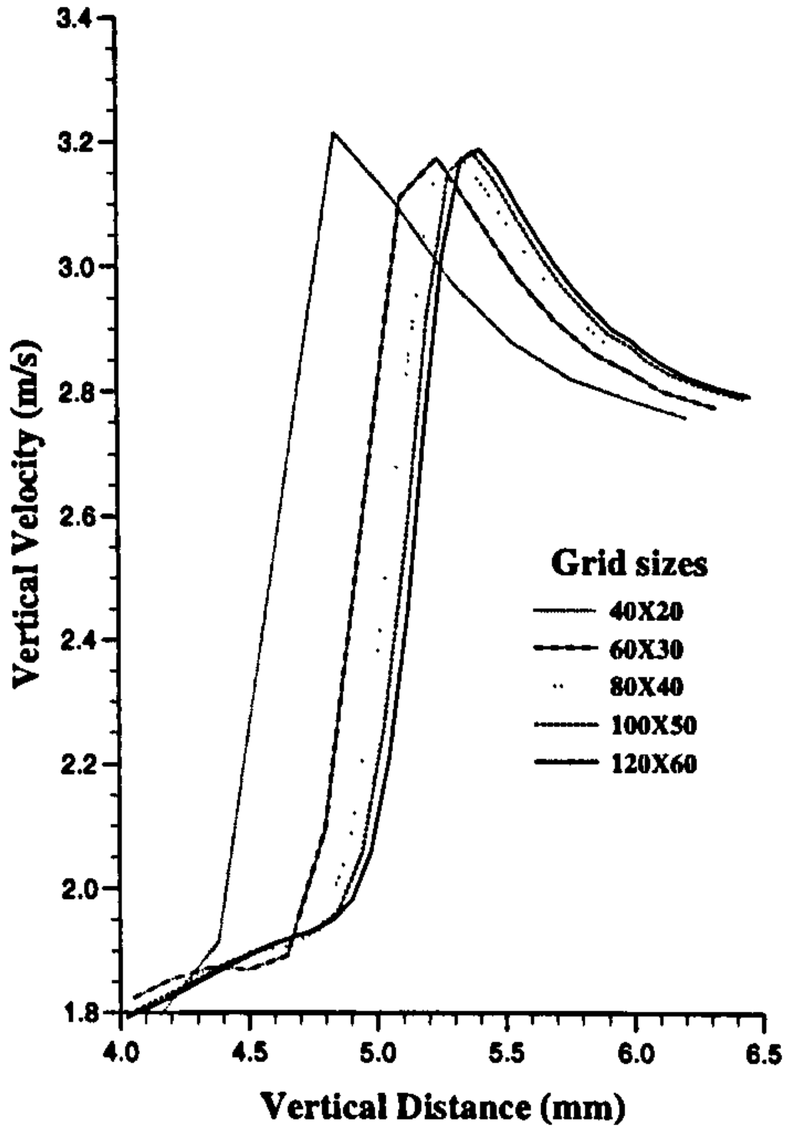

(a)

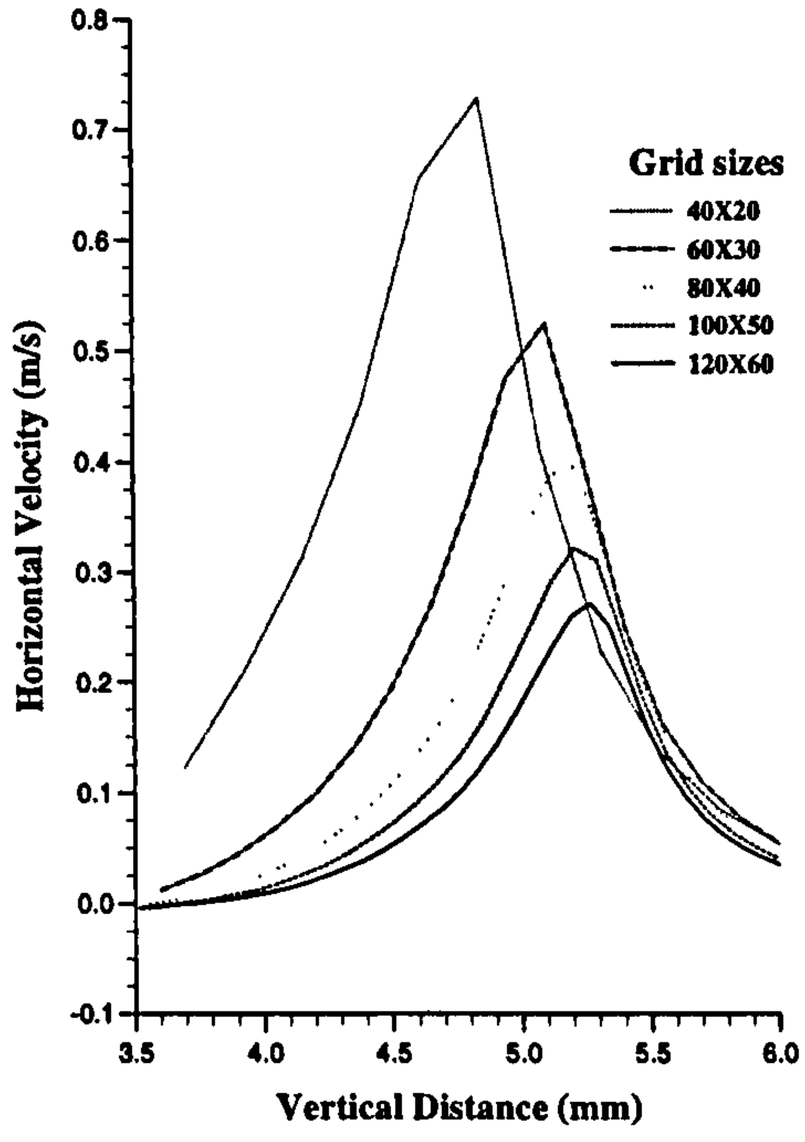

(b)

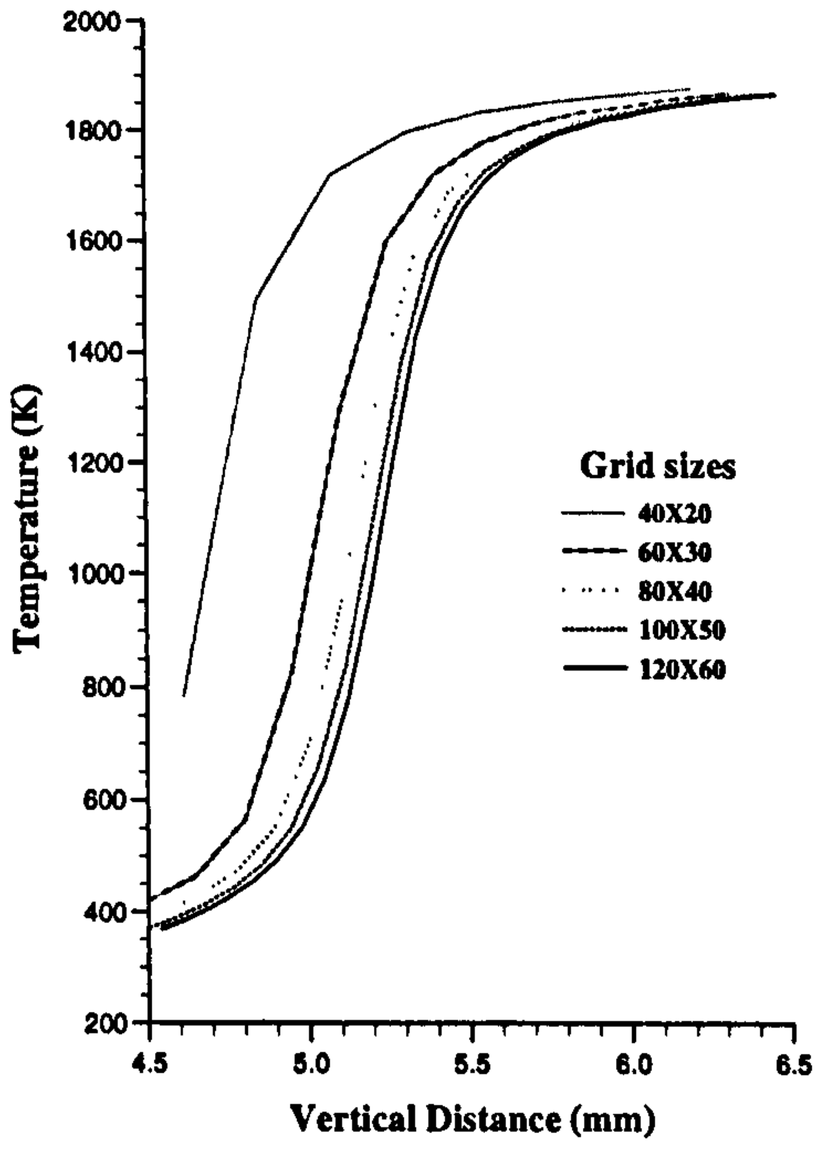

(c)

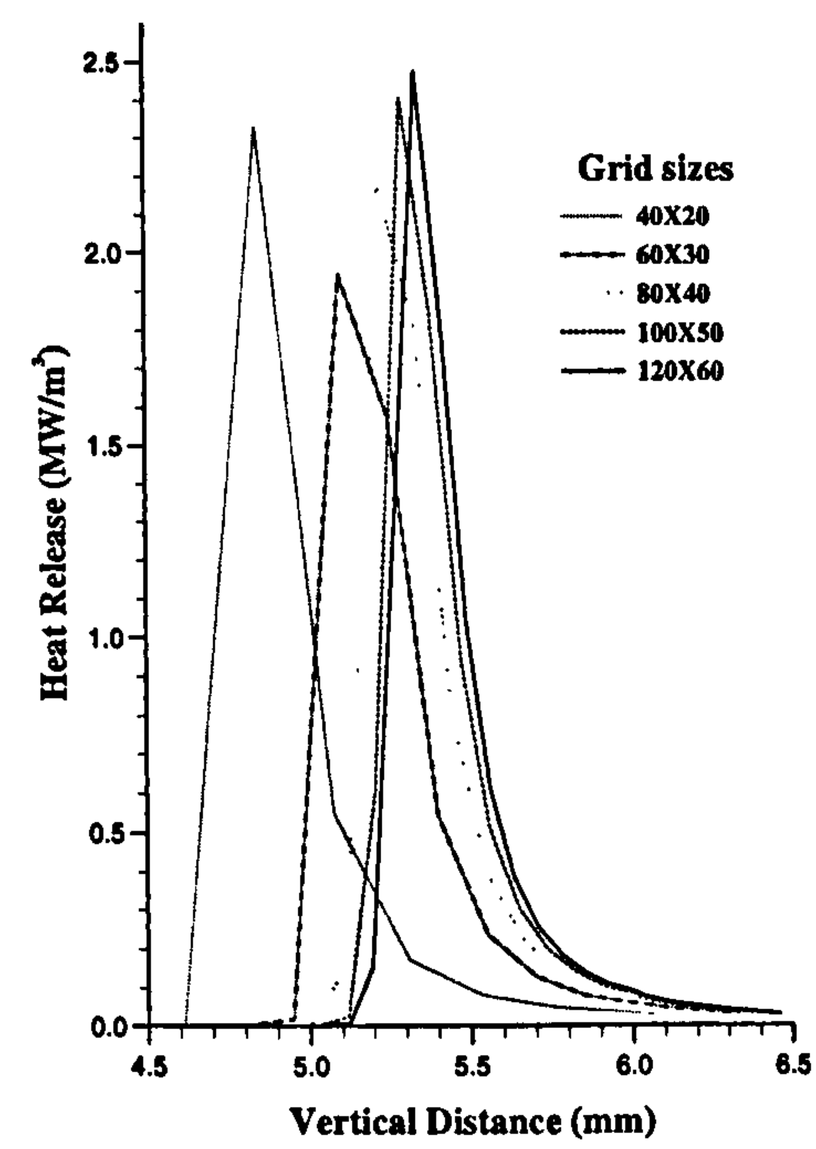

(d)

Fig. 5.7 Computed results with QUICK scheme, along the symmetry axis for grid sizes of 40 x 20, 60 x 30, 80 x 40, 100 x 50 and 120 x 60.

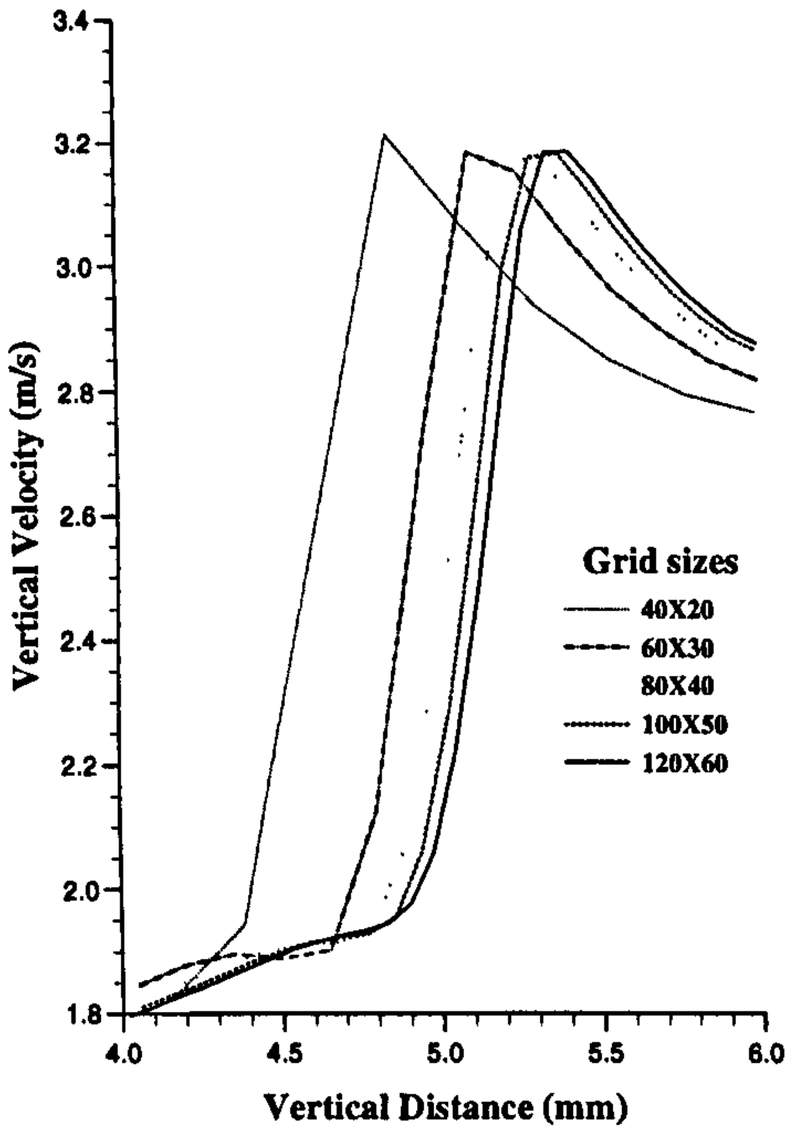

(a)

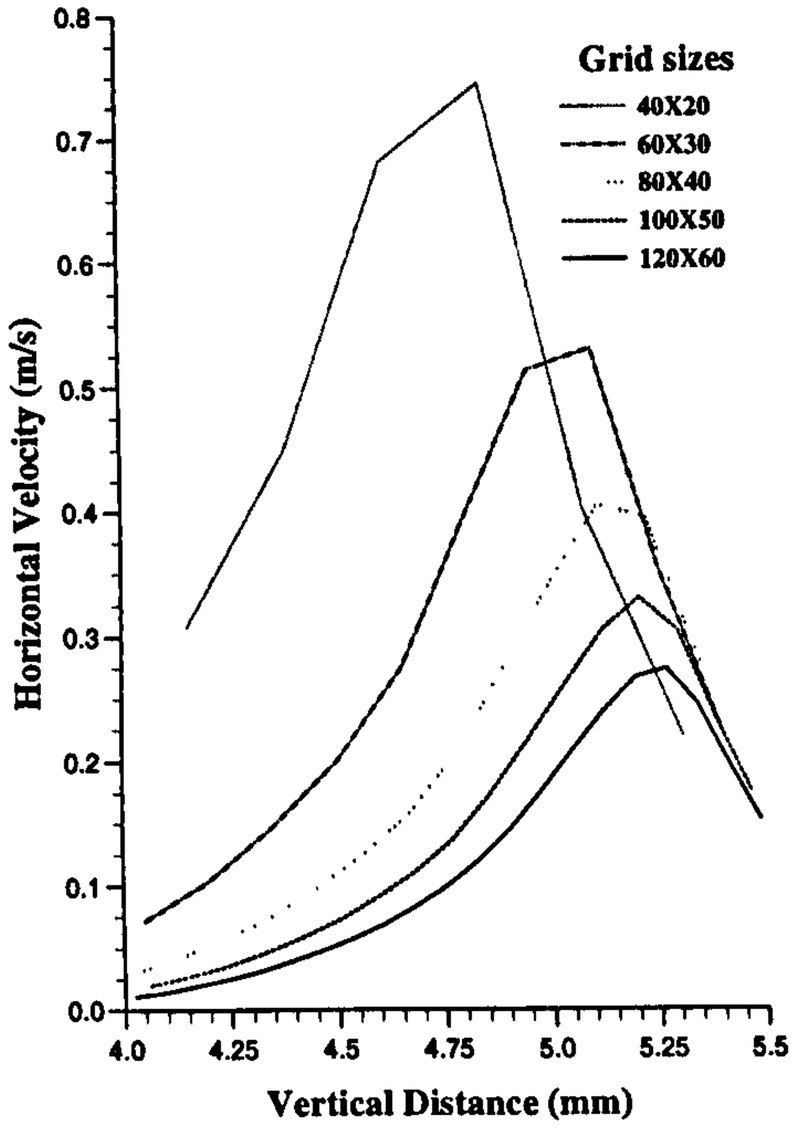

(b)

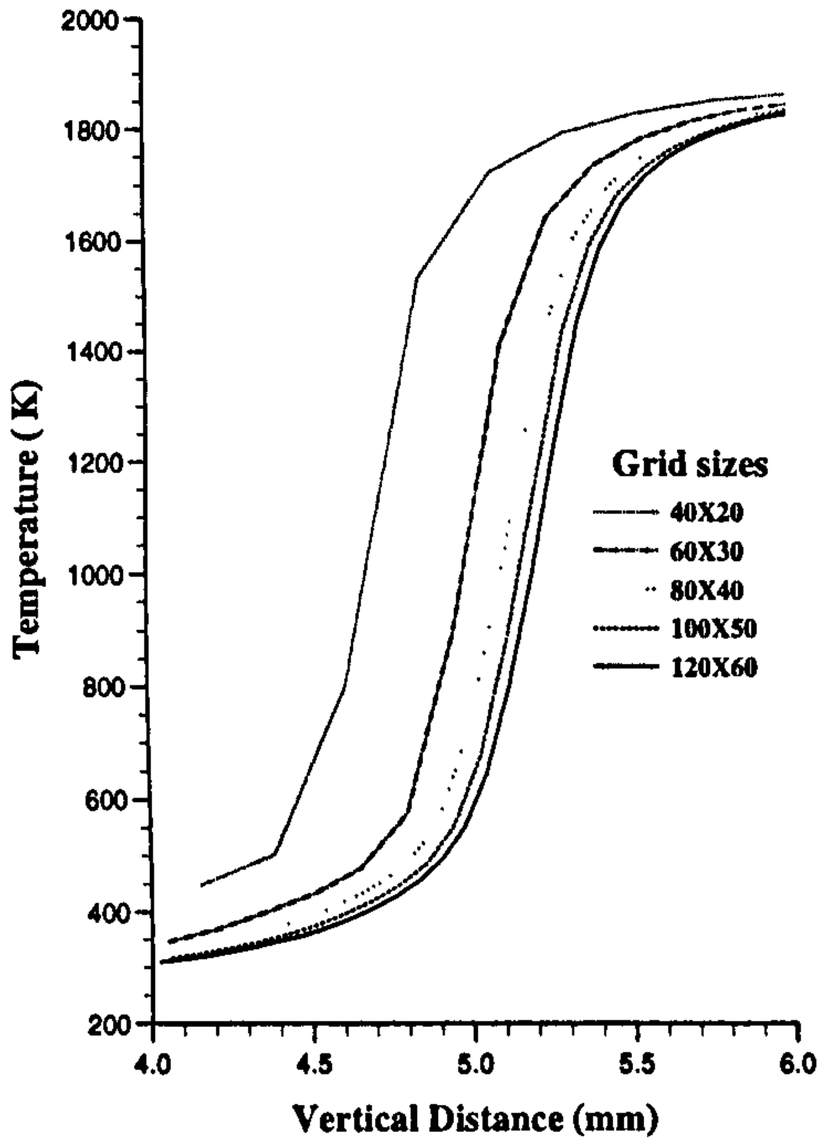

(c)

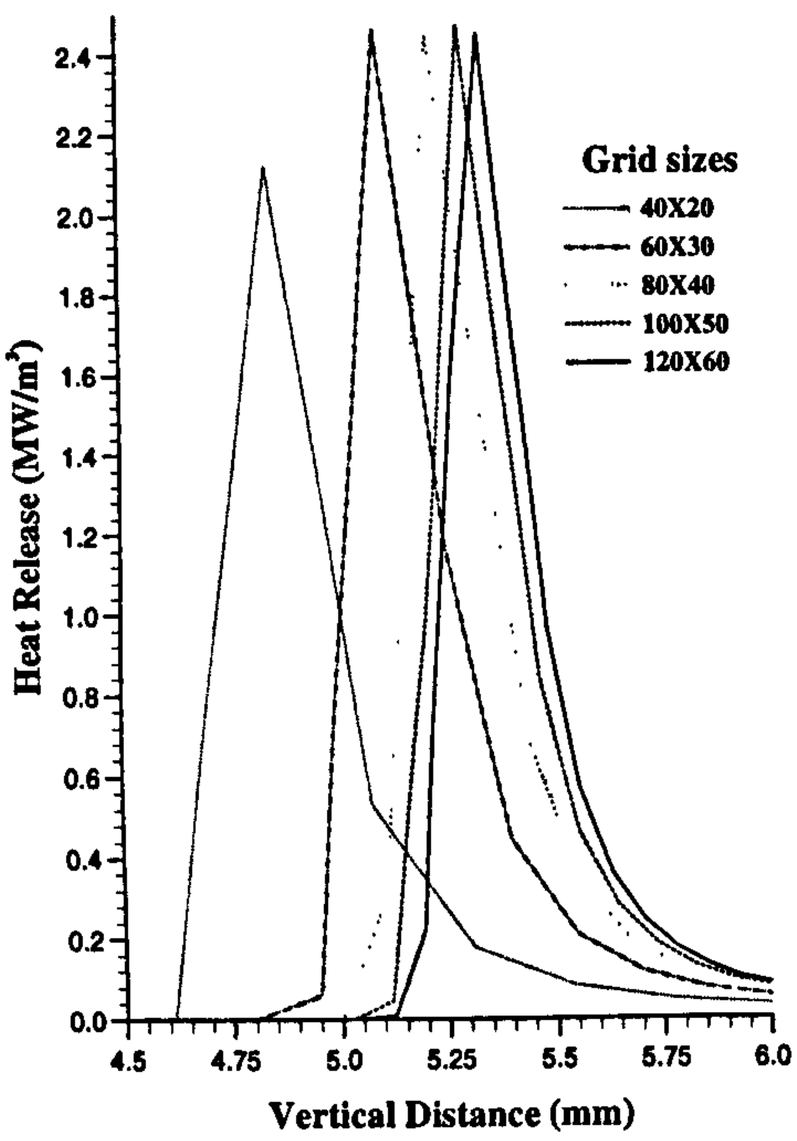

(d)

Fig. 5.8 Computed results with hybrid scheme, along the symmetry axis for grid sizes of 40 x 20, 60 x 30, 80 x 40, 100 x 50 and 120 x 60.

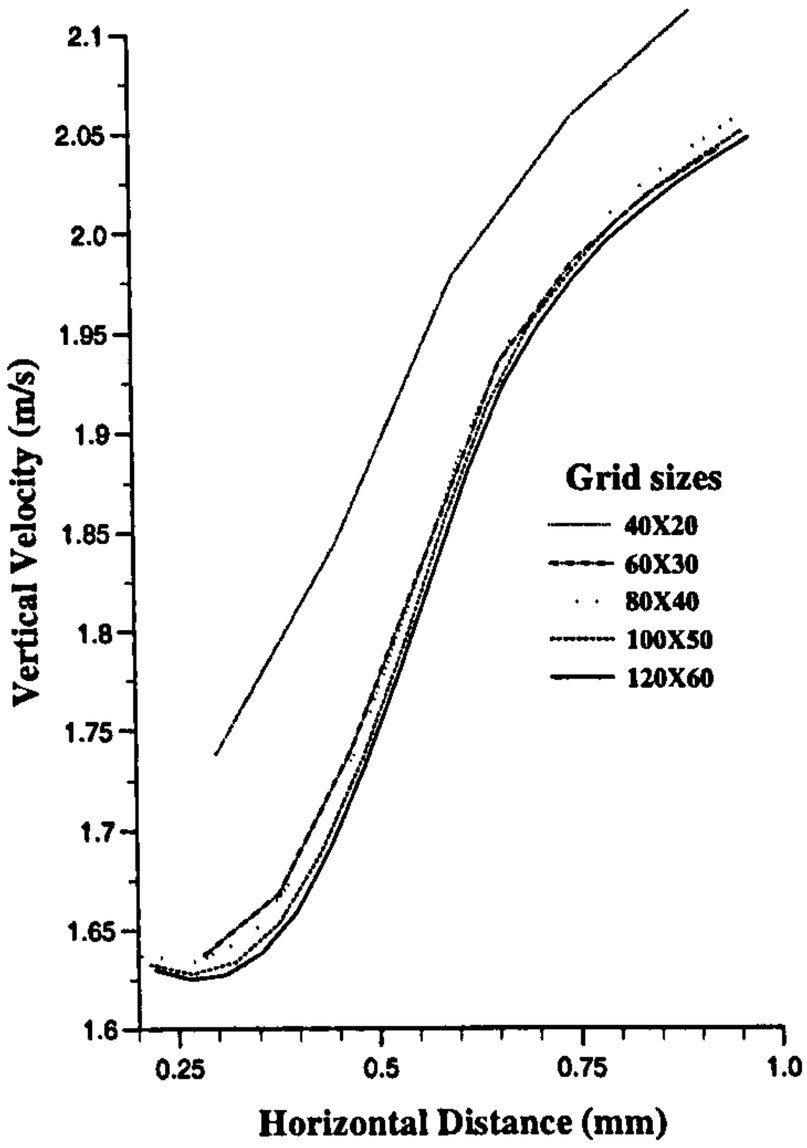

(a)

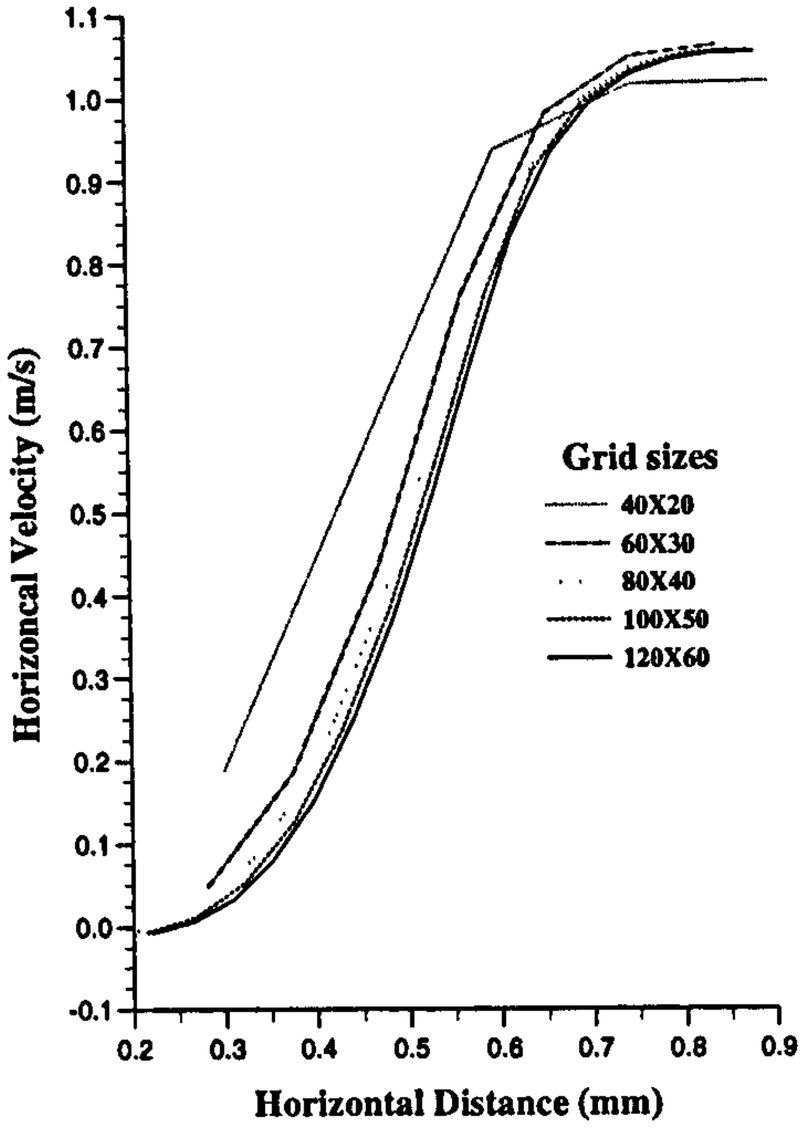

(b)

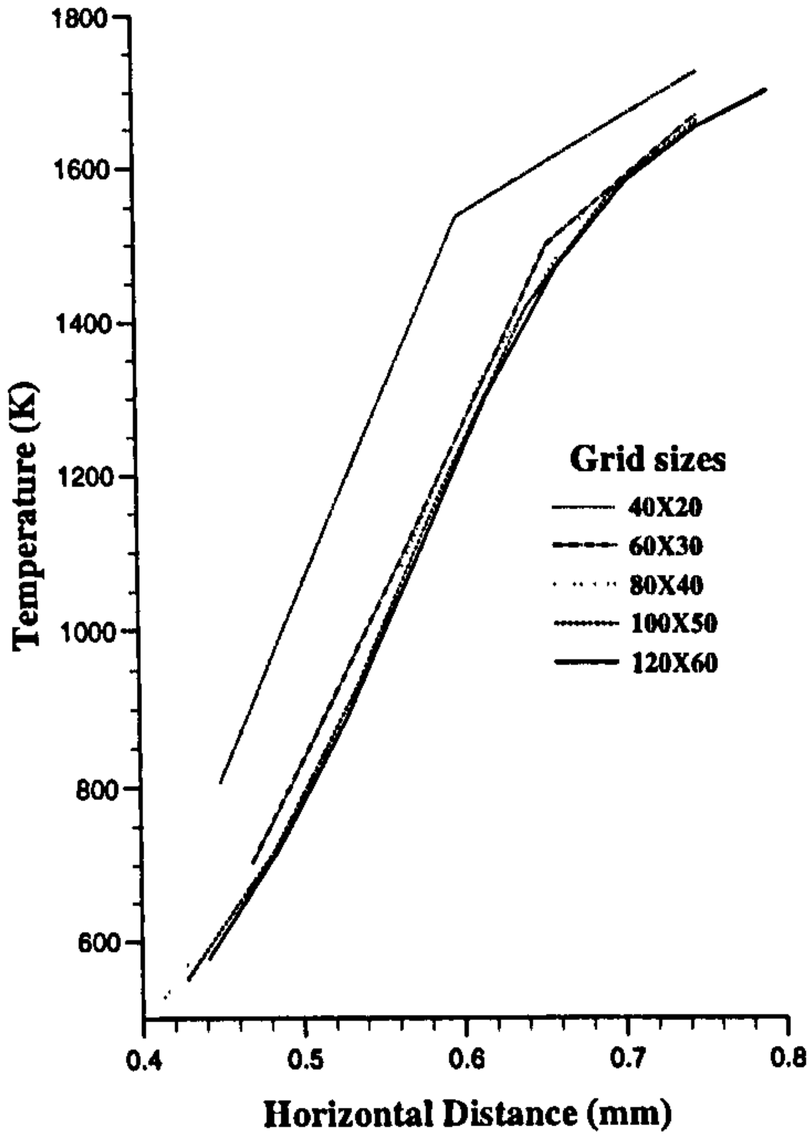

(c)

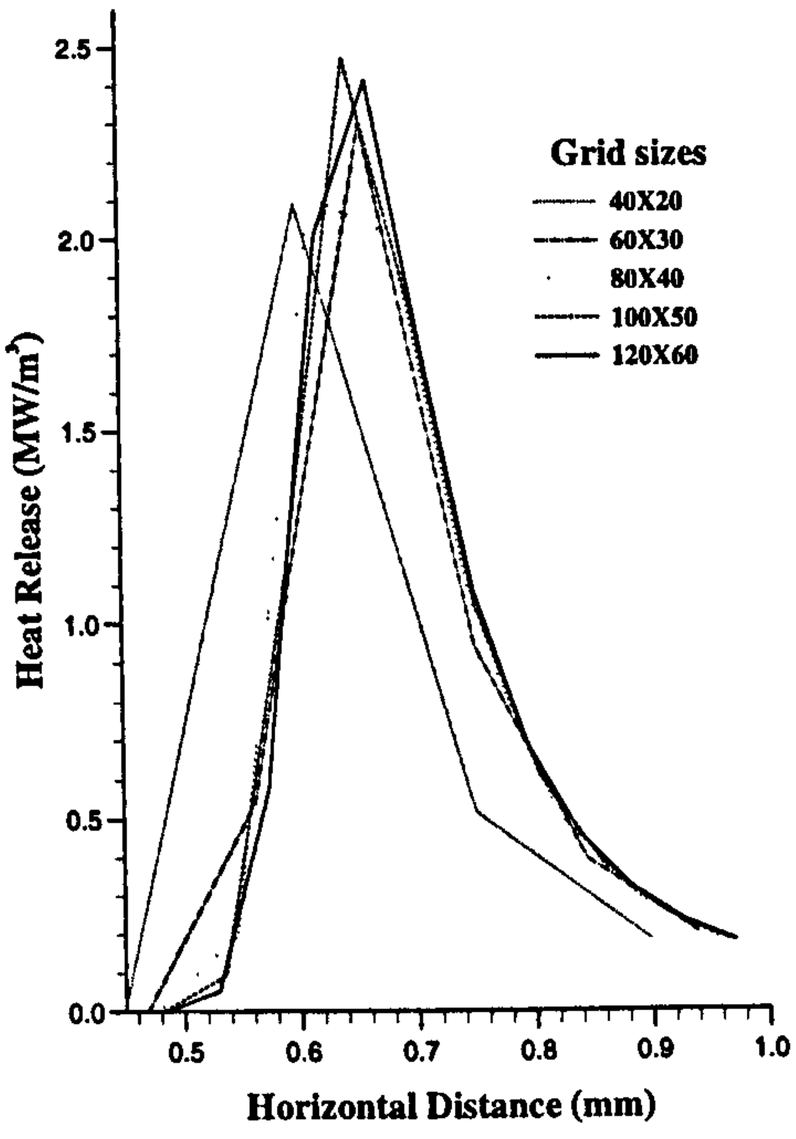

(d)

Fig. 5.9 Computed results with CCCT scheme, along a height of 3 mm for grid sizes of 40 x 20, 60 x 30, 80 x 40, 100 x 50 and 120 x 60.

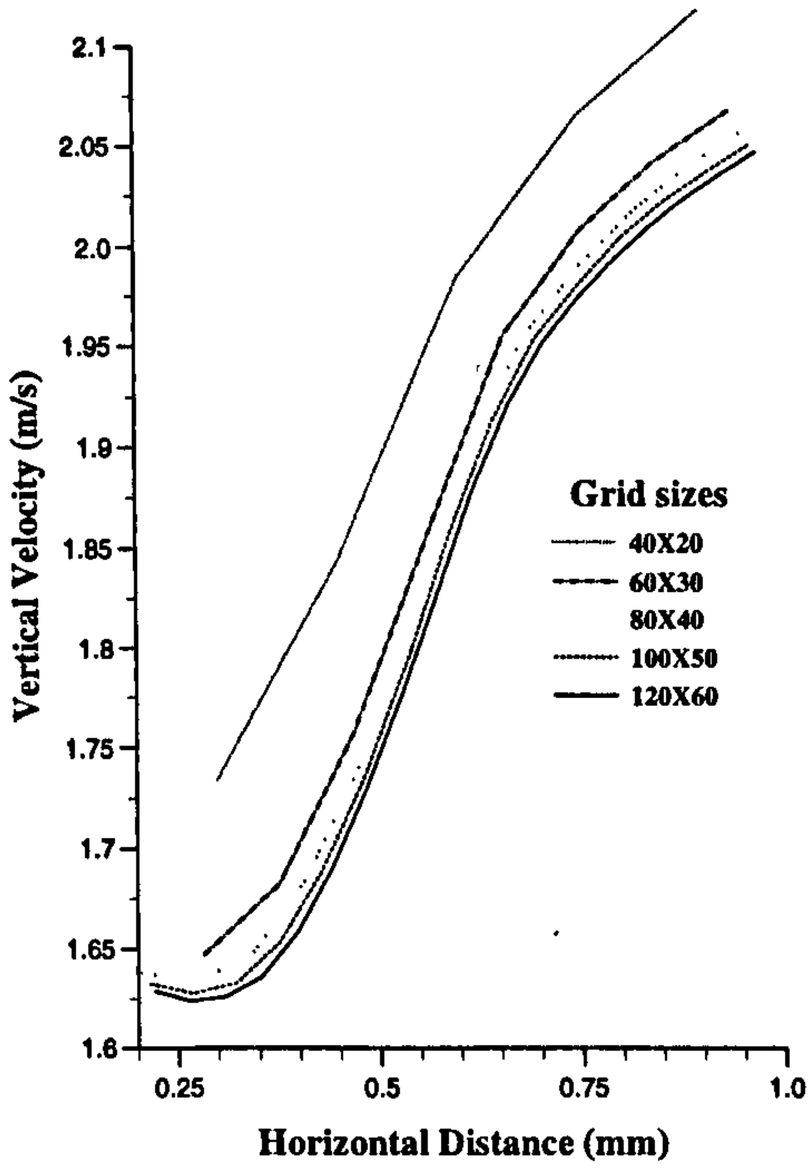

(a)

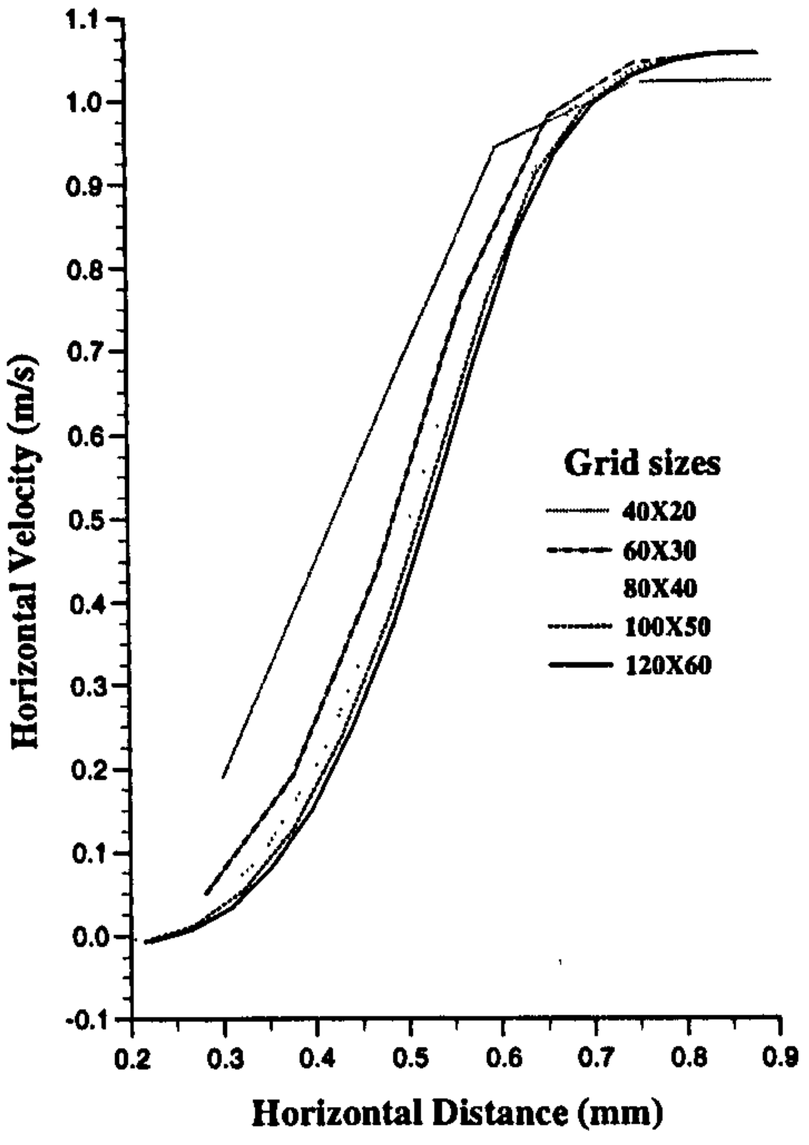

(b)

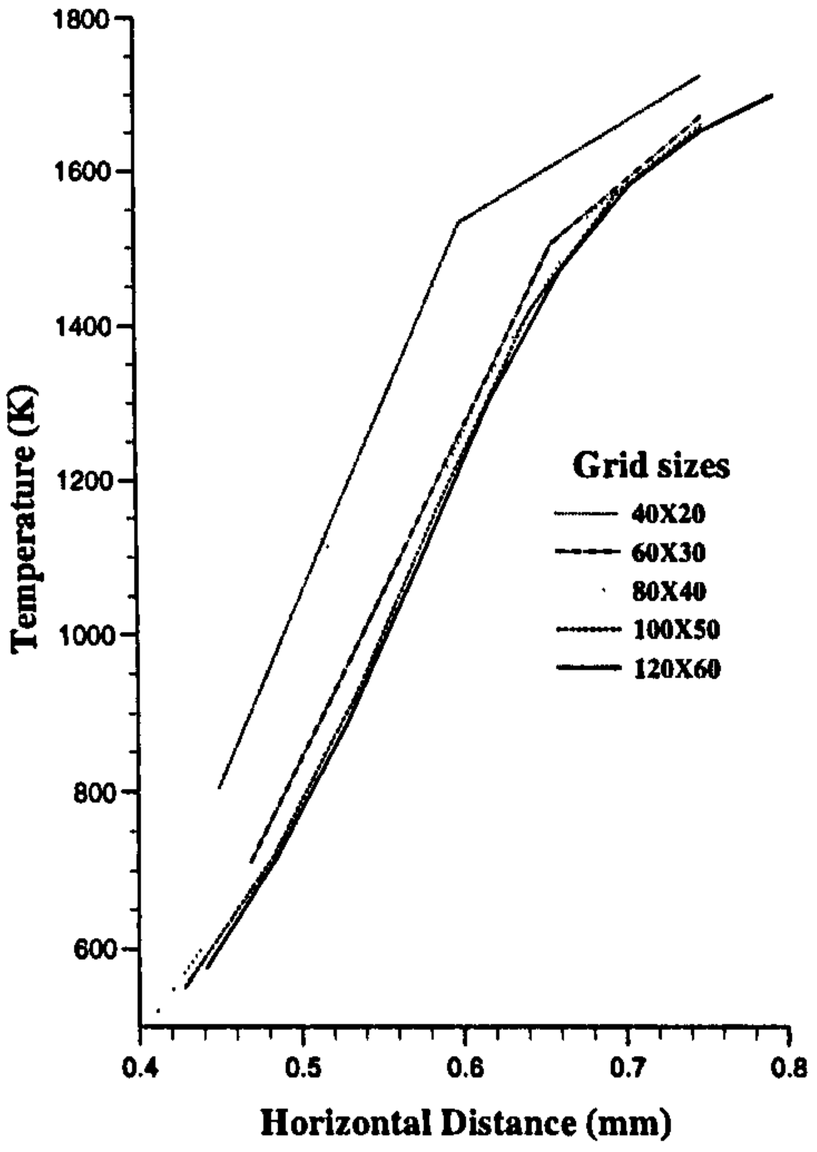

(c)

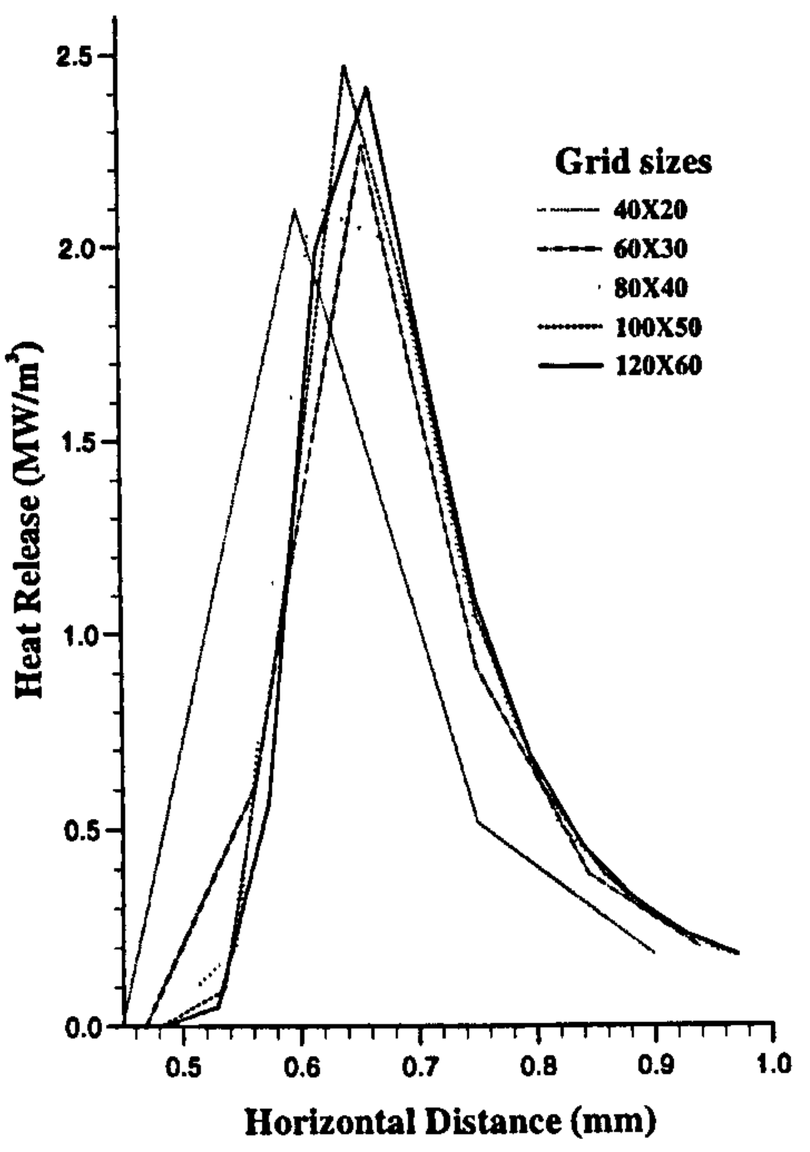

(d)

Fig. 5.10 Computed results with QUICK scheme, along a height of 3 mm for grid sizes of 40 x 20, 60 x 30, 80 x 40, 100 x 50 and 120 x 60.

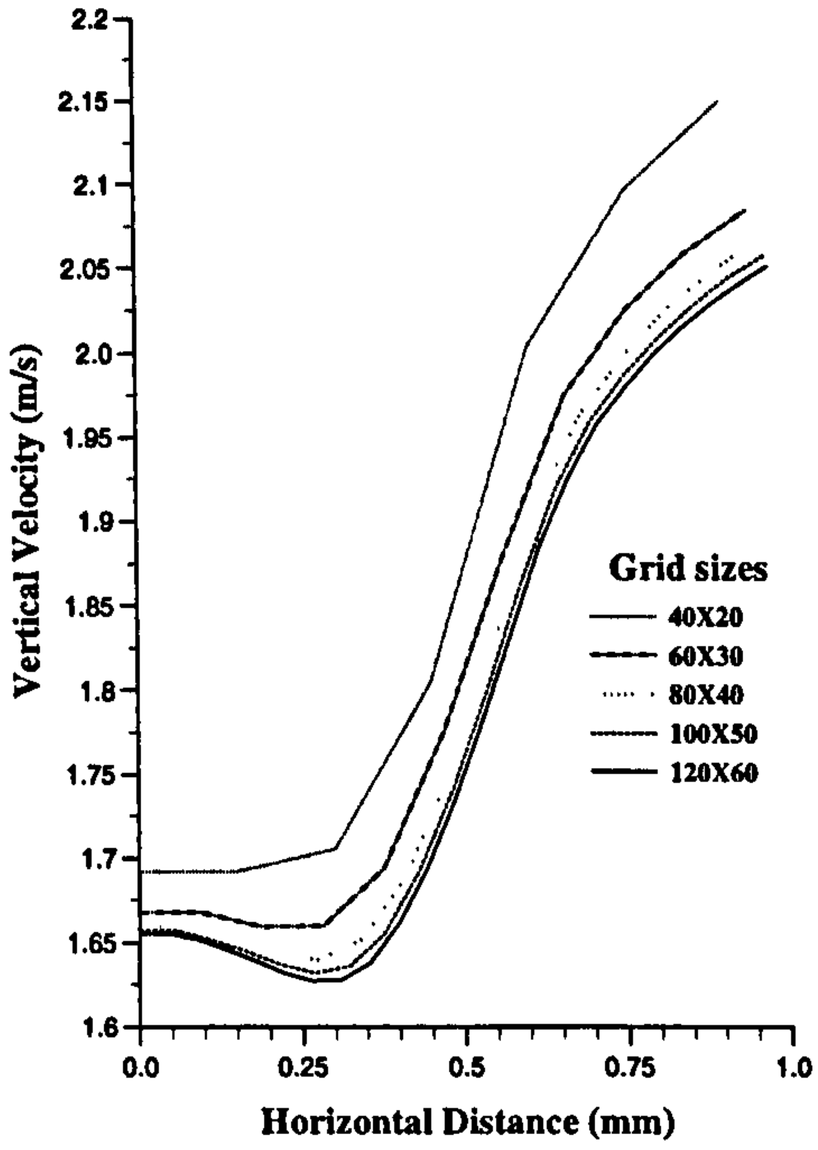

(a)

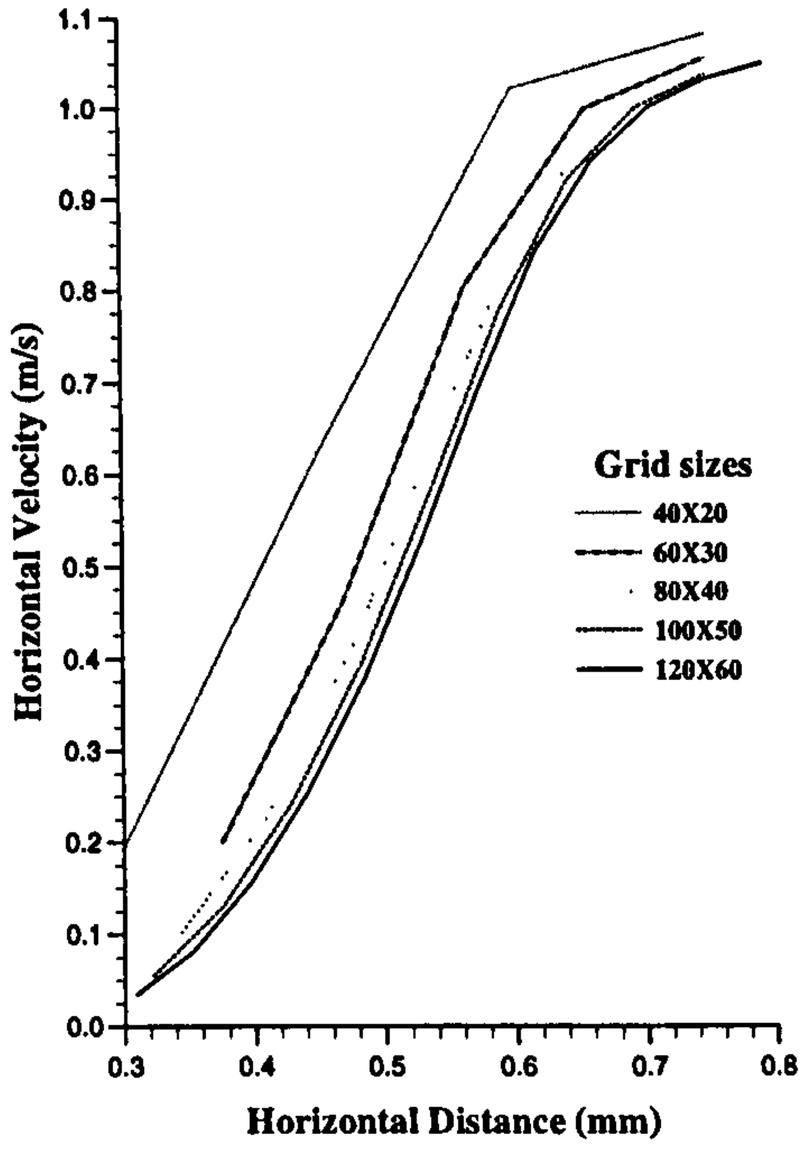

(b)

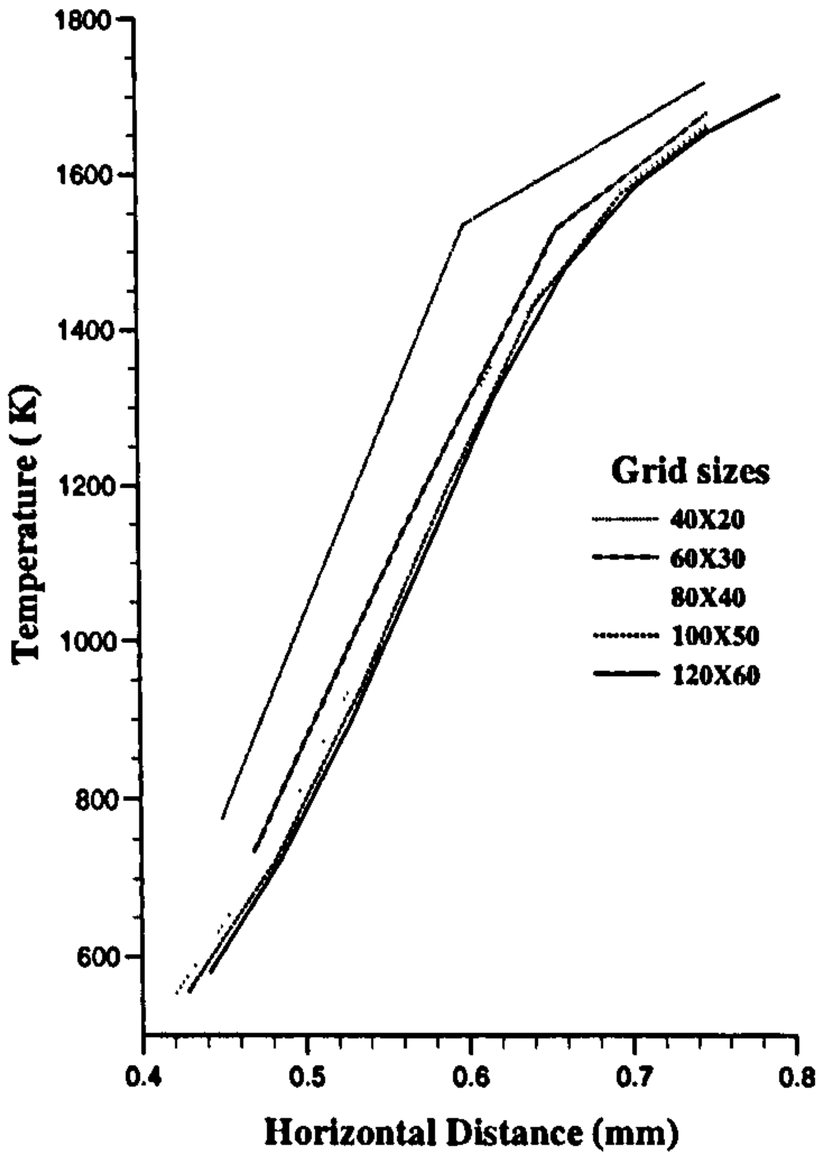

(c)

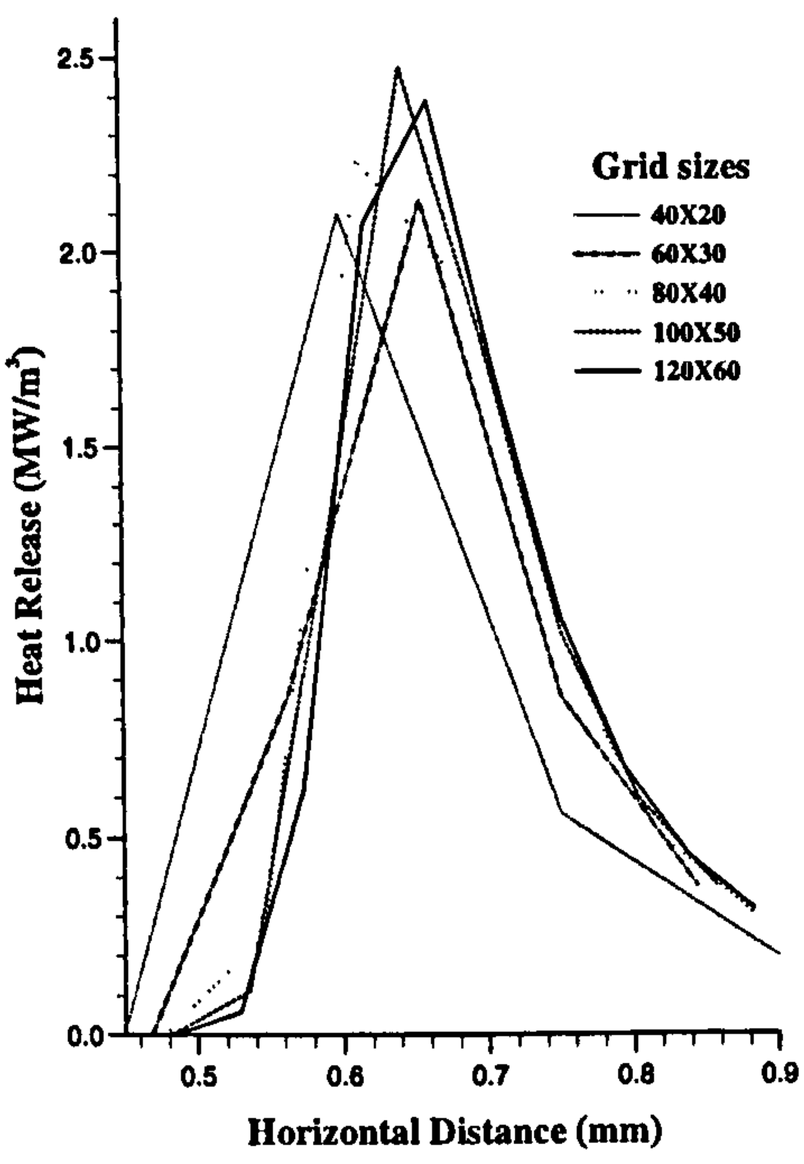

(d)

Fig. 5.11 Computed results with hybrid scheme, along a height of 3 mm for grid sizes of 40 x 20, 60 x 30, 80 x 40, 100 x 50 and 120 x 60.

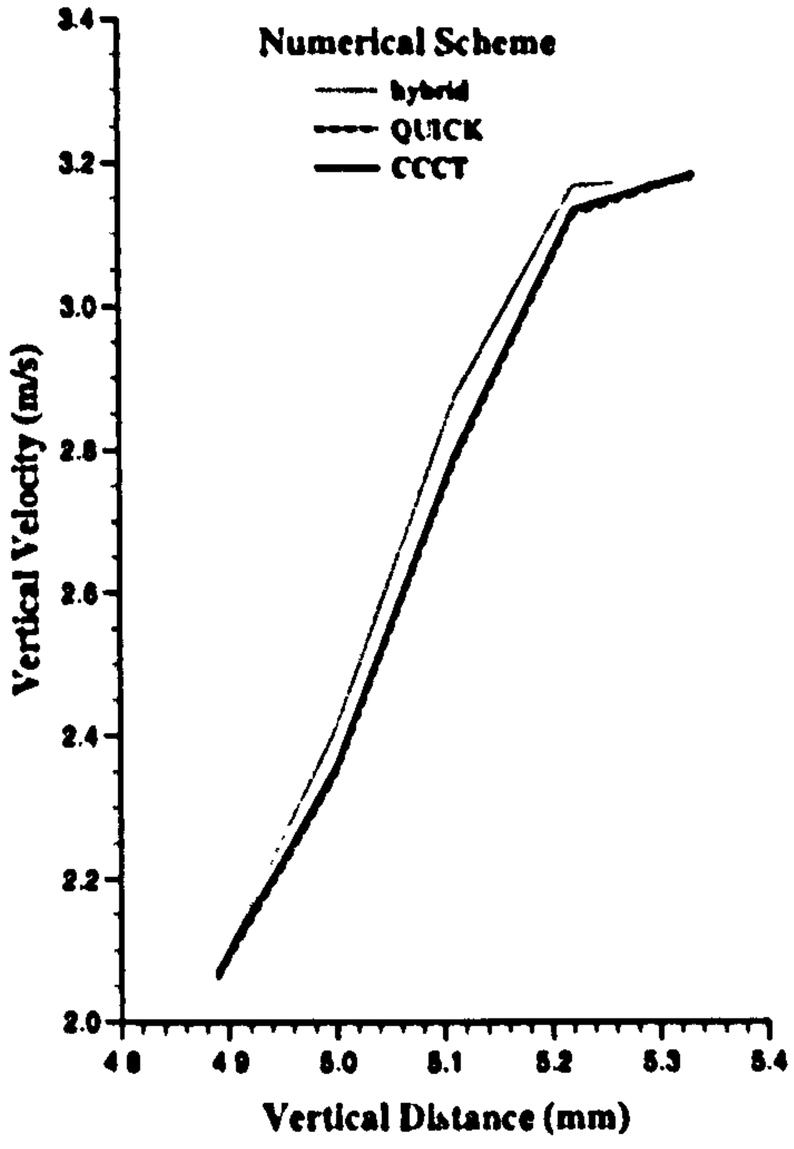

(a)

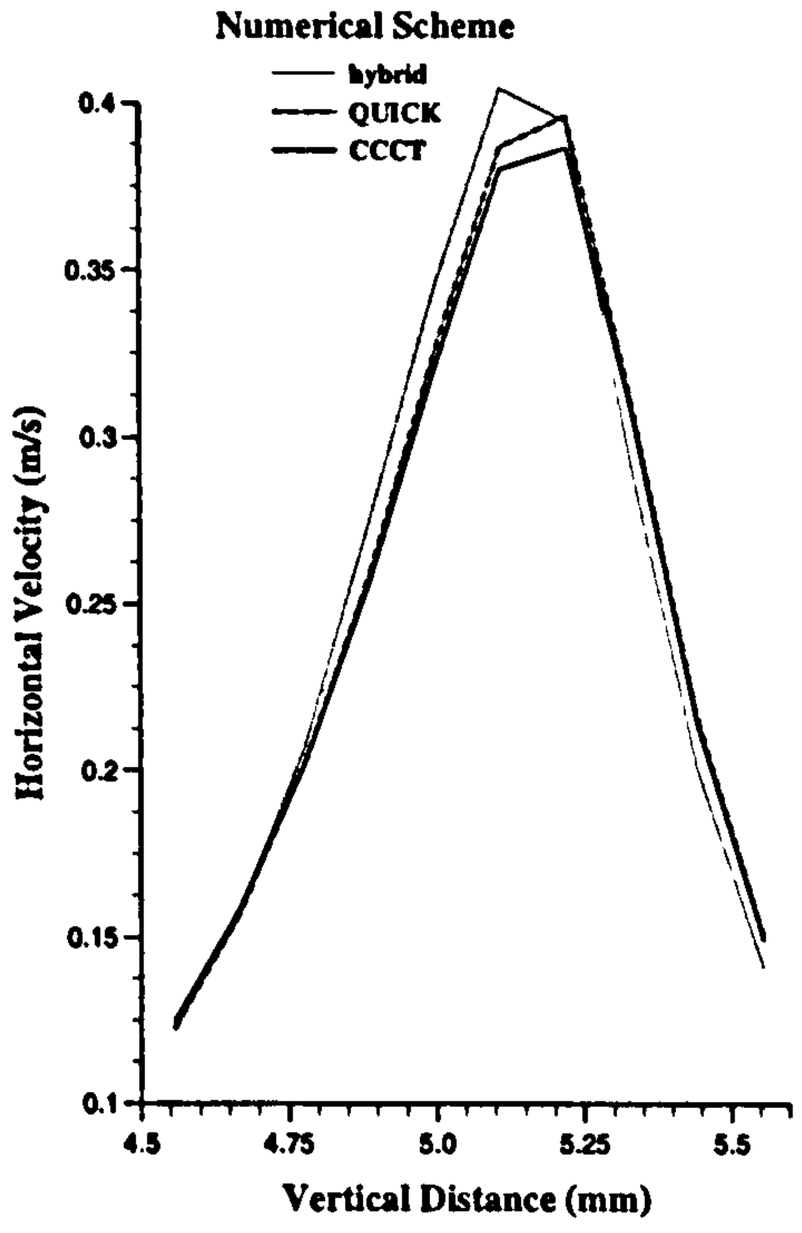

(b)

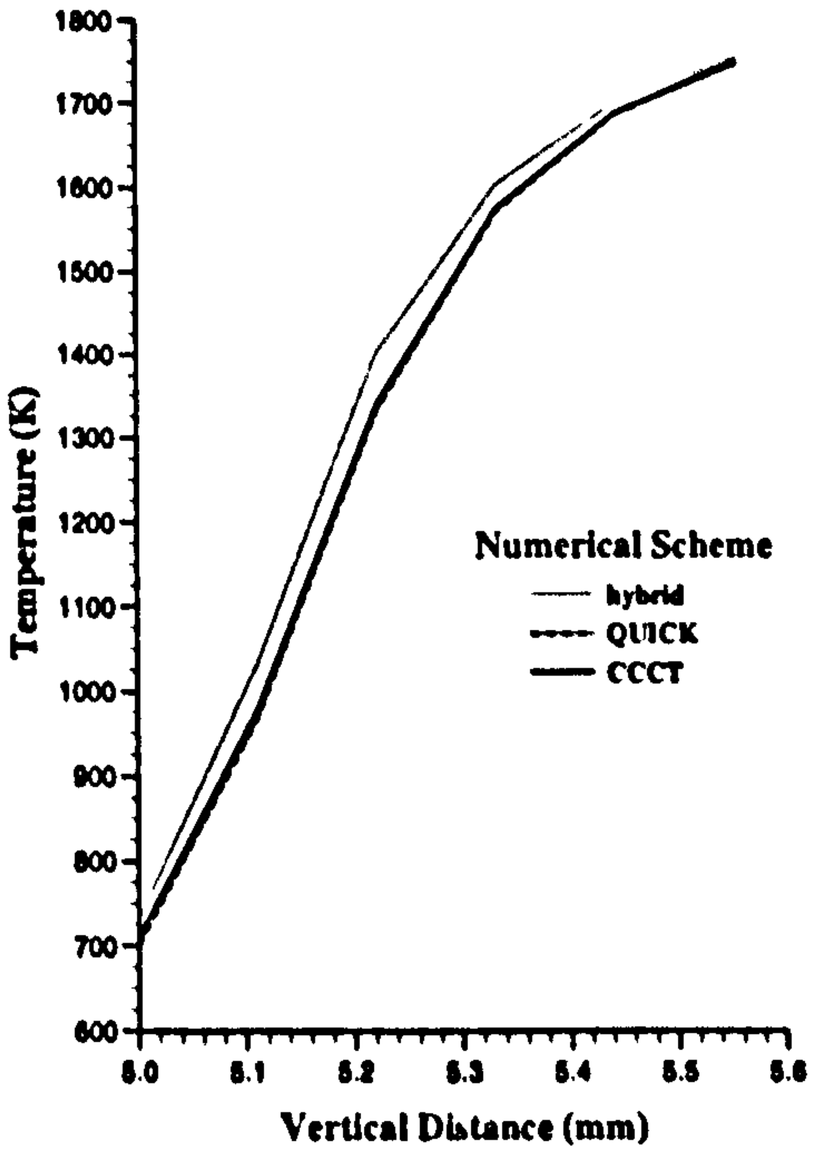

(c)

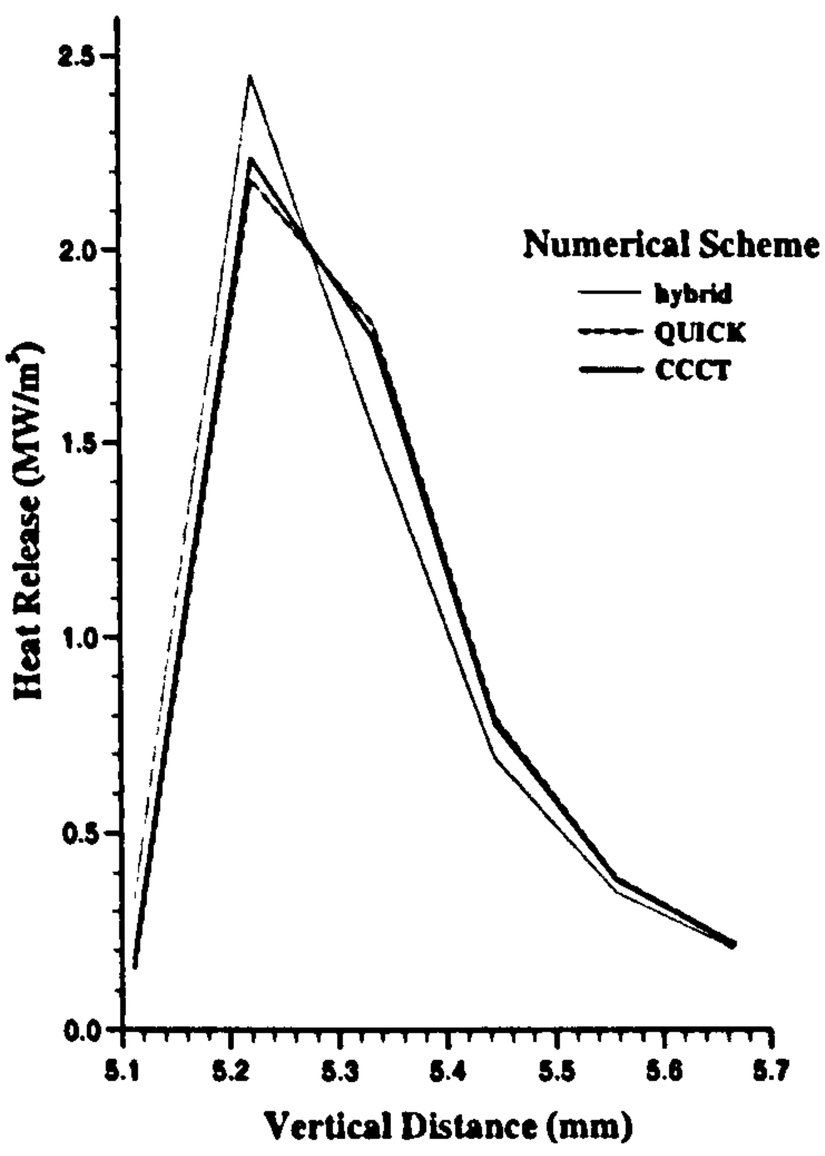

(d)

Fig. 5.12 Computed results with hybrid, quick and CCCT numerical schemes, along the symmetry axis, on a 80 x 40 grid. (a) vertical velocity, (b) horizontal velocity, (c) temperature and (d) heat release rate.

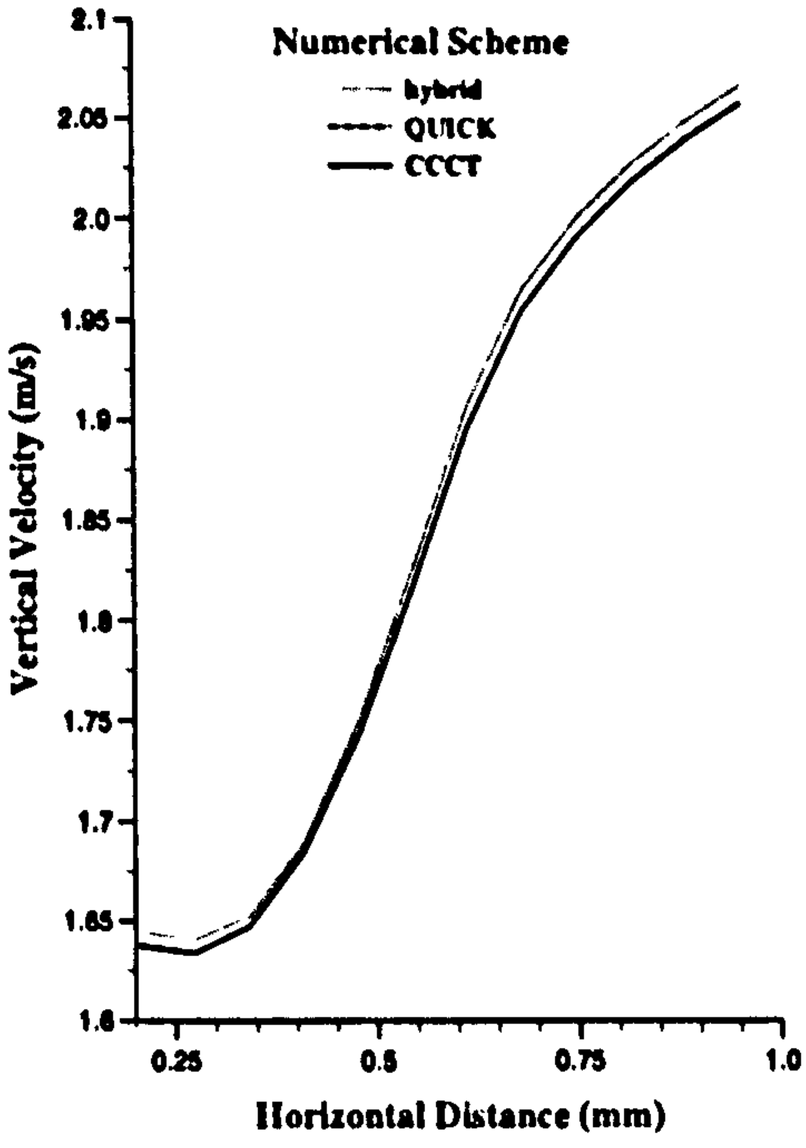

(a)

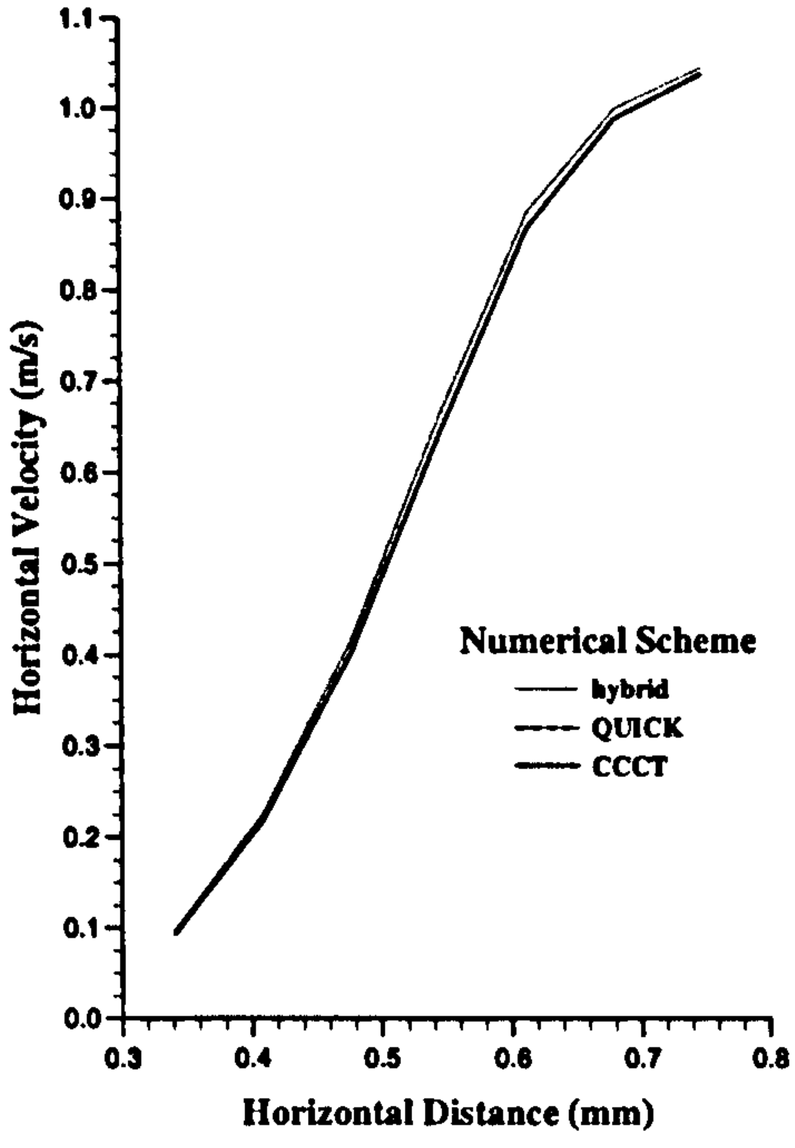

(b)

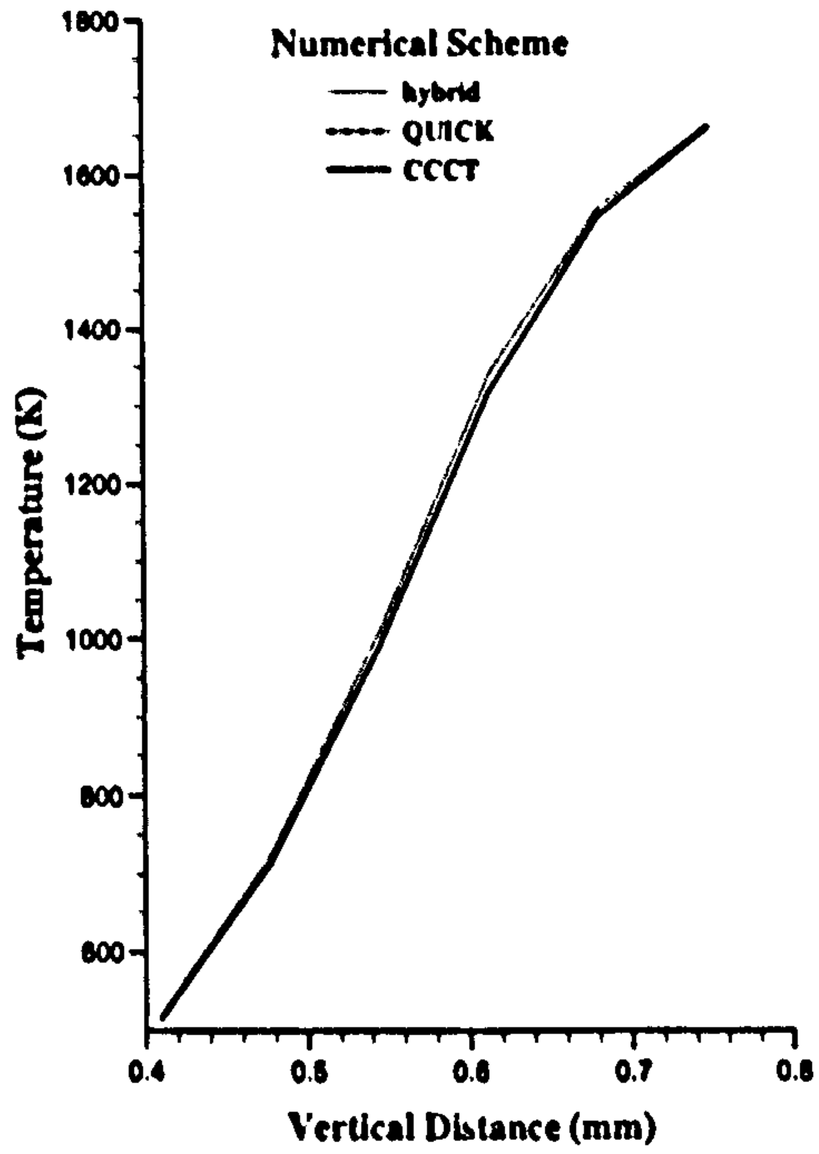

(c)

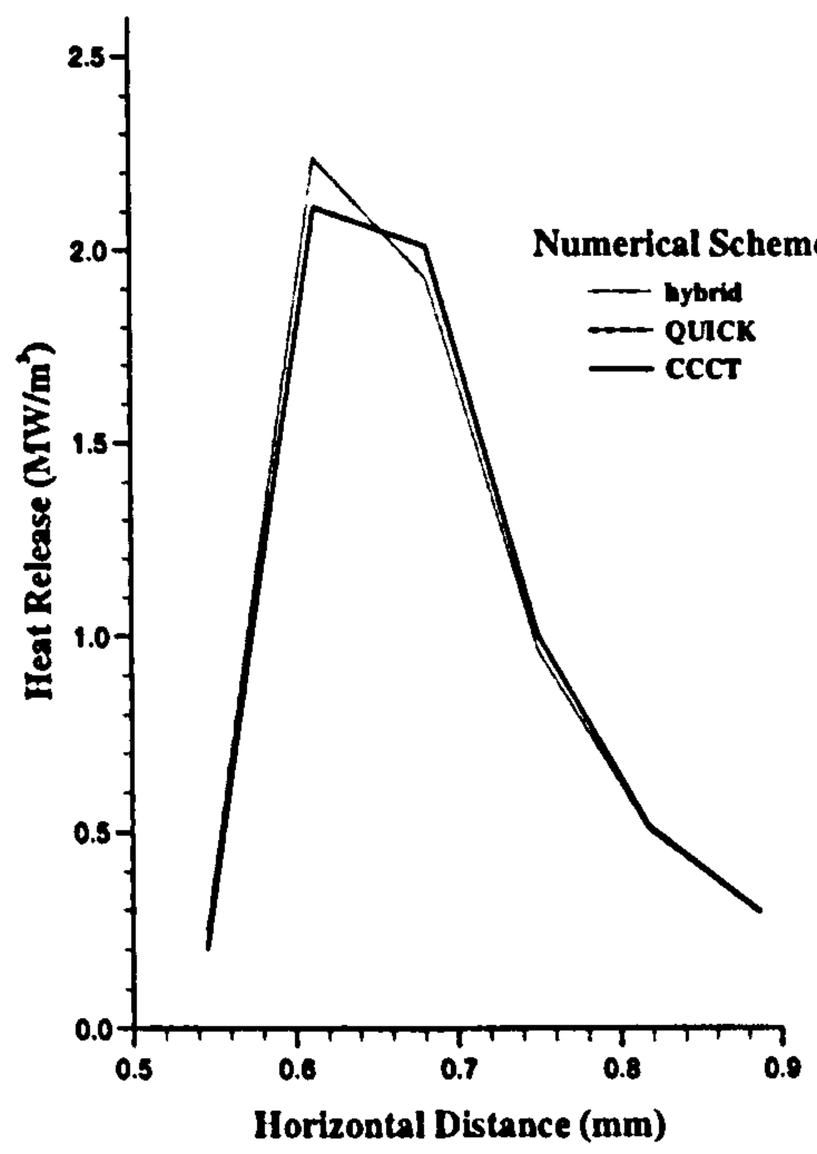

(d)

Fig. 5.13 Computed results with hybrid, quick and CCCT numerical schemes, along a height of 3 mm, on a 80 x 40 grid. (a) vertical velocity, (b) horizontal velocity, (c) temperature and (d) heat release rate.

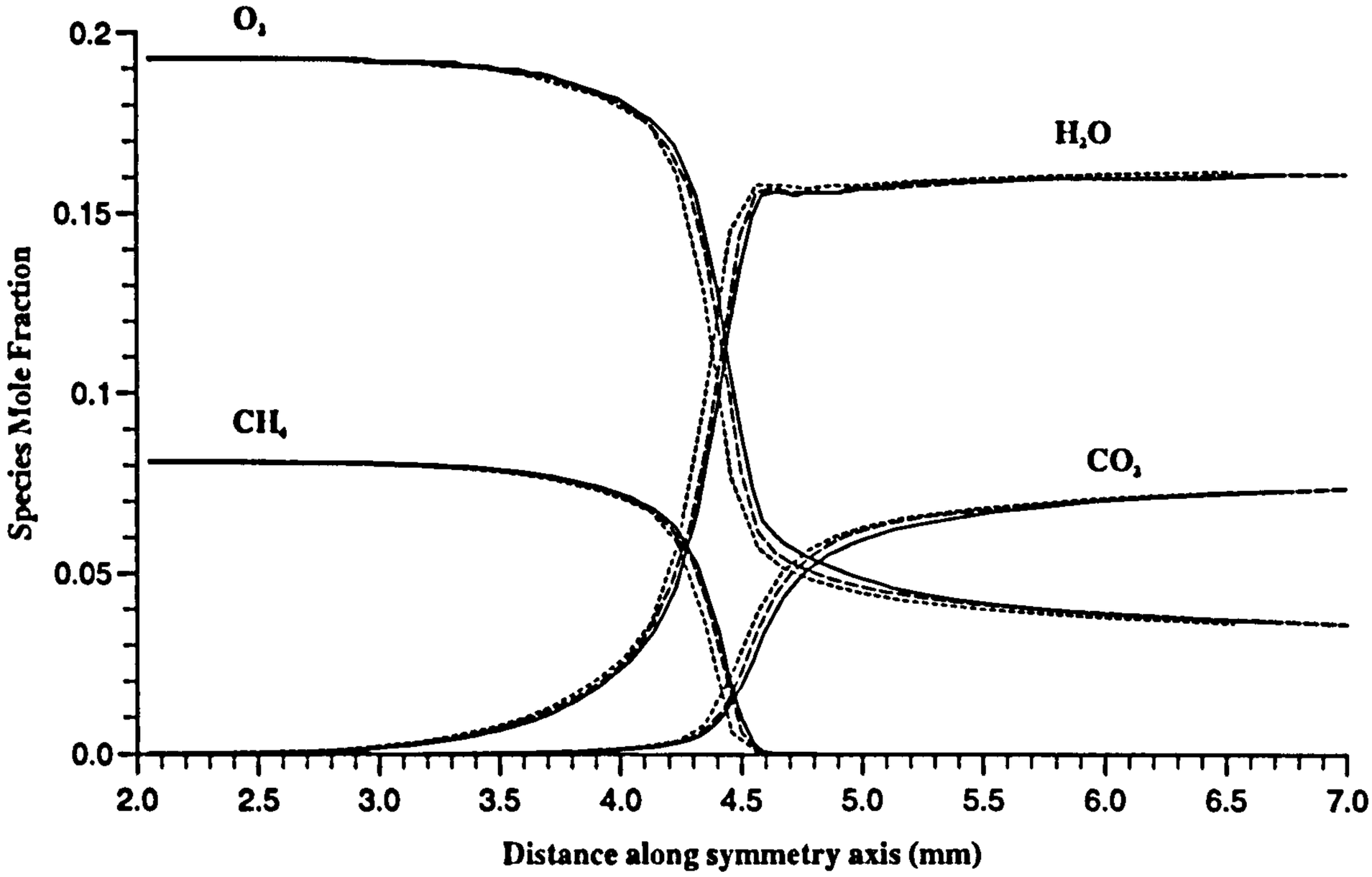

Fig. 5.14 Comparisons of mole fractions for major species along the symmetry axis with 140x140 ____ , 90x70 ..... and 60x40 ..... grids.

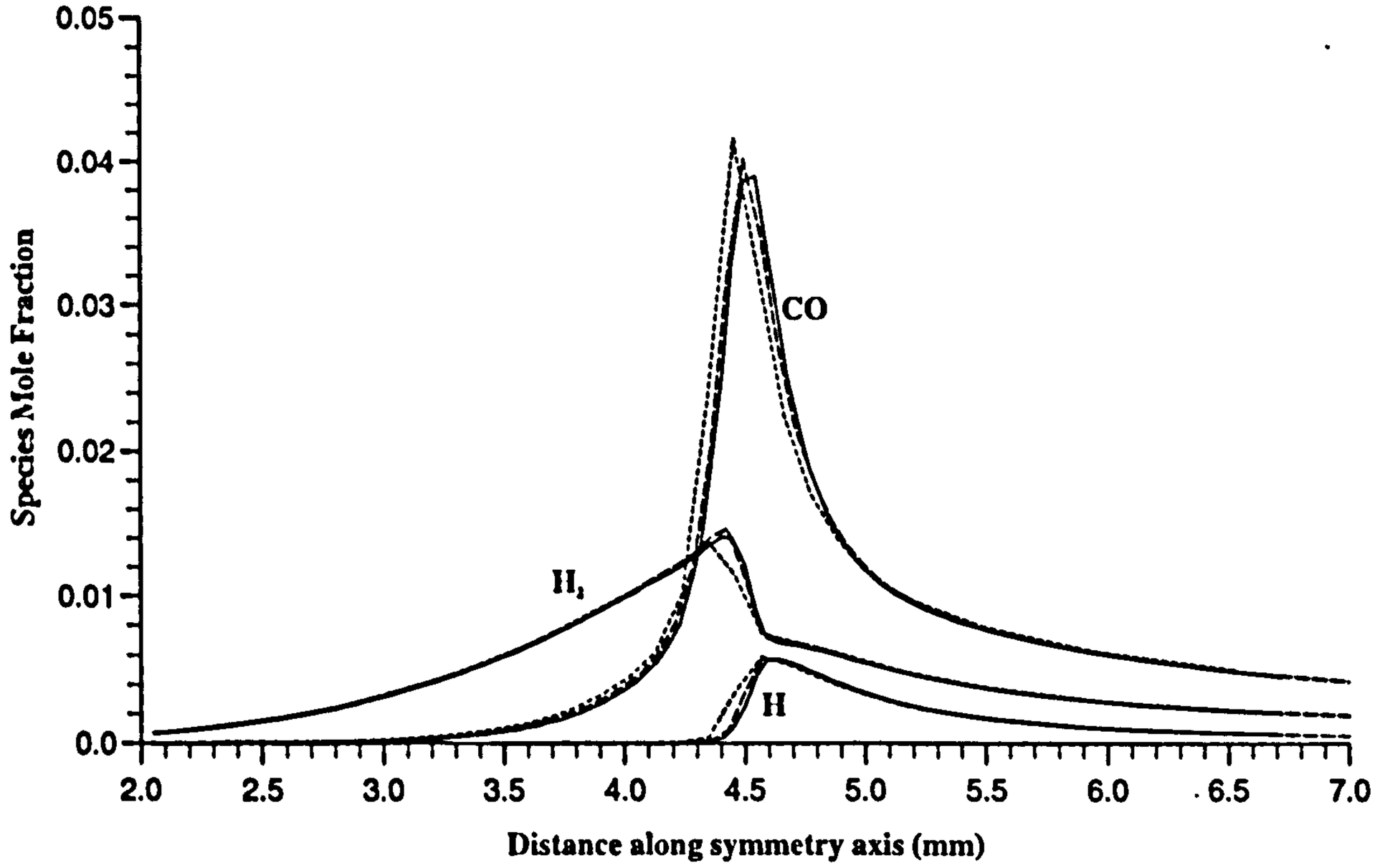

Fig. 5.15 Comparisons of mole fractions for minor species along the symmetry axis with 140x140 ____ , 90x70 ..... and 60x40 ..... grids.

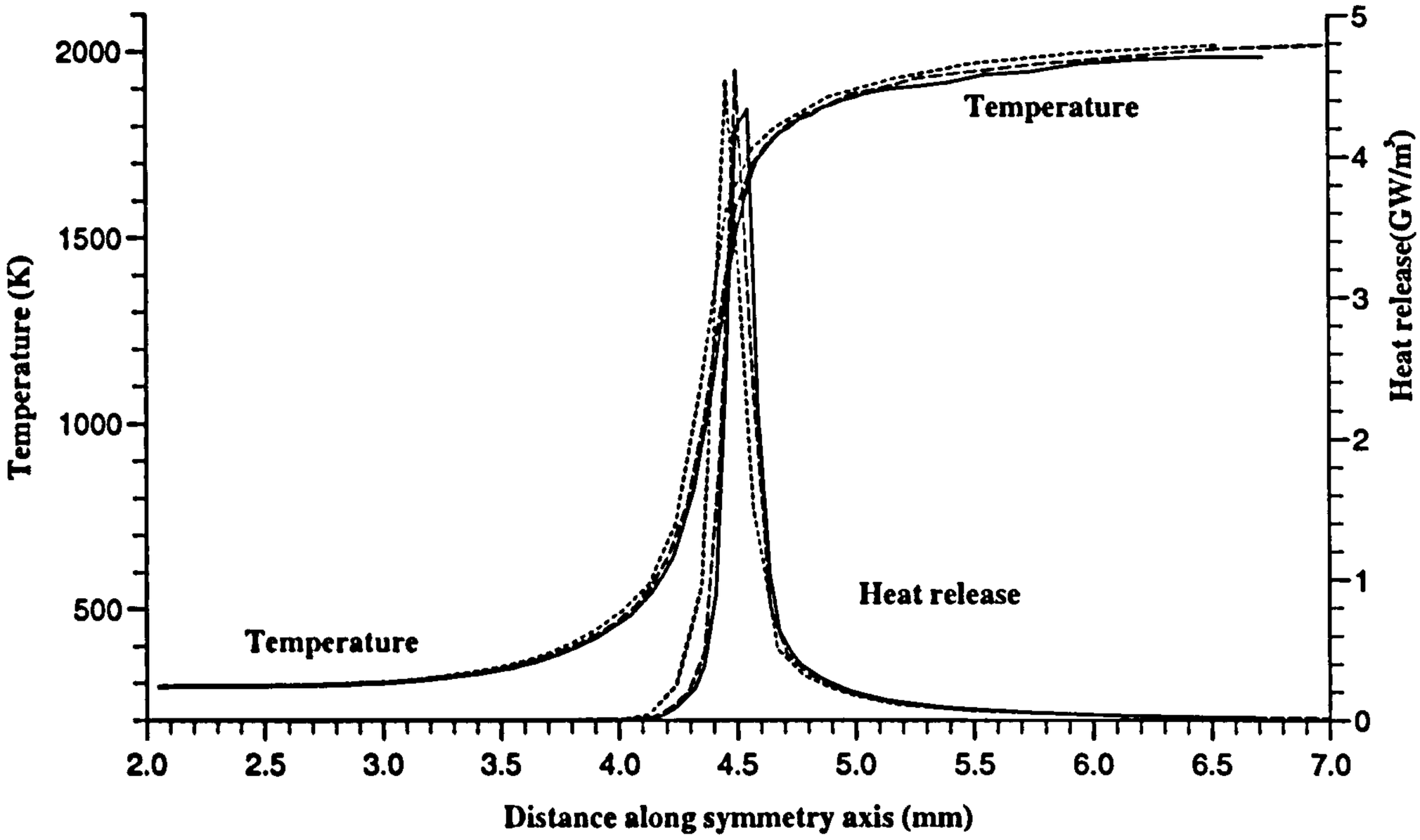

Fig. 5.16 Comparisons of temperature and heat release rate along the symmetry axis with 140x140 ___ , 90x70 ----- and 60x40 ..... grids.

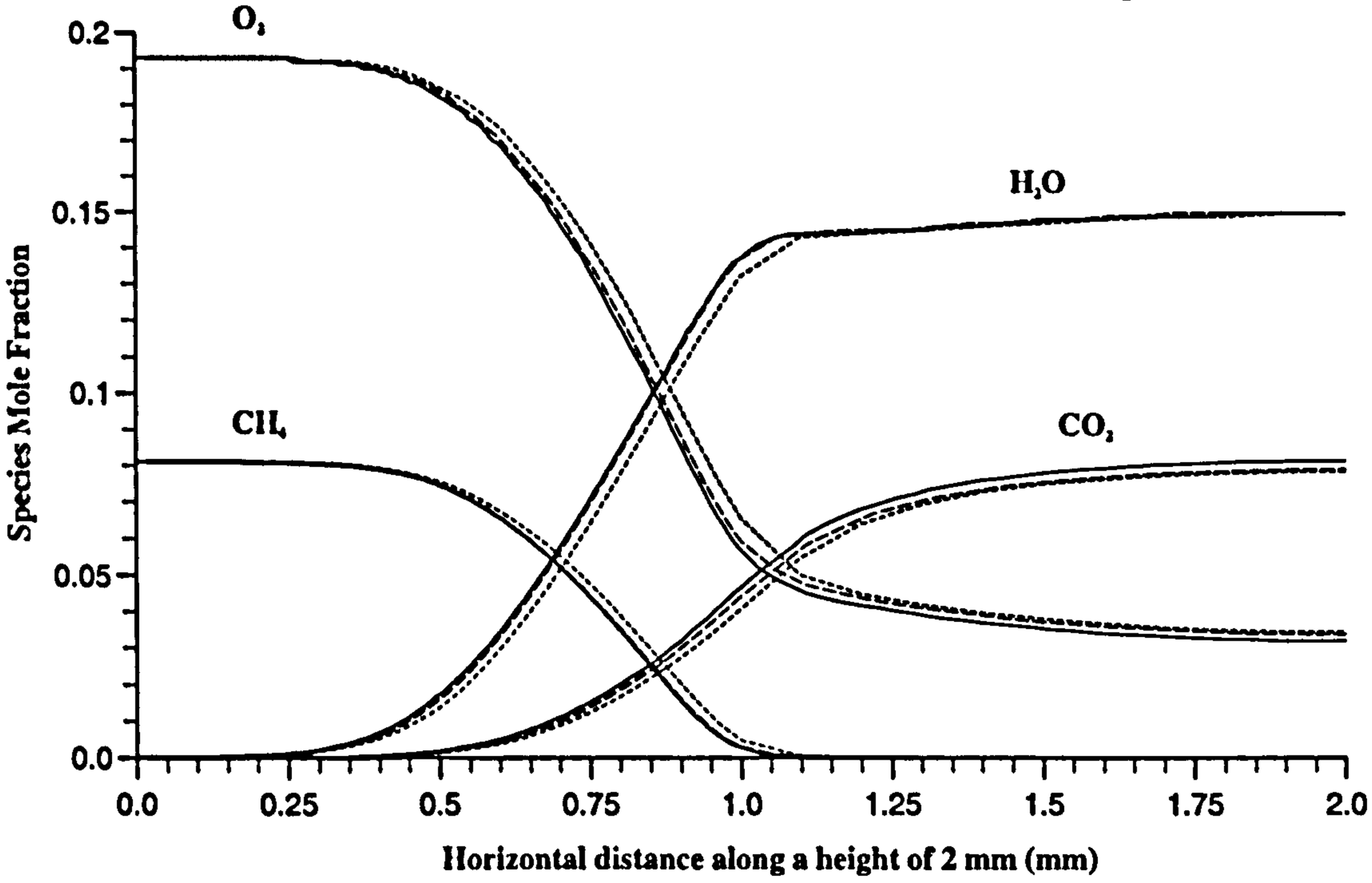

Fig. 5.17 Comparisons of mole fractions for major species along a height of 2 mm with 140x140 ___ , 90x70 ----- and 60x40 ..... grids.

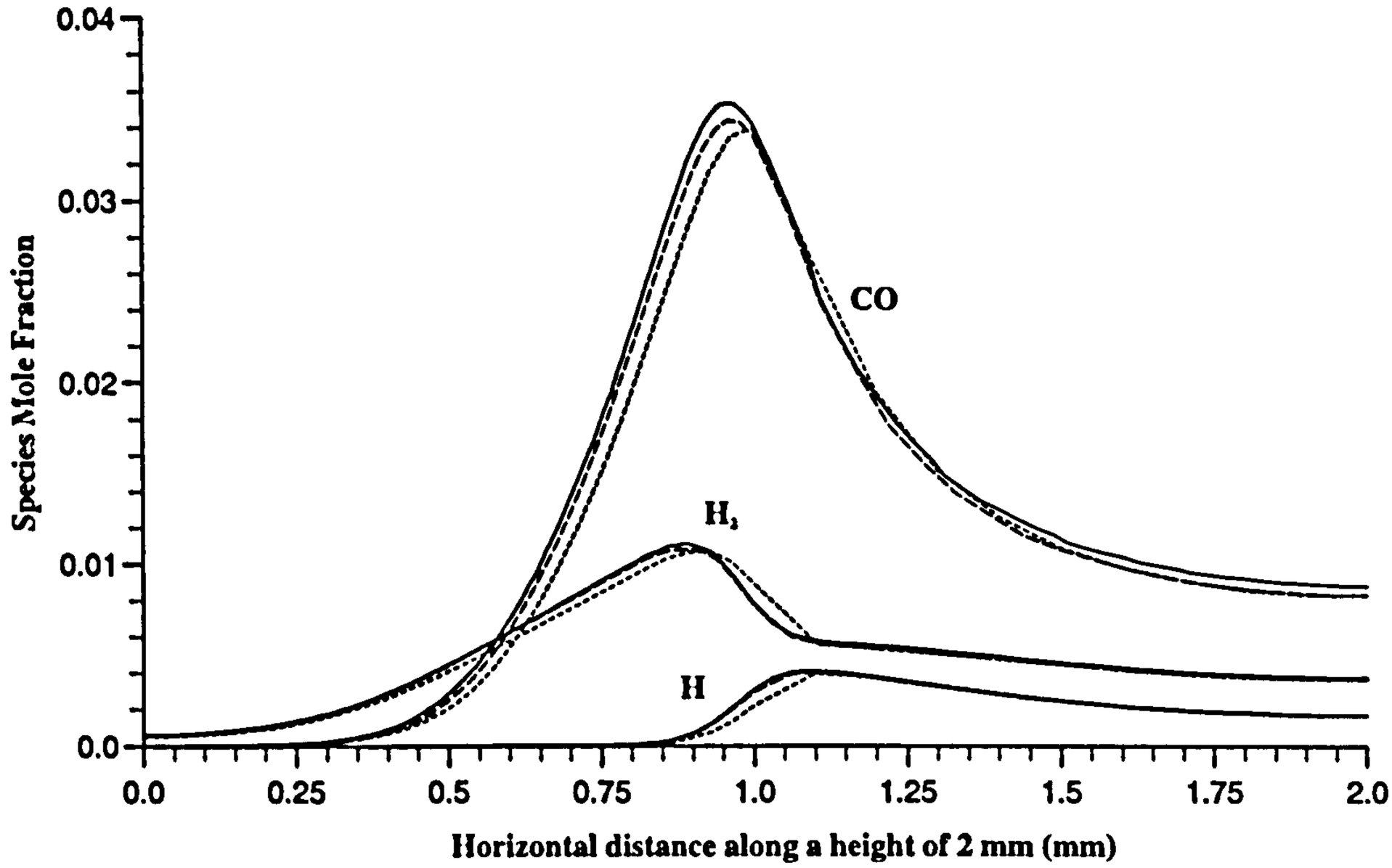

Fig. 5.18 Comparisons of mole fractions for minor species along a height of 2 mm with 140x140 ___ , 90x70 ..... and 60x40 ..... grids.

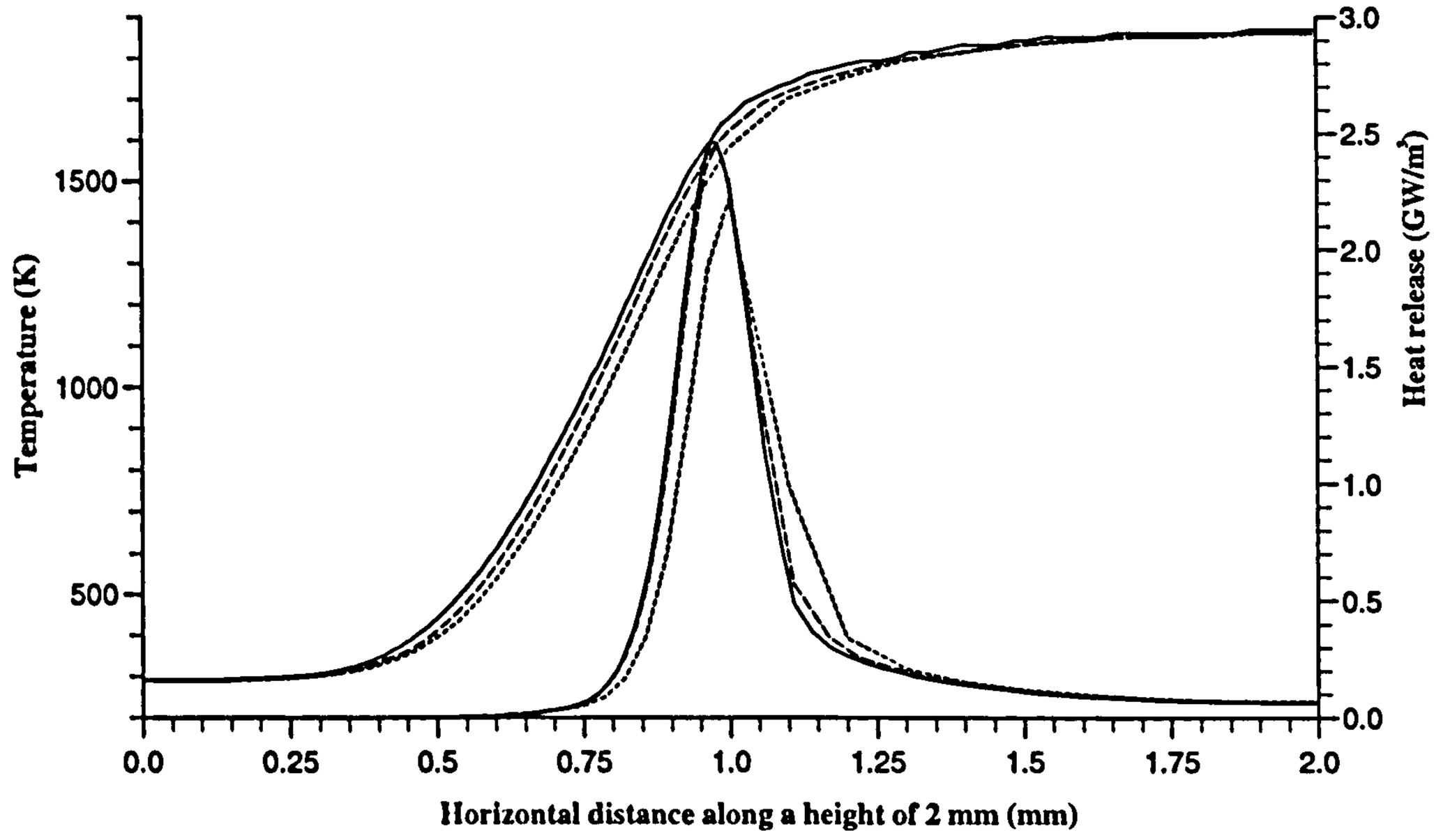

Fig. 5.19 Comparisons of temperature and heat release along a height of 2 mm with 140x140 ___ , 90x70 ___ and 60x40 ..... grids.

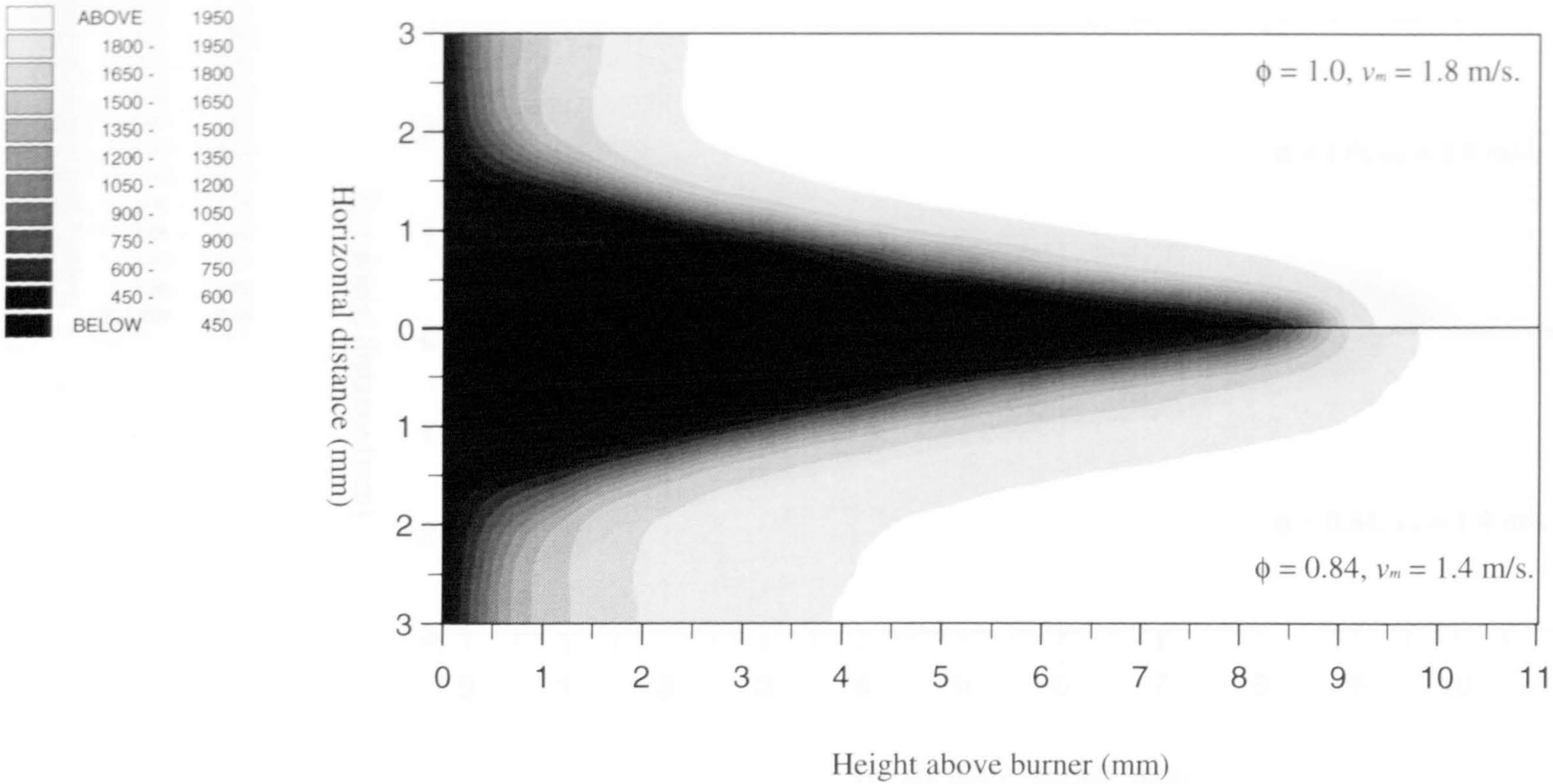

Fig. 5.20 Computed isotherms (K) for the two axisymmetric slot burner flames.

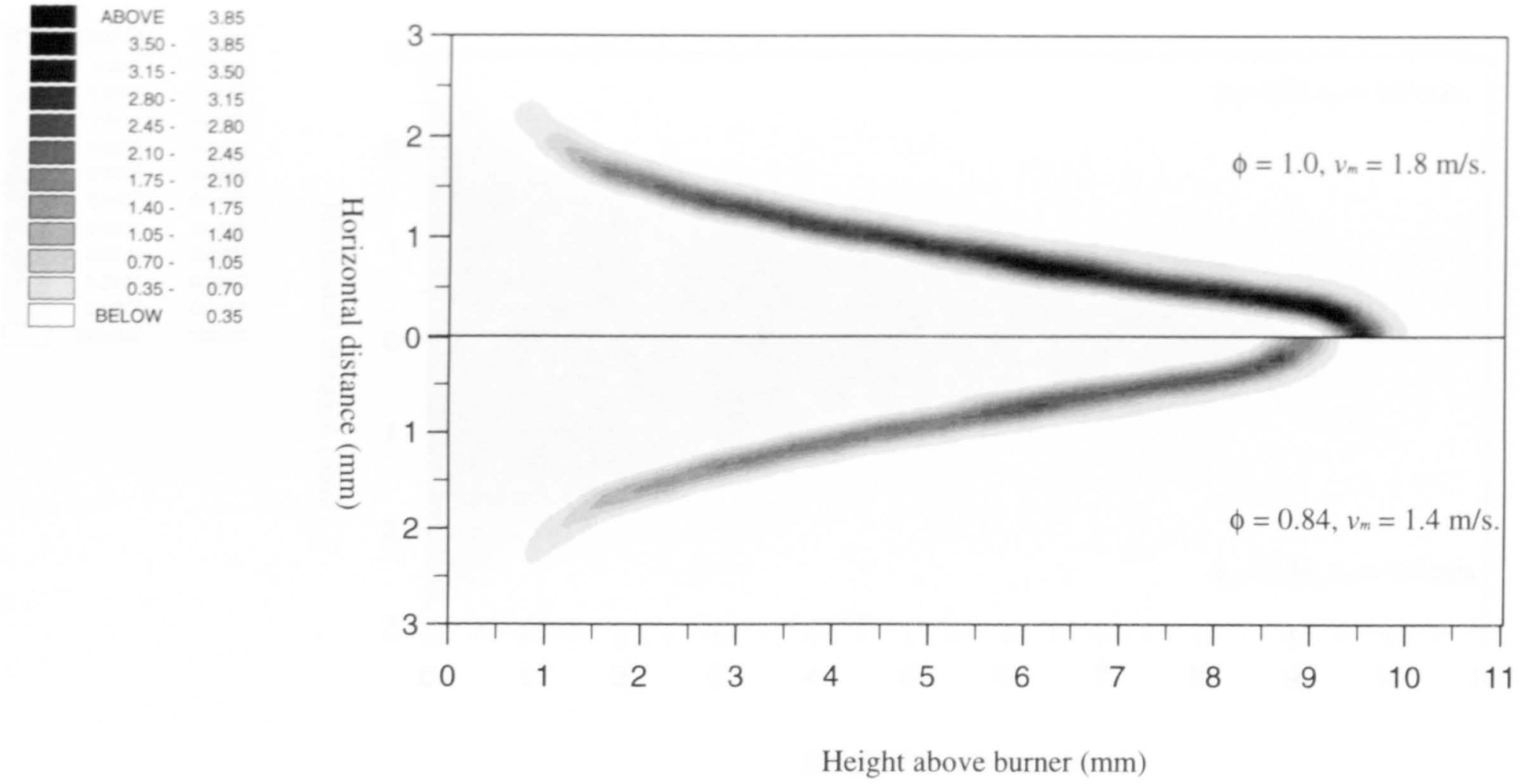

Fig. 5.21 Computed volumetric heat release (GW/m^3) contours for the two axisymmetric slot burner flames.

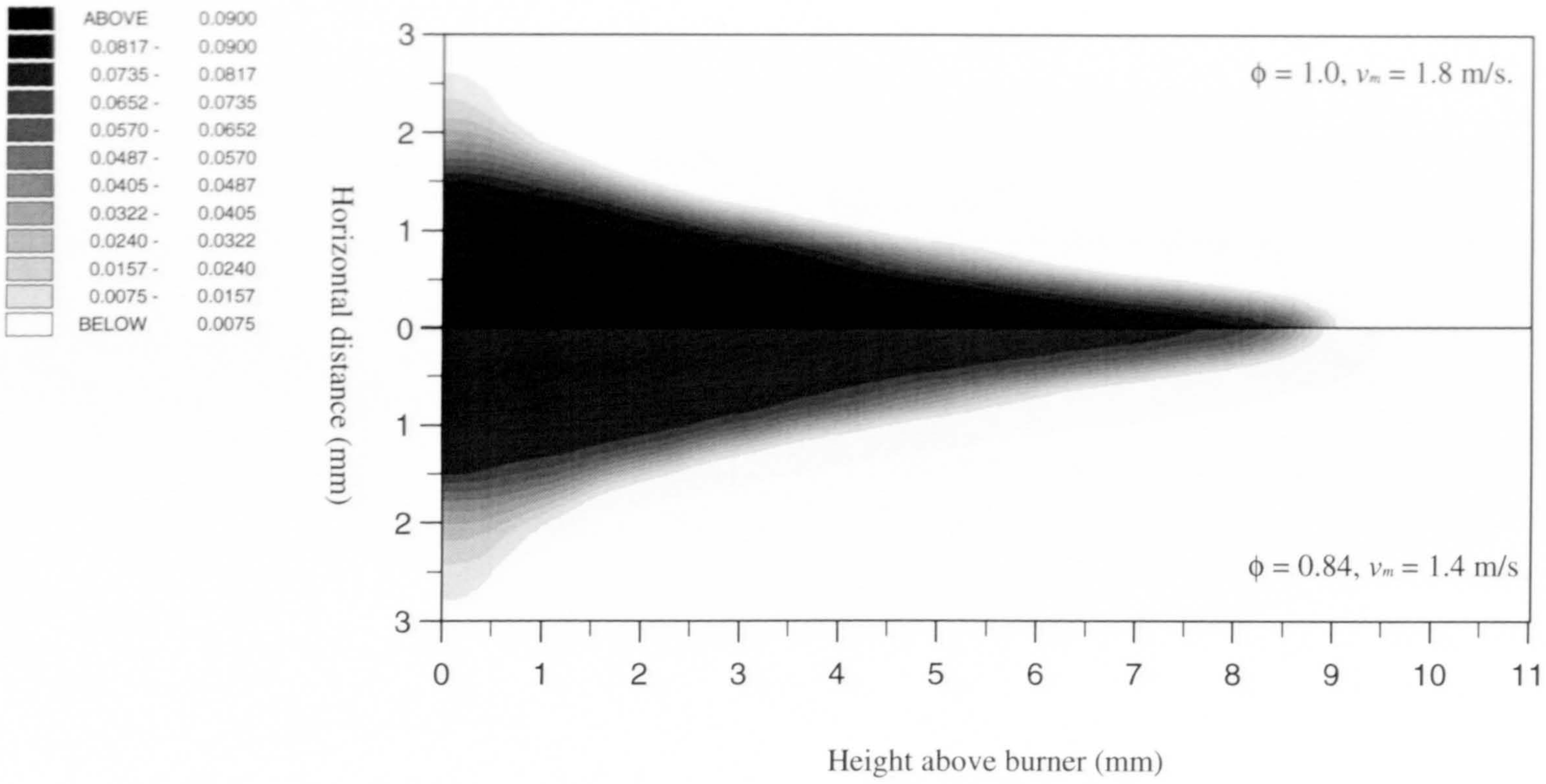

Fig. 5.22 Computed methane isopleths for the two axisymmetric slot burner flames.

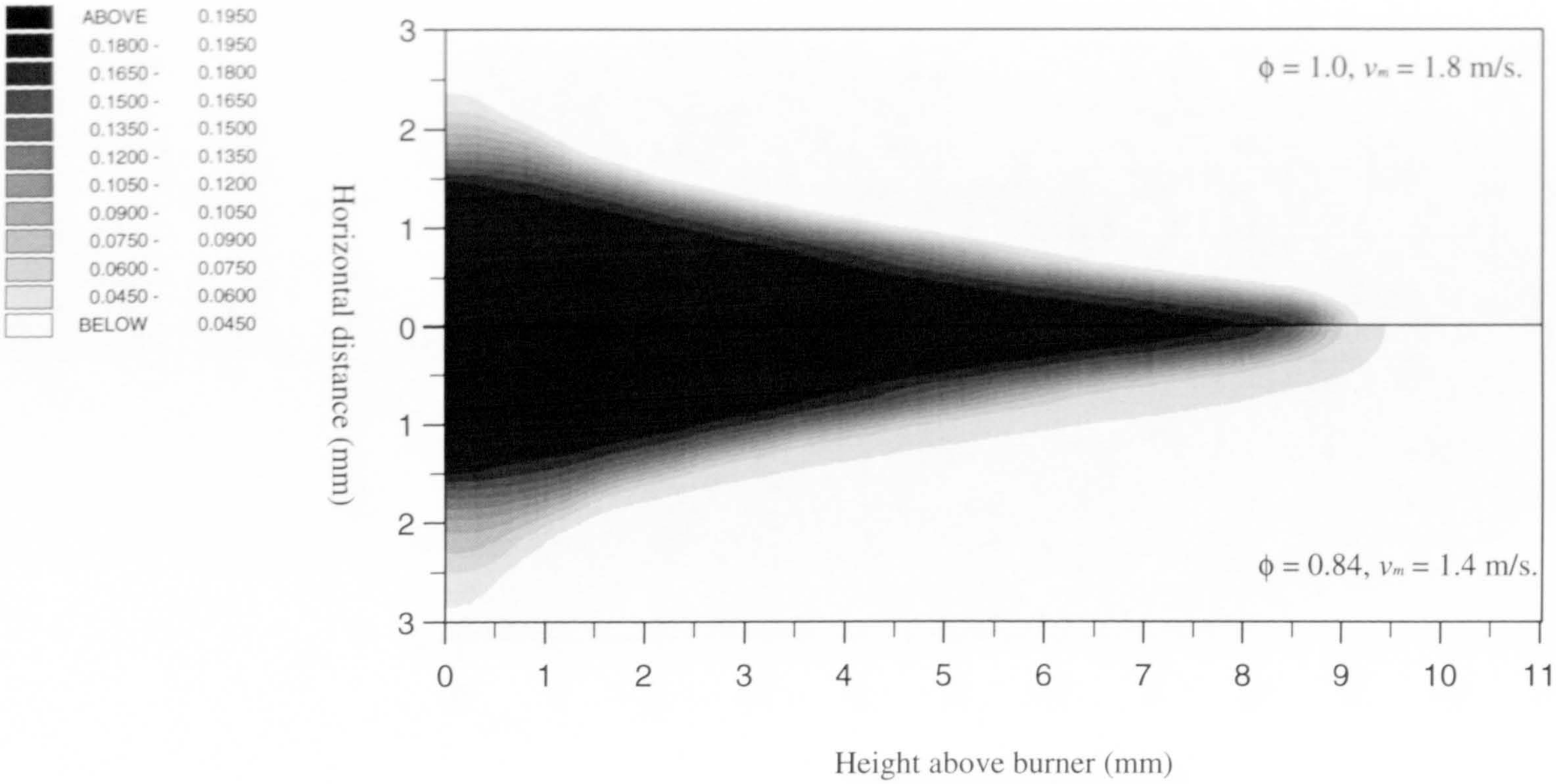

Fig. 5.23 Computed oxygen isopleths for the two axisymmetric slot burner flames.

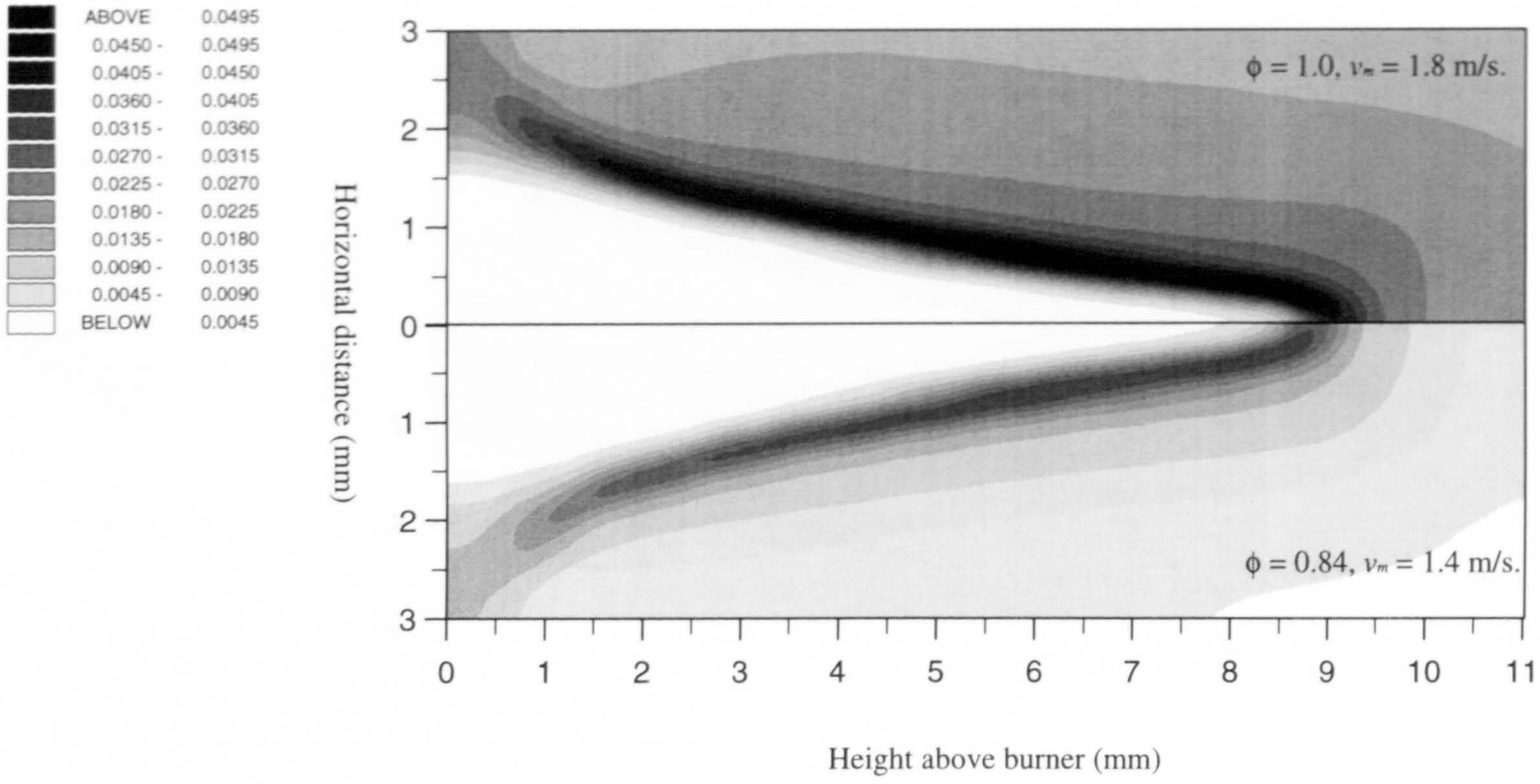

Fig. 5.24 Computed carbon monoxide isopleths for the two axisymmetric slot burner flames.

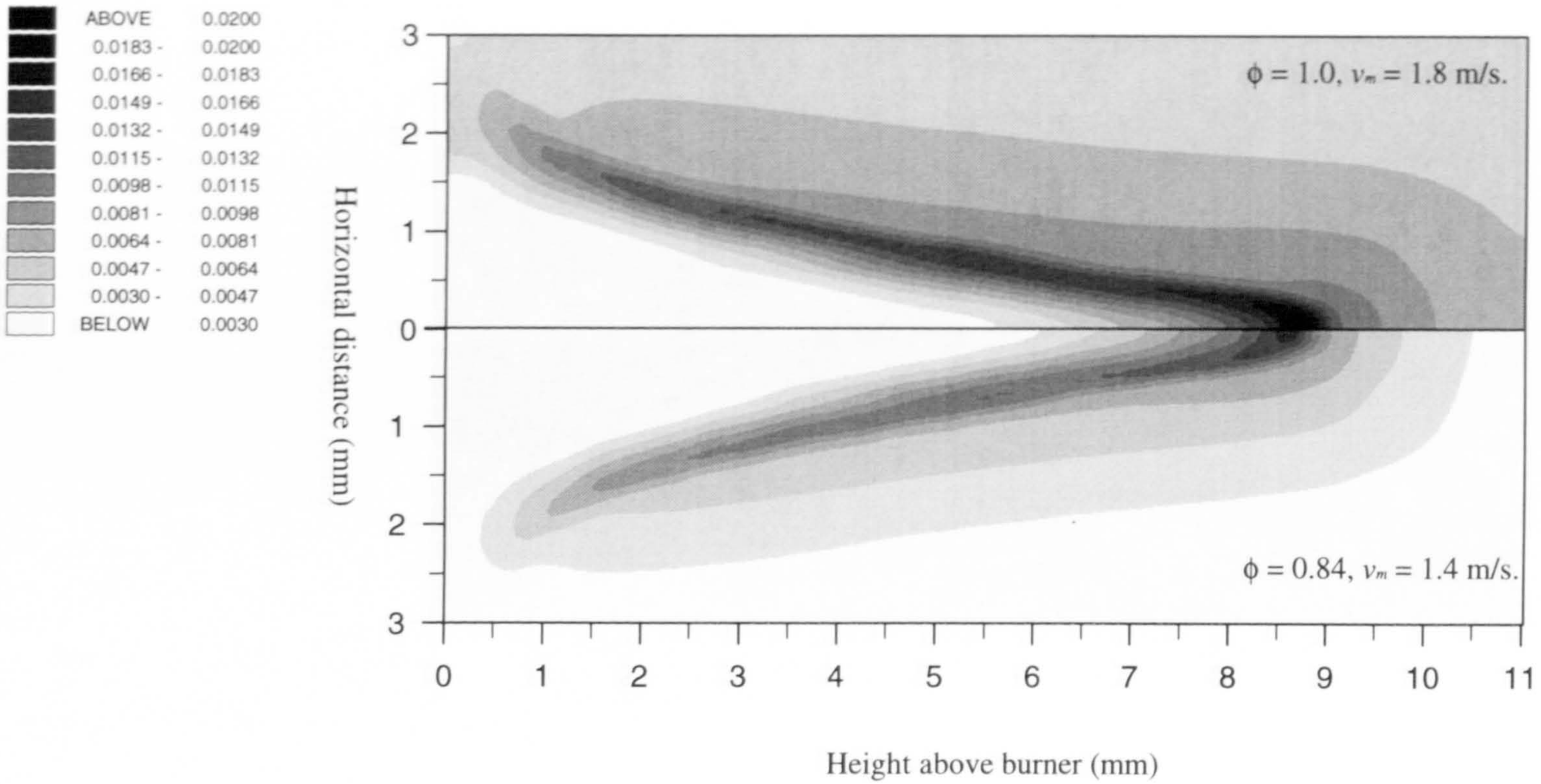

Fig. 5.25 Computed hydrogen isopleths for the two axisymmetric slot burner flames.

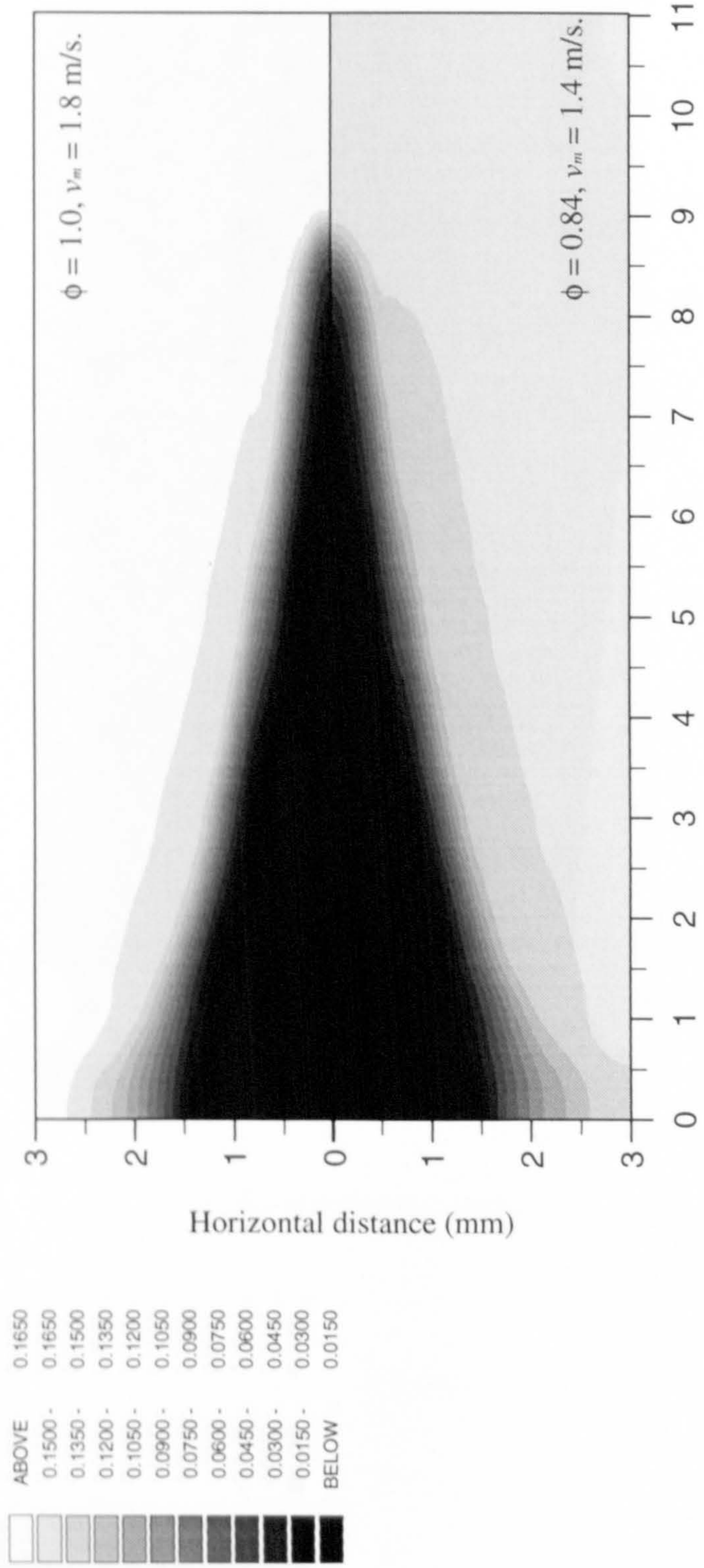

Fig. 5.26 Computed water isopleths for the two axisymmetric slot burner flames.

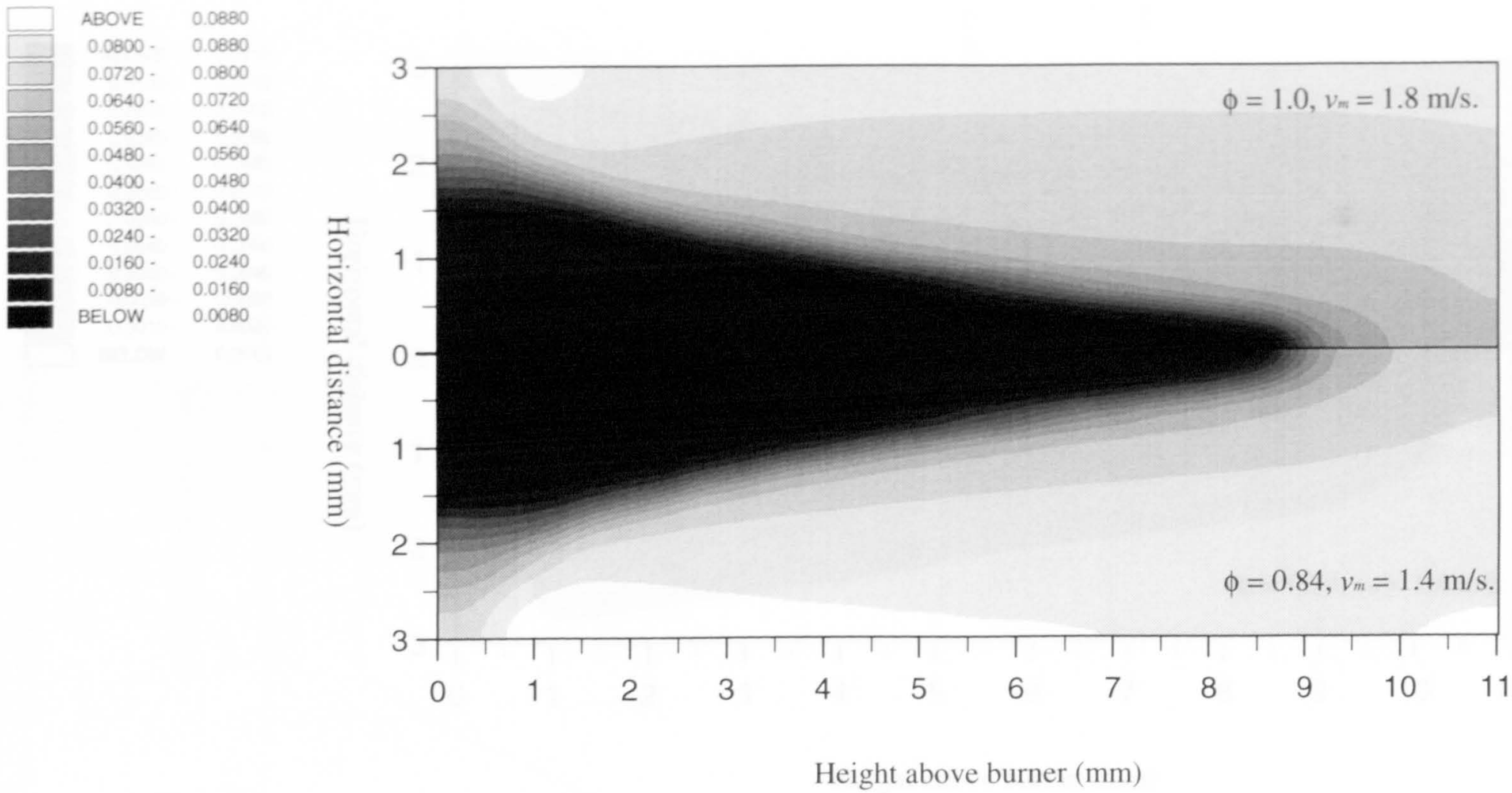

Fig. 5.27 Computed carbon dioxide isopleths for the two axisymmetric slot burner flames.

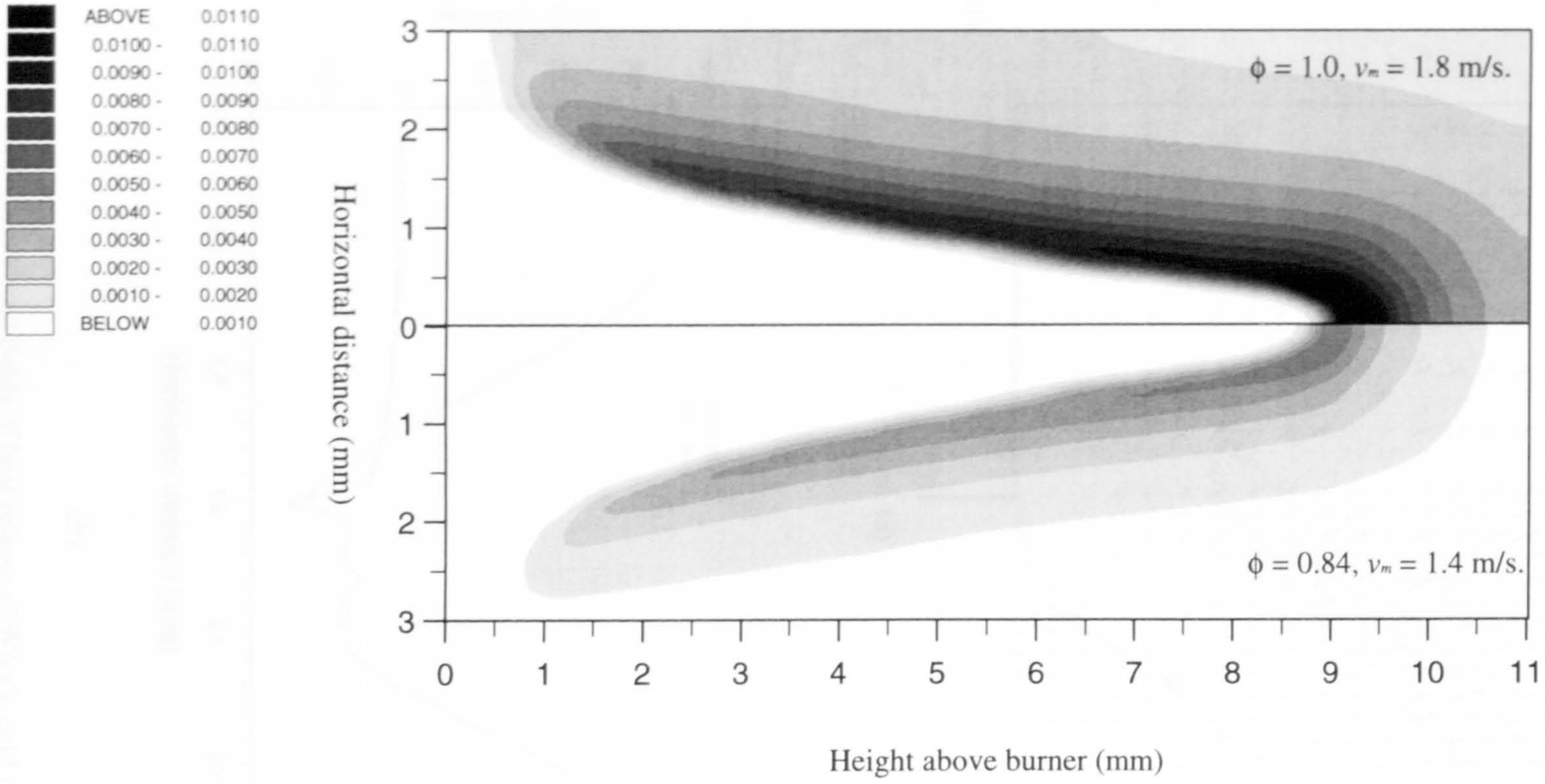

Fig. 5.28 Computed hydrogen ion isopleths for the two axisymmetric slot burner flames.

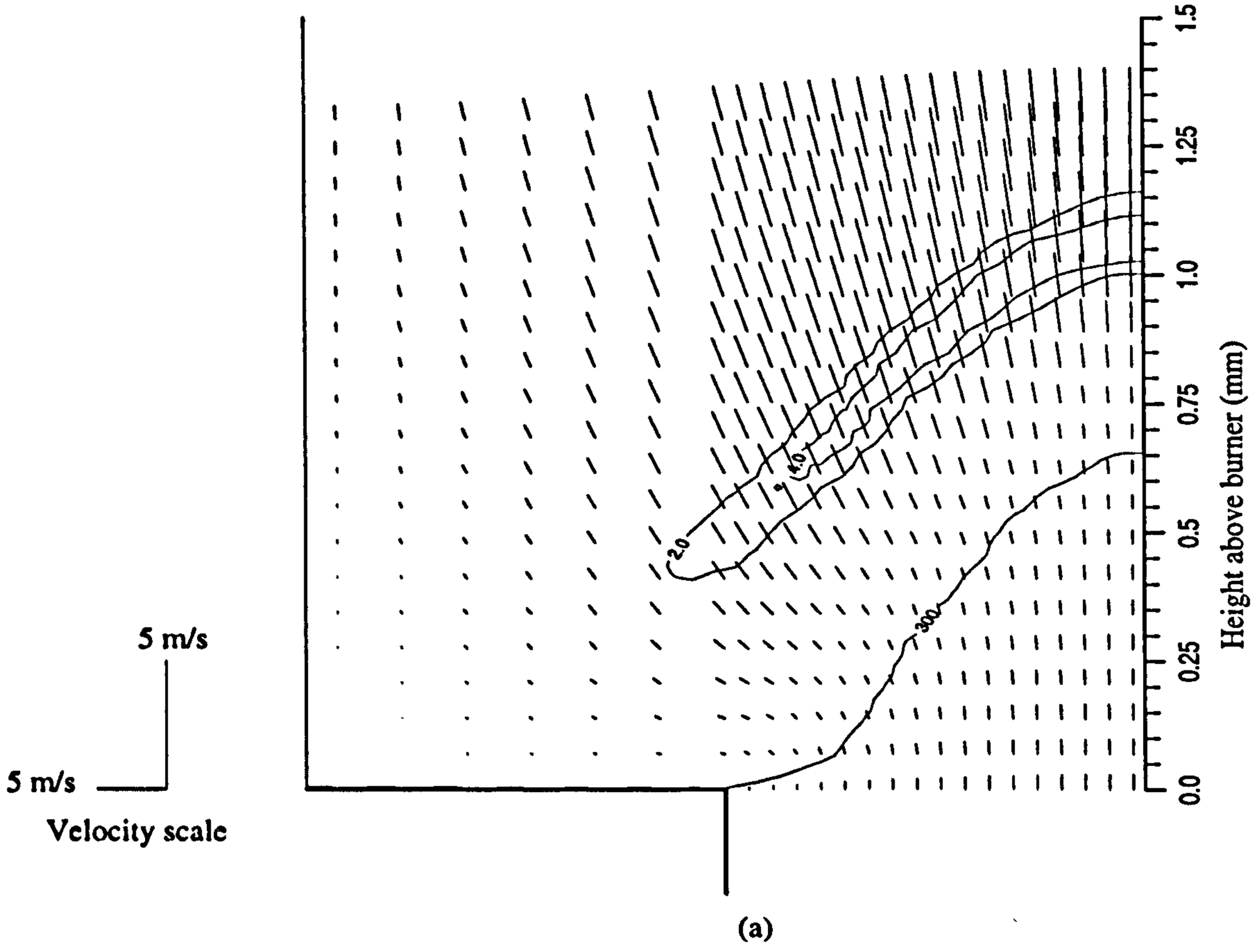

(a)

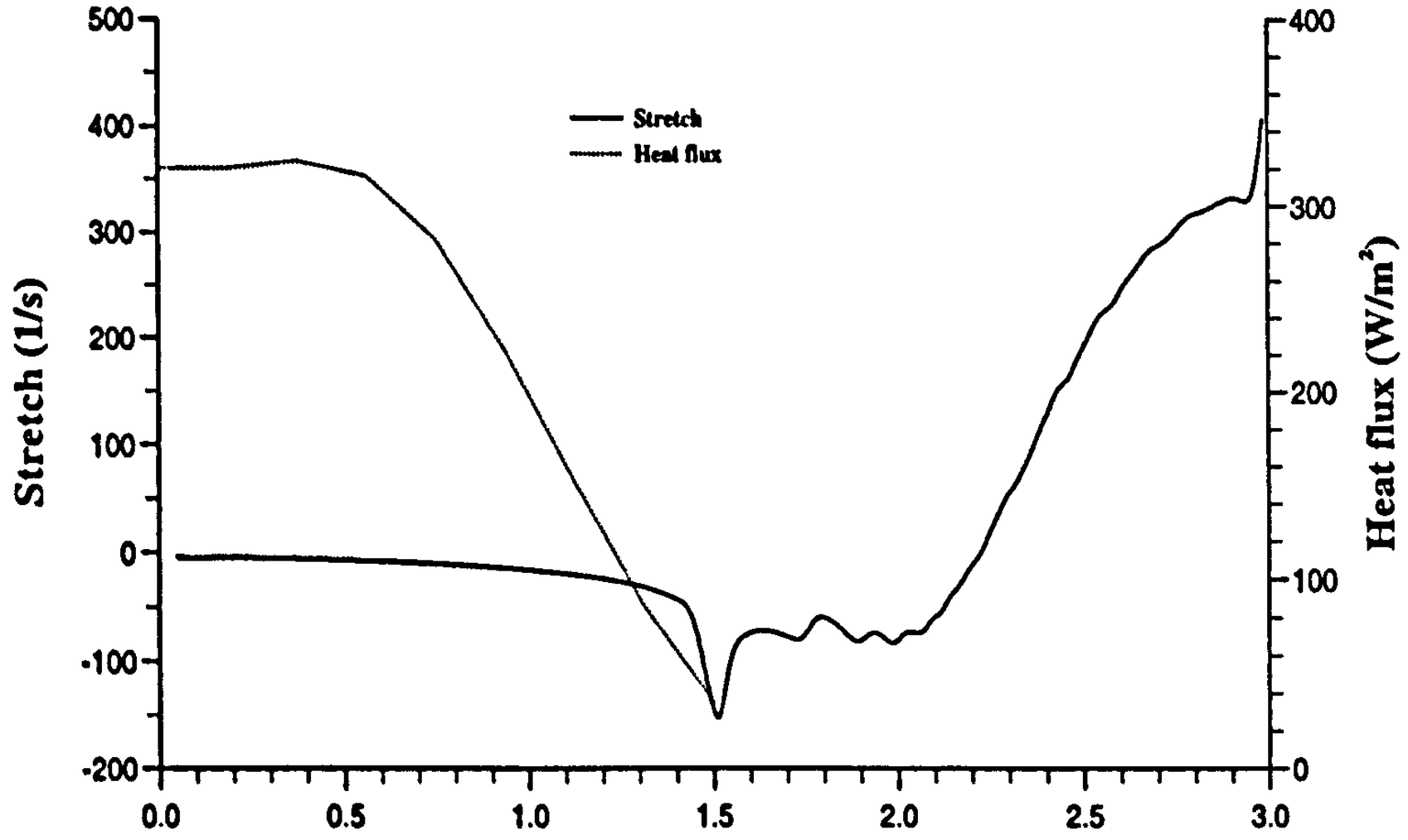

(b)

Fig. 5.29 (a) Two-dimensional fields of heat release (GW/m³), cold isotherm (300 K), and velocity, and (b) their corresponding stretch rates and heat flux, for stoichiometric methane-air with $v_m = 0.4$ m/s.

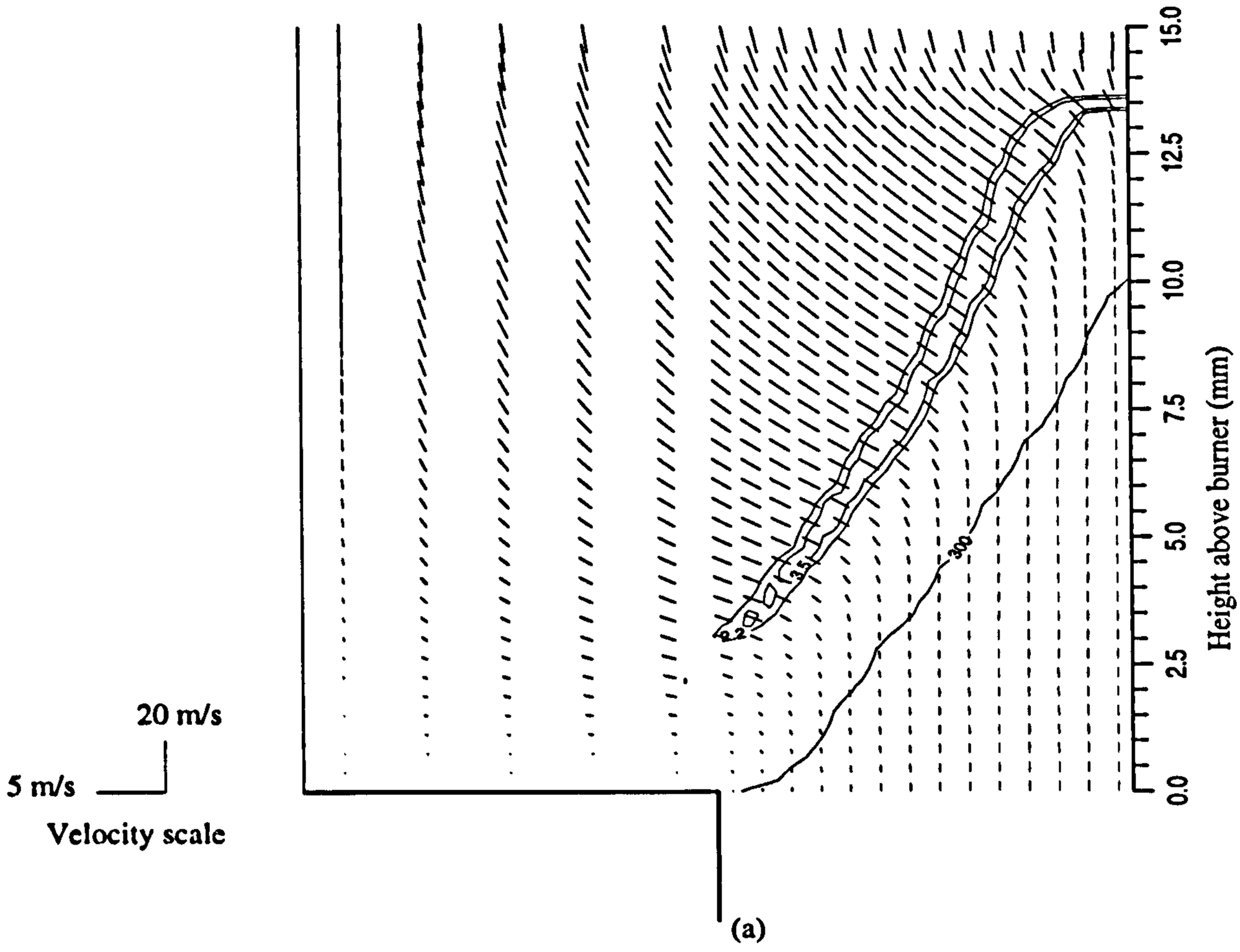

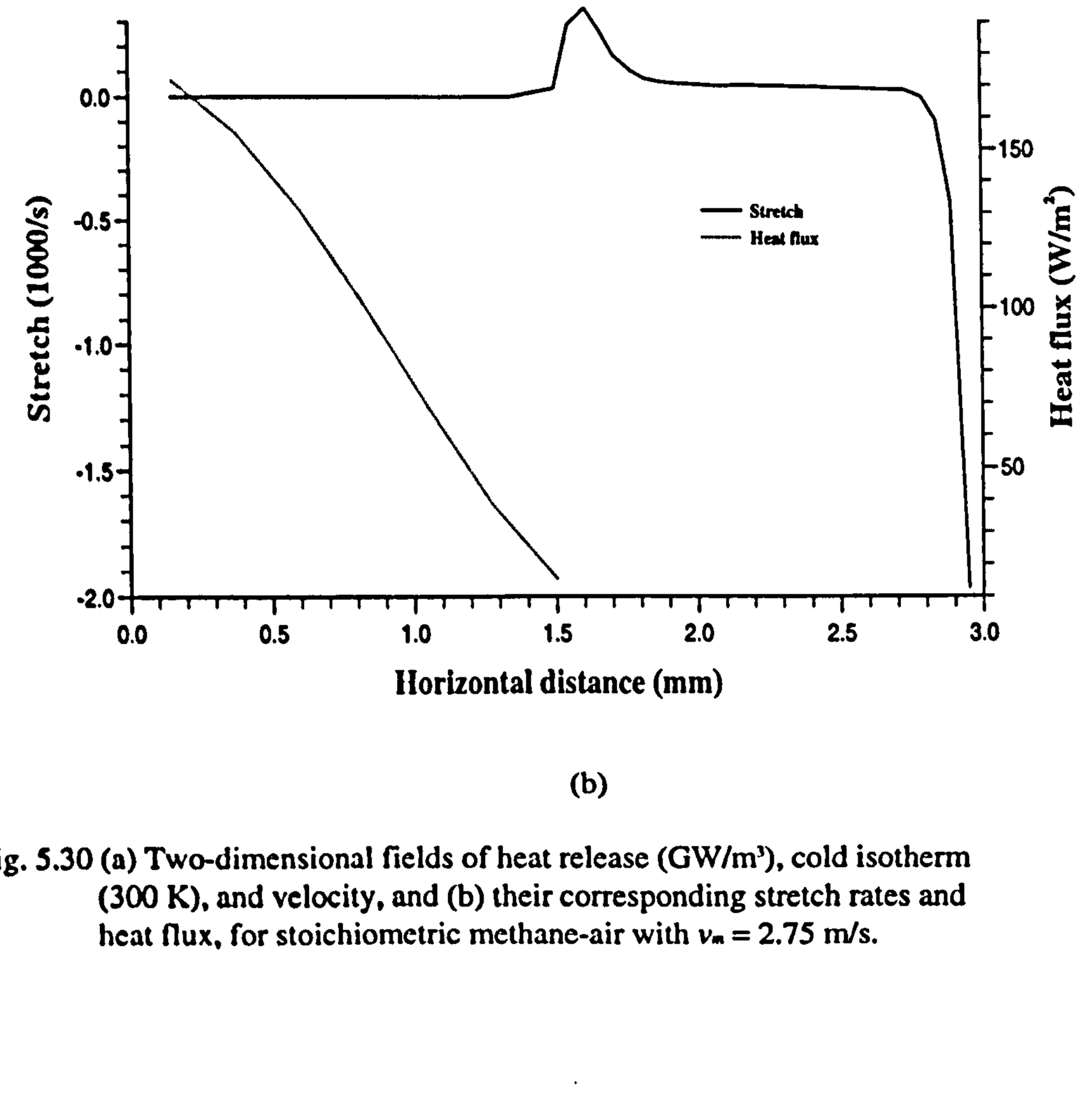

Fig. 5.30 (a) Two-dimensional fields of heat release (GW/m³), cold isotherm (300 K), and velocity, and (b) their corresponding stretch rates and heat flux, for stoichiometric methane-air with $v_m = 2.75$ m/s.

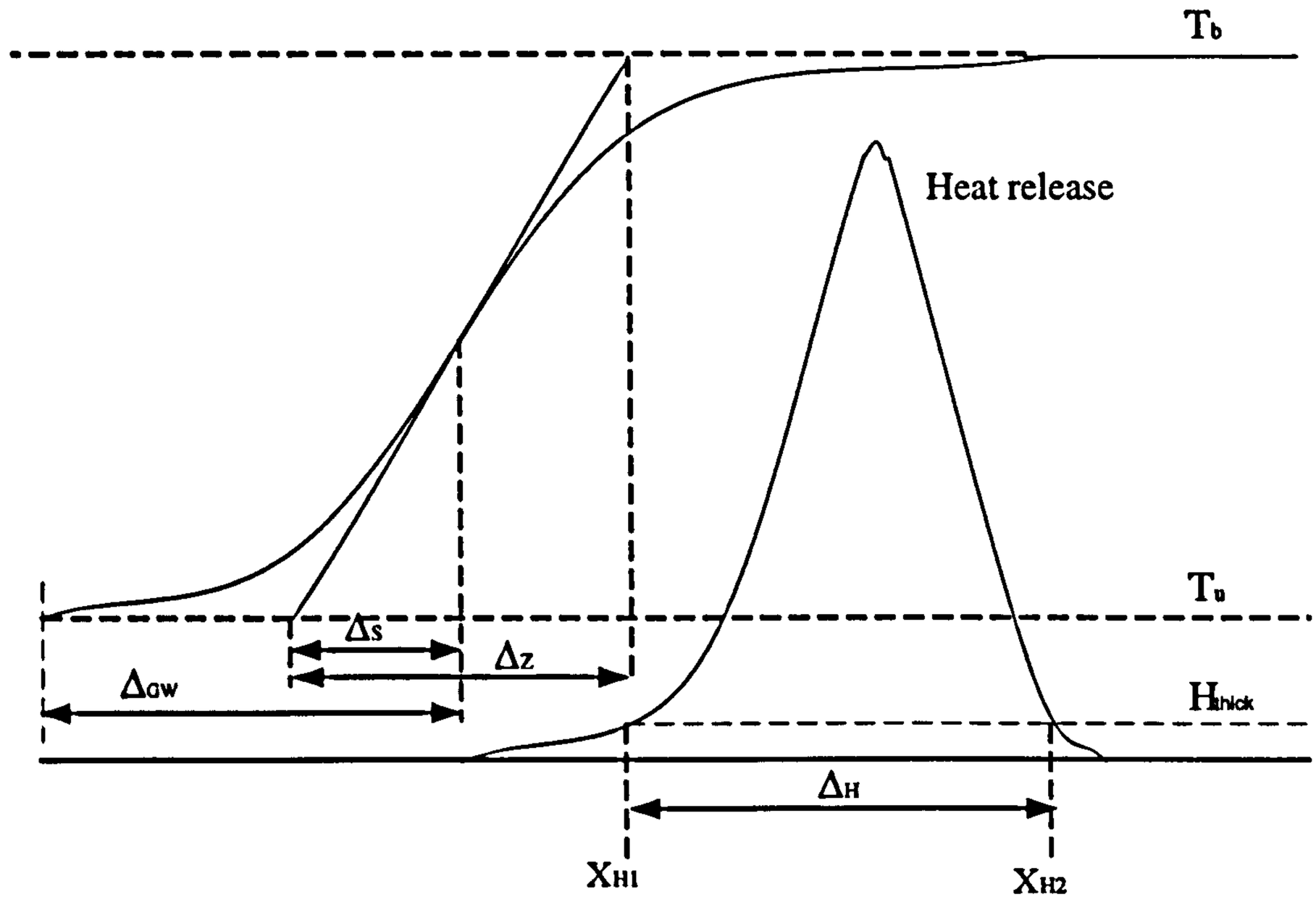

Fig. 5.31 Temperature and heat release profile across the flame front.

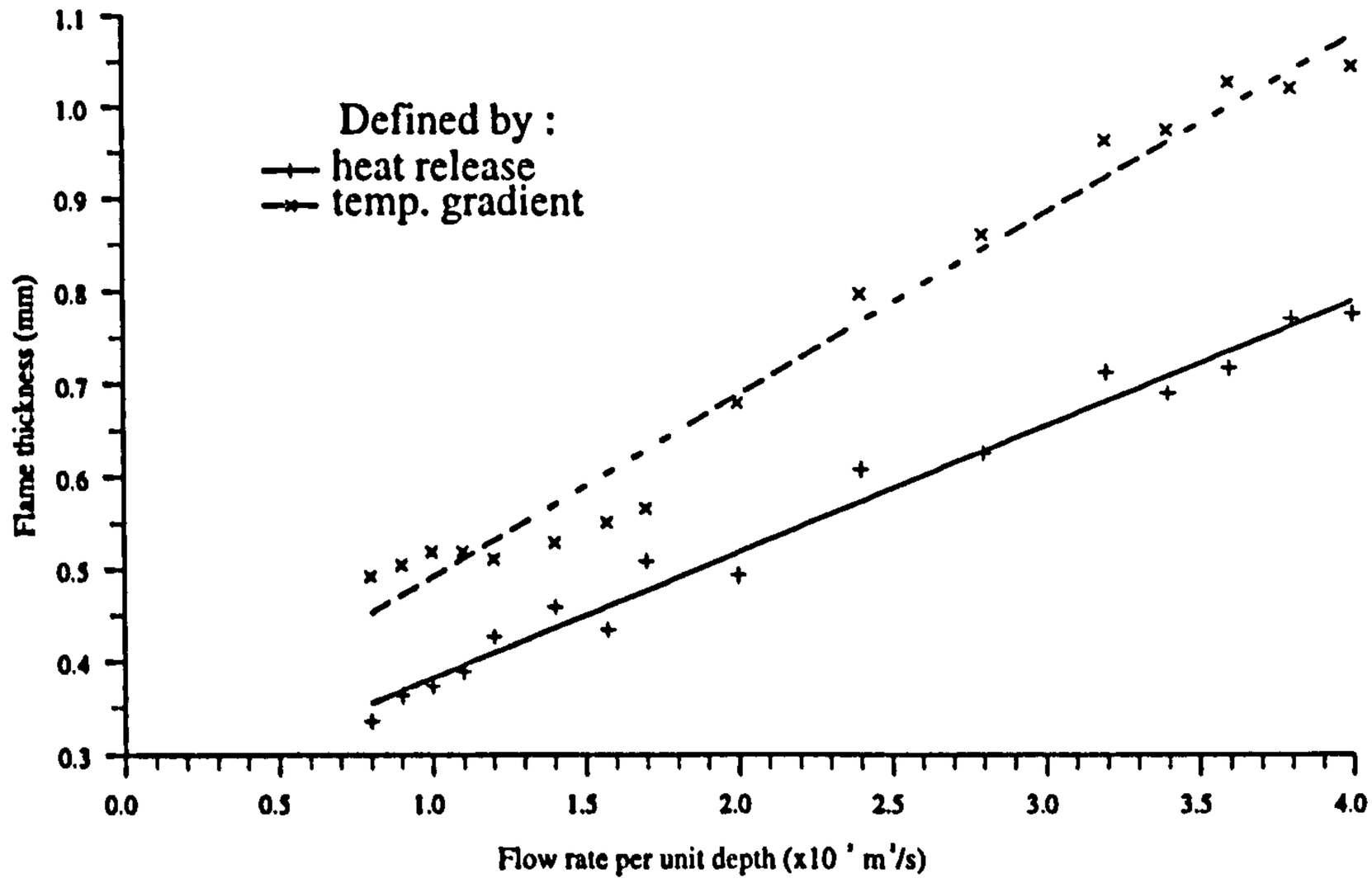

Fig. 5.32 Computed flame thickness with 2 mm slot width and $\phi = 0.75$.

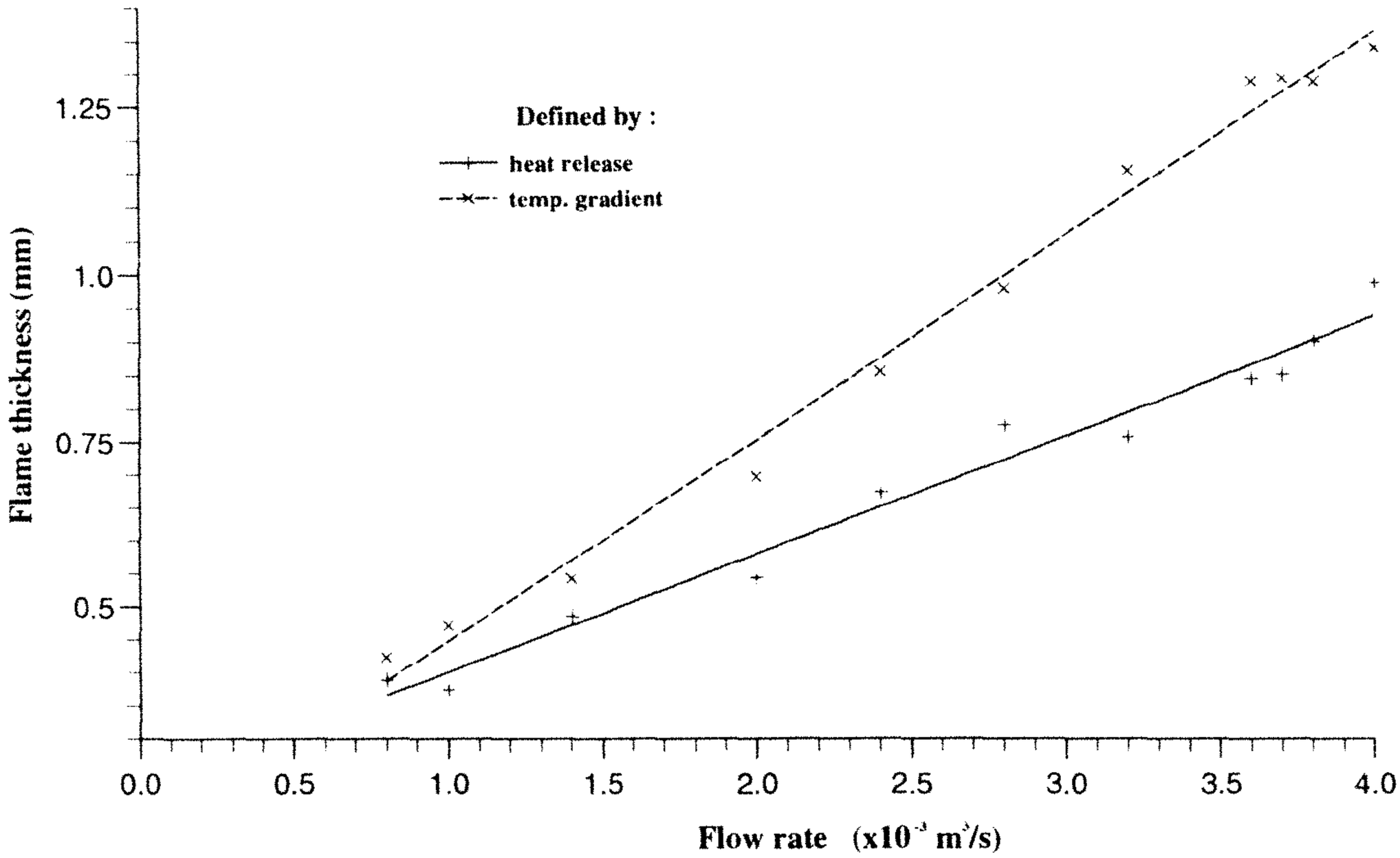

(a)

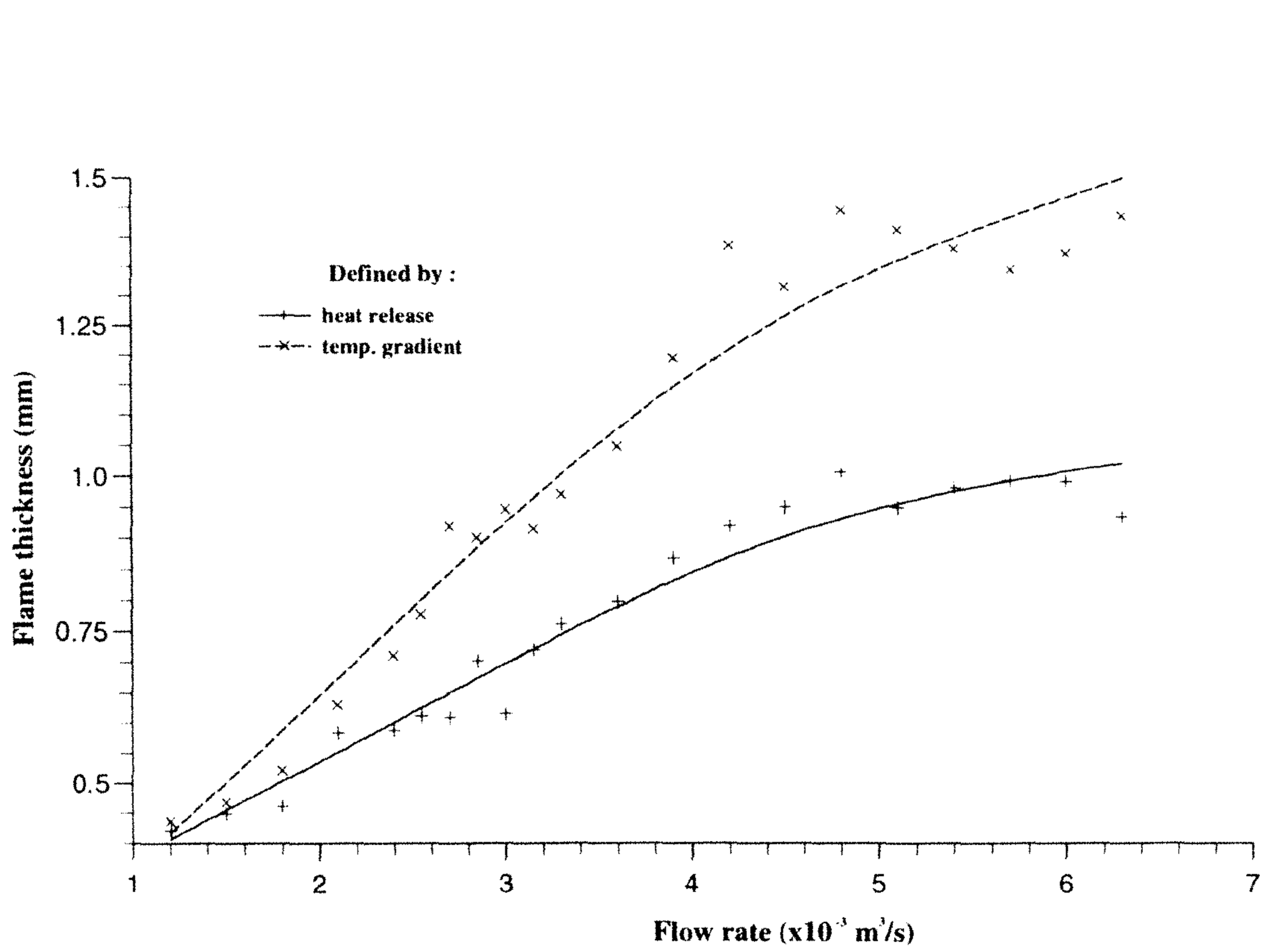

(b)

33 Computed flame thickness with $\phi = 0.84$ and (a) 2 mm slot width, (b) 3 mm slot width.

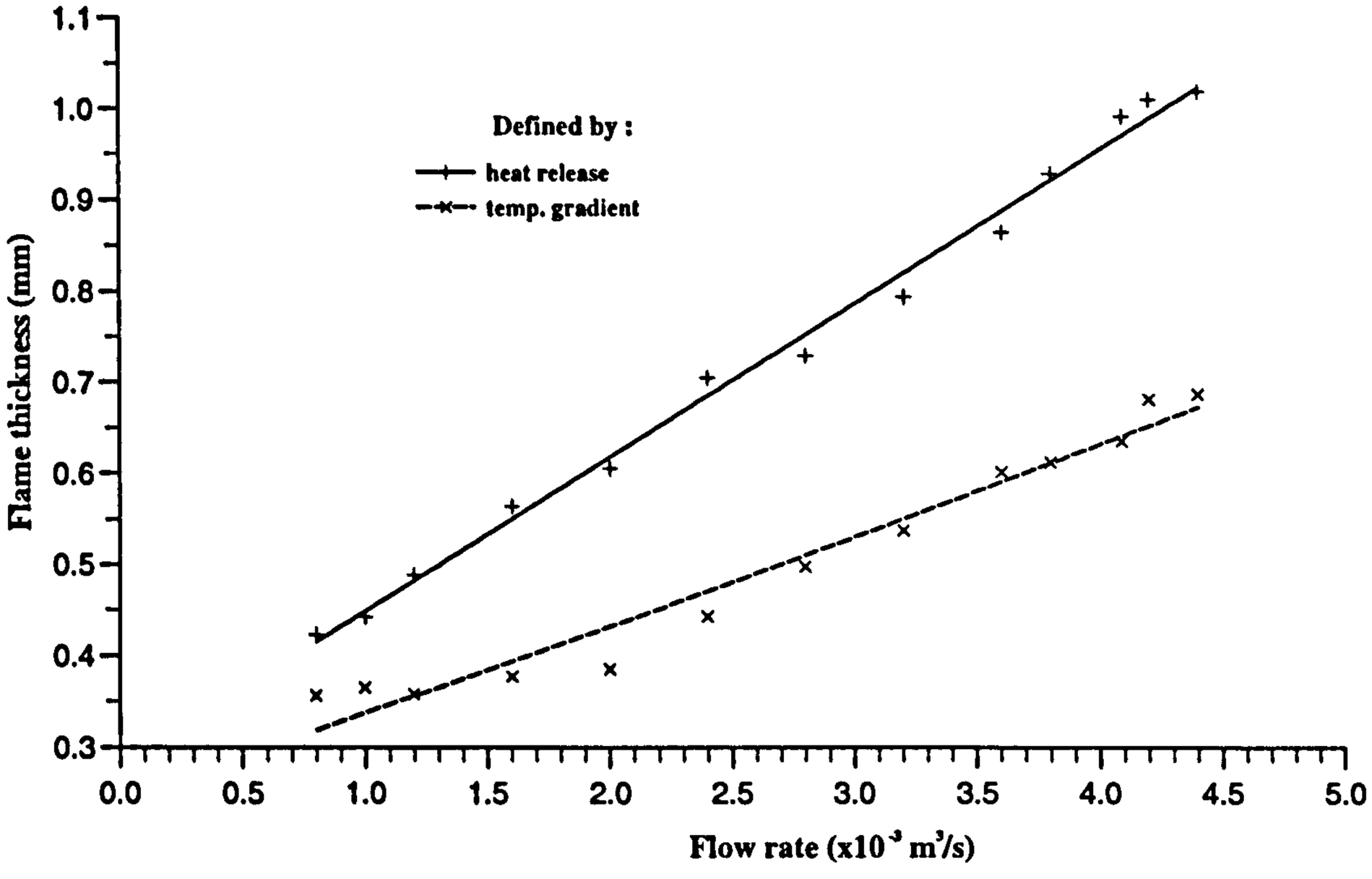

(a)

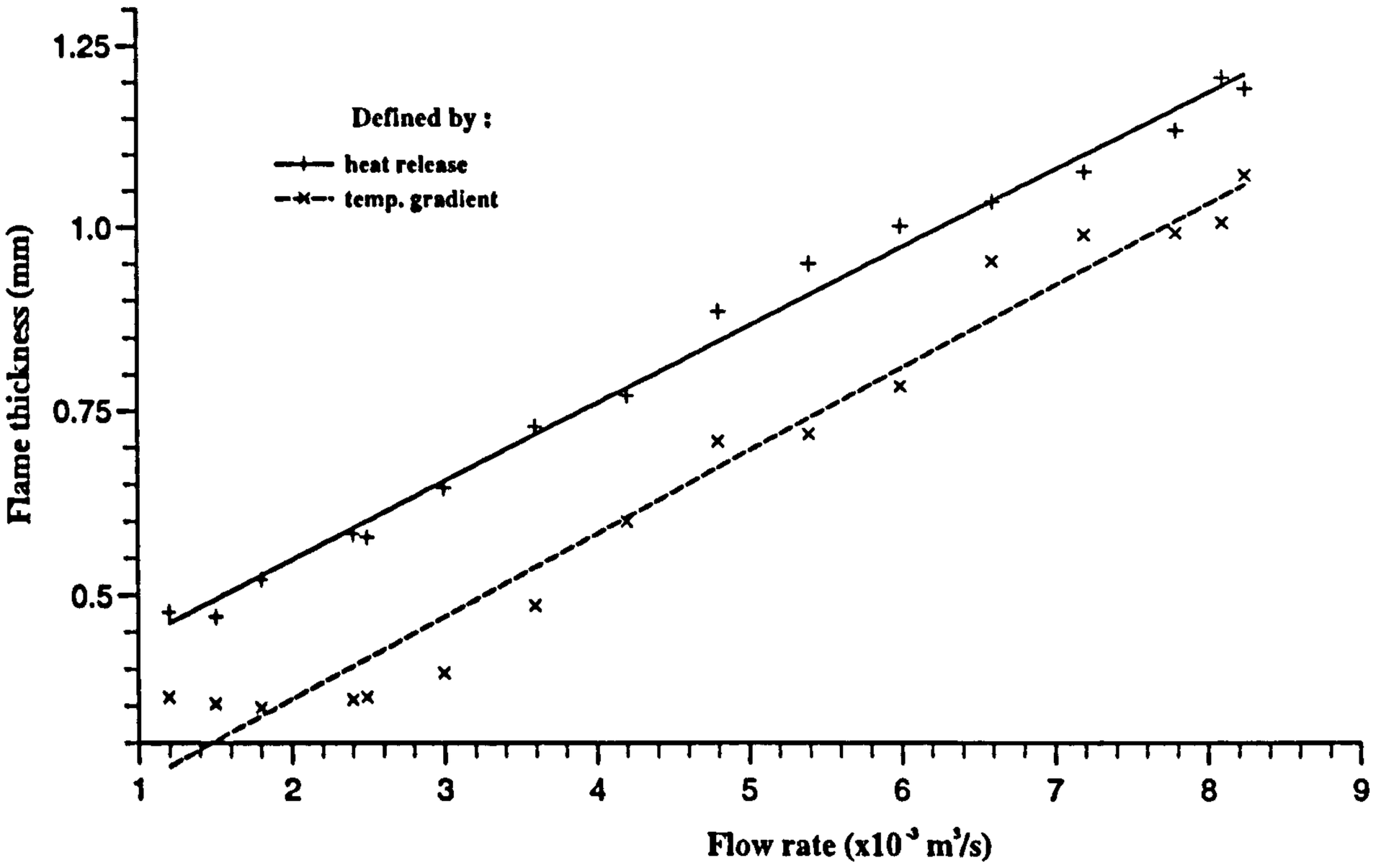

(b)

Fig. 5.34 Computed flame thickness with $\phi = 1.0$ and (a) 2 mm slot width, (b) 3 mm slot width.

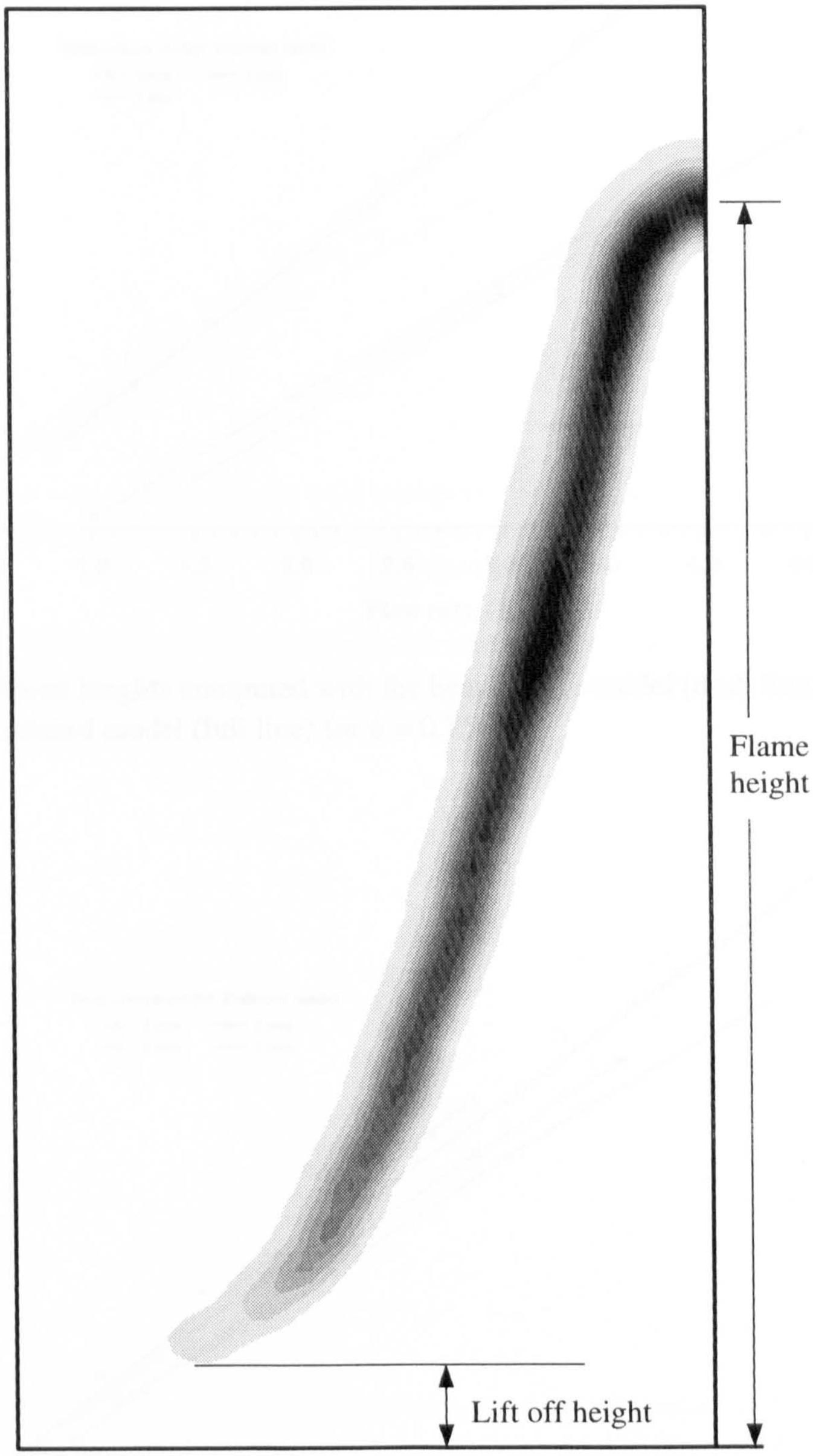

Fig. 5.35 Definition of lift off height and flame height with a heat release contour.

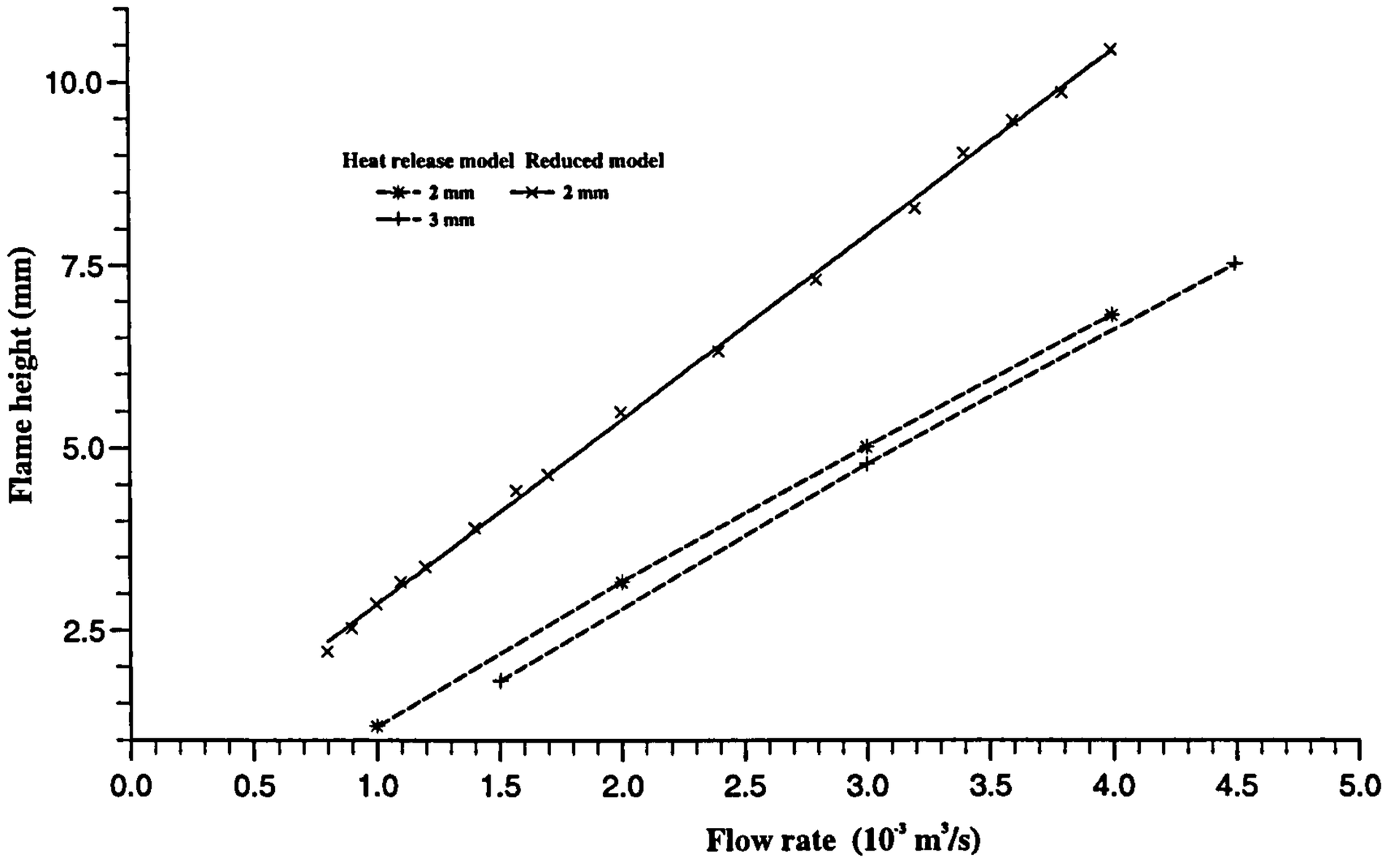

Fig. 5.36 Flame heights computed with the heat-release model (dash line) and the reduced model (full line) for $\phi = 0.75$.

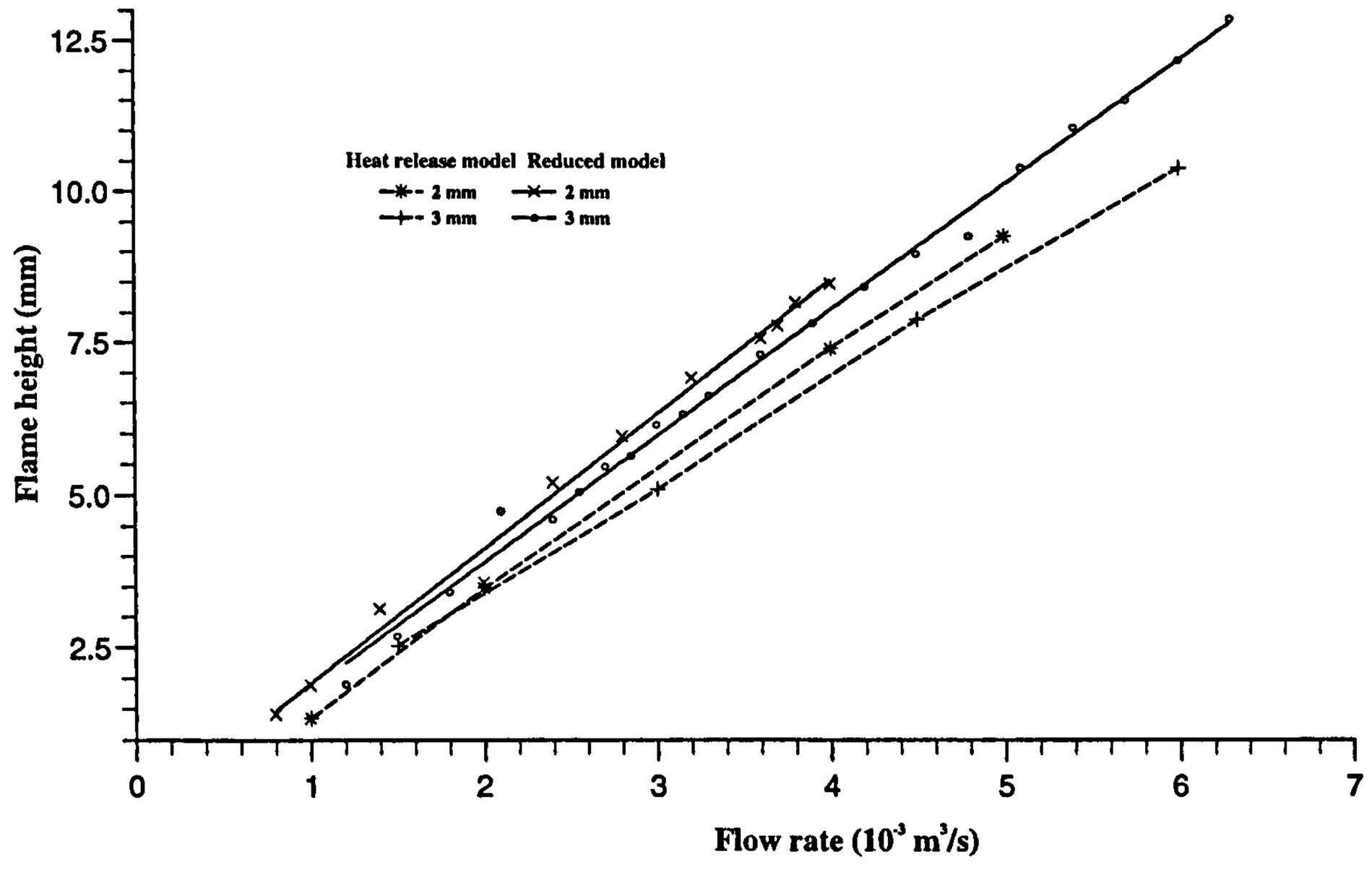

Fig. 5.37 Flame heights computed with the heat-release model (dash line) and the reduced model (full line) for $\phi = 0.84$.

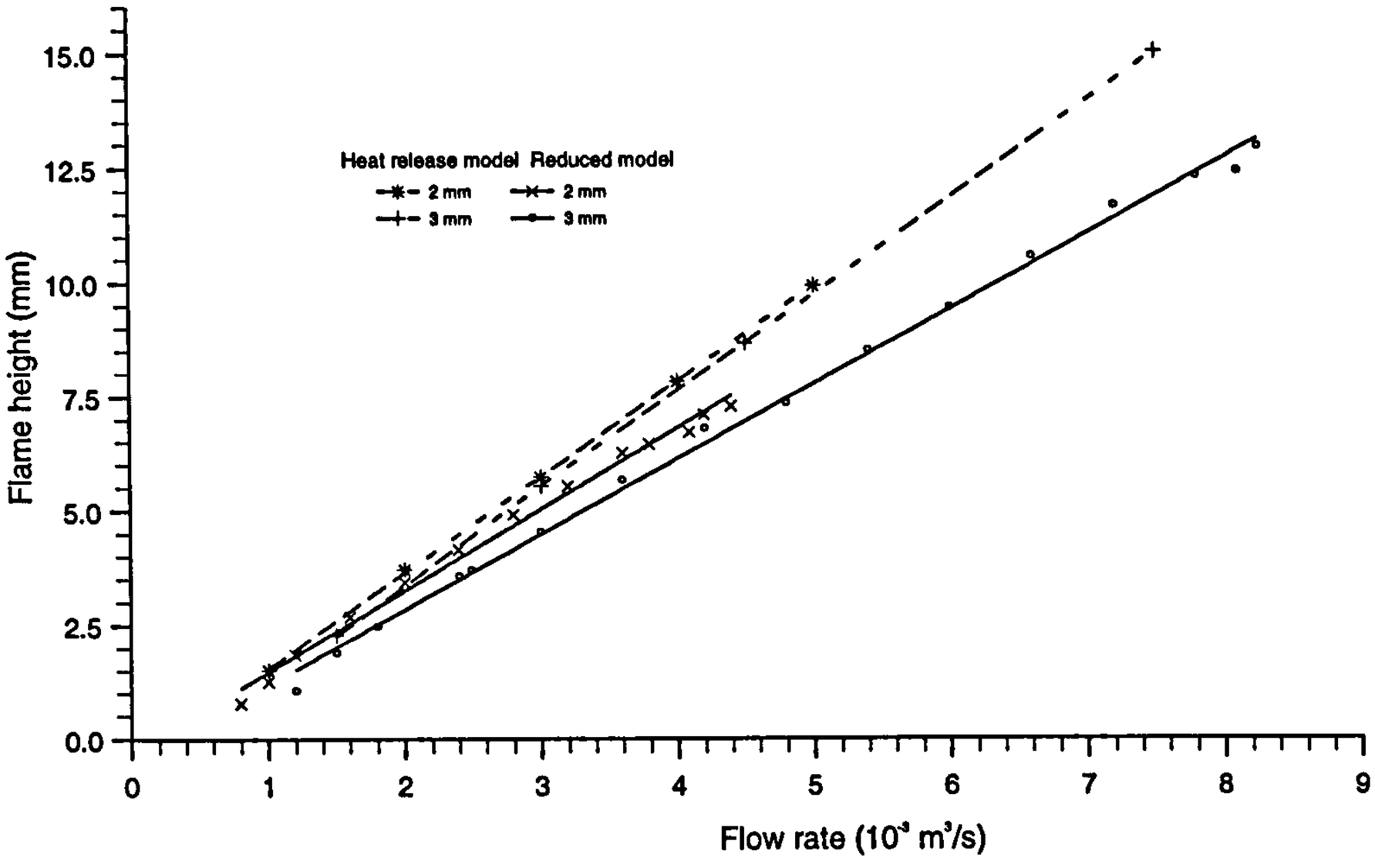

Fig. 5.38 Flame heights computed with the heat-release model (dash line) and the reduced model (full line) for a stoichiometric mixture.

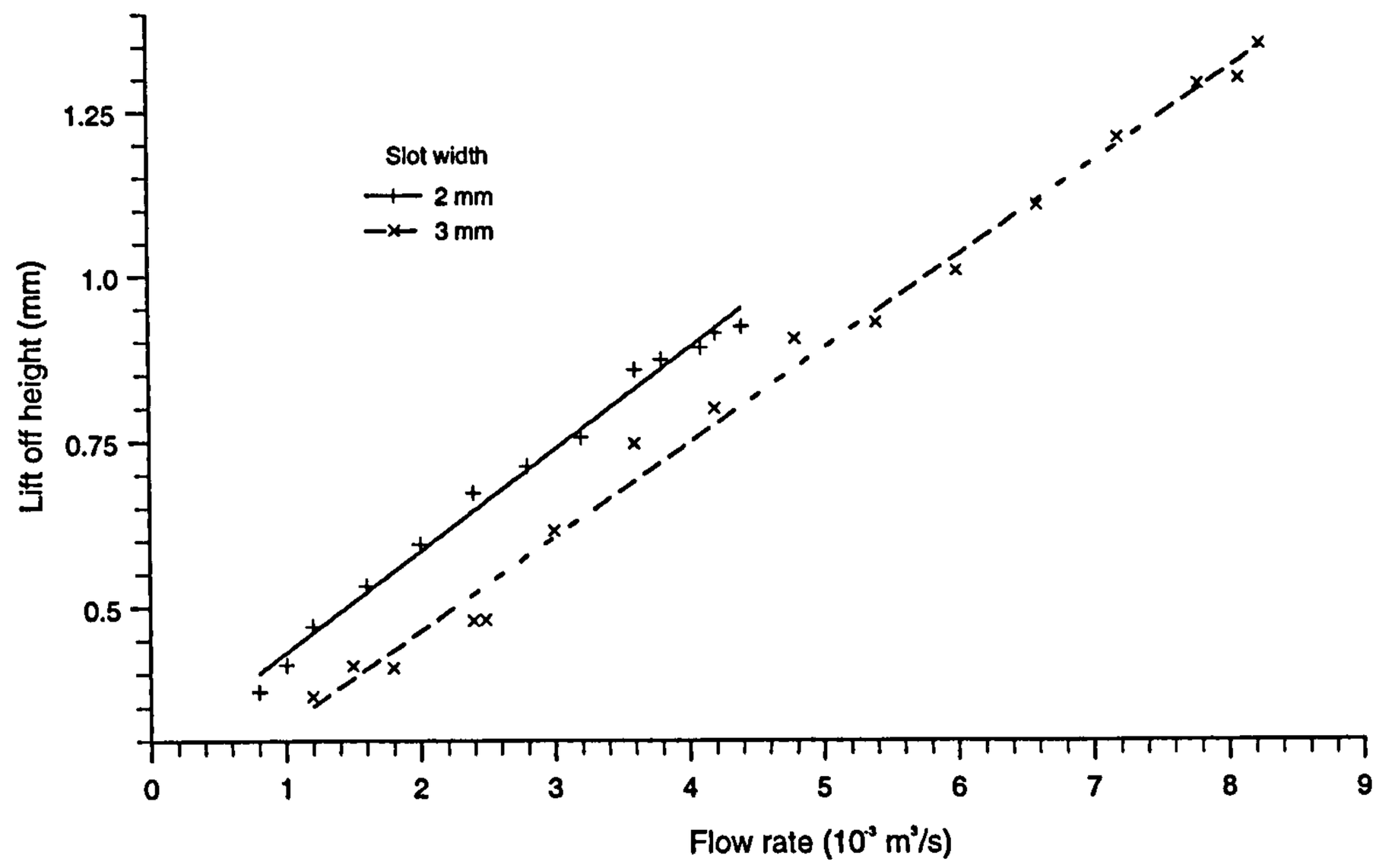

Fig. 5.39 Computed lift off height with stoichiometric methane-air for 2 mm and 3 mm slot widths.

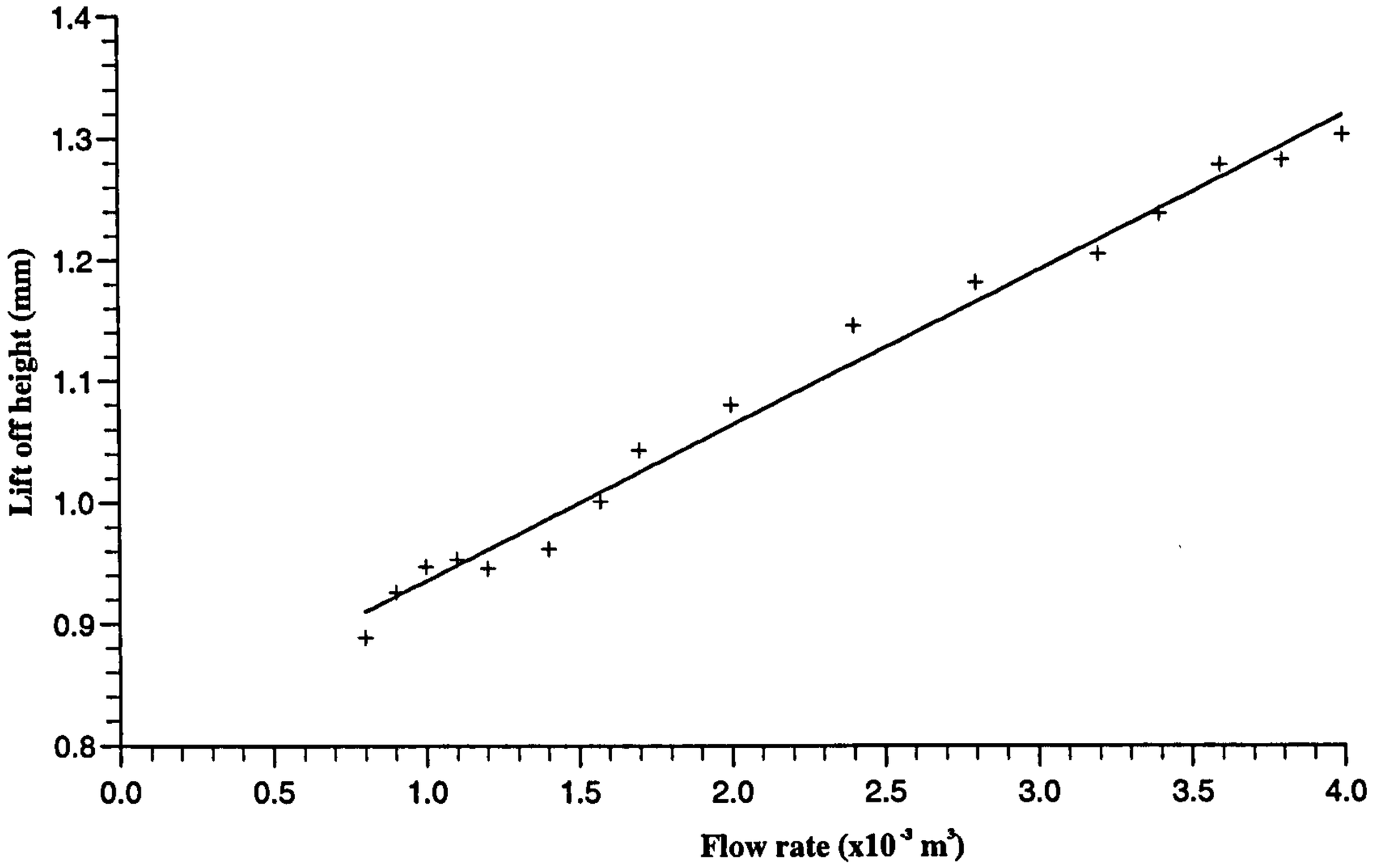

Fig. 5.40 Computed lift off height for 2 mm slot width and $\phi = 0.75$.

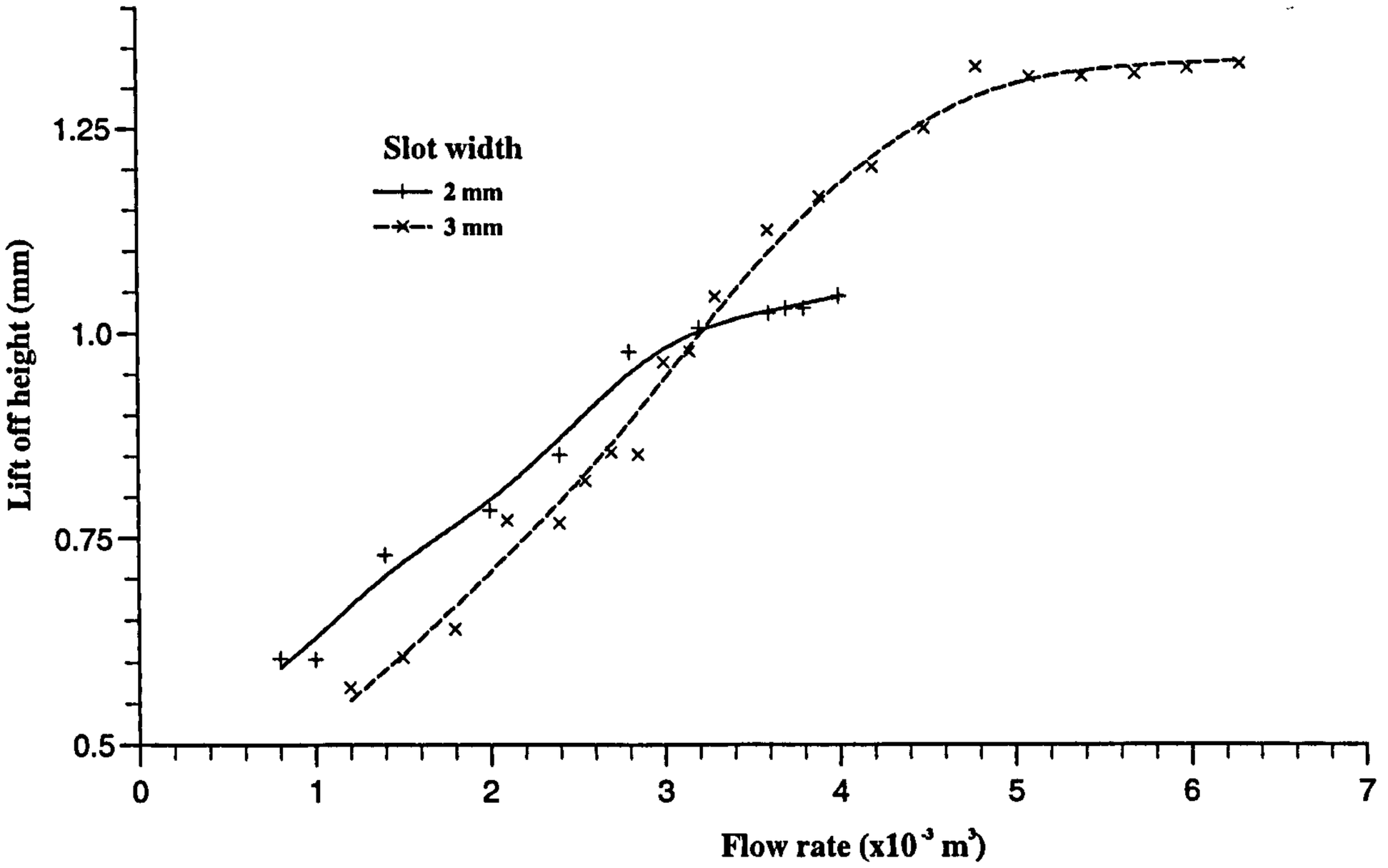

Fig. 5.41 Computed lift off height with $\phi = 0.84$ for 2 mm and 3 mm slot widths.

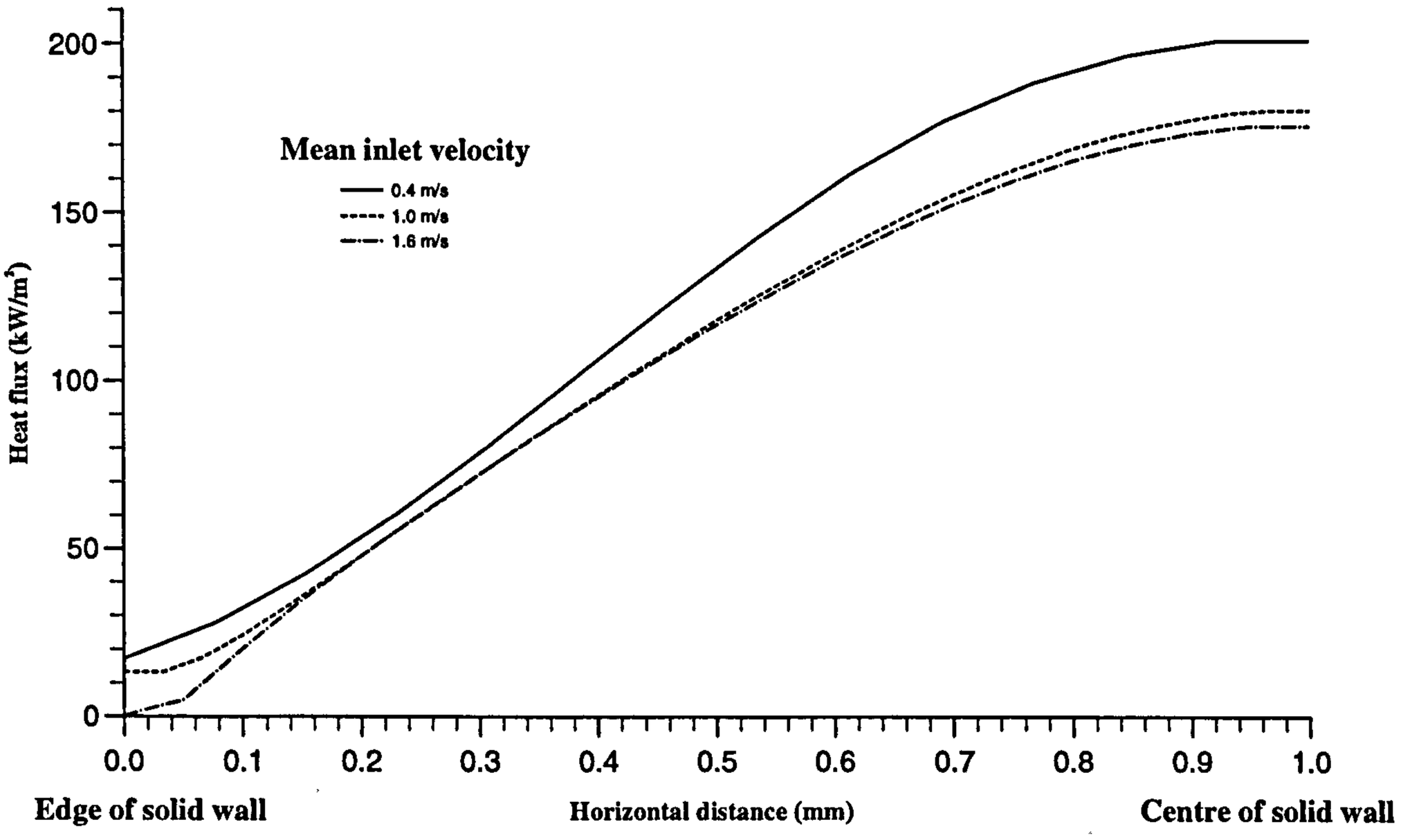

Fig. 5.42 Computed heat flux across a 2 mm slot at different flow rates for $\phi = 0.75$.

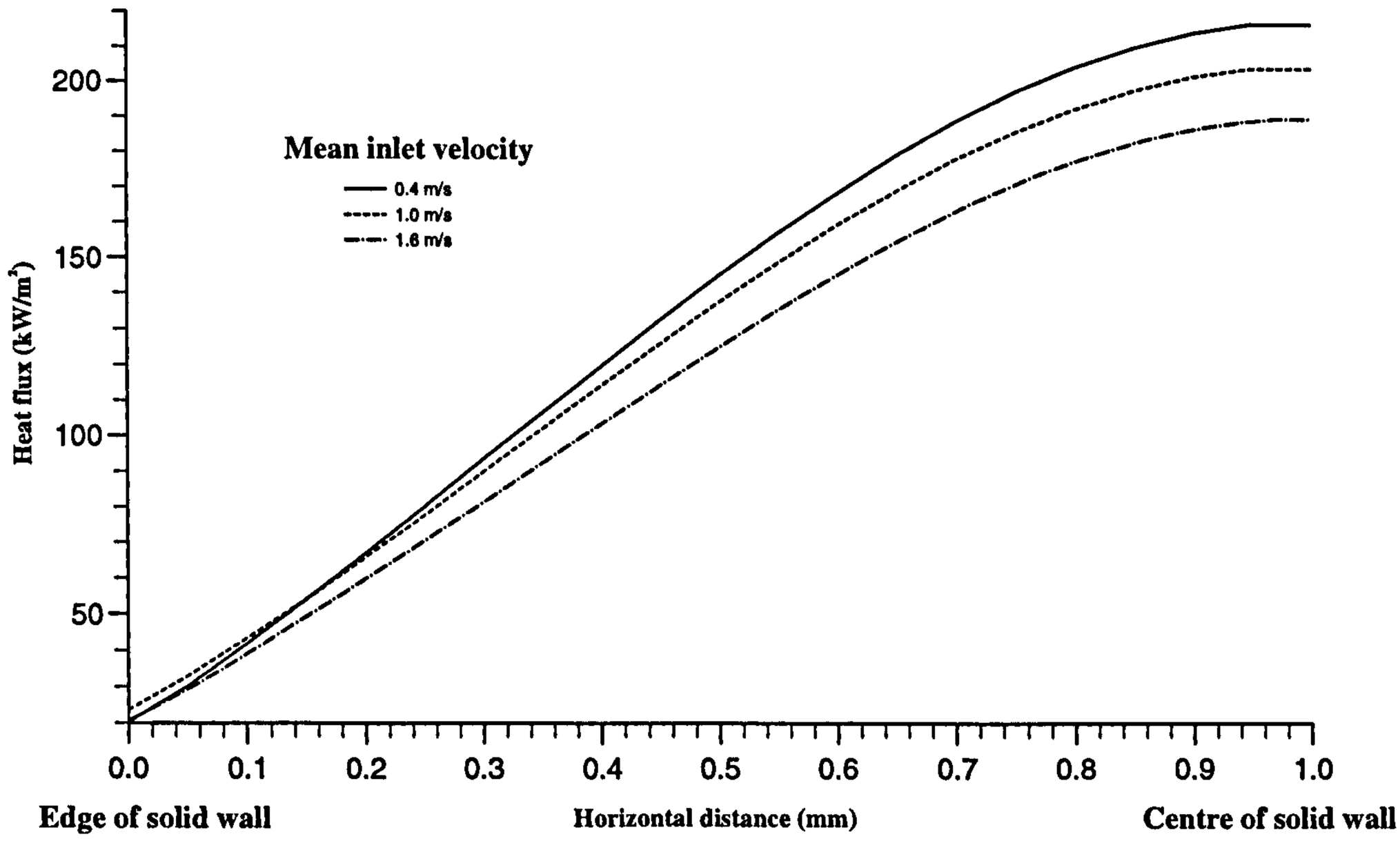

Fig. 5.43 Computed heat flux across a 2 mm slot at different flow rates for $\phi = 0.84$.

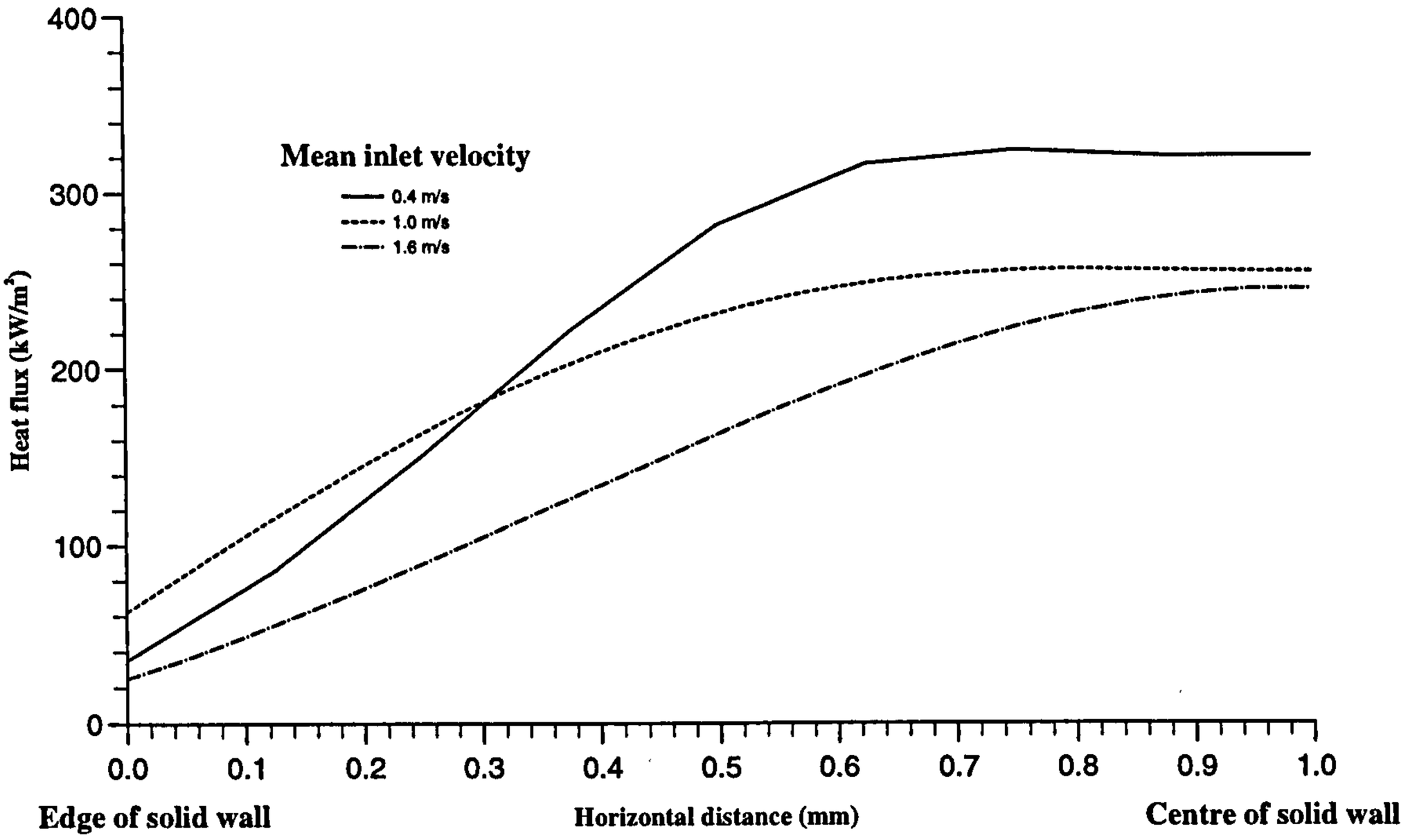

Fig. 5.44 Computed heat flux across a 2 mm slot at different flow rates for stoichiometric mixtures.

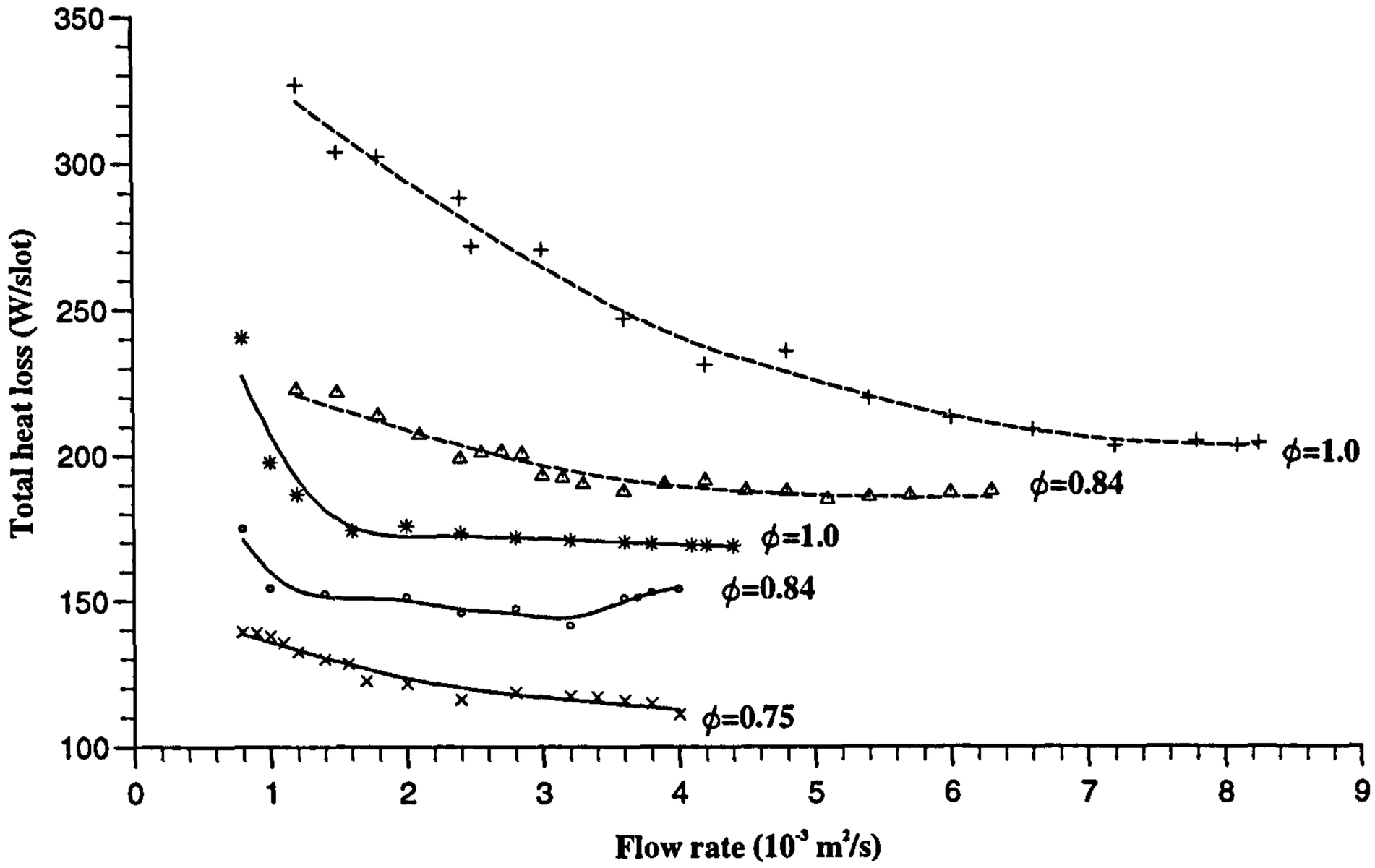

Fig. 5.45 Computed heat loss per unit slot depth for the configurations with 2 mm (full lines) and 3 mm (dash lines) slot widths.

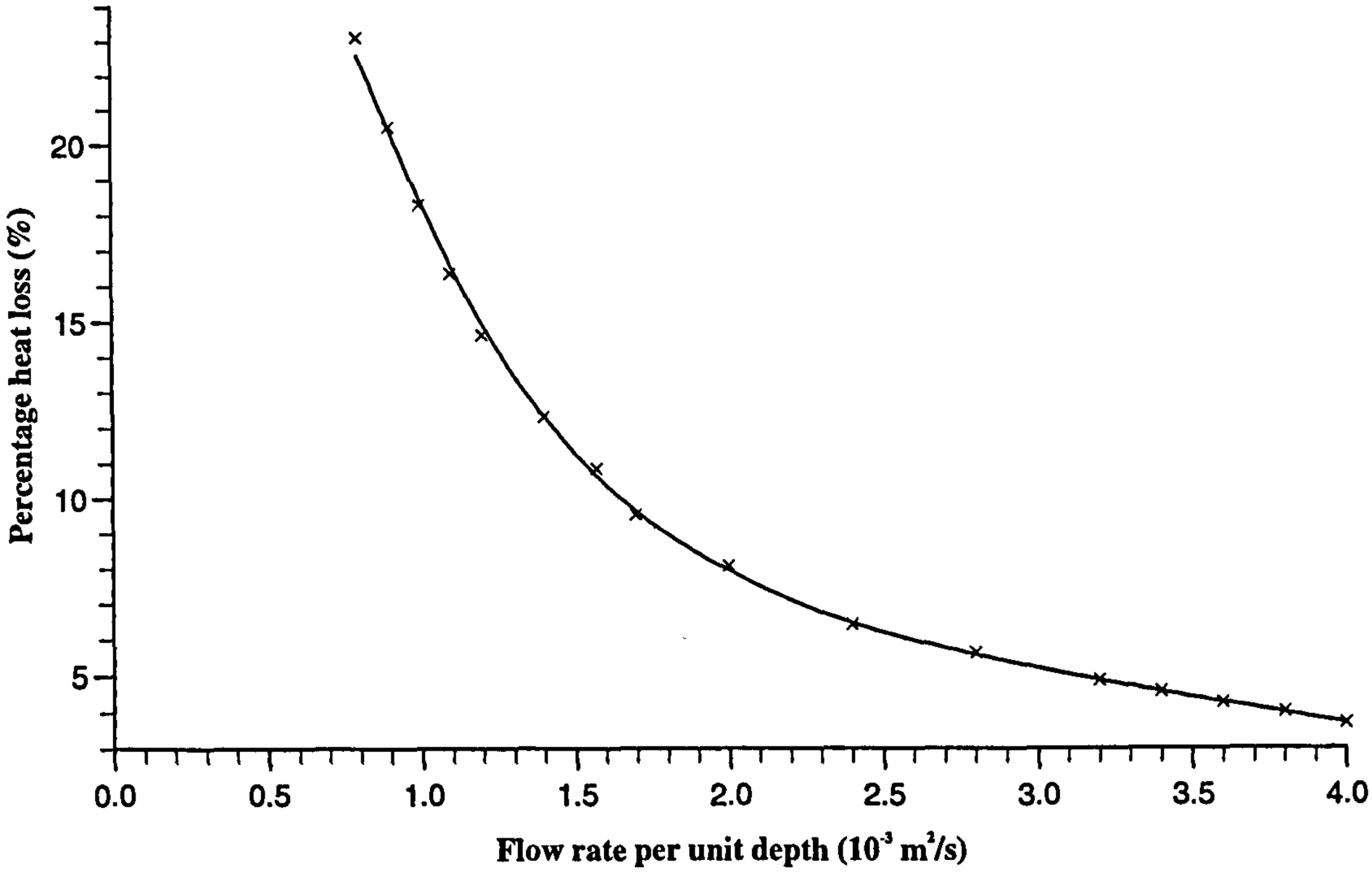

Fig. 5.46 Computed percentage heat loss (heat loss/heat input) for the 2 mm slot width geometry with $\phi = 0.75$.

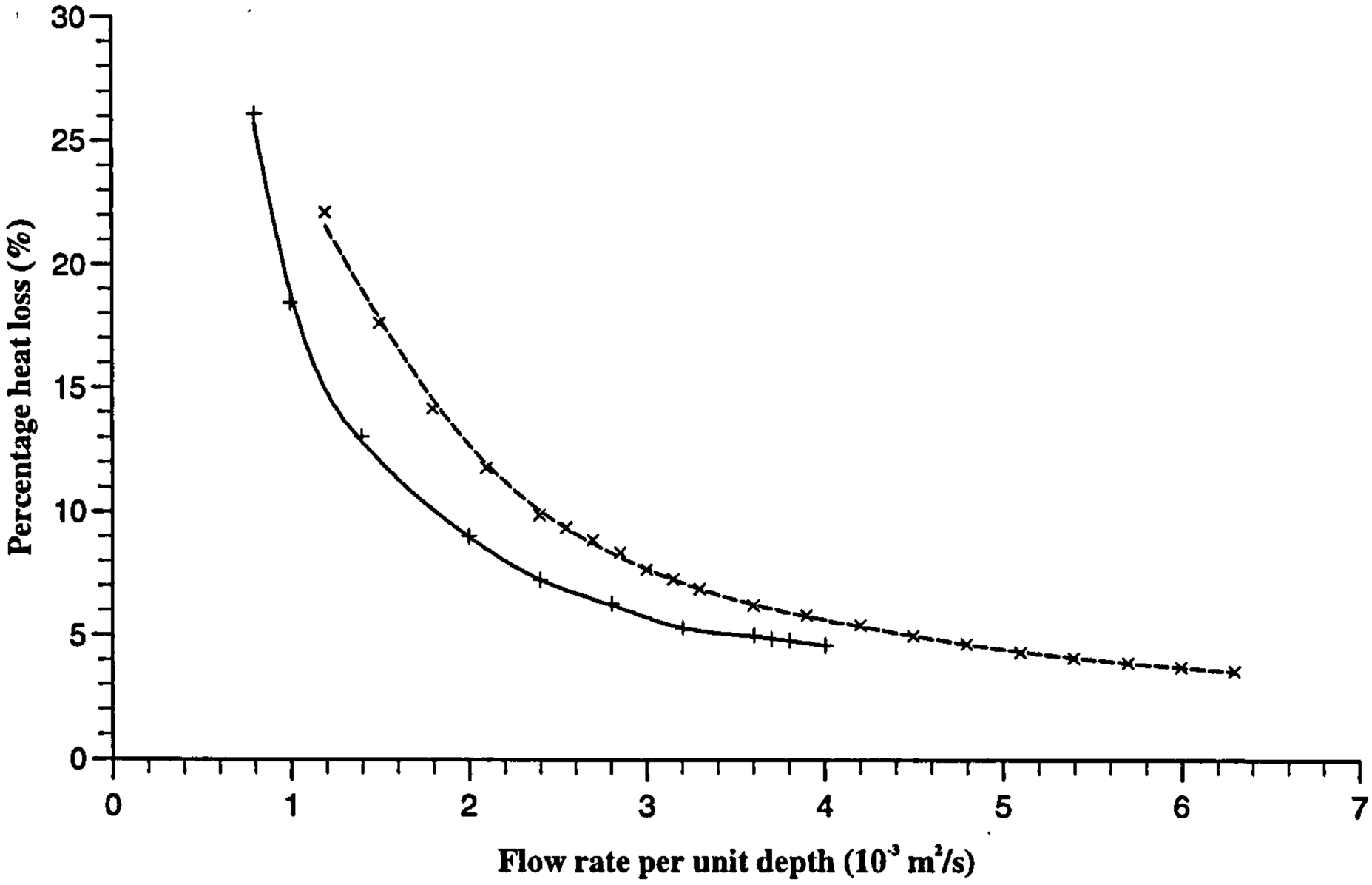

Fig. 5.47 Computed percentage heat loss (heat loss/heat input) for the 2 mm (full lines) and 3 mm (dash lines) slot widths with $\phi = 0.84$.

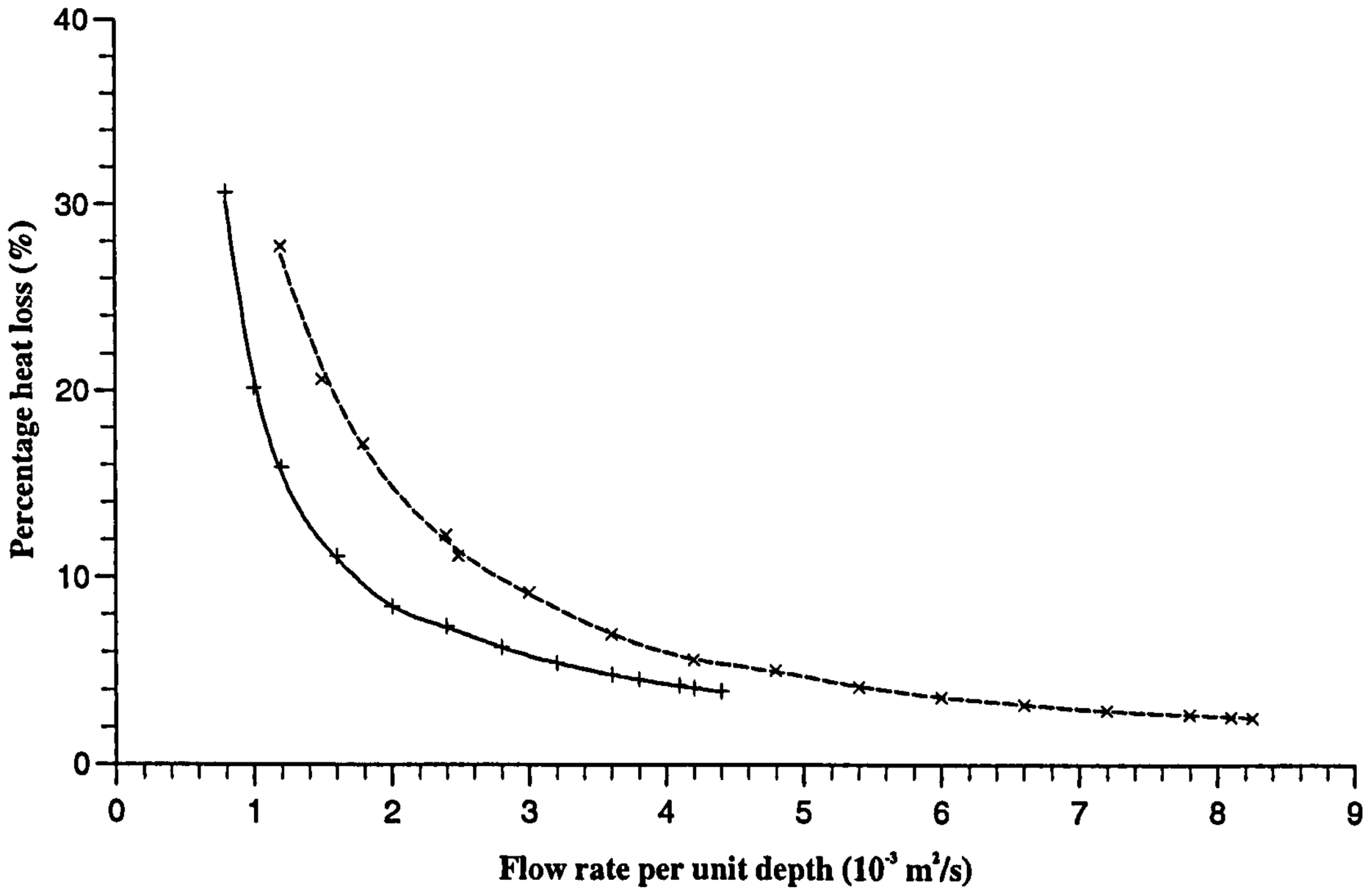

Fig. 5.48 Computed percentage heat loss (heat loss/heat input) for the 2 mm (full lines) and 3 mm (dash lines) slot widths with $\phi = 1.0$.

CHAPTER SIX
Experimental Validation with Slot Burner

6.1 Introduction

The major objective of the experimental investigation was to obtain data for validating the computational predictions of the two-dimensional flame on a slot burner, with premixed methane and air. For temperature measurements, intrusive devices such as a thermocouple can seriously perturb the flow pattern and flame behaviour. They have limited spatial resolution and cannot be used for temperatures in excess of the melting point of the hot junction materials. Furthermore, corrections must be applied that depend upon the radiative heat loss and the convective heat gain. For these reasons, it was decided to employ the recently developed Coherent Anti-Stokes Raman Spectroscopy (CARS) technique. The technique is non-intrusive, has a small measuring volume (~ 3 mm in length and 100 μm in width) and is sufficiently accurate (± 30 K). In the present work, the length of the measurement volume could be aligned along an isotherm in the direction of the slot. The slot burner was developed and kindly made available by British Gas plc. Some modifications were made to it to obtain a flow pattern more suited for the CARS measurements. The primary task of the experiments was to map the two-dimensional temperature fields for the burner, at various flow rates and equivalence ratios. These could then be compared with the computed isotherms.

The CARS technique is highly specialised and the experimental work was in cooperation with Dr. M. Scott, who had spent some six years on CARS measurement, and was responsible for setting up and utilising the technique, whilst the author was responsible for providing the flames suitable for the measurements. Having been

involved in the experiments, the author has gained some knowledge of the basic principles and safety procedures for this technique. The CARS technique for temperature measurements is well documented in many textbooks (Wilson and Hawkes 1987, Hecht 1975), and detail of the present CARS system has been described by Bradley *et al.* (1992). This Chapter describes any subsequent modifications to the system. It also outlines the technique and experimental programme, as well as describing the modifications to the slot burner. Experimental and computed temperatures are compared.

6.2 The CARS System

6.2.1 CARS theory

Laser spectroscopy techniques rely on the interaction of electromagnetic radiation with atoms and molecules. A molecule can occupy various discrete energy states or levels. The energy level of a molecule can be changed by a number of effects, including chemical reaction, collisions with other molecules, temperature change or radiation absorption or emission.

When photons collide with a molecule, they are absorbed if the energy of the radiation corresponds to the separation of two of its energy levels, otherwise, the radiation will either be transmitted or scattered. Of the scattered radiation, a small amount is of increased or decreased wavelength. This scattered radiation is referred to as Stokes, or anti-Stokes, Raman scattering, respectively. In the former, the molecule becomes excited, and in the latter an excited molecule is de-excited.

In the CARS technique, incident laser beams of frequencies w_p and w_s, termed the pump and Stokes beams, respectively, interact to generate a polarisation field which produces coherent radiation at a frequency $w_{as} = 2w_p - w_s$, termed the anti-Stokes or CARS signal beam. When the frequency difference $w_p - w_s$ is close to the frequency, w_v, of a Raman resonance of a certain species, for example nitrogen, the magnitude of the radiation at w_{as} is resonantly enhanced and is uniquely characteristic of that species. The CARS process is illustrated in Figs 6.1. Figure 6.1a shows the beam crossing

geometry, whilst Fig. 6.1b illustrates the associated energy level diagram. Molecules of the species under investigation are excited by photons at w_p from energy level h_1 to h_3 (Fig. 6.1b). These molecules are then forced down to level h_2, where further excitation is provided by the second pump beam. The CARS signal beam is provided as the molecules drop back to their initial state h_1, either by spontaneous or stimulation emission from other photons in the CARS beam. It might be expected that signal generation could take another path. However, transitions do not occur between all energy levels, and only occur in accordance with statistically controlled, quantum-mechanically derived selection rules.

For CARS spectrum generation, a broadband Stoke source was employed. This approach enables the entire spectrum to be generated by a single laser pulse of approximately 15 ns duration. This naturally leads to weaker signals, but generates the entire CARS spectrum with each individual pulse, permitting, in principle, instantaneous measurements of medium properties.

6.2.2 The integrated CARS laser system

An integrated CARS laser system was supplied by Spectron Laser System Ltd. This comprised a Q-switched SL800 pulsed Nd:YAG and a SL4000 pulsed dye lasers. Both lasers were mounted back to back on the same optical bench, which is supported by a single, centrally located shaft. This allows the whole assembly to be rotated through 180°, bringing either laser to the 'top' position for laser adjustment. The receiving optics and the CCD camera were mounted on a separate optical bench, which is fixed to the floor (Fig. 6.2). The laser system remained stationary during an experiment, while the burner was traversed perpendicular to the laser beams.

The Nd:YAG laser is a high power two stage system, with a separate oscillator and amplifier, to produce laser radiation at 1064 *nm* (infra-red). This is doubled through a crystal to yield a beam of visible light at 532 *nm* (green). Q-switching is used to obtain the required intense, narrow pulse. The dye laser produces broad band radiation for the Stokes beam at 600-610 *nm* (red/orange). The dye solution for the N_2

spectra was Rhodamine 640 (*Rh* 640) dissolved in a mixture of methanol and distilled water. For each measurement, when operating at 10 Hz, the laser produces a 15 *ns* pulse with up to 350 *mJ* at 532 *nm* and 35 *mJ* at 600-610 *nm*.

The measurement volume is determined by the zone of overlap of the intersecting laser beams (typically 1-5 mm). The length of the CARS control (or measuring) volume for the present CARS system, determined by Scott (1992), was 3 mm and an estimated measurement diameter 100 μm.

6.2.3 Modifications to the CARS system

The photo diode array camera used in previous experiments (Scott 1992) was replaced by a Charge Coupled Device (CCD) camera. This camera offered several advantages including higher resolution, increased dynamic range and a linear response to light (Rakestraw *et al.* 1989). The camera was a Princeton Instruments TE/CCD-512 system with an ST-130 controller interface. With the photo diode array camera, Scott (1992) had estimated the accuracy of temperature measurements in the range 1500 to 2000 K to be ± 30 K. With its replacement by the CCD video camera, the spectral noise was reduced (Scott 1992), and accuracy was estimated to be ± 25 K for temperatures above 1500 K.

A Dell Computers, System 433 with 16 Mb RAM and a 120 Mb hard disk drive was used in conjunction with the Harwell CARP-PC and QUICK-PC software to generate and match spectra. At a single measurement point in the flame, 200 individual spectra initially were recorded. This was reduced to 150 and then 100 in subsequent experiments, to speed up the measuring and processing time. To obtain temperatures from the experimental spectra, these spectra were matched to theoretical spectra at known temperatures. The accuracy of such a procedure depended upon the experimental technique and the data analysis. The computer code for the analysis of N_2 spectra was CARP-PC, with which a library of 20 theoretical spectra at known temperature and pressure were generated. Detailed matching with experimentally obtained spectra was performed with QUICK-PC. This was capable of reducing

analysis time by interpolating between the library of theoretical spectra, generated by CARP-PC, to find the best fit to measured spectra. Typically, two hours were required to process 200 spectra.

It was necessary to reject those measured spectra which were not theoretically well matched, possibly due to low signal/noise ratio or dust particles. The computer codes QUICK-PC provided an indication of the closeness of experimental to theoretical spectra by summing, over all wave numbers within the spectra, the square of their difference. In the current analysis, a spectrum was automatically rejected by the code for three conditions. First, if the sum of square failed to decrease, second, if the theoretical spectra library range was exceeded and third, if a maximum iterations of 150 had failed to produce a match. The number of accepted spectra varied from point to point. These values, after removing rejected data, together with the mean temperatures and standard deviation, are listed in Appendix B. Typically, about 50% of those spectra measured in the reaction zone were rejected. This fell to about 20% in the unburnt and burnt regions.

6.3 Instrumentation

6.3.1 Burner requirements

The general arrangement of the apparatus is shown schematically in Fig. 6.2 and photographically in Fig. 6.3. A multiple slot burner of sufficient length could provide symmetrical flame conditions, compatible with those of the computations. It was necessary to evaluate the velocity profile, so that it could be compared with modelling predictions. For the flame to be assumed two-dimensional, the length of the slot must be long compared to its width. This also ensured that the temperature field at the plane of measurement was not affected by any gas entrainment at the two ends. This arrangement also was ideally suited for CARS measurement in that the length of the measuring volume, which could be approximately 3 mm in the direction of the laser beams (Scott 1992, Bradley *et al.* 1992), could be aligned parallel to the slot and along

an isotherm. Fully developed parabolic flow was assured by a ratio of slot width to burner tube length of 3 : 50.

6.3.2 Features of the burner

The burner, shown photographically in Fig. 6.4 and sectioned in Fig. 6.5, had five slots of 50 mm length and 3 mm width in the horizontal plane. Measurements were made on the flame at the centre slot. The two adjacent slots created the symmetry boundary conditions, and the outer slots prevented air entrainment. The centre lines of the slots were pitched 3 mm apart. The burner was made up of five 6 mm thick brass plates, and a 3 mm thick endplate. It had been used in various research applications by British Gas. Air entrainment at the two ends was eliminated by shields of flowing nitrogen. During an experiment, the flow rate of nitrogen was so adjusted as to give the same mean flow velocity as that of the methane-air mixture.

Careful design attempts had been made to obtain uniform flow of the mixture through the burner. The required uniform flow pattern was progressively obtained through a number of modifications. The burner construction details are illustrated in Fig. 6.5. The 12 mm thick ceramic block had a rectangular cross section of 50 mm by 60 mm, and was packed with 1 mm diameter channels through its thickness. For ease of manufacturing, rectangular channels with cross sections of 1 mm by 3 mm, and a length of 20 mm, were machined in the slot plates.

The mixture entered the bottom of the burner via a number of rectangular openings cut in the otherwise sealed pipe. The flow pattern at this position, marked 'A' in Fig. 6.6, would be highly non-uniform. The mixture passed through the ceramic block packed with small straight holes. This block reduced the fluctuations in upstream pressure and flow velocity (position B). Additionally, the ceramic block acted as a flame trap should the flame flash back during an experiment.

A more uniform flow passed through another set of channels some 13 mm downstream. Flow uniformity was improved further by passing through these channels

(position D). There followed a length of 50 mm for the flow to fully develop above the burner (position E).

6.3.3 Burner modifications

Despite these attempts to obtain a uniform flow, preliminary tests revealed a very rough flame surface, with erratic flow patterns and obvious unequal flow rates at each end. This was accentuated at high flow rates (> 2 m/s). This was disappointing, not least because at this stage, it was not possible to re-design the burner. However, some modifications were possible.

A close inspection of the flow patterns (Fig. 6.6) suggested a longer development length was required. To this end, a square sectioned steel tube of 195 mm length, (C) on Fig. 6.7, was inserted between the ceramic block (B) and the upper body (D). These provided an extra 195 mm length for the flow to develop. As illustrated in Fig. 6.7, a more uniform, roughly parabolic, flow profile could now be expected at the end of the tube (C). Downstream of the rectangular channels (D), equalisation of the pressures and velocities at the centre and the two sides generates small 'ripples'.

At low flow rates, the amplitude of these ripples was small, and was effectively zero at the burner exit (E), where it remained reasonably flat. However, at moderate flow rates (~ 1 m/s), the amplitude of the ripples at position D was large and ripples of unacceptable amplitude were observed at the exit (E).

The task was now to remove or reduce the magnitude of the ripples generated at position D. Of the various remedies tested, (e.g. inserting glass or steel balls of various sizes) the most successful involved wire mesh. Two layers of very fine wire meshes, with approximately 0.3 mm pitch, 3 mm apart, were placed at position D perpendicular to the direction of flow. They were effective in reducing the magnitude of the ripples, which only became visible at the much higher flow velocity of 4 m/s.

6.3.4 The burner

The burner was mounted so that the laser beams ran parallel to the slots. This was to locate the longer dimension of the CARS control volume along the slots, and achieve a better spatial resolution on the two-dimensional plane perpendicular to the slots. The burner was mounted on an independent traversing table. Traversing was possible in all three directions. Movements were measured by three independent dial gauges with an accuracy of $\pm$ 0.01 mm. Before an experiment began, it was necessary to create a measurement datum. A convenient one was the lowest position along the axis of symmetry, as indicated in Fig. 6.8. During the setting up procedure, the horizontality of the burner was checked with a spirit level, and adjusted by means of packing where necessary.

To set the vertical reference position, a non-reflective ruler was placed on top of the burner (Fig. 6.9a), with the laser switched to a low intensity setting. The vertical datum was determined by traversing the burner vertically such that only half of the slightly out-of-focus laser beam appeared on the ruler. To locate the vertical alignment, with the ruler still in position, the burner was traversed along the path of the laser beams. If the laser beam image on the ruler did not move horizontally, the burner was assumed to be aligned with the laser beam (Fig. 6.9b). To set up the horizontal reference position, the distances of the laser beam image to the two edges of the burner were measured. The burner was traversed horizontally until these distances were equal and the image of the laser appeared at the centre (Fig. 6.9c). The laser beams could not be focused on an edge of the burner as two of the beams were impeded (Fig. 6.9d). Surface temperatures were measured with a thermocouple touching the top surface of the centre burner tube. They were monitored periodically, and the steady values for the various flows are given in Table 6.1.

Table 6.1

Measured steady burner tube temperatures for various mixtures and flow conditions.

ϕ	v_m (m/s)	Burner tube temperature (K)
1.0	2.0	353
1.0	1.2	356
0.84	2.0	334
0.84	1.2	339
0.84	0.6	343
0.75	1.2	318
0.65	1.2	309

6.3.5 Mixture supply

Independent flow control systems were used for fuel and air, with precise control of both gases. Figure 6.10 illustrates schematically the mixture supply system, with independent flow monitoring and control. Compressed pure methane (99.995% purity) from the British Oxygen Company was used in bottled form. During an experiment, the reduced cylinder pressure was monitored by a pressure gauge. An on/off valve also was provided in this supply line. Downstream, the required pressure was accurately maintained with a dome valve (pressure controlling valve) and monitored by a pressure gauge. Further downstream, a metering orifice was installed. The volumetric flow rate was calculated from the pressure drop across the orifice, measured by a water or mercury manometer. Orifice plates of different diameters were available and were selected according to the flow rate. The upstream density was obtained from the corresponding pressure and temperature. Upstream pressure was measured by the pressure gauge, while upstream temperature was assumed equal to room temperature. The required flow rate was obtained by a control valve located further downstream, with fine adjustment provided by a needle valve.

The volumetric flow rate Q was calculated with the expression :

$$Q = \frac{C_o}{\rho_d}\sqrt{\rho_u H} \tag{6.1}$$

where C_o Orifice constant, obtained by calibration,

H Differential pressure head,

ρ Density of gas.

Subscript u refers to upstream conditions, and subscript d to downstream conditions. The orifice constant is configuration dependent, and was calibrated for the flow metering system, by plotting flow rates Q, obtained by measuring the gas, methane or air, volume with a wet drum meter at a given time, against $\sqrt{\rho_u H}/\rho_d$. Any derivation of pressure and temperature from the calibration condition was corrected by application of the ideal gas law. The room (downstream) temperature and pressure were measured just before the start of the experiment. These two measurements enabled the downstream gas density to be determined. The upstream pressure was maintained by the dome valve.

The air supply was very similar to that for the fuel, in that the flow rate was controlled by two valves, and measured by a similar orifice and manometer. Upstream pressure was also maintained by a dome valve. Air, however, was supplied from a compressed air line from the central system. A drying tube was provided to remove any moisture and lubricant in the air line. Compressed nitrogen, for eliminating air entrainment (Fig. 6.5), also was supplied from a gas bottle. Its volumetric flow rate was monitored by a rotameter, and the upstream pressure maintained at the valve. During an experiment, the flow rate was adjusted to give the same velocity as that of the methane-air mixture at the burner exit.

The required mixture stoichiometry was achieved by controlling the individual flow rate of methane and air. Flow velocities at the burner exit were calculated by dividing the estimated total volumetric flow rate by the total cross section area of the five slots. This method assumed equal distribution of flow among all five slots for which the burner had been designed. It would have been preferable if time had been available to make independent anemometry measurements.

6.4 Test Procedure

Before an experiment, the following procedures were followed :

1. Room temperature and atmospheric pressure were measured, and the manometer height was calculated according to Eq. 6.1 to give the flow rate.
2. The CARS background light level was measured, with the Stokes beam blocked to inhibit CARS signal generation. This value was then subtracted from all experimental spectra.
3. The burner attained a steady state, monitored by the thermocouple temperature measurements. This typically took around fifteen minutes.

In general, temperature measurements for a particular set of conditions required approximately four hours, with measurements being taken continuously.

6.5 Experimental Results

6.5.1 Photographic observations

The influence of two major variables was investigated, namely the stoichiometry and flow rate. Photographs were taken for equivalence ratios of 0.6, 0.75, 0.84 and 1.0, and mean inlet velocities of 0.6, 1.2, 2.0 and 4.0 m/s. Unfortunately, the lean mixture ($\phi = 0.6$) at a mean inlet velocity of 1.2 m/s became unstable during the CARS measurements. These were subsequently abandoned. Furthermore, erratic flow profiles observed at 4.0 m/s precluded accurate CARS measurements at that flow rate. CARS temperatures were, therefore, obtained for mixtures with equivalence ratios of 0.75, 0.84 and 1.0, and mean inlet velocities of 0.6, 1.2 and 2.0 m/s. Flame photographs showed flames to become unstable with increasing flow rates and leaner mixtures. The flames of greatest length tended to have a rough surface.

In order to investigate the influence of mixture and flow rate on flame structure, a number of photographs were taken. For an average inlet velocity of 1.2 m/s, Fig. 6.11 illustrates the front (a - d) and corresponding side views (e - h) of flames with different

equivalence ratios. It is clear that, with increasing equivalence ratios, flame height decreases, associated with an increase in burning velocity. With decreasing flame height, the flame surface area becomes smaller, and the flame becomes more intense and stable. This reduction in flame height with increasing equivalence ratio confirms the general trend obtained computationally (Figs. 5.36-5.38), while the increase of burning velocity is in agreement with the findings in Chapter 7.

With increasing flow rate, Fig. 6.12 shows the front (a - d) and side views (e - h) of lean (ϕ = 0.84) methane-air flames. These photographs illustrate that, with increasing flow velocity, flames become progressively taller. This is explained by the fact that for this burner configuration, the burning velocity remains almost constant. At higher flow rates, there is an increase in magnitude of the negative stretch at the flame tip and this results in an increase in burning velocity. There is also an increased positive stretch at the base, which results in a decrease in burning velocity. Consequently, a larger flame surface is required to burn the increased flow. It is also to be noticed that, at high flow rates, the magnitude of the ripple at the flame surface is increased. This is probably a consequence of the flow system rather than the behaviour of the flame itself.

In the present study, the mean flow velocity at the burner exit is calculated by assuming a uniform distribution of flow over the five slots. From the side views in Fig. 6.12 (b, d, f, h), it would appear that this assumption is not entirely warranted, as the inner flames have different heights and the outer ones have lifted outer edges. A remedy would be to redesign the burner to provide separately controlled mixtures to each slot, but this was not possible within the time constraints of this experimental programme. Another remedy would have been to measure the velocity profiles directly by Laser Doppler Velocimetry, but again time was not available. Hence, velocities were estimated on the assumption of uniform flow to each slot.

6.5.2 CARS thermometry measurements

The measuring and processing of CARS spectra was a lengthy procedure, and hence the number of readings was limited. It was decided to concentrate measurements

in the reaction zone where rapid changes of temperature occurred. Relatively few measurements were taken in the preheat and burnt gas zones, where the temperature remained almost constant. However, although the recorded spectra were displayed simultaneously on the computer monitor, it was only possible to estimate temperatures very approximately from such spectra, prior to full processing. Inevitably, some measurements were stopped before the traverse into the burnt zone had been completed.

All the measured temperatures are tabulated in Appendix C, in which the range of matched temperatures and the standard deviations also are given. The scatter is greatest in the reaction zone, where cold and hot gas might possibly co-exist within the measurement volume. Under these conditions, the apparent CARS temperatures is weighted to the lower value. More detailed statistical analysis, preferably separately applied to measurements obtained in the three zones, might reduce the scatter in the measurements. However, this was beyond the time limit allowed for the present thesis.

Measurements shown that the set-up reference position (Fig. 6.8) did not always lie on the centre line of the slot. This is shown in Fig. 6.13 by the temperature contours for 1000 K (representative of the position of the reaction zone). The zero position in Fig. 6.13 represents the set-up reference position. In two cases ($\phi = 0.84$, $v_m = 1.2$ m/s and $\phi = 1.0$, $v_m = 1.2$ m/s) measurements were made before the problem of misalignment had been recognised and only half the flame was mapped. By noting the relative centre position from Fig. 6.13, the centre position of the axis of symmetry was found and appropriate compensation made. It was not possible to focus the laser beams in regions closer than 0.6 mm from the burner slot vertically, because of obstruction by the slot (Fig. 6.9d). Unfortunately, this is an important region for flame stabilisation and the identification of the thermal boundary conditions.

The burner tube temperature was an important parameter, in controlling the flame. It is important for validation of the model that the modelled and experimental temperatures be the same. Earlier computations were based on a burner tube temperature of 290 K. This value exaggerated the heat loss to the burner tube, as a low

tube temperature gave rise to large temperature gradient and heat flux. This showed the importance of experimental measurements. The thermocouple temperatures were monitored periodically, and the steady values for the various flows are given in Table 6.1. In general, for leaner mixtures and higher flow velocities, the temperatures were relatively low, indicating relatively smaller amounts of heat loss to the burner tube, due to the lower heat release for lean mixtures and the larger flame lift off height at the higher flow rate (section 5.4.4).

6.6 Comparison of the Experimental Results with Model Predictions

6.6.1 Matching of flame heights

When selecting a condition, it was natural to chose a computed condition that was compatible with an experiment. However, it was soon realised that the computed flame heights were different from those measured. Photographs (Figs. 6.11 and 6.12) revealed that the three centre flames all had slightly different flame heights and that the two outer flames were lifted. This suggested that the flow was not equally distributed across the five slots. This was a set back that, as already explained, could not be remedied.

In order to make comparisons with computed predictions, the measured burner tube temperatures (Table 6.1) were used in the computations as a boundary condition, and computed results were selected which gave the same flame heights as those measured. The matching of flame height was achieved by selecting an inlet flow velocity for the mathematical model at the same equivalence ratio. Details of the different velocities are presented in Table 6.2.

Table 6.2

Velocities used for flame height matching.

ϕ	v_{exp} (m/s)	v_{comp} (m/s)	Flame Height (mm)
0.75	1.2	1.5	13.1
0.84	0.6	0.9	5.4
0.84	1.2	1.4	8.6
0.84	2.0	2.0	12.2
1.0	1.2	1.3	6.4
1.0	2.0	2.0	8.9

Here, v_{exp} and v_{comp} represent the mean experimental and computed inlet velocities, respectively. Flame height was defined as that of the 1000 K isotherm above the burner at the axis of symmetry. The flame heights were those measured, and the computed ones were within 0.2 mm of these. The Table shows that greater discrepancies occurred with the leaner mixtures and the lower flow rates. The computed and measured burner tube temperatures were those given in Table 6.1.

6.6.2 Comparison of results

The computed and measured two-dimensional temperature contours are compared in Figs. 6.14 to 6.18, whereas Figs. 6.19 to 6.24 give a more detailed comparison on a point by point basis, in the form of temperature against height above burner plots, for different horizontal distances from the axis. The horizontal distance and height above the burner are defined in Fig. 6.8.

6.6.2.1 Flame shape

Comparisons of flame shapes are best visualised with the two-dimensional isotherms shown in Figs. 6.14 to 6.18. Due to the limited spatial resolution of the measurements, some degree of waviness is observed on the interpolated measured isotherms. The figures, nevertheless, show good agreement between computed and

measured flame shapes. A small zone near the base was excluded in the measurements because it could not be accessed by lasers beams (Fig. 6.9d).

6.6.2.2 Burnt temperature

Significant differences were observed between predicted and measured burnt gas temperatures. These differences, to some degree, were dependent on the flow rate and equivalence ratio. A comparison is presented in Table 6.3. For the measured burnt temperature, the maximum temperature in the result set was used. Computed temperature at the corresponding position yielded the computed burnt temperature (T_{comp}). The maximum and minimum temperature were taken from those temperatures obtained by spectra matching, the mean temperature and standard derivation, δ, also were obtained from the measured temperatures.

Table 6.3

Comparison of measured maximum and computed temperatures.

ϕ	v_m (m/s)	T_{comp}	T_{mean}	x (mm)	y (mm)	T_{max}	T_{min}	δ (K)	N_T	N_a
0.75	1.2	1835	1630	0.20	14.00	1810	1430	79.5	100	87
0.84	0.6	1850	1673	0.00	6.00	1883	1476	89.6	200	151
0.84	1.2	1970	1754	0.00	10.00	2024	1488	93.7	200	114
0.84	2.0	2010	1906	0.00	15.00	2067	1623	77.1	150	109
1.0	1.2	2140	1934	0.20	8.00	2120	1712	70.8	200	148
1.0	2.0	2140	2072	0.00	11.00	2252	1803	88.7	100	85

In the Table, x denotes the horizontal distance and y the height above burner. T_{mean} is the calculated mean temperature, in K, while T_{max} and T_{min} are the maximum and minimum measured temperature in K, obtained from the accepted CARS spectra. The standard derivation of the temperature measurements is given by:

$$\delta = \sqrt{\frac{1}{N_a}\sum_{i=1}^{N_a}(T_i - T_{mean})^2} \qquad (6.3)$$

where N_a is the number of accepted spectra readings, N_T is the number of total spectra obtained in the experiment, and T_i is the ith temperature reading. As shown in the Table, although the differences between the computed and the measured mean temperatures are significant, the value of δ is about 80 K. The scattering, though mainly due to the fluctuations in CARS measurements, might also partially result from flow fluctuations.

It is unfortunate that more measurements were not obtained downstream. The computed burnt temperatures were close to the adiabatic flame temperature, suggesting some heat loss to the burner. On the other hand, the measured burnt temperatures were substantially lower than the adiabatic, indicating significantly more heat loss in the experiments. The values of the computed heat loss depend on the accuracy of the measured burner tube temperature and this might have been insufficient to designate the heat loss accurately. The material of the burner was brass and heat would rapidly be conducted from the surface.

Another source of error might arise from the heat loss by radiation, as this was not included in the mathematical models. Its effect, however, is believed small. As a result of a quite separate study, Dixon-Lewis (1995) has suggested radiative heat loss might result in a reduction of final gas temperature of approximately 20 K in a stoichiometric methane-air flame.

6.7 Summary

In summary, there is generally good agreement between computed and measured temperatures. In general terms, the computed flame structure has been validated. There does, however, appear to be some difficulty in accurately computing the heat loss from the gases to the burner.

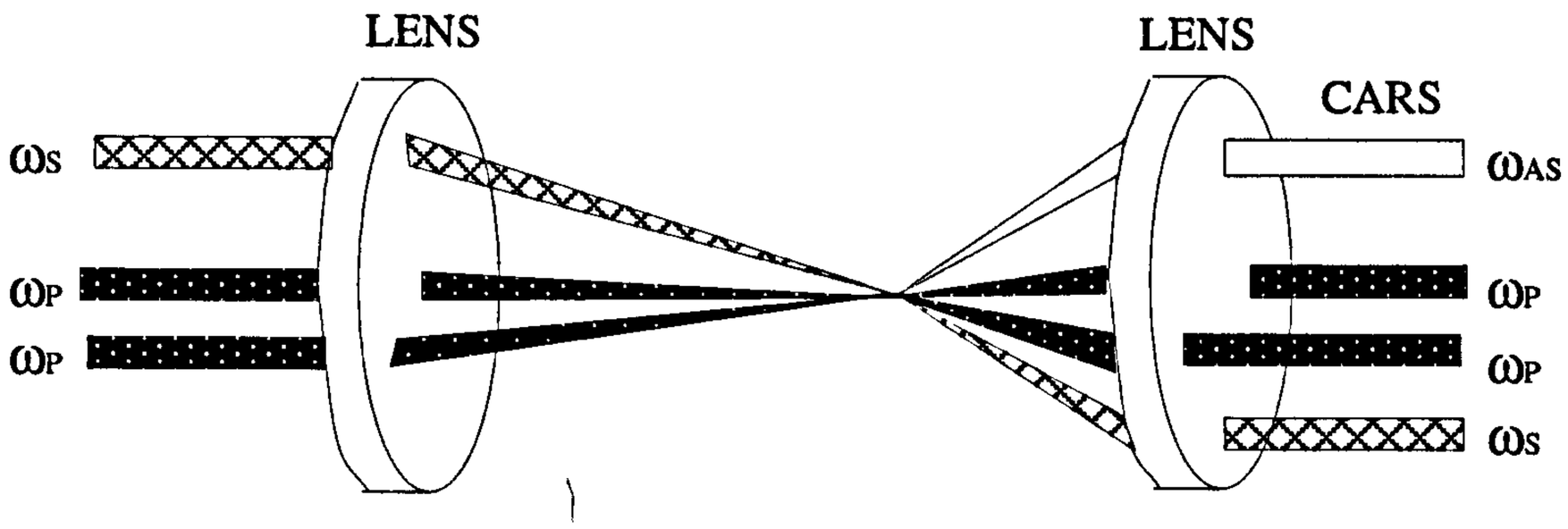

(a) Laser beam crossing geometry

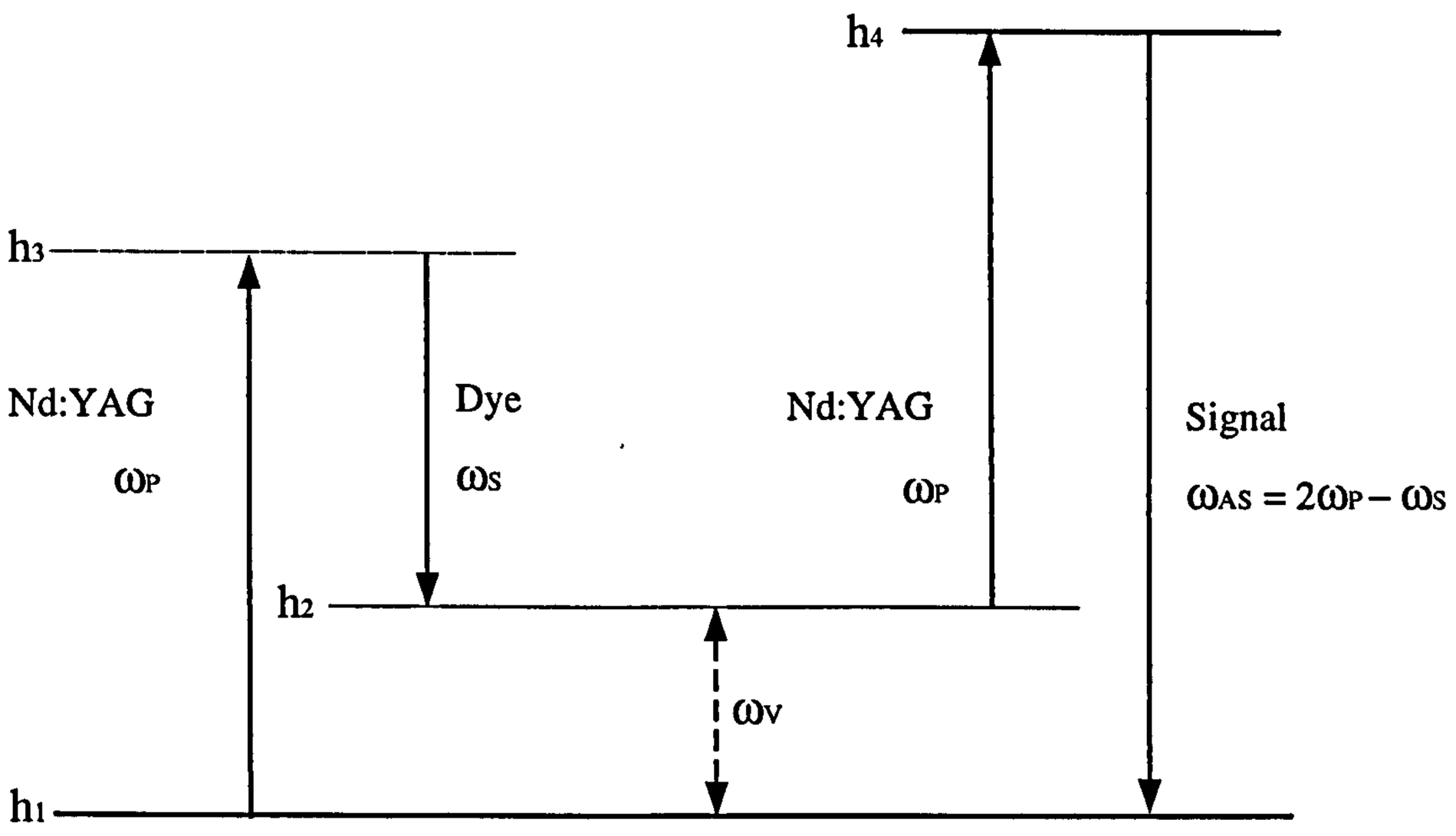

(b) Energy Level diagram

Fig. 6.1 Theory of Coherent Anti-Stokes Raman Spectroscopy.

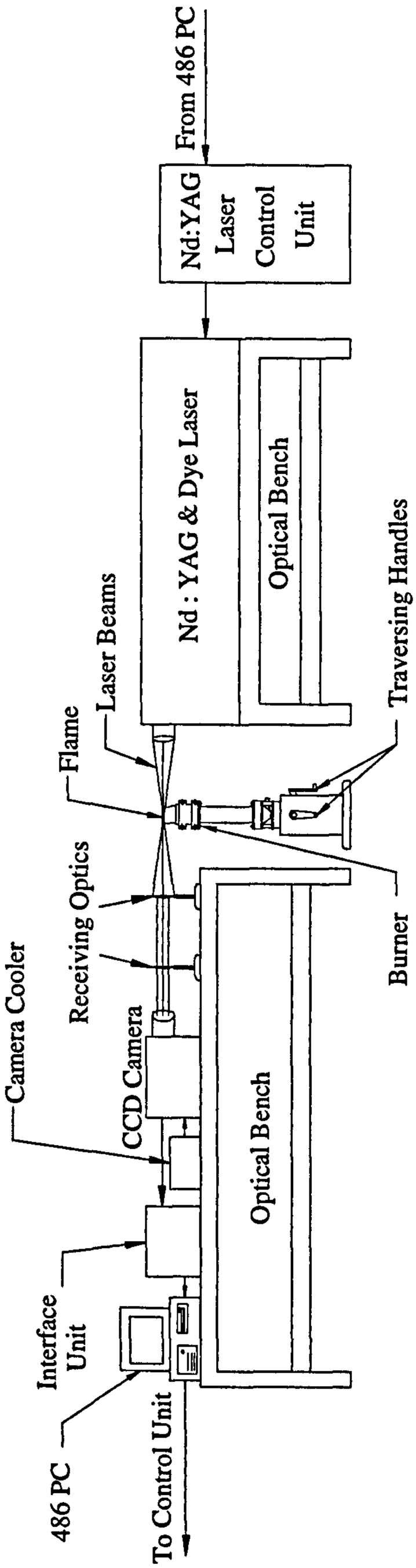

Fig. 6.2 Schematic diagram of the CARS rig.

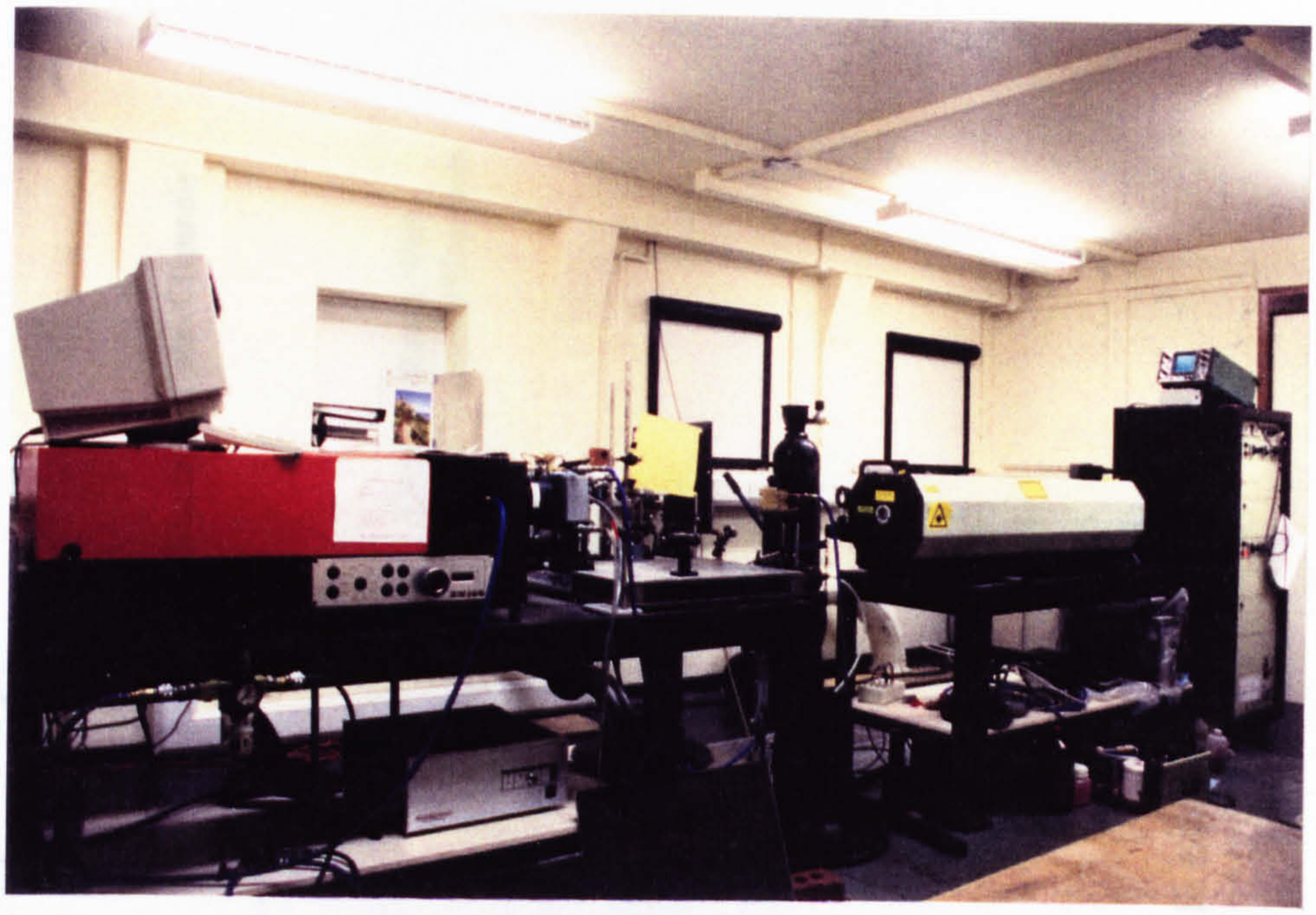

Fig. 6.3 Photographic view of the CARS rig.

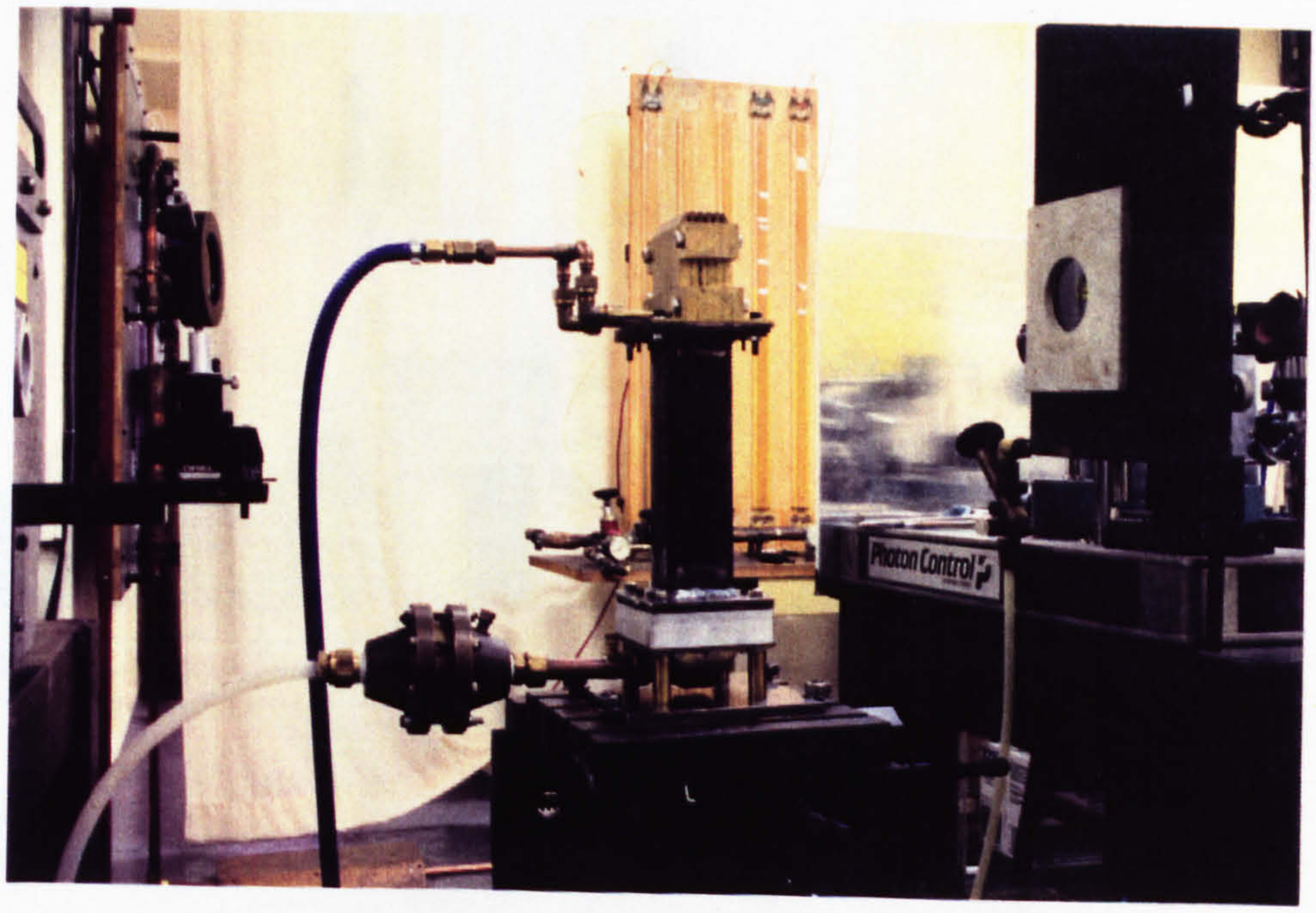

Fig. 6.4 Photographic view of the slot burner.

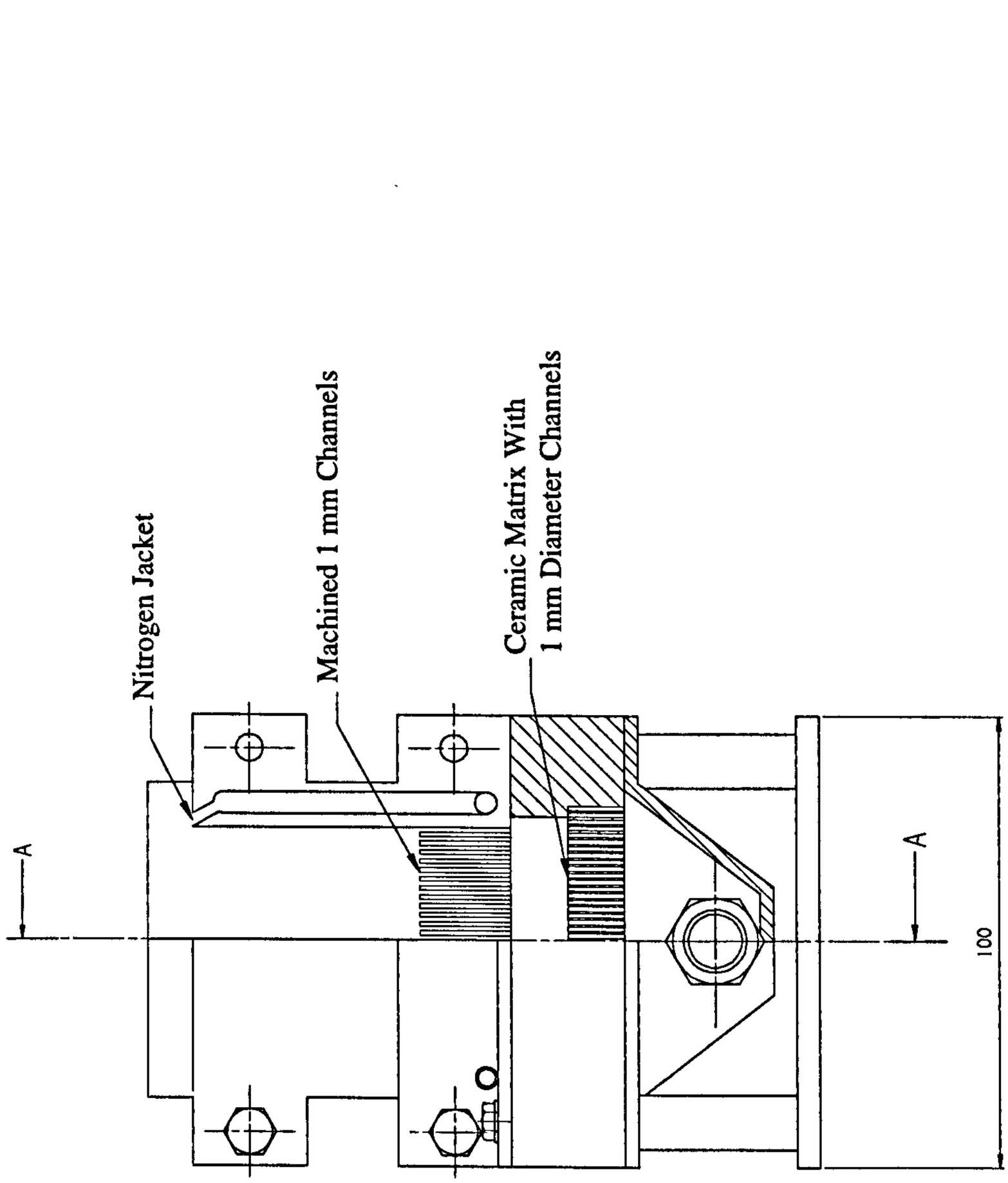

Fig. 6.5 Assembled British Gas slot burner.

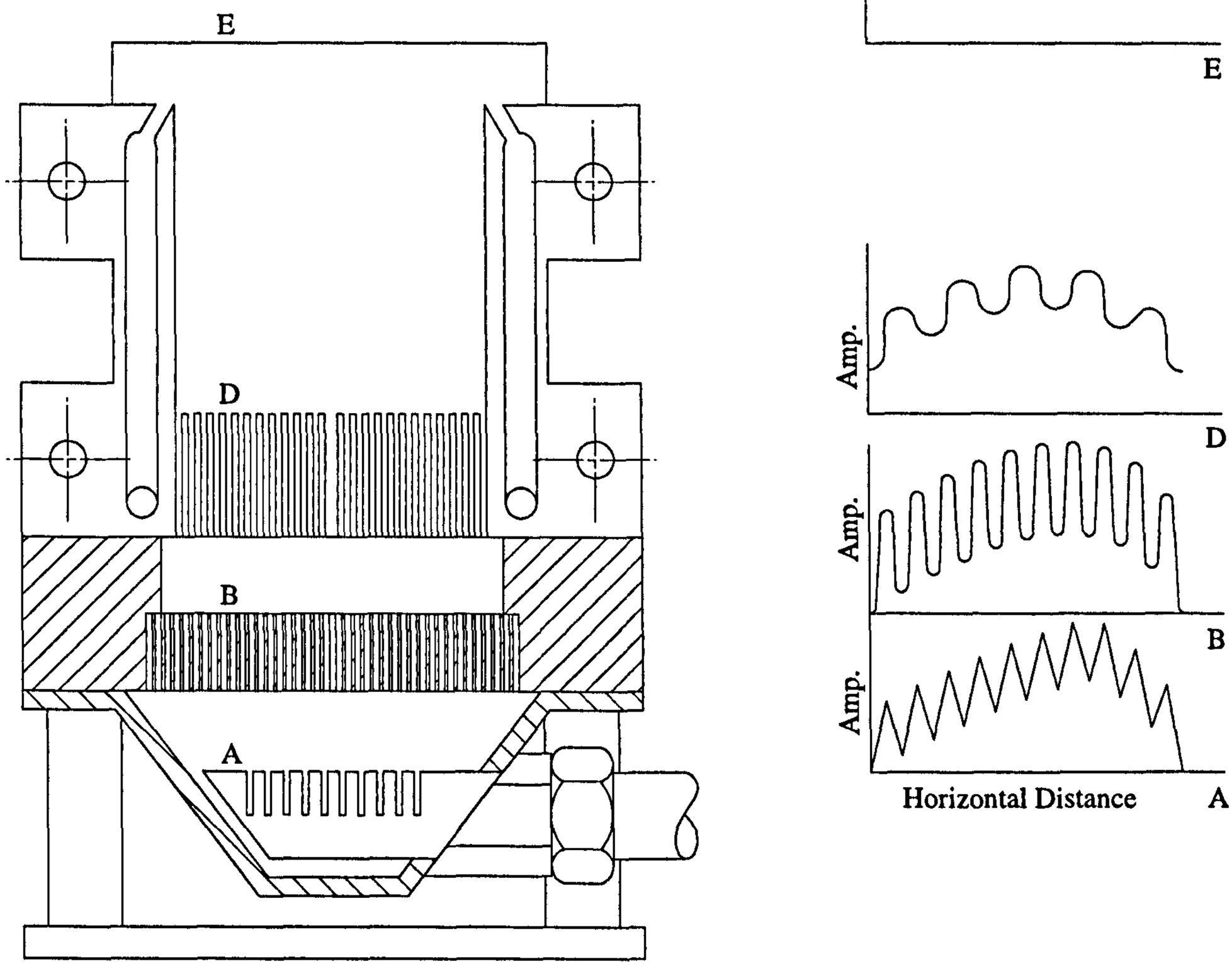

Fig. 6.6 Flow patterns at various positions (A, B, D and E) of the slot burner.

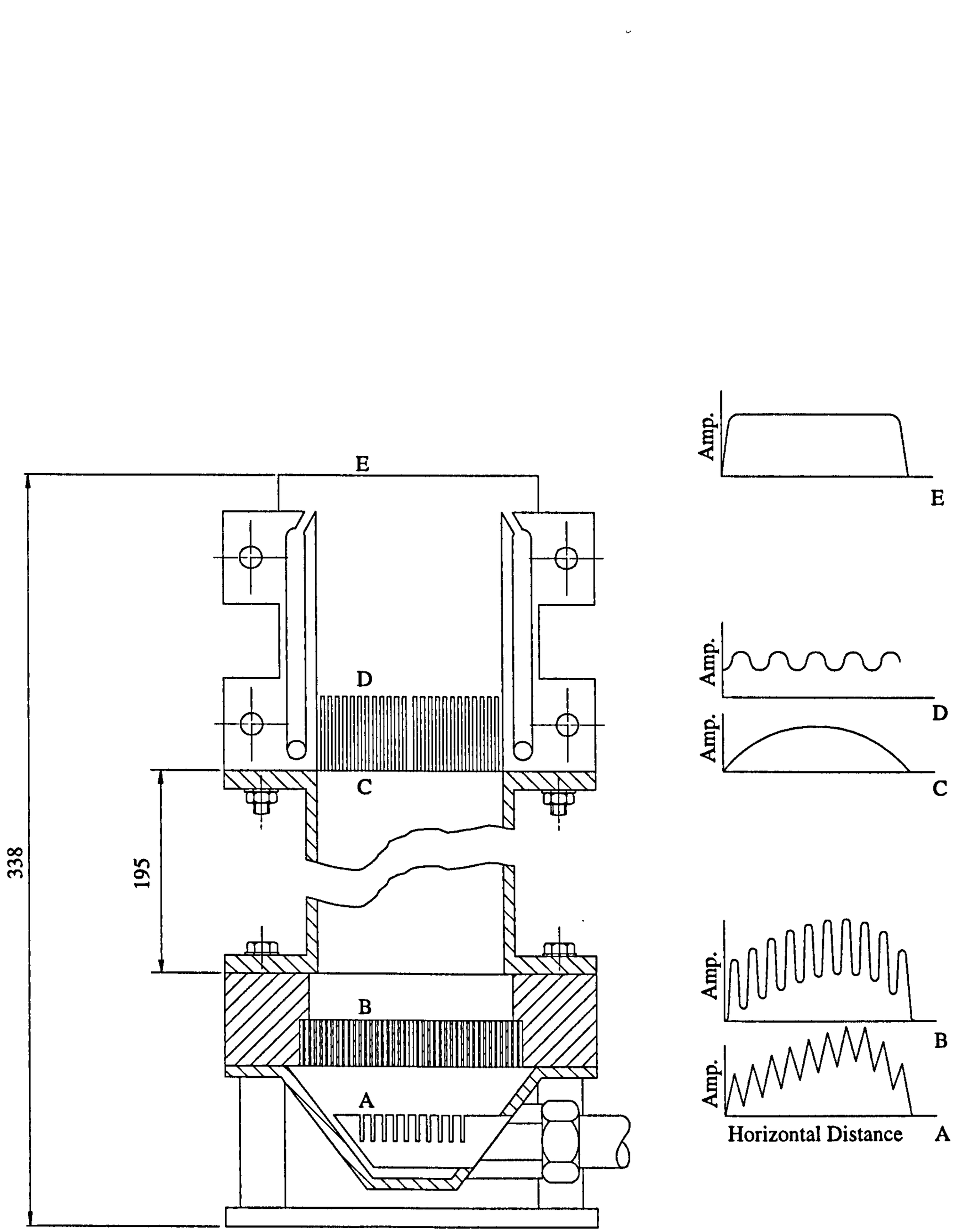

Fig. 6.7 Modified slot burner with improved flow patterns at outlet E.

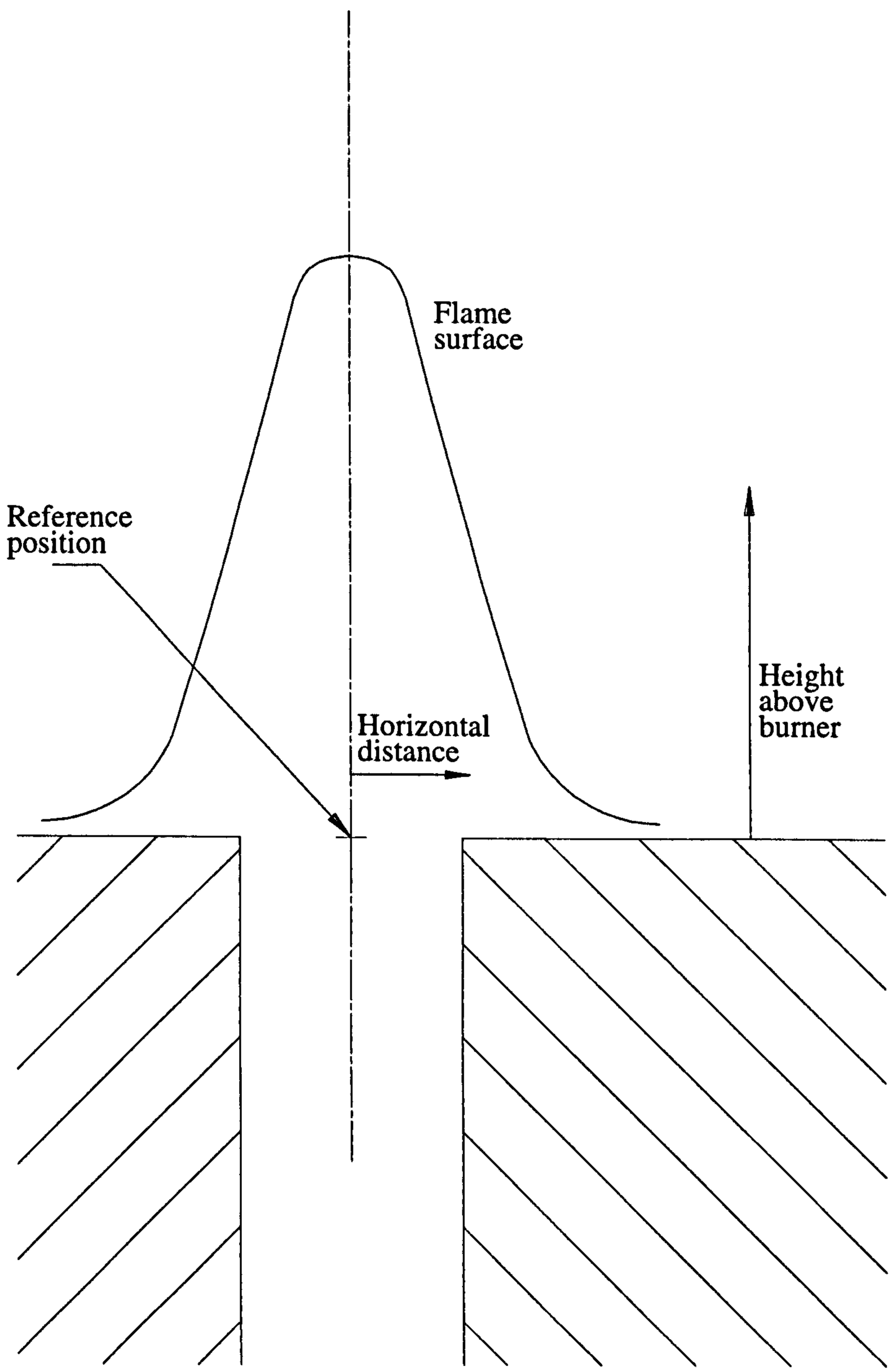

Fig. 6.8 Nomenclature and reference position for burner.

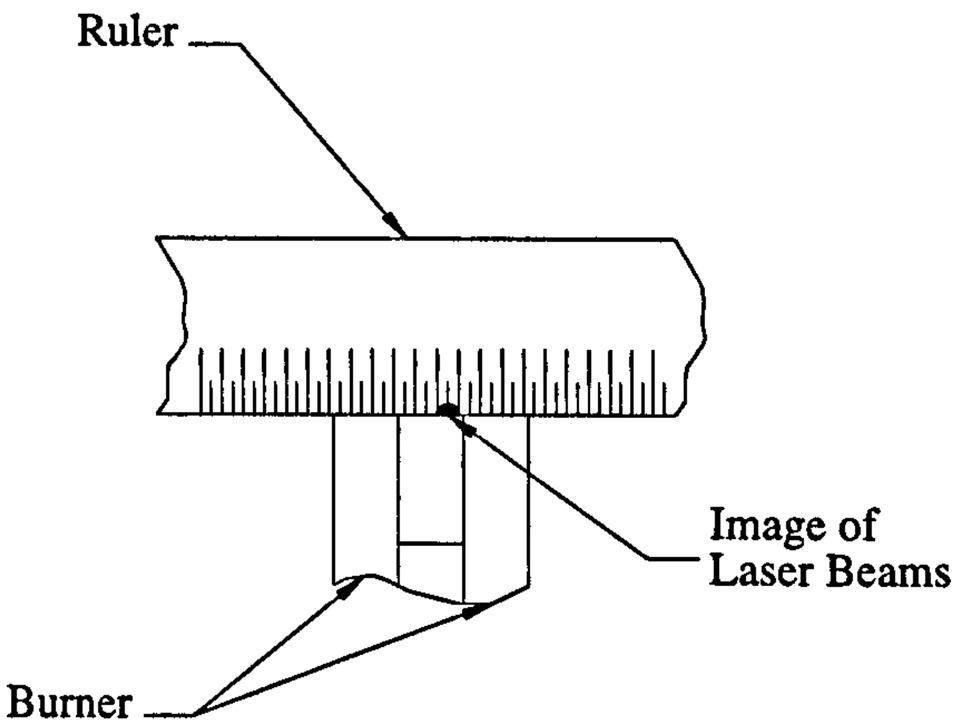

(a) Vertical Reference

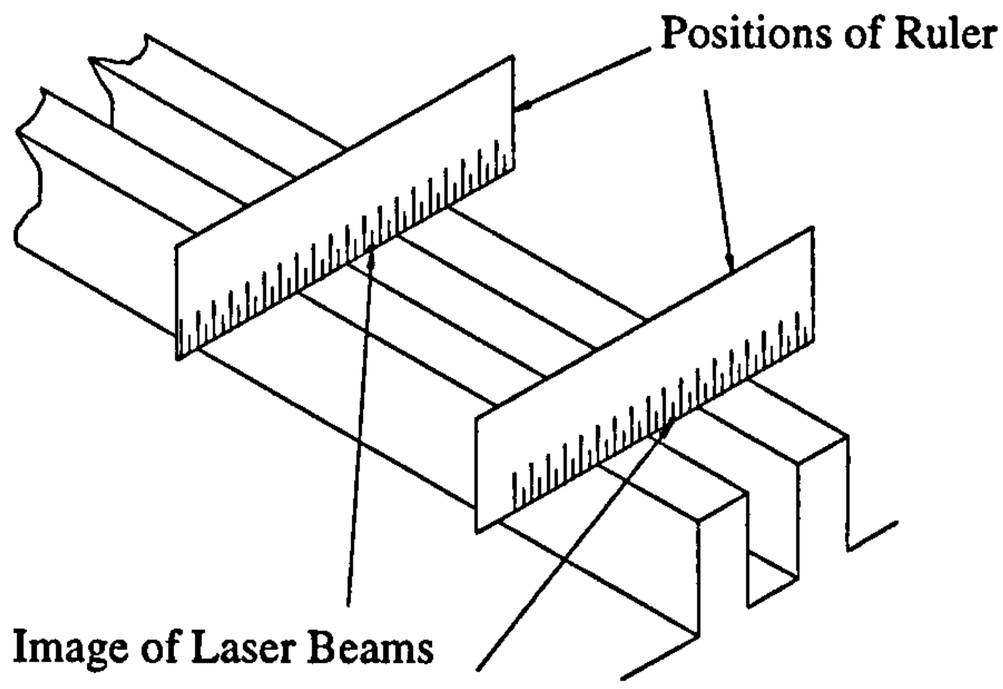

(b) Axial Alignment

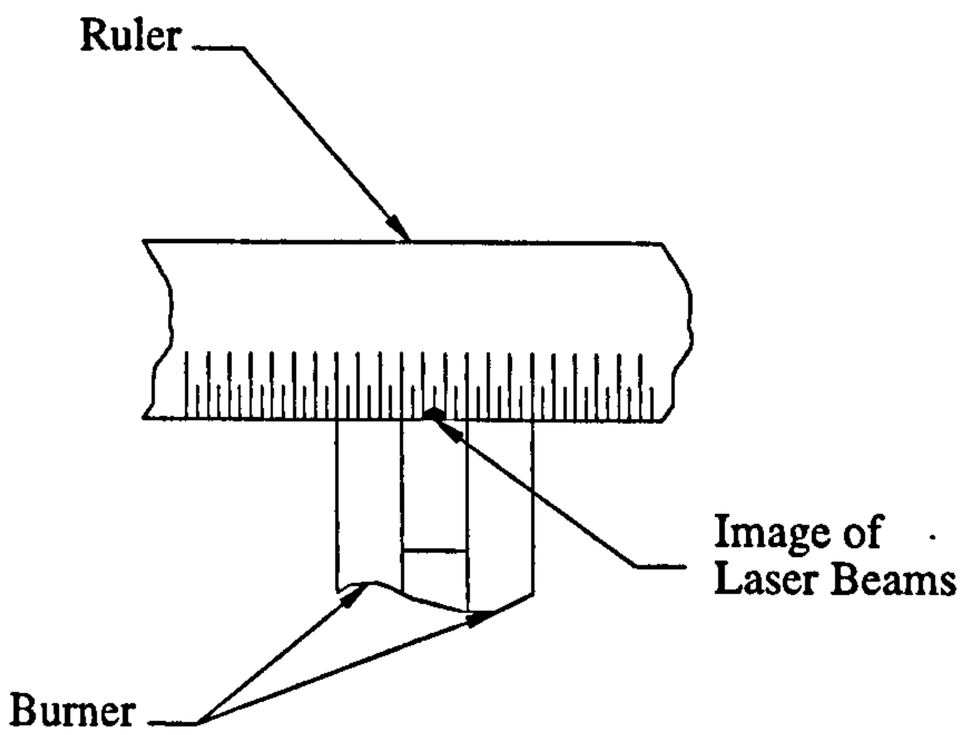

(c) Horrizontal Reference

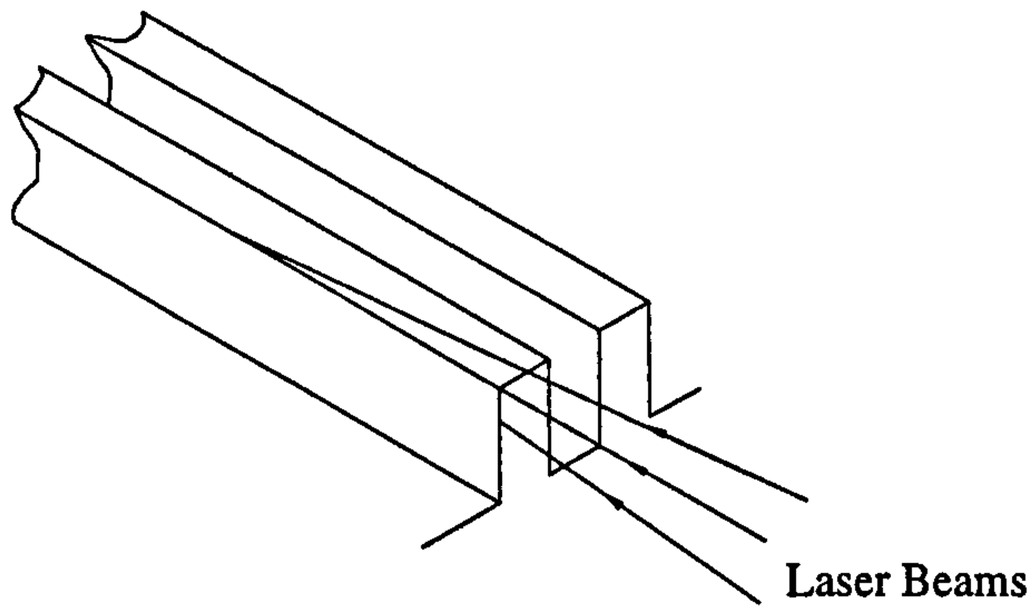

(d) Focus Problem

Fig. 6.9 Location of beams for CARS measurement.

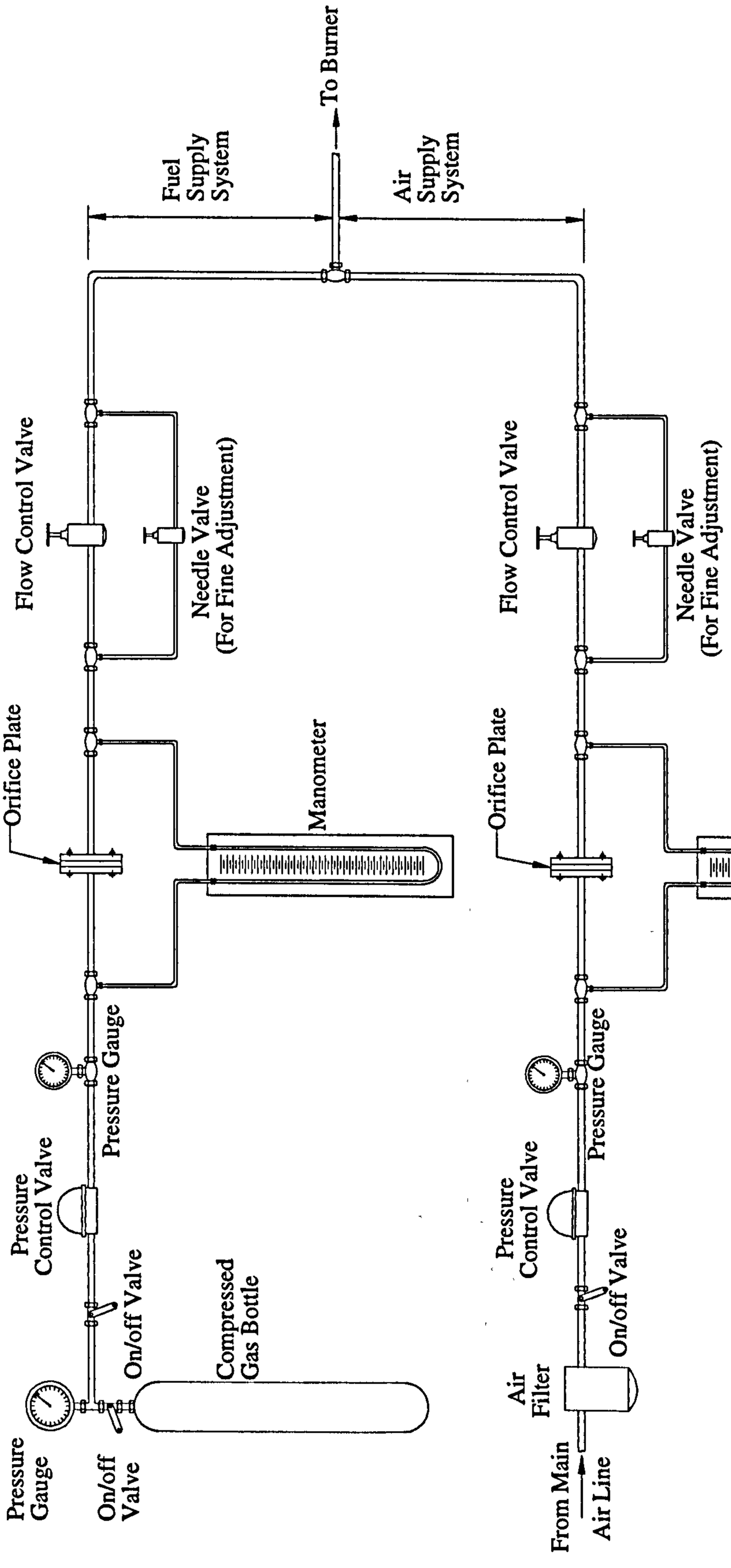

Fig. 6.10 Mixture supply system.

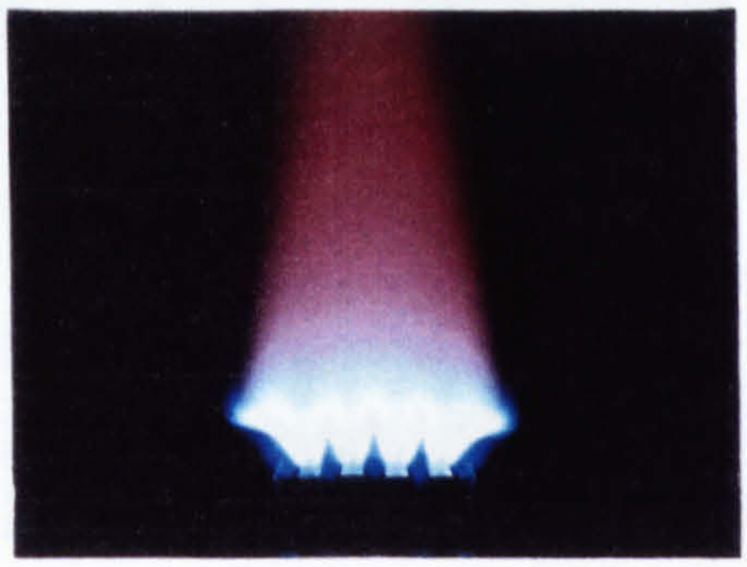

(a) $\phi = 1.0$

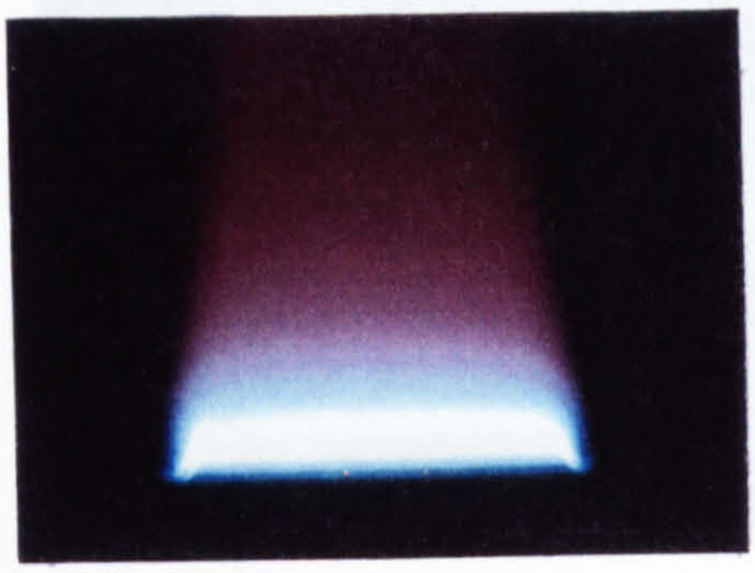

(e) $\phi = 1.0$

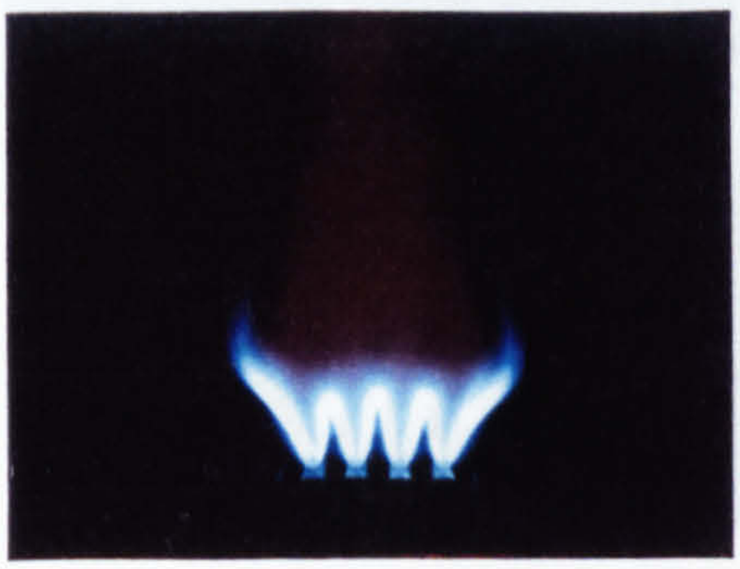

(b) $\phi = 0.84$

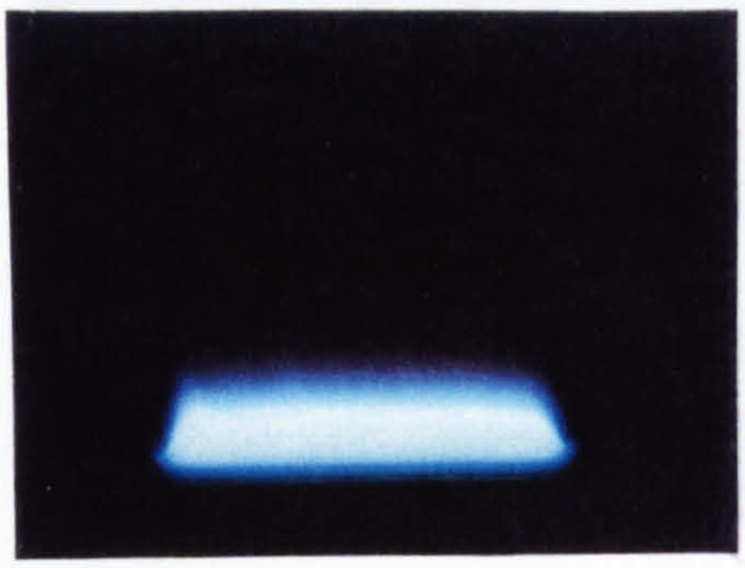

(f) $\phi = 0.84$

(c) $\phi = 0.75$

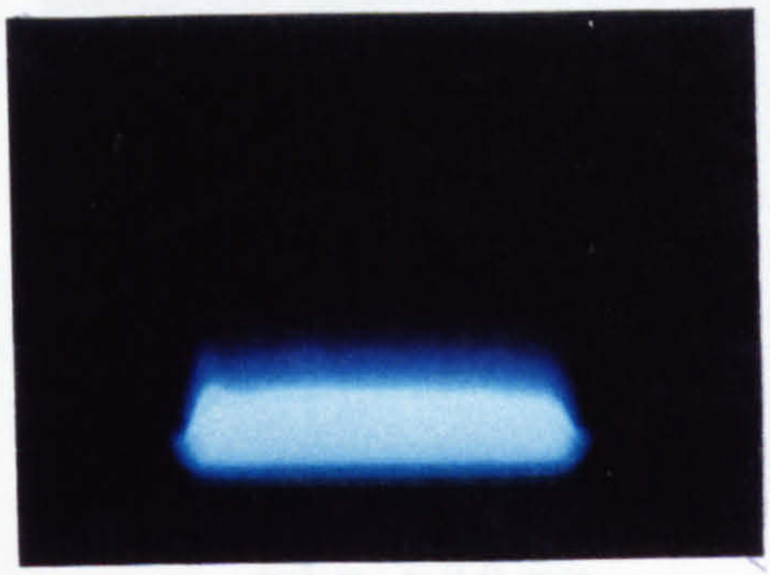

(g) $\phi = 0.75$

(d) $\phi = 0.6$

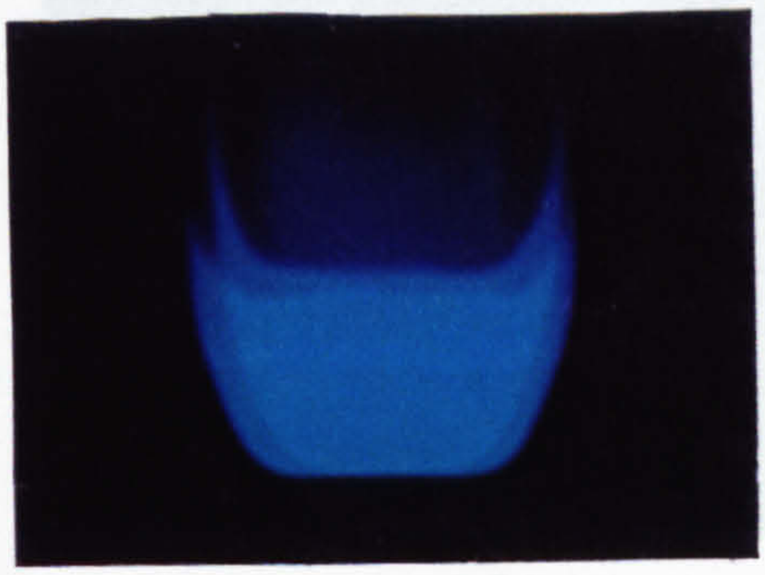

(h) $\phi = 0.6$

Fig. 6.11 Variation of flame shape with equivalence ratio for a given inlet velocity (v_m = 1.2 m/s).

(a) v_m = 0.6 m/s

(e) v_m = 0.6 m/s

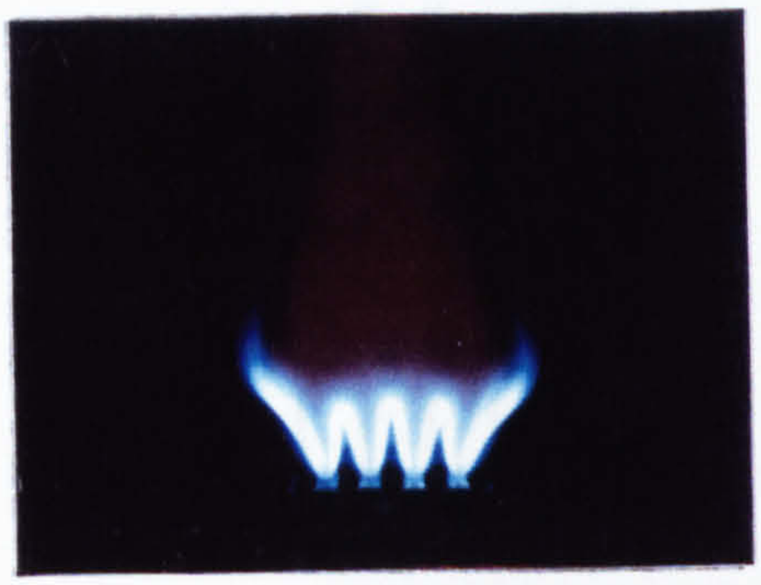

(b) v_m = 1.2 m/s

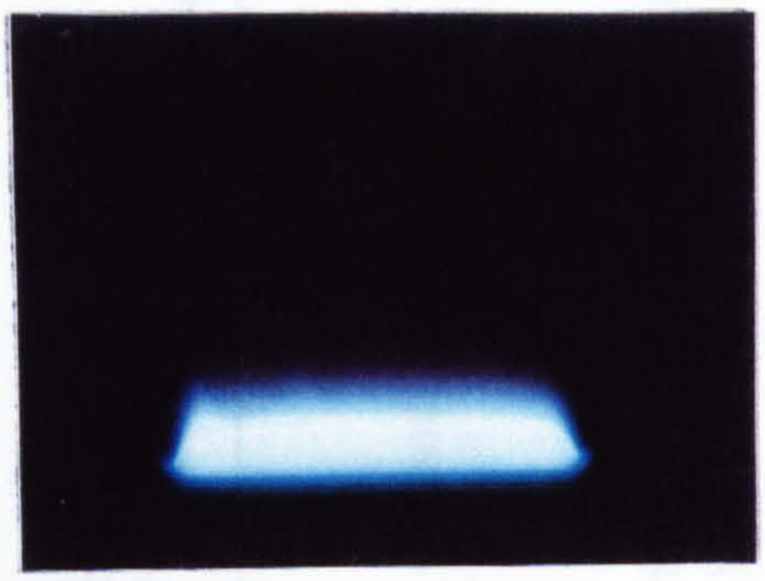

(f) v_m = 1.2 m/s

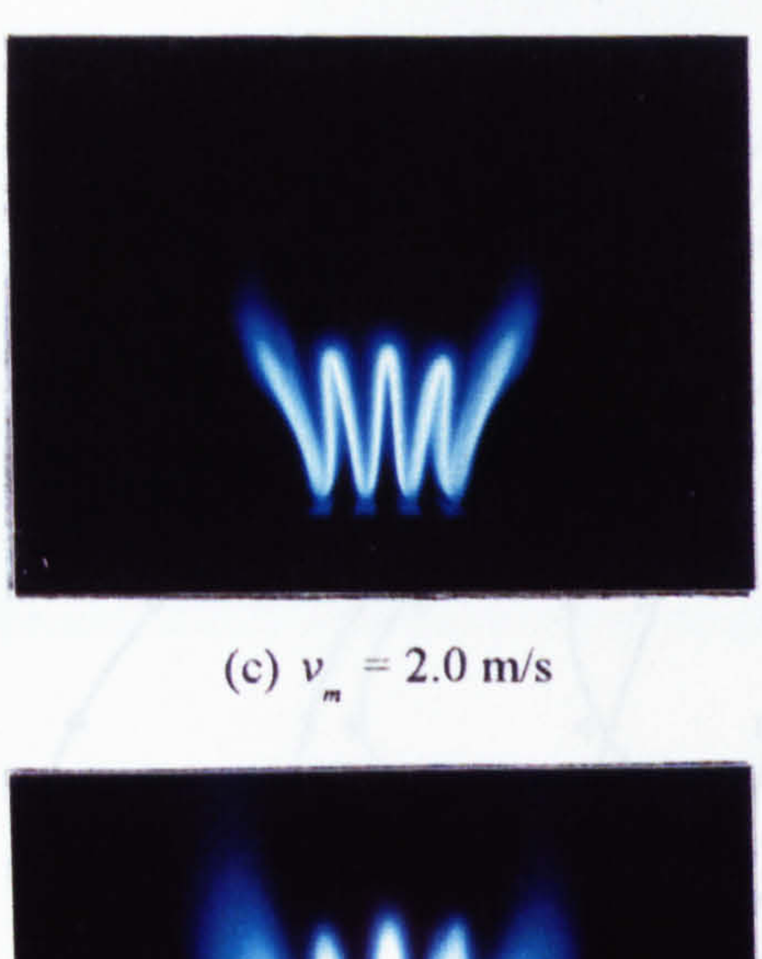

(c) v_m = 2.0 m/s

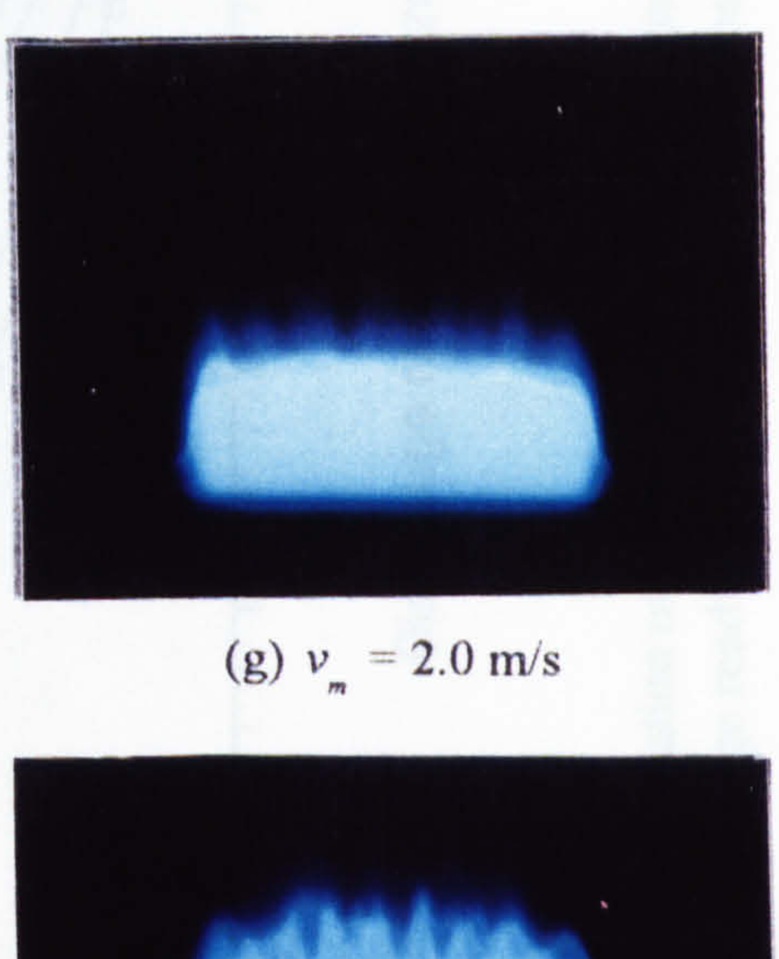

(g) v_m = 2.0 m/s

(d) v_m = 4.0 m/s

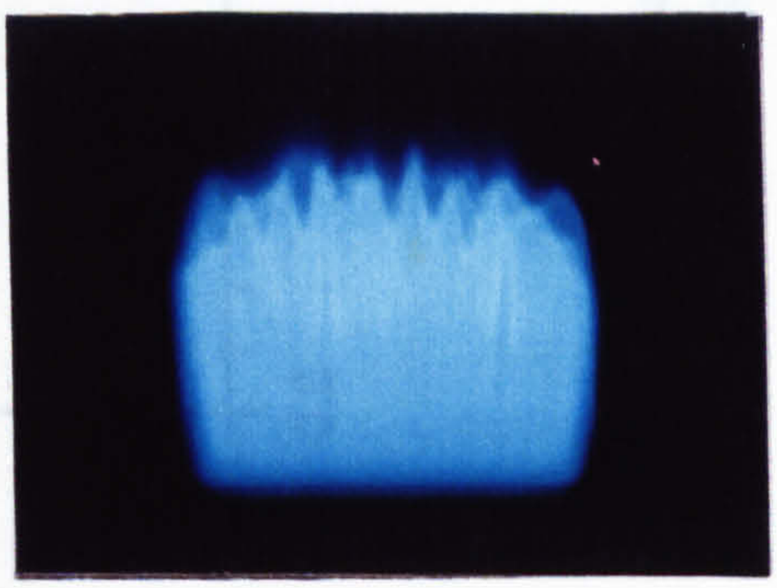

(h) v_m = 4.0 m/s

Fig. 6.12 Variation of flame shape with flow rate for a given mixture (ϕ = 0.84).

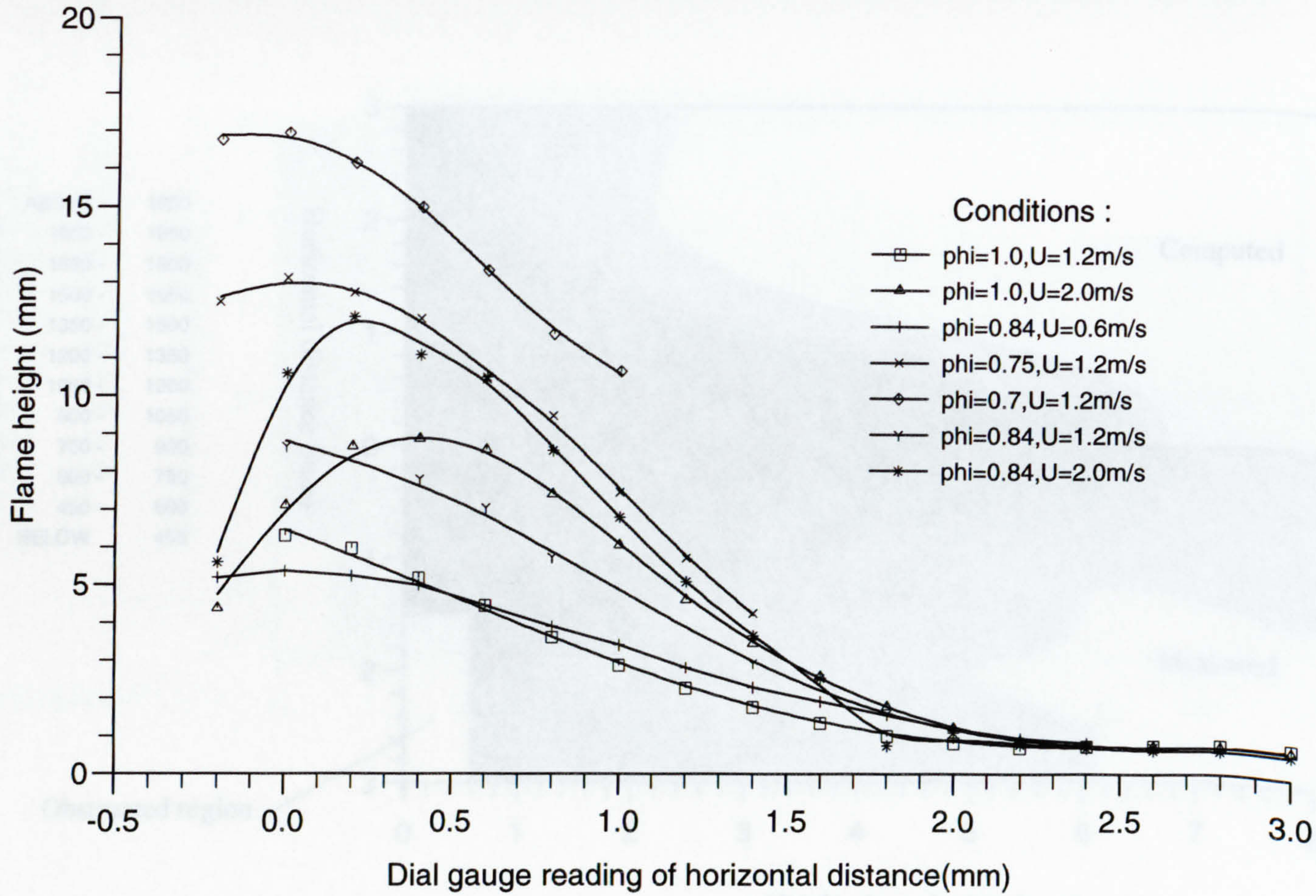

Fig. 6.13 Determination of symmetry axis shift for various mixtures and flow conditions. (Zero gauge reading represents reference position.)

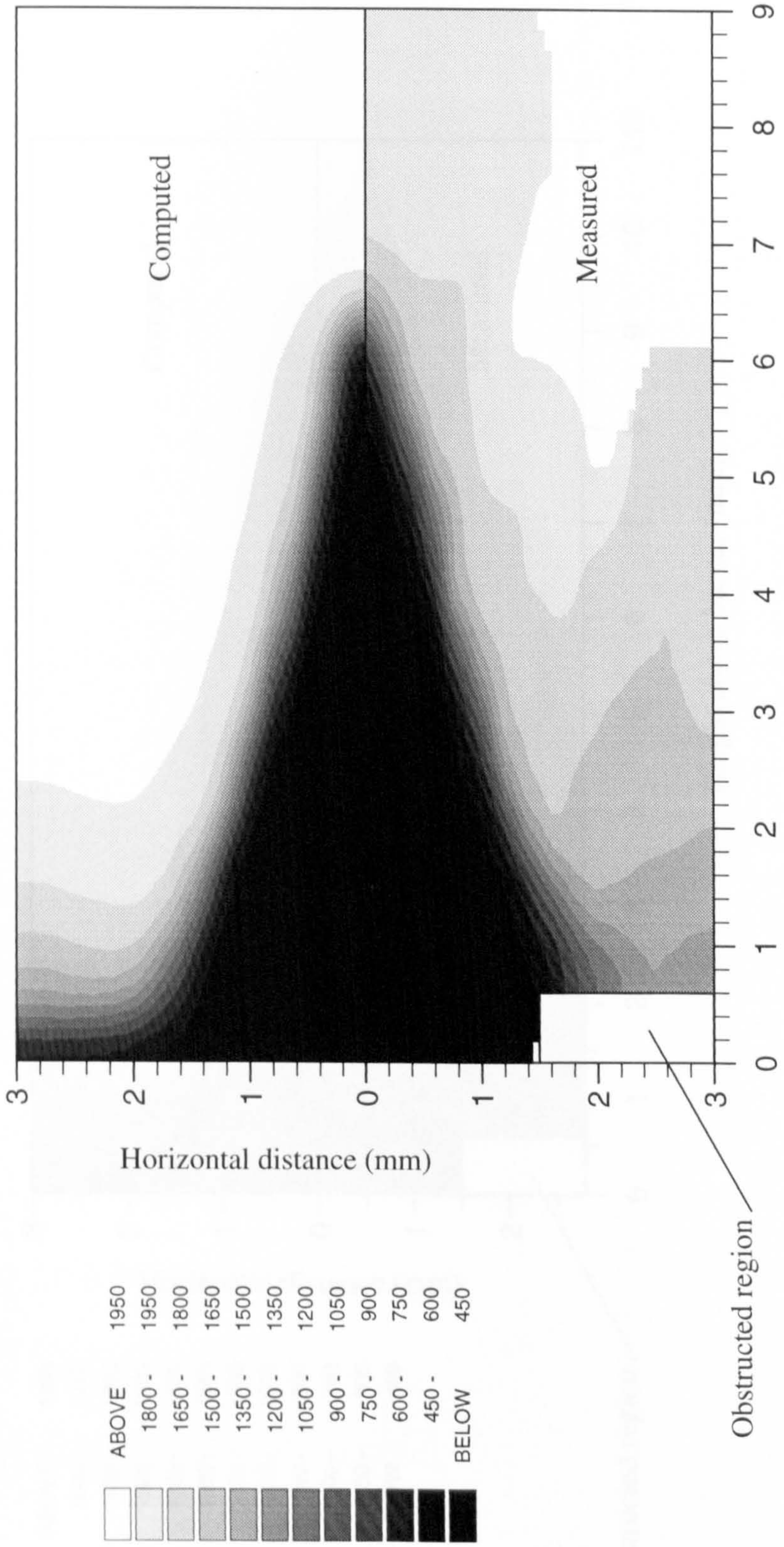

Fig. 6.14 Comparison of measured and computed two-dimensional isotherms with $\phi = 1.0$, $v_m = 1.2$ m/s.

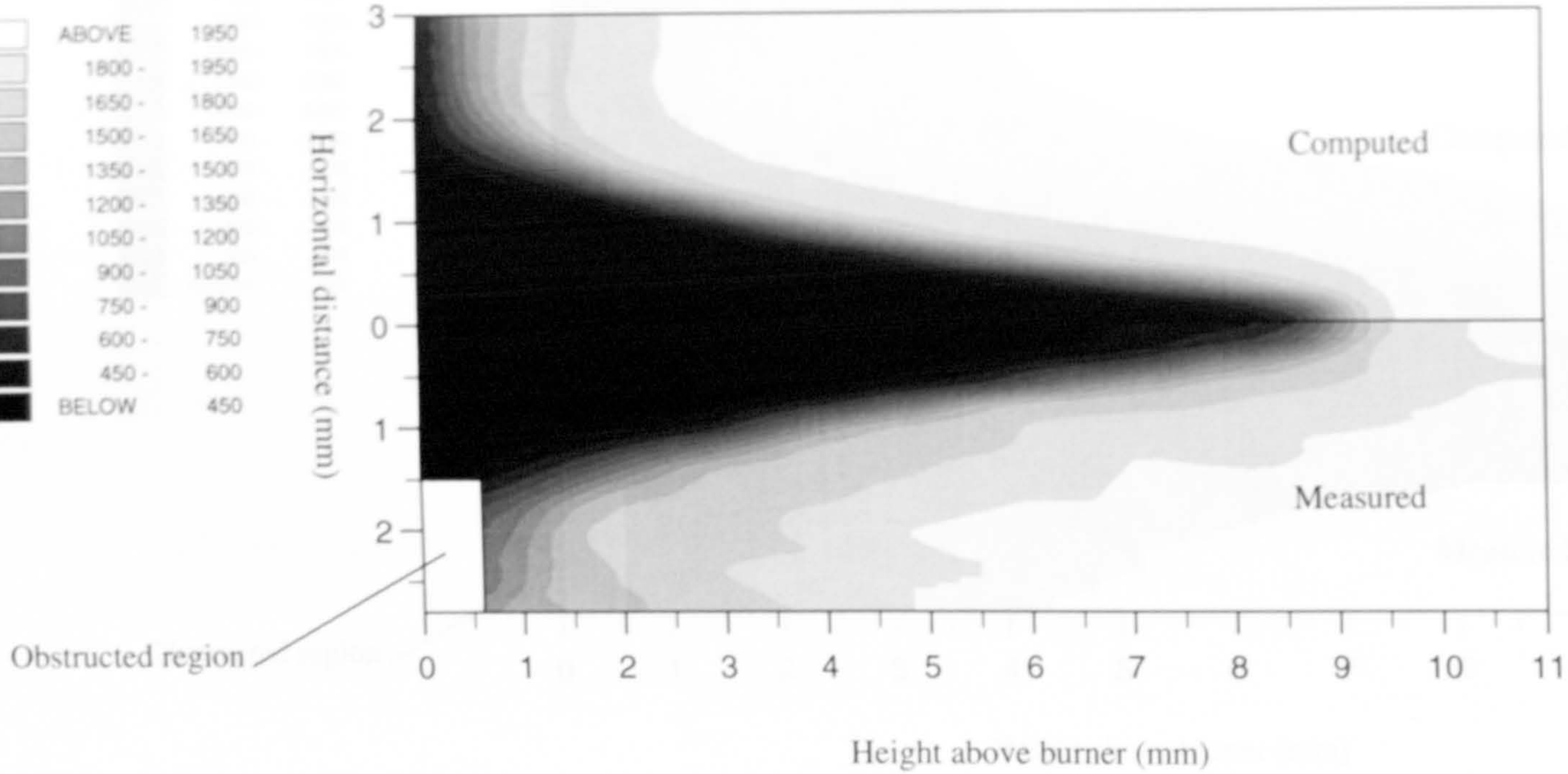

Fig. 6.15 Comparison of measured and computed two-dimensional isotherms with $\phi = 1.0$, $v_m = 2.0$ m/s.

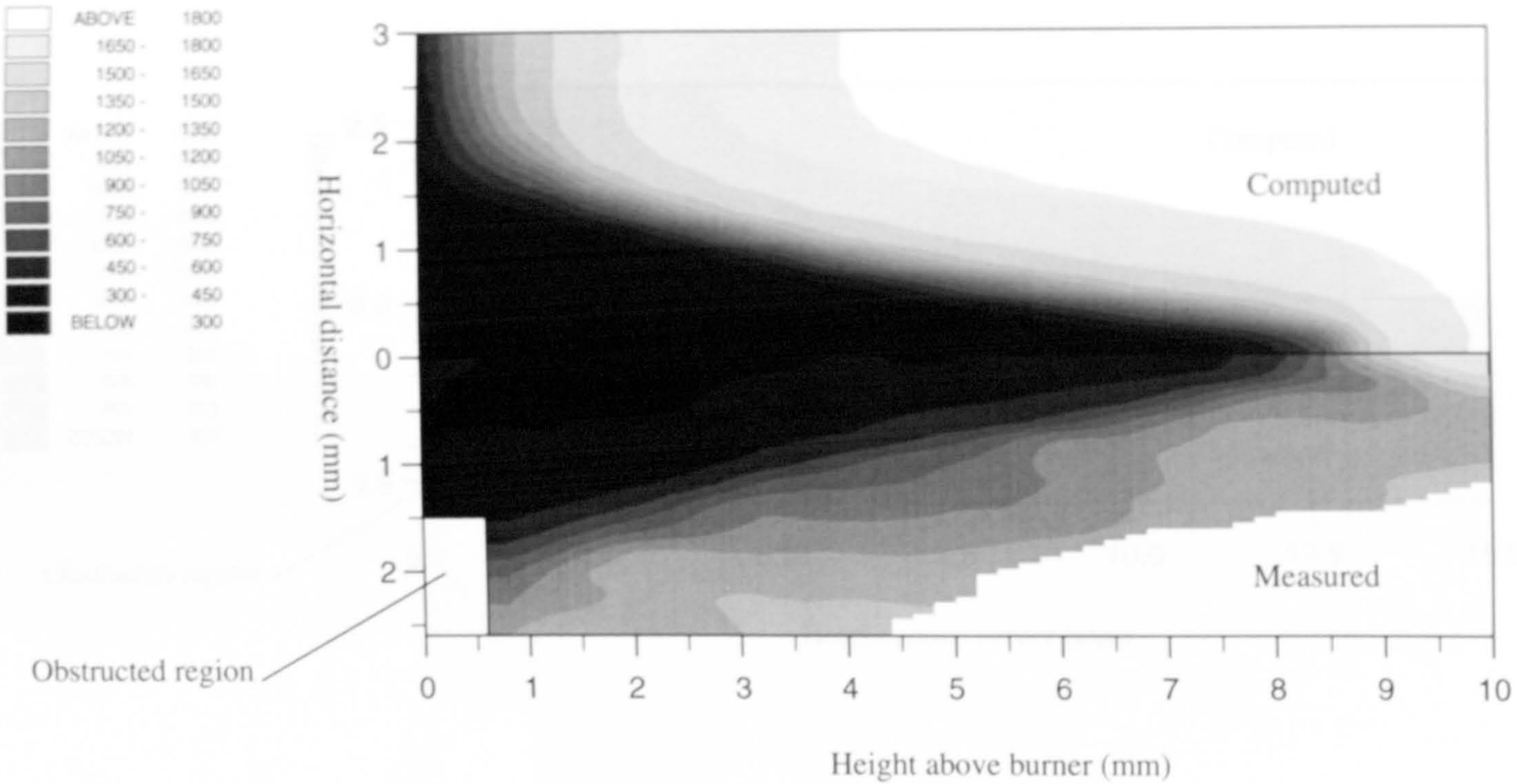

Fig. 6.16 Comparison of measured and computed two-dimensional isotherms with $\phi = 0.84$, $v_m = 1.2$ m/s.

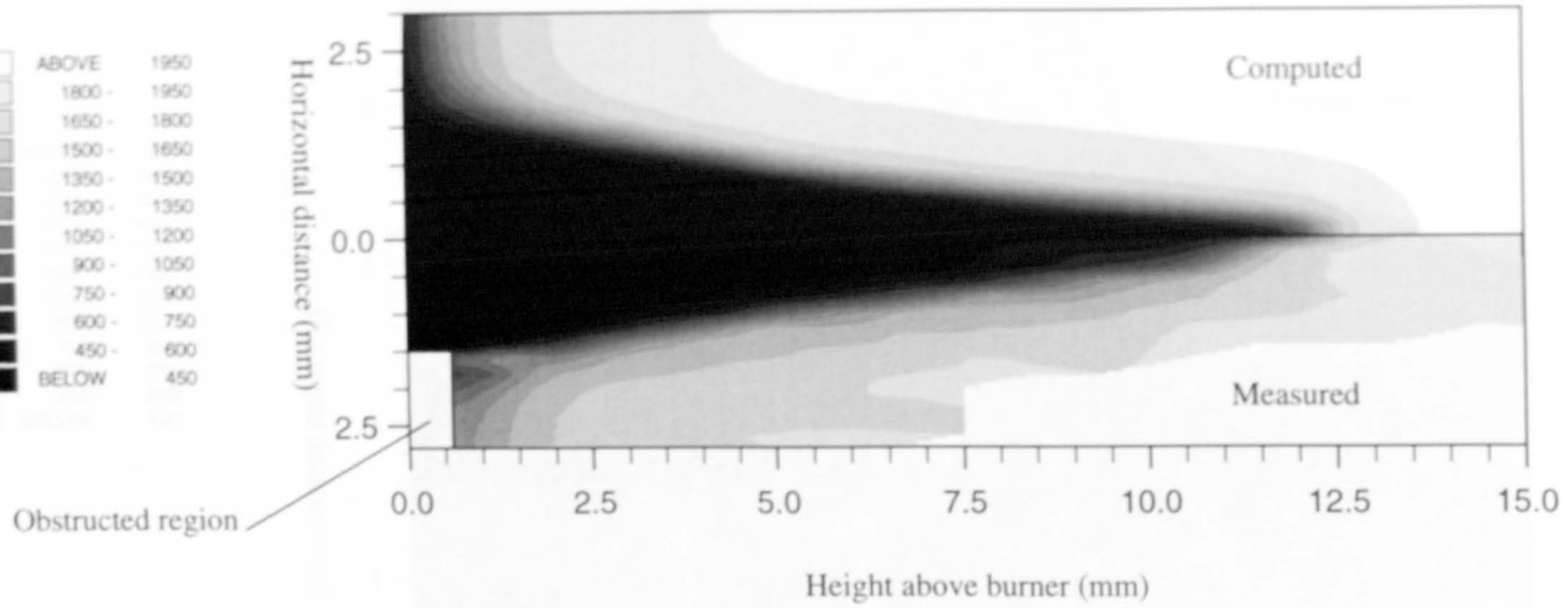

Fig. 6.17 Comparison of measured and computed two-dimensional isotherms with $\phi = 0.84$, $v_m = 2.0$ m/s.

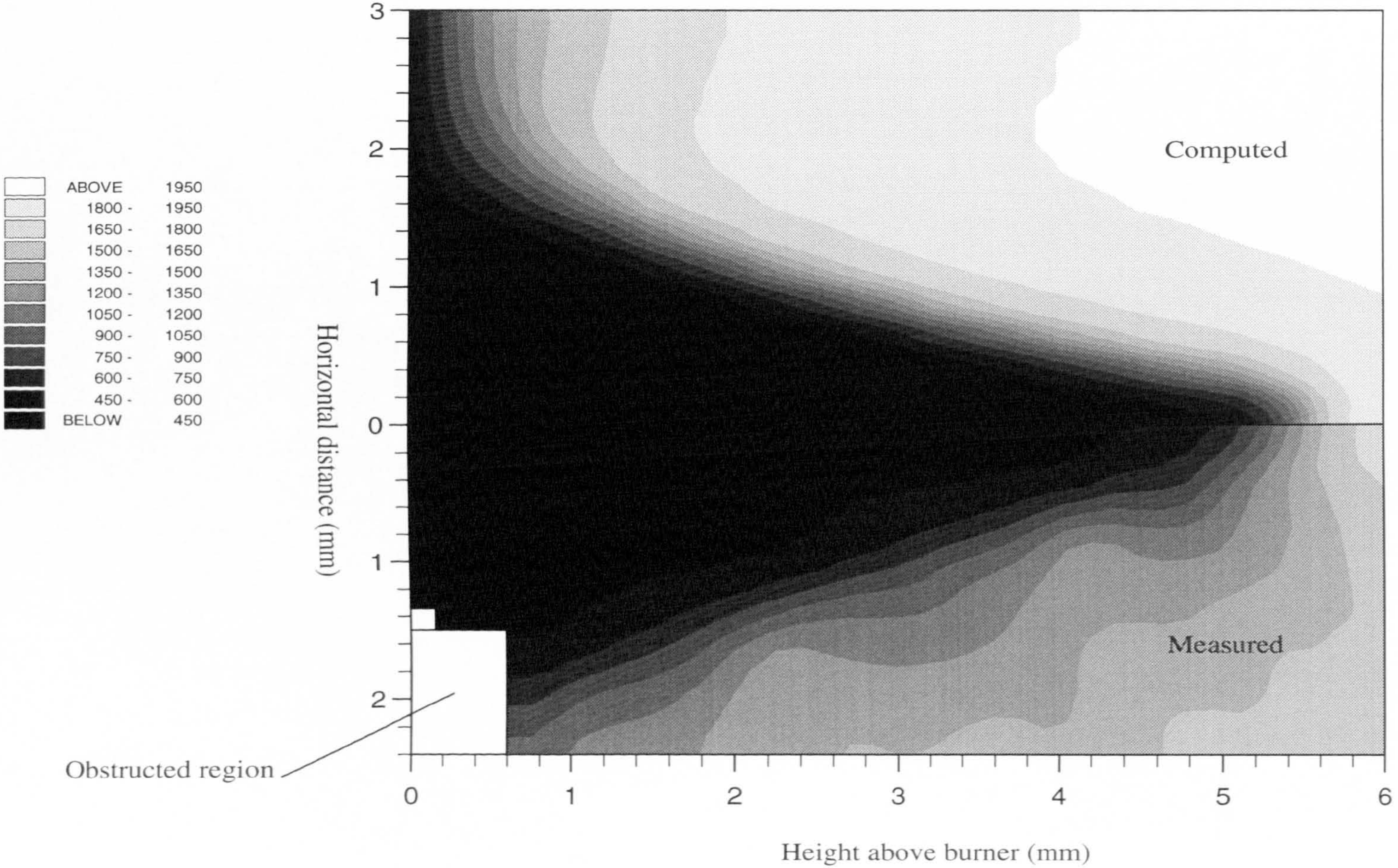

Fig. 6.18 Comparison of measured and computed two-dimensional isotherms with $\phi = 0.84$, $v_m = 0.6$ m/s.

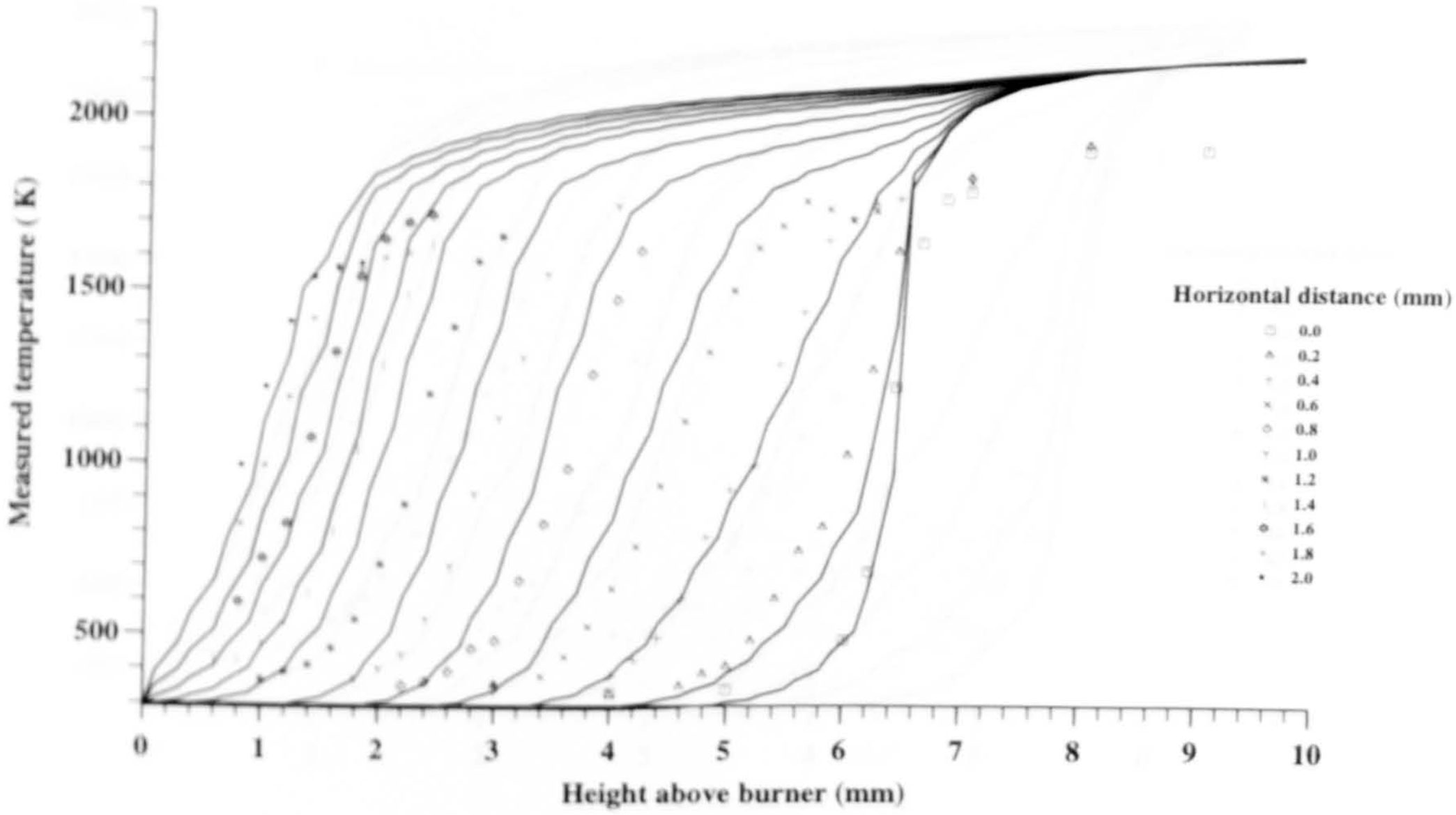

Fig. 6.19 Comparison of measured (points) and computed (line) temperature profiles, with $\phi = 1.0$, $v_{in} = 1.2$ m/s.

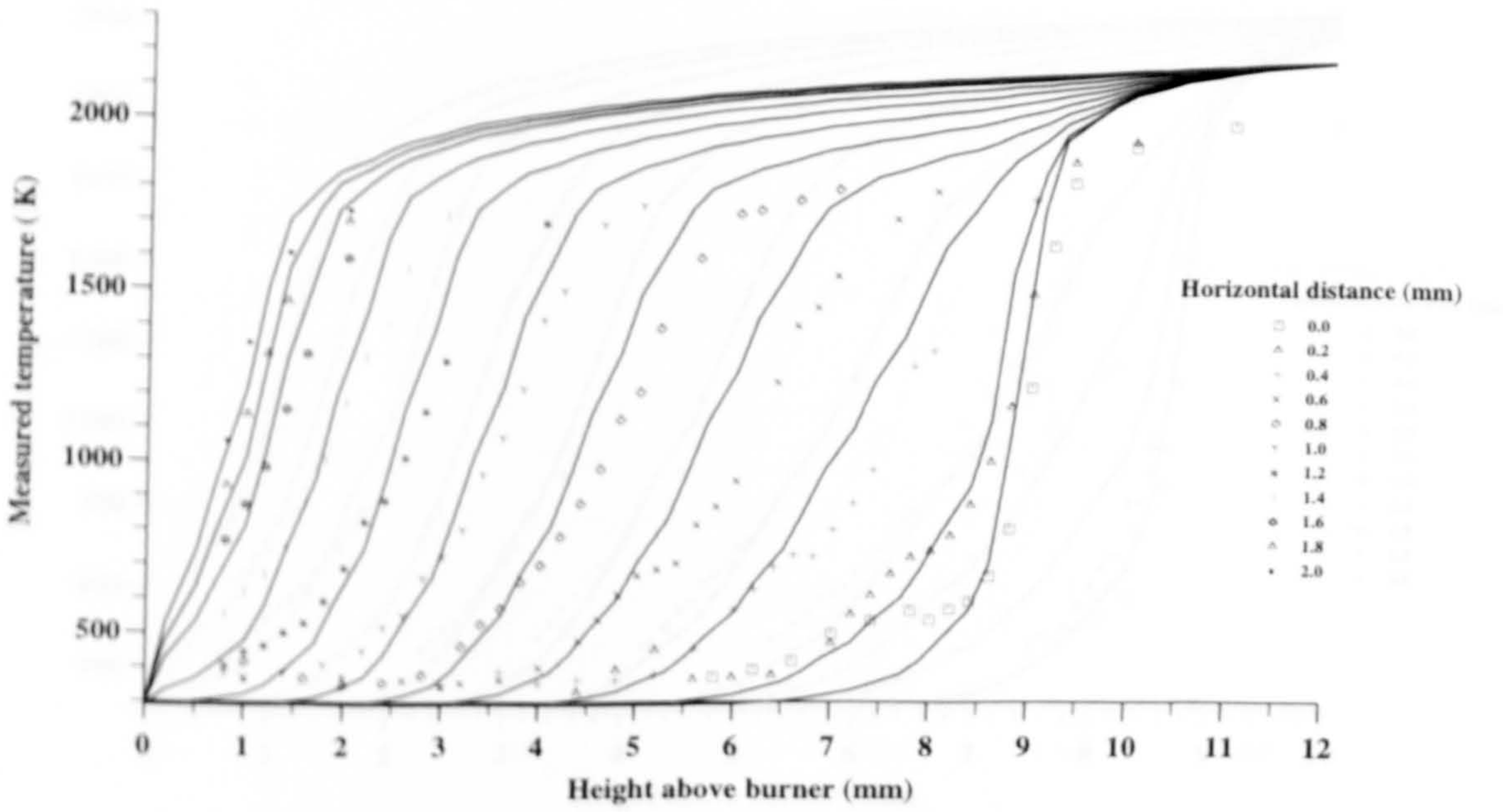

Fig. 6.20 Comparison of measured (points) and computed (line) temperature profiles, with $\phi = 1.0$, $v_{in} = 2.0$ m/s.

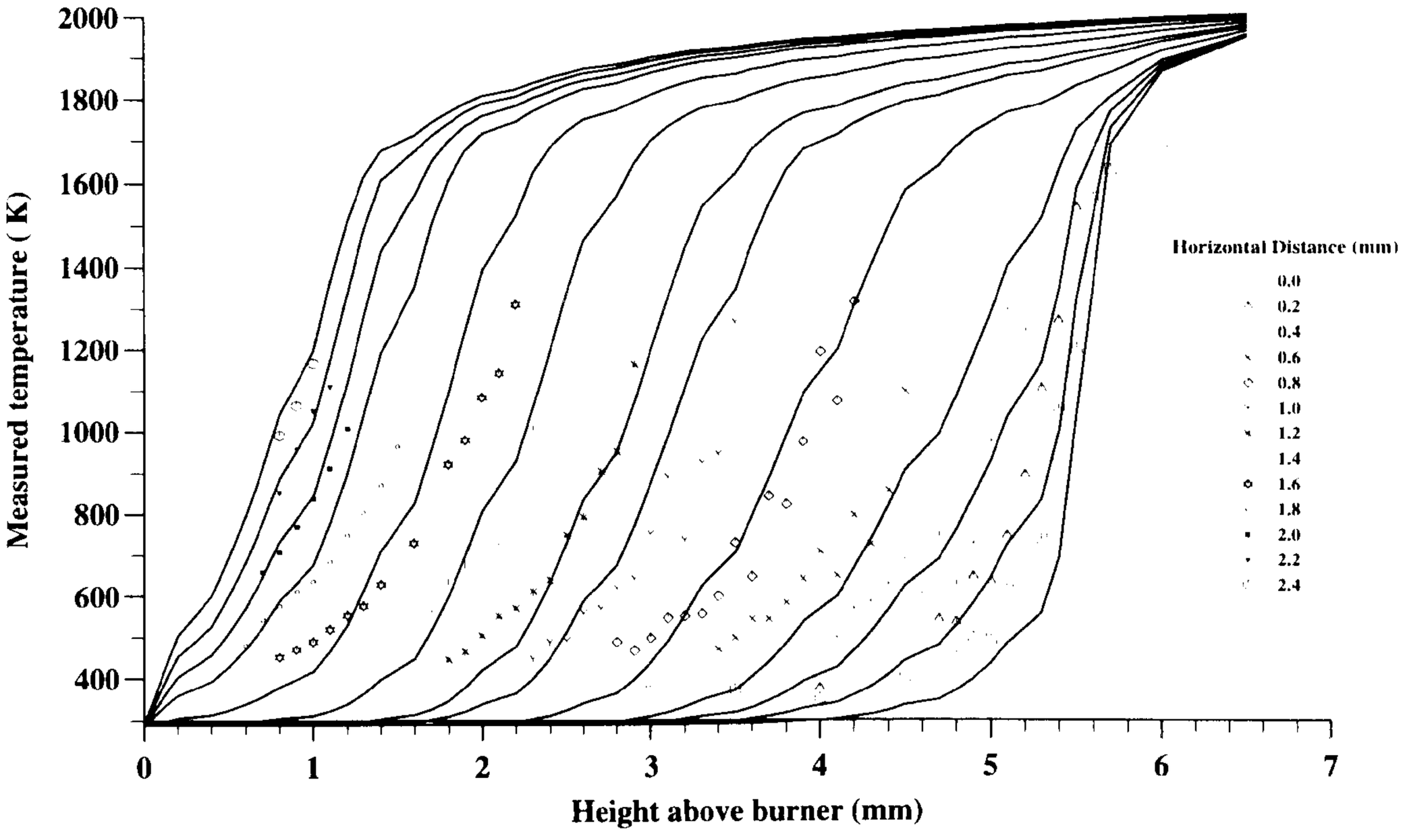

Fig. 6.21 Comparison of measured (points) and computed (line) temperature profiles, with $\phi = 0.84$ and $v_m = 0.6$ m/s.

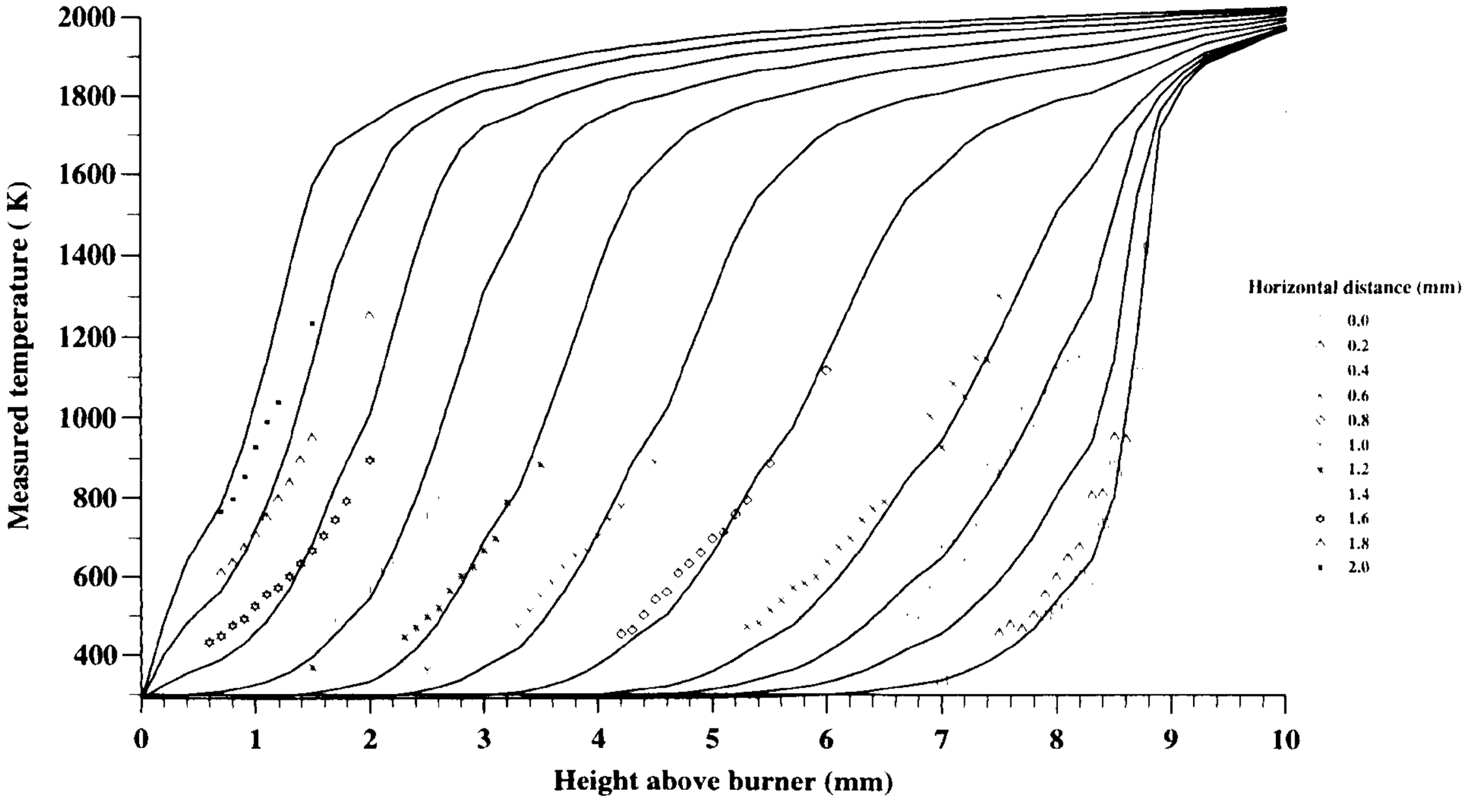

Fig. 6.22 Comparison of measured (points) and computed (line) temperature profiles, with $\phi = 0.84$ and $v_m = 1.2$ m/s.

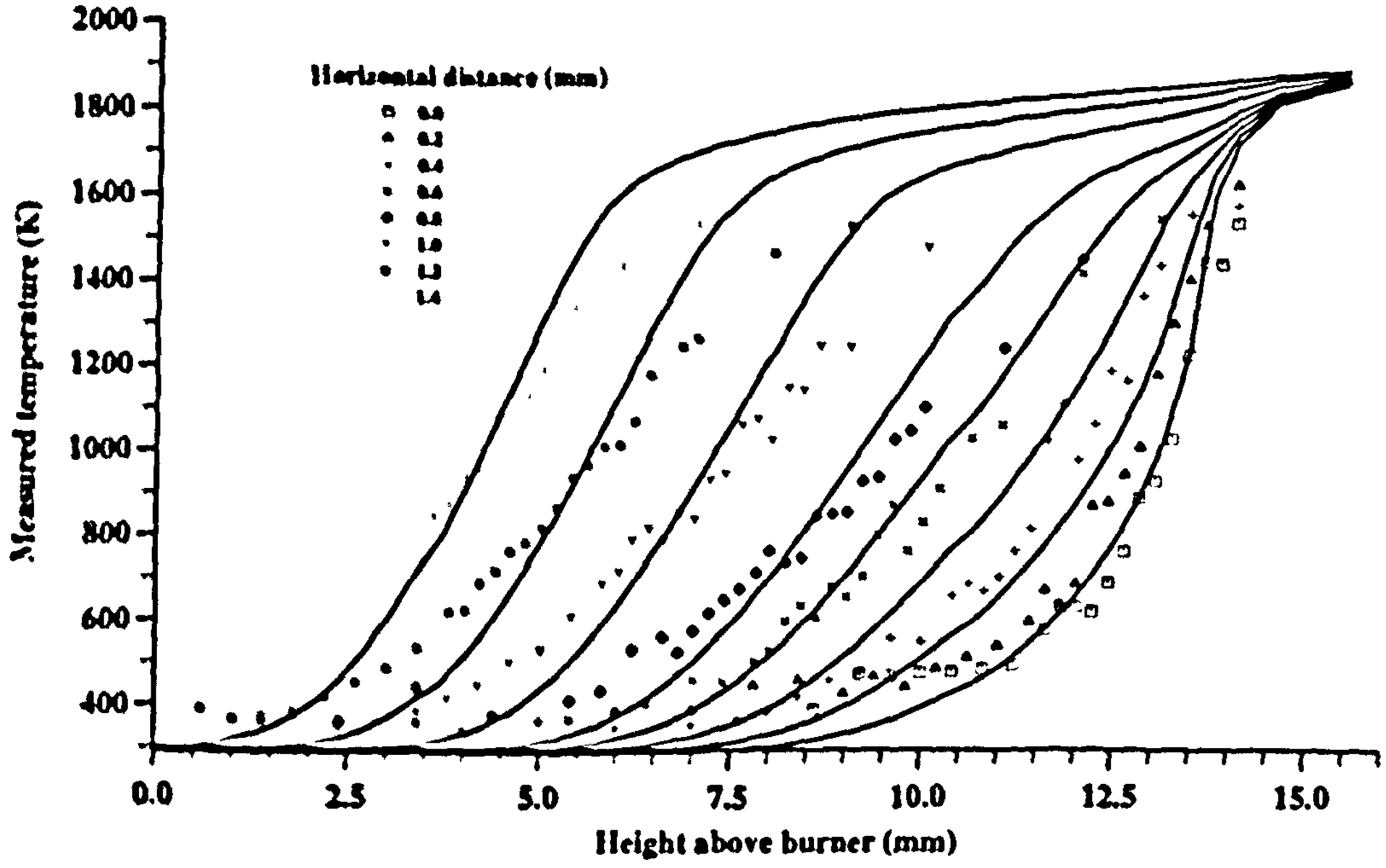

Fig. 6.23 Comparison of measured (points) and computed (line) temperature profiles, with $\phi = 0.75$, $v_\infty = 1.2$ m/s.

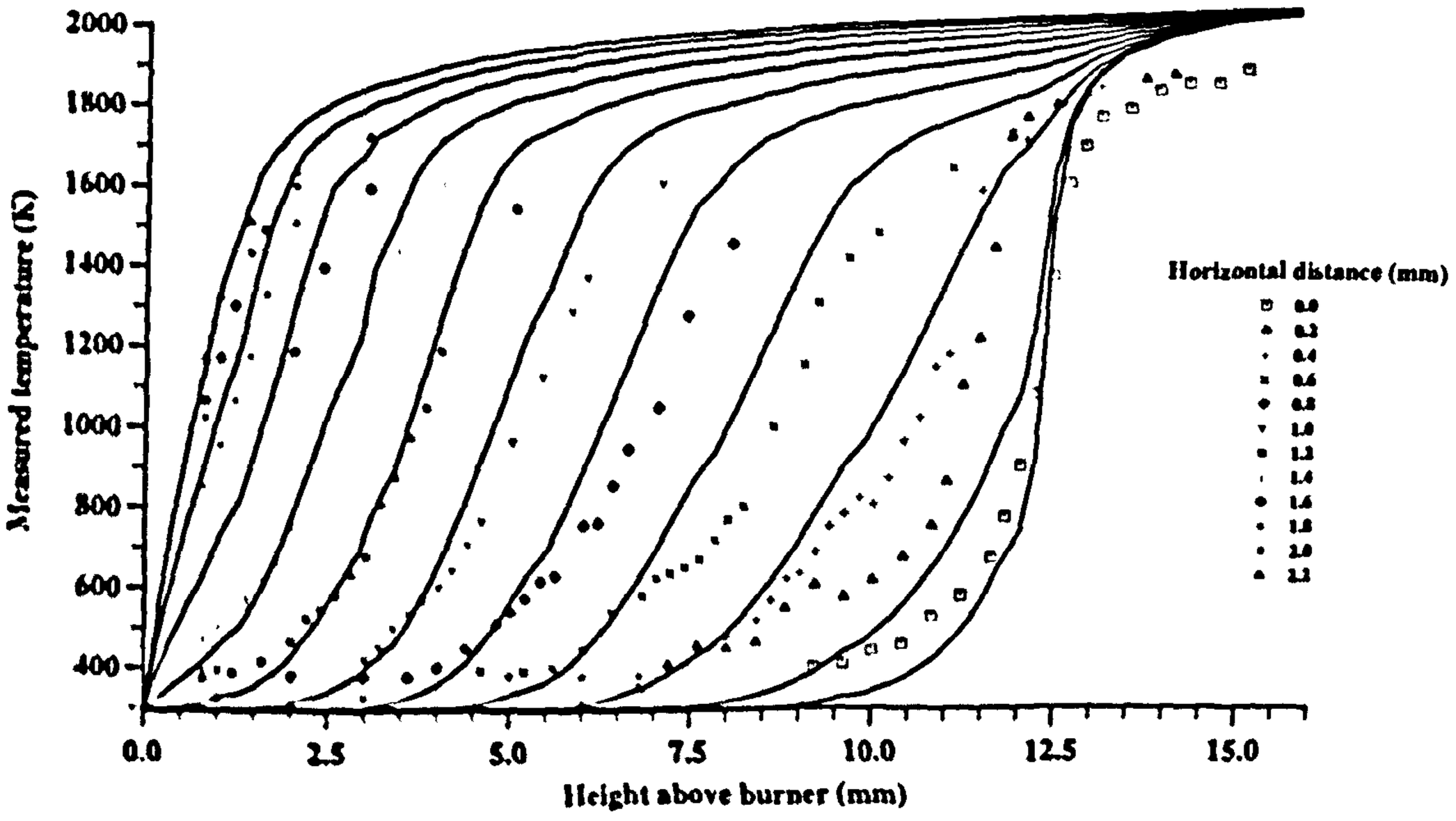

Fig. 6.24 Comparison of measured (points) and computed (line) temperature profiles, with $\phi = 0.84$, $v_\infty = 2.0$ m/s.

CHAPTER SEVEN
Burning Velocities of Stretched Flames

7.1 Introduction

Asymptotic analyses (Klimov 1963, Matalon 1983, Tien and Matalon 1991, Garcia-Ybarra *et al.* 1984), together with both computational studies (Dixon-Lewis and Islam 1983, Dowdy *et al.* 1990) and experimental measurements (Law 1988, Taylor 1991, Searby and Quinard 1990, Tseng *et al.* 1993) have shown flame stretch to affect significantly the laminar burning velocity of a premixed flame. The mechanism responsible for this behaviour arises from interactions between the diffusion of various key species, conduction, and flame stretch. This causes the rate of propagation of the flame surface to be either retarded or enhanced. Recent experimental evaluations and numerical simulations of premixed flames have studied neutral preferential-diffusion, where laminar burning velocities might be expected to be independent of stretch (Kwon *et al.* 1992, Kwon and Faeth 1992). The present computations provide an excellent opportunity to study the effects of stretch on burning velocity over a range of stretch values in a two-dimensional field.

While stationary two-dimensional laminar diffusion flames with realistic chemical kinetics have been simulated computationally (Smooke *et al.* 1989, 1990, Prasad and Price 1992, Coelho and Pereira 1993), as far as is known, the present study is the first of two-dimensional premixed flames. It has provided a stretch domain covering a negative stretch of the order 10^4 s^{-1} to a positive stretch of the same order. This compares with a typical experimental working range of 70-400 s^{-1} (Ali *et al.* 1993). The negatively stretched flame tips provide a convenient starting point for the investigation of negative

stretch effects. These have received little attention, yet they are of vital importance to fundamental combustion research.

Some controversial issues are considered, centred around the definitions of burning velocity and flame stretch and variation of burning velocity with stretch rate are presented. The Markstein length is introduced to correlate burning velocity and stretch and the concept of multiple Markstein length is introduced to explain the non-linear relationship between burning velocity and stretch. Values of Markstein lengths are suggested and compared with experimental values, where these are available.

7.2 Burning Velocities

The term "burning velocity" without any reference to stretch is strictly only meaningful in the context of a planar flame in a one-dimensional flow system. Unfortunately, such flames only exist on computers. Accurate determination of the burning velocity is still one of the most important practical aspects of combustion, representing as it does the influence of chemical kinetics upon the burning rate.

Andrews and Bradley (1972a, 1972b, 1973) showed there was a wide scatter in measured values of burning velocity. The authors suggested that the scatter was to some extent, a consequence of different measurement techniques and definitions of burning velocity. It now would appear that part of the scatter is due to different stretch rates in the different measurements.

7.2.1 Definition

Burning velocity can be considered as a physico-chemical constant for a given combustible mixture under given conditions of temperature and pressure. It is the velocity, relative to the unburnt gas, with which a plane, one-dimensional flame front travels along the normal to its surface. It is the eigenvalue of the one-dimensional flame equations (Andrews and Bradley 1972). This one-dimensional definition is clear and unambiguous: the upstream velocity of the cold gas into a planar, one-dimensional flame is constant, so there is no difficulty in designating its correct value. The difficulty is that real flames are not one-dimensional. It is therefore necessary to decide what

measurements to make on real flames and how to obtain some sort of relation with a flame that is planar and one-dimensional.

7.2.2 Reference surface

For a one-dimensional steady planar flow the mass flux, M, is constant, and the burning velocity is given by $u_l = M/\rho_u$, where ρ_u is the density of the unburned gas. In more general circumstances, however, this definition is less helpful as the mass flux varies with distance through the flame. Indeed, a characteristic burning velocity can be defined with reference to a well-defined spatial flame front location. This location can be chosen in an arbitrary, but consistent, way. For example, in measuring the burning velocity of a stretched flame, investigators have used different reference positions such as the point of minimum velocity (Wu and Law 1985, Law *et al.* 1986), the point of maximum velocity (Mendes-Lopes and Daneshyar 1985), or the upstream boundary of the luminous zone (Smith *et al.* 1989). The term "burning velocity" becomes precise only when the flame thickness tends to zero, but this is of little help in practical problems.

Thus, in general, an unique reference surface must be defined to specify a burning velocity. Although the reference surface can be a species isopleth, a pressure isobar, a specified volumetric heat release rate contour or a contour of any constant property, it is typically an isotherm. However, for the two-dimensional axisymmetric flame considered in the present study, with an equivalence ratio of 0.84, and slot of width 2 mm and a mean inlet velocity of 0.4 m/s, the burning velocity can differ by a factor of 4, along the symmetry axis, depending on the choice of isotherm (Fig. 7.1). If the burning velocity is defined as the rate of disappearance of a reactant, then the cold isotherm at T_u should be used. If burning velocity is defined as the rate of appearance of product, then the hot isotherm T_b would be more appropriate. In an ideal one-dimensional flat flame, both definitions would have the same mass flux and be unambiguous. However, in realistic multi-dimensional flames, or even one-dimensional spherical flames, the mass flux according to different definitions can be very different.

In 1972, following convention, Andrews and Bradley considered the reference surface to be that of the cold reactants and used an isotherm of 298 K as that surface. In their survey of burning velocities, they corrected burning velocity measurements to a datum of 298 K.

Based on computations of a divergent stream tube configuration for mixtures of methane-air and hydrogen-air, Dixon-Lewis and Islam (1982) suggested a different reference surface for the calculation of burning velocity. In their computational experiment, nine methane-air flames, containing between 6.0 and 11.6 per cent methane initially, and all with an initial temperature of 298 K, were investigated, with stream tubes of different divergences. By plotting the apparent burning velocities (obtained by dividing the mass flux by the initial gas density at 298 K) against the associated temperature, they observed that such burning velocities became equal to the burning velocity of a one-dimensional flame at a fixed temperature, irrespective of the divergence. For methane-air flames, these temperatures, for equivalence ratios of 1.0, 0.84 and 0.75, were 1640 K, 1540 K and 1480 K, respectively. The authors adopted these temperatures, which gave the one-dimensional burning velocity, as the reference isotherm for burning velocity measurements. They also found that the reference isotherms all corresponded approximately with the positions of maximum overall reaction rate.

Taking a stationary spherical flame as an example, Taylor (1991) defined the reference surface as "the locus points in a spherical flame where the mass flux equals that of the corresponding planar flame". The surface was determined by comparing flames modelled in planar and spherical geometries. The reference surface position and temperature were obtained from the spherical modelling results by reading off the required properties at the zone with a mass flux equal to the planar value. Since such a reference surface usually occurs in a region where the temperature varies very rapidly, the author suggested it was necessary to quote the temperature at the reference surface position, rather than the position. With this approach, the interpolated reference planes for methane-air flames with equivalence ratios of 1.0, 0.84 and 0.75 were 1450 K, 1360 K and 1330 K, respectively. These approaches of Dixon-Lewis and Islam (1982)

and Taylor (1991) have the complication that the surface is defined in terms of a surface that is mixture and geometry dependent.

7.2.3 Evaluation of burning velocity

In the present work, it is necessary to select a reference temperature slightly higher than the initial reactant temperature. For the present analysis, a temperature of 300 K is selected for an initial temperature of 290 K. As illustrated by a set of results computed with the present reduced model (Fig. 7.1), a temperature of 300 K co-incidentally corresponds to the minimum gas velocity. The minimum gas velocity has been regarded as the burning velocity in the studies of burning velocity and flame stretch (Law, 1988 and Dixon-Lewis 1984), though these authors did not show to which temperature the minimum velocity referred.

For stationary flames, the burning velocity is equal in magnitude and opposite in direction to the gas velocity at the defined surface. Thus, on the chosen isotherm, the burning velocity is defined as the gas velocity normal to the reference surface (Fig. 7.2). Vertically, the gas temperature rises from the initial temperature of 290 K to the adiabatic temperature. Along the axis, there exists an unique position where the temperature is equal to 300 K. The two orthogonal gas velocity components, u and v, are linearly interpolated to give values at this isotherm. The component normal to the isotherm is evaluated from these two interpolated velocity components to yield the burning velocity.

7.2.4 Burning velocity distribution within a flame

While large variations of burning velocity in a two-dimensional curved flame were noted some time ago (Andrews and Bradley 1972, Linnett 1953, Lewis and von Elbe 1961), burning velocities in such flames have not been comprehensively measured. This is explained by the problems faced by analytical and experimental approaches. Analytically, the major task has been the addition of realistic chemical kinetics to previous asymptotic analyses restricted to weak stretch, whereas in a real flame, the stretch rate can be high at the flame tip and base. Experimentally, a highly curved flame

surface had to be mapped precisely in order to determine the stretch accurately. Figure 7.3 presents computed burning velocities from the present studies for a stochiometric, two-dimensional flame, at different horizontal distances, for mean inlet flow velocities of 0.4, 0.6 and 1.0 m/s.

At the low inlet velocity (0.4 m/s), the burning velocity has a fairly uniform value across the tip and flank of the flame that decreases near the base. As the inlet velocity increases, burning velocities increase substantially at the tip. As will be shown in the next section, curvature stretch dominates at high flow rates. These observations, to some extent, demonstrate the hypothesis of Markstein (1964) that increases and decreases in burning velocities are a consequence of flame curvature, a hypothesis investigated in Sections 7.5 and 7.6. In addition to the influence of curvature, velocity gradient effects (aerodynamic straining) also are considered.

7.3 Flame Stretch

The concept and definition of flame stretch have been introduced in Chapter 1, while expressions for such stretch have been presented in Chapter 2. Here, the stretch expressions are applied to the numerical solutions of the mathematical models. These are used to explain the different burning velocities along an isotherm. This is also necessary for the correlation of burning velocities. With the present study, flame stretch is evaluated at an isotherm of 300 K, identical to that at which the burning velocity is evaluated. Stretch is evaluated with Eq. 2.43, with geometrical parameters and velocity linearly interpolated in the vertical (y) direction.

In the present two-dimensional computations, there are large variations in flame stretch. Typically, for an equivalence ratio of 0.84, slot width of 2 mm and mean inlet velocity of 1 m/s, Fig. 7.4 shows the against horizontal distance, distribution of total stretch and its strain and curvature component terms, along a 300 K isotherm. The total stretch is the sum of its components, aerodynamic straining, positive for a diverging flow field, and curvature stretch, of the same sign as the radius of curvature. Moderate stretch rates were observed near the base where the flame is positively stretched, but very high negative stretch rates (compression rates) occured near the tip. It also is clear

that the total stretch, except when its magnitude is small, is dominated by the curvature component. At a lower mean inlet velocity of 0.4 m/s, with the same mixture and slot width, the distribution of stretch is very different. As illustrated in Fig. 7.5, the flame base is negatively stretched, while the flame tip is positively stretched, although with a much smaller magnitude. This situation is completely opposite to that occurring at the high flow rates. Furthermore, the stretch, except when its magnitude is small, is now dominated by aerodynamic straining.

Clearly, the straining term provides negative stretch at the base and positive stretch at the tip, whereas the curvature term provides positive stretch at the base and negative stretch at the tip. At high flow rates, the curvature term dominates and the flame tip is negatively stretched, whereas at low flow rates, the strain term dominates and the flame tip is positively stretched. These observations are very useful if the effects of curvature stretch and aerodynamic straining are to be studied separately.

7.4 Burning Velocity of a Stretched Flame

Whereas previous burning velocity and stretch correlations have been based on experimental and asymptotic analysis, the present study uses a computational approach. So far as realistic elementary reaction schemes are used, the present analysis is realistic. Methane-air mixtures with equivalence ratios of 0.75, 0.84 and 1.0, a mean inlet velocity of 0.6 m/s, and a slot width of 2 mm were investigated. In order to avoid the complication of defining flame thickness, the Markstein length is used throughout this thesis, not the Markstein number, which is the ratio of Markstein length to flame thickness.

In the positively stretched region, all three mixtures, with equivalence ratios of 1.0, 0.84 and 0.75, though in a non-linear fashion, showed a decrease of burning velocity with stretch (Fig. 7.6). The decrease is at first rapid, then remains fairly steady until close to the maximum stretch rate, where the burning velocity decreases rapidly. In the region between zero and maximum stretch, the burning velocity - stretch relationship is approximately linear. This is the region where most Markstein lengths have been evaluated, and suggest a linear relationship. However, the non-linear behaviour near the

zero stretch region suggests that the evaluation of unstretched laminar burning velocity by extrapolation may be inaccurate.

In the negatively stretched region, the burning velocities of all three mixtures decrease with increasing stretch (Fig. 7.7). Linear relationships are observed away from the region of zero stretch, where the burning velocity decreases rapidly. However, unlike the positive stretch region, the linear relationship holds up to the minimum stretch rate obtained, indicating that a higher burning velocity can be obtained with a smaller (more negative) stretch rate. The increase of burning velocity in a negatively stretched region provides a means of obtaining a useful increase in burning rate.

Figure 7.8 illustrates the burning velocities of the three mixtures over the full range of stretch rates. Apart from the region of low stretch, the relationship of burning velocity to stretch is fairly linear, with similar gradients. This is explained in Section 7.3.2, in terms of curvature stretch dominating regions away from the zero stretch region, where a combination of curvature stretch and aerodynamic straining probably exists. As expected, burning velocities increase with equivalence ratio.

7.5 Markstein Length

7.5.1 Introduction

At present, most Markstein lengths are obtained either by asymptotic analysis (Clavin and Joulin 1989, Rogg and Peters 1990), in which the lengths are defined at a cold surface, or experimentally (Law *et al.* 1986, Searby and Quinard 1990, Taylor 1991, Tseng *et al.* 1993). In cases of the latter, the lengths have been measured at various temperatures and transformed to either a hot or cold isotherm. With computational methods, Markstein lengths have been obtained for one-dimensional counter flow configuration (Rogg 1988). However, such methods are still in their infancy. Possibly, this is the first time that a two-dimensional model with realistic elementary reactions has been used to evaluate Markstein lengths.

The effects of positive stretch on flame stretch have been explored by numerous experimentalists with stagnation flow (Law *et al.* 1986), expanding spherical flames

(Taylor 1991, Tseng *et al.* 1993) and the so called "direct" method (Searby and Quinard 1990), for a range of stretch rates, up to extinction. Such techniques are described briefly in Section 7.5.3. However, the influences of negative stretch have received little attention, largely because it is not attained in the above configurations, although, the influences of negative stretch on Bunsen flame tips have been investigated qualitatively by Law (1988), Law *et al.* (1982, 1986) and Mizomoto *et al.* (1984).

The presently derived values of Markstein lengths will now be discussed and compared with previous analytical and experimental values. All Markstein lengths from the present study are defined in terms of the 300 K isotherm, the same datum for burning velocity and stretch. Unfortunately, other values of Markstein lengths for similar two-dimensional models are not available. The present results are therefore compared with 'one-dimensional' theoretical and experimental values. First, theoretically evaluated Markstein lengths and some estimated values are presented, followed by experimental values with a brief description of the methods used. Computational methods are then described, and finally, the present compared with the previous values.

7.5.2 Theoretical evaluation

As described in Section 1.5.3, an appropriate theoretical expression for comparison with the computational values of Markstein length is Eq. 1.14, derived from the work of Clavin and Joulin (1983) for weakly stretched flames. The density ratio σ is obtained from initial and final adiabatic temperatures. The integral was performed numerically at various values of σ using Simpson's rule. Less straightforward terms to estimate are the flame thickness, δ, and the Zel'dovich number, β. They are not known '*a priori*' as they depend upon the flame structure and properties. Since precise agreement between asymptotic theory and computational results is not expected, a simple and generally used expression for flame thickness is:

$$\delta = \frac{\lambda_u}{\rho_u u_l C_p}. \tag{7.1}$$

Another expression is:

$$\delta = \frac{\nu}{u_l}, \tag{7.2}$$

in which ν is the dynamic viscosity.

For thermal conductivity and specific heat, it is not obvious which values in the real flame should be used, since both composition and temperature are changing in the region that they are intended to characterise. While Clavin and co-workers (1984) recommended the use of burnt gas values, Searby and Quinard (1990) and Deshaies and Cambray (1990) calculated the thermal conductivity in the unburned gas. Since the laminar burning velocity is evaluated at the unburned temperature, it is reasonable to calculate the thermal conductivity and specific heat at this same value. They are so calculated using the procedures presented in Chapter 3.

The unstretched laminar burning velocity, u_l, is evaluated at the 300 K isotherm at a position where the stretch is zero. The values are 0.24 m/s, 0.30 m/s and 0.40 m/s for equivalence ratios of 0.75, 0.84 and 1.0, respectively. The Lewis number has been defined in Chapter 1 (Eq. 1.13): the thermal conductivity λ, the density ρ, the specific heat C_p and the binary diffusion coefficient D are calculated at the unburnt temperature by the methods presented in Chapter 2. The binary diffusion coefficient is based on the deficient species and nitrogen. The Zeldovich number β is defined in Chapter 1 (Eq. 1.15). All terms are known except for the activation energy, for which the value determined by Taylor (1991) of 46.5 (± 2.7) kcal/mol was used. Thus, the Markstein length can be evaluated from Eq. 1.14, and values are given in Table 7.1.

Table 7.1

Markstein lengths $\mathcal{L}$ evaluated with Eq. 7.1 and other values used.

ϕ	σ	δ (μm)	β	*Le*	$\mathcal{L}$ (mm)
0.75	0.150	94.6	9.96	1.025	0.044
0.84	0.146	73.2	9.74	1.025	0.033
1.0	0.136	56.8	9.15	1.026	0.025

Rogg and Peters (1990), by replacing the single-step irreversible global reaction with a three step reduced mechanism in the asymptotic analysis, derived another theoretical expression for Markstein length:

$$\mathcal{L} = \frac{\delta\sigma}{1-\sigma}\left[\ln\sigma^{-1} + \frac{2(L_e - 1)}{\varepsilon z}\int_0^{\frac{1-\sigma}{\sigma}} \frac{\ln(1+x)}{x}dx\right]. \qquad (7.3)$$

Here, the numerical values and relationships suggested by the authors are used: the Lewis numbers were assigned values of 0.2, 0.3, 1.07, 0.74, 1.14, 1.05 and 0.97 for H, H_2, CO, H_2O, CO_2, O_2 and CH_4, respectively. For μ and λ/C_p, the relationship:

$$\mu = \lambda/C_p = 10^{-3}(T/1600)^{0.75}\ \text{g/(cm s)}, \qquad (7.4)$$

proposed by the authors was adopted here, with the temperature, T, in degrees Kelvin. The pressure and initial temperature were taken as 1 atm and 300 K. Equation 7.3 is similar to Eq. 1.14 of Clavin and Joulin, except that the Zeldovich number β is replaced by $4/\varepsilon z$. The thickness of the oxidation layer, ε, and the stretch variable, z, are functions of various species mole fractions and chemical reaction rates and are evaluated at the fuel consumption layer.

In their paper, Rogg and Peters (1990) calculated the Markstein number for stoichiometric methane-air, and proposed a value of 2.23. The equivalent Markstein length with a flame thickness calculated from Eq. 7.1 is 0.1 mm. However, with their expression, evaluation of Markstein length for other mixtures requires the mole fractions of some minor species in the fuel consumption layer, and these can only be obtained from one-dimensional modelling. This requires the generation of another model, which was not attempted in the present project for reasons of time.

7.5.3 Experimental evaluation

Experimental methods have been the most common way of determining Markstein lengths (Law *et al.* 1986, Searby and Quinard 1990, Taylor 1991 and Faeth *et al.* 1992, Ali *et al.* 1993). In the equation of burning velocity:

$$u_l - u_n = \mathcal{L}\, S, \tag{7.5}$$

S is given by Eq. 1.11. The unstretched laminar burning velocity u_l and Markstein length $\mathcal{L}$ are constant for a given mixture. In an experiment, stretched burning velocities u_n and the local stretch rates at the flame front must be measured. Values of u_l and $\mathcal{L}$ can be obtained from there.

This section presents, in Table 7.2, a number of Markstein lengths evaluated experimentally. They are obtained from various experimental configurations one dominated by flame straining (Law *et al.* 1986), and three others where straining as well as curvature exist (Searby and Quinard 1990, Taylor 1991 and Tseng *et al.* 1993, Ali *et al.* 1993). These Markstein lengths are derived by a number of different techniques, described below. The present study will show the importance of distinguishing between curvature and aerodynamic strain influences upon flame stretch. This was not appreciated at the time of these studies and this, together with inherent errors, and the variety of techniques can explain the large scatter in the results.

Table 7.2

Comparison of Markstein lengths $\mathcal{L}$ (mm).

Sources	$\phi = 0.75$	$\phi = 0.84$	$\phi = 1.0$
Clavin & Joulin (1983)	0.044	0.033	0.025
Law *et al.* (1986)	-0.21*	-0.18	-0.12*
Rogg (1988)	0.045	0.047	0.071
Rogg & Peters (1990)			0.1
Searby & Quinard (1990)	0.28*	0.23*	0.21
Taylor (1991)	0.047*	0.04*	0.10
Tseng *et al.* (1993)	0.017*	0.057*	0.11
Ali *et al.* (1993)	0.21*	0.18*	0.20
Present Study	0.026	0.071	0.107

* Evaluated with linear interpolation.

Among these four groups of researchers, Taylor (1991), Tseng *et al.* (1993) and Ali *et al.* (1993) used the expanding spherical flame method. These exploded mixtures in a spherical chamber with a central spark ignition. The spark energy was adjusted to a minimum in order to minimise effects of initial flame acceleration by excessive spark energy. Flame speeds were measured by shadowgraph or schlieren cine photography and the flame radius r plotted against time. The instantaneous gradient gave the instantaneous flame speed, which then plotted against $2/r$ to yield the Markstein length from the slope whilst u_l was found by extrapolating back to zero stretch. Size limitations of the chamber precluded the measurement of flames of large radius and small stretch. Also, results from flames of small radius are unreliable as spark effects become significant. Although results with a stretch rate as high as $S = 7600$ s^{-1} were reported for hydrogen flames (Kwon *et al.* 1992), the working range of such experiments was typically limited to a flame radius of 5-30 mm, giving an equivalent stretch (S) of 70-400 s^{-1} (Ali *et al.* 1993).

Law *et al.* (1986) used an alternative configuration in which flame stretch was obtained by opposed flows. The gases could either be brought to stagnation by two identical opposed jets, or by the reactive mixture flowing from a cylindrical tube and impinging onto a flat surface. Either way, the flame surface is nearly flat, and the small flame curvature is estimated by superimposing a circle of known radius to the digitised video picture of the flame. Velocity gradients were deduced from LDV velocity measurements. Burning velocity also was taken by LDV velocity measurements.

With Searby and Quinard (1990), the Markstein length was determined from direct measurements of the local burning velocity of a corrugated flame. A quasi-planar laminar premixed flame was established in a steady periodic shear flow. The burner head was rectangular in cross section and a number of equidistant tubes were placed perpendicular to the direction of flow. The external diameter of the tubes was such that the flow around them was laminar. The resultant flame, thus, took the form of a two-dimensional sinusoidal sheet with a wave length of wrinkling equal to the spacing of the tubes. With this method, Searby and Quinard (1990) suggested that the calculated Markstein length had an error of over 100 %. Fresh mixture was seeded with a fine mist

of oil droplets which vaporised in the preheat zone. The droplets in the unburnt gas scattered the laser light whilst the burnt gas was transparent. The local position of the front was detected by imaging the laser sheet onto a vertical array of photo diodes, whilst the velocity of the flow field was measured by Laser Doppler Velocimetry.

7.5.4 Computational evaluation of a single Markstein length

Due to the non-linear nature of the burning velocity against stretch curve, it seemed at first inappropriate to fit a Markstein length over the whole range of stretch rate presented in Fig. 7.8. Therefore, in order to make comparisons with experimental results, a range was selected, similar to that used in experiments, between 70-400 s^{-1}, for the calculation of Markstein length. As shown in Fig. 7.6, burning velocity varied more or less linearly with stretch in the region of 70-400 s^{-1} for equivalence ratios 0.75, 0.84 and 1.0. It is to be noted that accurate evaluation of stretch required temperature fields to be computed on a very fine grid as stretch is highly sensitive to the grid size. The results presented here were all obtained on a grid of size 140 × 140. A moderate flow rate of 0.6 m/s gave a relatively short flame height, so that a high density of grid nodes was obtained. For the region of 70-400 s^{-1}, Markstein lengths could be estimated using the formulation given in Eq. 7.5 together with Eq. 1.11.

Thus, if the computed data are fitted with the least square method (Figs. 7.9 to 7.14), the Markstein length is the gradient of the best fit line, and the laminar burning velocity u_l the interception with $A^{-1}\,(dA/dt) = 0$.

Table 7.3

Computationally evaluated Markstein lengths $\mathcal{L}$ (mm).

$\phi = 0.75$	$\phi = 0.84$	$\phi = 1.0$
0.026	0.071	0.107

7.5.5 Comparison of values

The values of Markstein lengths $\mathcal{L}$, estimated in this way, for the three equivalence ratios are tabulated in Table 7.2. Significant variations in values are observed. Indeed,

even a general trend is none too clear. For example, Tseng *et al.* (1993), Rogg (1988) and the present study suggest an increase of Markstein lengths with equivalence ratio, whereas Searby and Quinard (1990) and Clavin and Joulin (1983) suggest a decrease, whilst Taylor (1991) and Ali *et al.* (1993) suggests a decrease followed by an increase. To some extent, the scatter of the Markstein lengths is probably related to the method of their determination. Importantly, different types of stretch may exist in different experimental configurations. This is illustrated by the aerodynamic strain dominance of the stagnation point flow configuration and the existence of both curvature stretch and aerodynamic straining in the expanding spherical flame. The isotherm at which the Markstein lengths defined also is important. While the present study adopted the conventional 300 K isotherm, experimental measurements required that the burning velocity and stretch be obtained at a higher temperature. Moreover, depending on the experimental technique used, the isotherms at which measurements taken are different. These factors all contribute to the scatter and the difficulty in comparing Markstein lengths. However, with the degree of scatter in mind, it is clear from Table 7.2 that the Markstein lengths obtained from the present study fell within the range set by the other measurements.

7.6 Multiple Markstein Lengths

Although some asymptotic analyses reveal a linear relationship between burning velocity and flame stretch, bearing in mind the complexities of flame structure, there is no reason why this should be universal. Indeed, there is no reason why curvature stretch should affect a flame in the same way as that arising from aerodynamic strain. However, without a detailed analytical solution and comprehensive experimental measurement, a linear relationship is, perhaps, the best one can propose without detailed chemical kinetics.

Based on a phenomenological analysis, Clavin and Joulin (1989) proposed the use of four Markstein lengths rather than one. With their expression (Eq. 1.16), two separate Markstein lengths were assigned for curvature stretch and straining. The two remaining terms were concerned with spatial and time dependent compressibility of the

fluid. These are most relevant to gasoline engine combustion, but they are generally ignored, and will not be considered here. With two Markstein lengths, $\mathcal{L}_c$ and $\mathcal{L}_s$, for curvature stretch and straining, Eq. 1.15 becomes:

$$u_l - u_n = \mathcal{L}_s n.\nabla v.n + \mathcal{L}_c u_n \left(\frac{1}{R_1} + \frac{1}{R_2} \right). \tag{7.6}$$

As far as is known, experimental and computational evaluations of these two separate Markstein lengths have not yet been attempted. In the following sections, they are evaluated systematically from the computational results.

7.6.1 Curvature and aerodynamic stretch

In a two-dimensional axisymmetric flame, and most practical flames, curvature and aerodynamic stretch co-exist. To determine their individual effects on burning velocity, they must be separated. In the present study, curvature stretch dominates at high flow rates while aerodynamic stretch dominates at low flow rates (Section 7.3). In the following analysis, curvature stretch was neglected at the low flow rate of 0.4 m/s and aerodynamic stretch at the high flow rate of 1.0 m/s.

7.6.2 Markstein length for curvature stretch

In the previous section, it was demonstrated that aerodynamic stretch can be neglected at high flow rate. In situations where only curvature stretch exist, Eq. 7.6 reduces to:

$$u_l - u_n = \mathcal{L}_c u_n \left(\frac{1}{R_1} + \frac{1}{R_2} \right). \tag{7.7}$$

With the expression derived for stationary two-dimensional flames (Eq. 2.43) gives:

$$u_l - u_n = \mathcal{L}_c u_n \left(\sin\alpha \frac{\partial \alpha}{\partial y} - \cos\alpha \frac{\partial \alpha}{\partial x} \right). \tag{7.8}$$

By plotting the normal burning velocity u_n against the curvature stretch along a 300 K isotherm, the gradient of the curve yields Markstein length $\mathcal{L}_c$. While the normal burning velocity value u_n at zero stretch yields the laminar burning velocity u_l. At mean flow velocity of 1.0 m/s, the Markstein lengths $\mathcal{L}_c$, obtained from graphs of burning velocity against stretch (Figs. 7.9, 7.11 and 7.13), for methane-air mixtures with equivalence ratios of 1.0, 0.84 and 0.75, were given in Table 7.4. As shown in Figs. 7.9, 7.11 and 7.13, the least square curve fitting method is applied to regions of high stretch, this is because the dominance of curvature stretch diminishes as the magnitude of stretch reduces (Section 7.3.2). With the present analysis, only regions where the magnitude of curvature stretch is ten times that of aerodynamic straining is considered. The positive sign of the length $\mathcal{L}_c$ clearly indicated that increases of curvature stretch decreases burning velocity.

Table 7.4

Computationally evaluated Markstein lengths $\mathcal{L}$, $\mathcal{L}_c$, $\mathcal{L}_s$ (mm).

	$\phi = 0.75$	$\phi = 0.84$	$\phi = 1.0$
$\mathcal{L}_c$	0.033	0.0114	0.0119
$\mathcal{L}_s$	-0.82	-0.65	-0.25
$\mathcal{L}$	0.026	0.071	0.107

Compared to the experimental values (Table 7.2), the present values were within the same order of magnitude of Clavin and Joulin (1983) and Rogg (1988) for all mixtures considered, although an order of magnitude difference is observed for stoichiometric mixtures when compared with the values of Taylor *et al.*, Tseng *et al.* and Bradley *et al.* The differences of lengths between the present study and experimental values arises from the different stretch ranges. The present lengths are obtained in the negative stretch whereas experimental values are obtained in the positive stretch region. With the present configuration, the positive curvature stretch rates are not large enough to justify a procedure that neglects aerodynamic straining, and Markstein lengths

obtained in the positive stretch region with the current procedure are not reliable. Another contribution to the differences in Markstein lengths is the different isotherms used in experiments and in the current evaluation. Taylor (1991) evaluated the length at a hot isotherm of 1450 K whereas the cold isotherm of 300 K is used in the present study.

7.6.3 Markstein length for aerodynamic straining

With curvature stretch neglected at low flow rates, Eq. 7.7 reduces to:

$$u_l - u_n = \mathcal{L}_s n.\nabla v.n \tag{7.9}$$

With the expression derived for stationary two-dimensional flames, Eq. 2.43:

$$u_l - u_n = \mathcal{L}_s \left[\cos^2\alpha \frac{\partial u}{\partial x} - \sin\alpha\cos\alpha \left(\frac{\partial u}{\partial y} + \frac{\partial v}{\partial x} \right) + \sin^2\alpha \frac{\partial v}{\partial y} \right]. \tag{7.10}$$

The stretched burning velocity is plotted against the square bracketed term in Eq. 7.10, both evaluated at the 300 K isotherm. The gradient yields the Markstein length for aerodynamic straining $\mathcal{L}_s$. For the present analysis, a low mean velocity of 0.4 m/s is used and the curvature stretch term is negligible. A ratio of at least 5 to 1 is used to ensure the dominance of aerodynamic straining. As shown in Figs. 7.10, 7.12 and 7.14, the least square curve fitting method is applied to regions of high stretch, because the dominance of aerodynamic straining diminishes as the magnitude of the stretch reduces (Section 7.3.2). The Markstein lengths, $\mathcal{L}_s$, obtained for equivalence ratios of 1.0, 0.84 and 0.75 are presented in Table 7.2. The values are more than an order of magnitude higher than those for curvature. Compared to the experimental values of Law *et al.* (Table 7.2), where aerodynamic stretch dominates, the Markstein lengths are all negative and of the same order of magnitude. It also is of interest to note that both studies of Law *et al.* (Table 7.2) and the present one show the lengths to increase with equivalence ratio.

7.6.4 Application to a stationary spherical flame

A stationary spherical flame is overall unstretched as the sum of contributions from the elementary terms that make up the stretch is zero. Both Taylor (1991) and Gu (1994) have shown that the burning velocity varies with flame radius if a reference surface of 300 K is used. These observations contradict with Eq. 7.5 which suggest that the burning velocity of a stationary spherical flame will be the same as a one-dimensional planar flame, as in both cases the overall stretch is zero. In this section, the concept of two Markstein lengths is applied to a stationary spherical flame, and offers an explanation of this observation.

Consider Eq. 7.6, for a one-dimensional planar flame, both strain and curvature stretch terms are zero, whereas for a spherical flame, these terms are not zero. They are equal and opposite in the case of a stationary spherical flame.

For such a flame, it has been shown that Appendix A:

$$\frac{1}{A}\frac{dA}{dt} = (u_n - u)\left(\sin\theta\frac{\partial\theta}{\partial x} - \cos\theta\frac{\partial\theta}{\partial y}\right), \tag{7.11}$$

for a spherical flame with radius r, Eq. 7.11 reduces to:

$$\frac{1}{A}\frac{dA}{dt} = -\frac{2u_n}{r} + \frac{2u_n}{r}.$$

$$= 0 \tag{7.12}$$

Substituting the straining and curvature terms into Eq. 7.6 gives:

$$u_l - u_n = \mathcal{L}_s\frac{2u_n}{r} - \mathcal{L}_c\frac{2u_n}{r}. \tag{7.13}$$

Thus, the burning velocities from a one-dimensional flat flame and a stationary spherical flame can only be identical if the contributions from the strain and curvature terms are the same, i.e. if they both have the same Markstein length ($\mathcal{L}_s = \mathcal{L}_c$).

For a stationary spherical flame, Clavin and Joulin (1989) deduced that:

$$u_l - u_n = (\mathcal{L}_c - \mathcal{L}_s)\frac{2u_n}{r} + 0\left(\frac{u_n d}{r}\right). \qquad (7.14)$$

However, the authors postulated that the burning velocities of a stationary spherical flame is always equal to that of a one-dimensional flat flame, and deduced that $\mathcal{L}_c = \mathcal{L}_s = \mathcal{L}$. From the modelling results of Taylor (1991) and Gu (1994), the reduction of burning velocity varied with radius and clearly $\mathcal{L}_c \neq \mathcal{L}_s$. Indeed, from their burning velocity against radius curve, there is an inverse dependence of burning velocity on radius, this reflects the $1/r$ factor in the $2U_n / r$ term above.

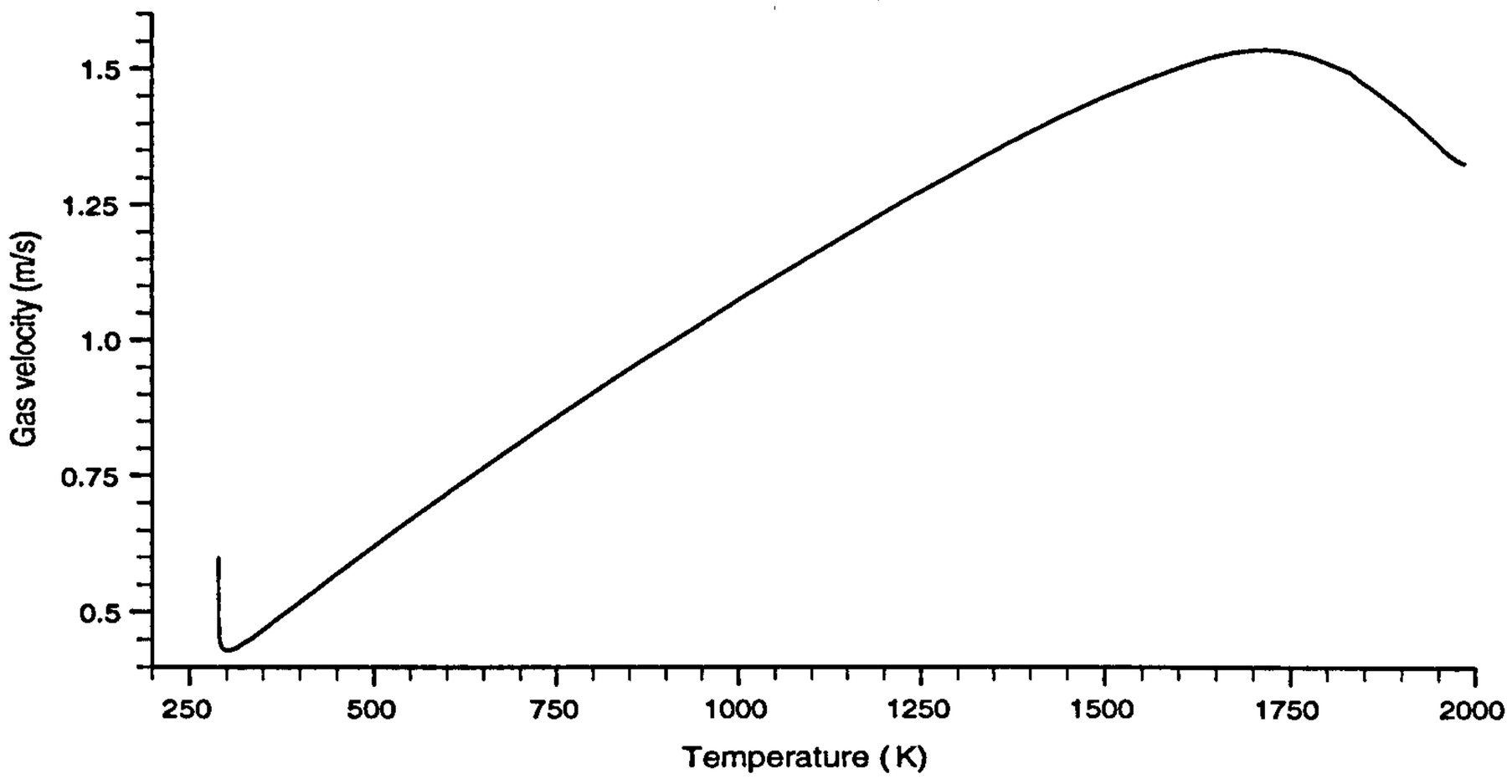

Fig. 7.1 Variation of burning velocity with temperature along the symmetry axis of an asymmetric flame with mean flow velocity v_m= 0.4 m/s and $\phi = 0.84$.

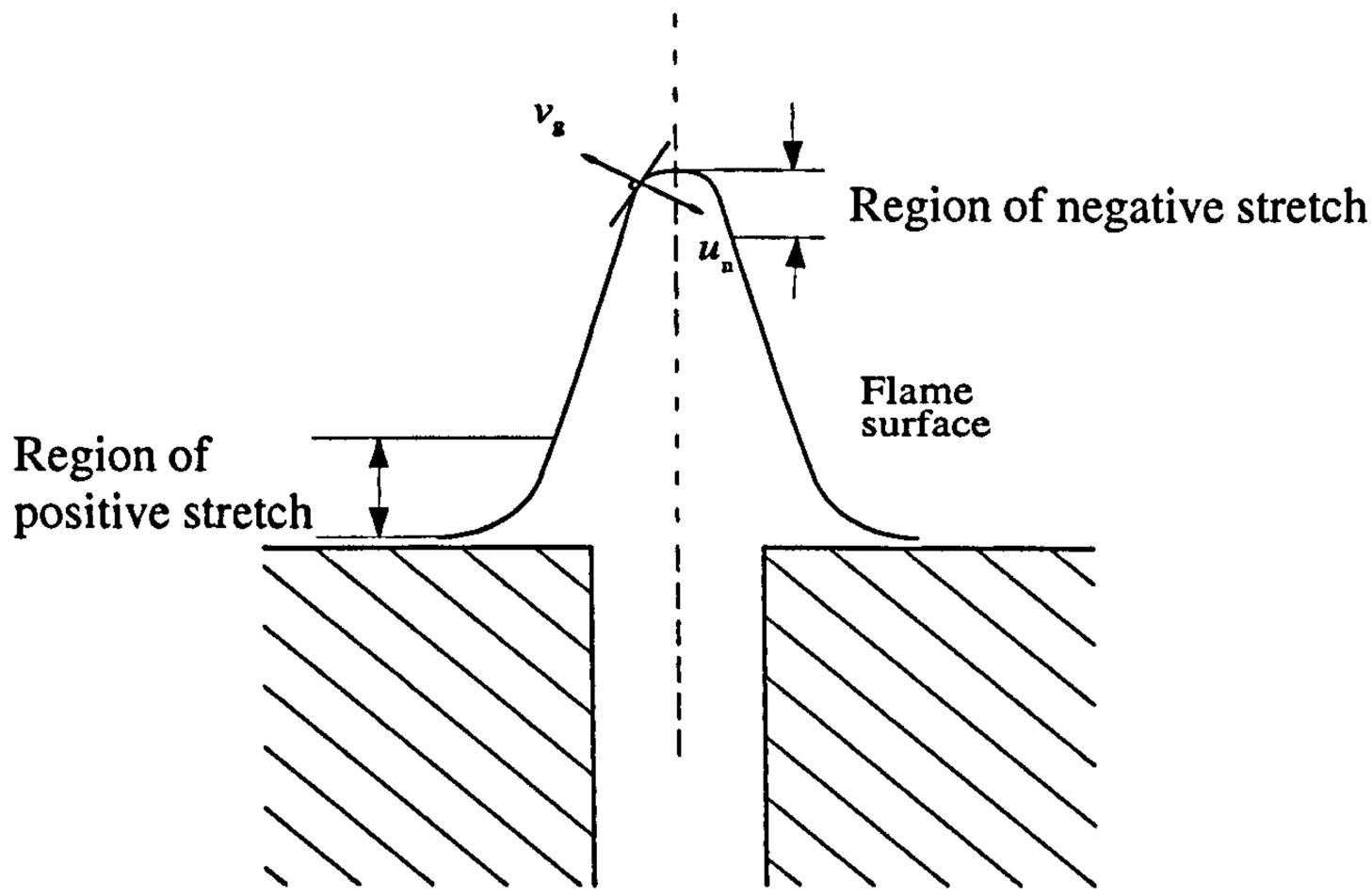

Fig. 7.2 Definition of burning velocity for a two-dimensional, stationary, curved flame.

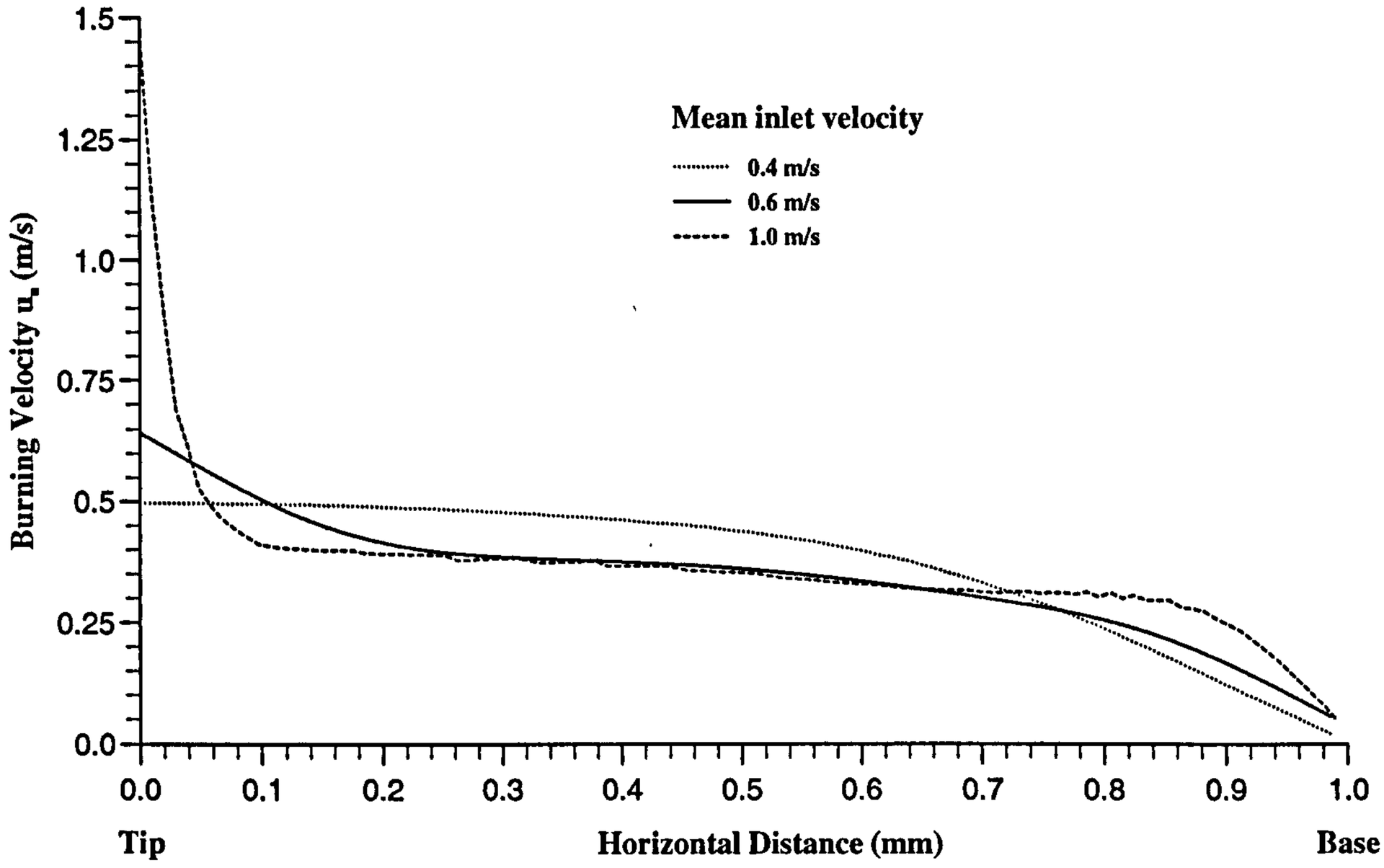

Fig. 7.3 Burning velocities along a 300K isotherm of a stoichiometric, axisymmetric, flame at various flow velocities.

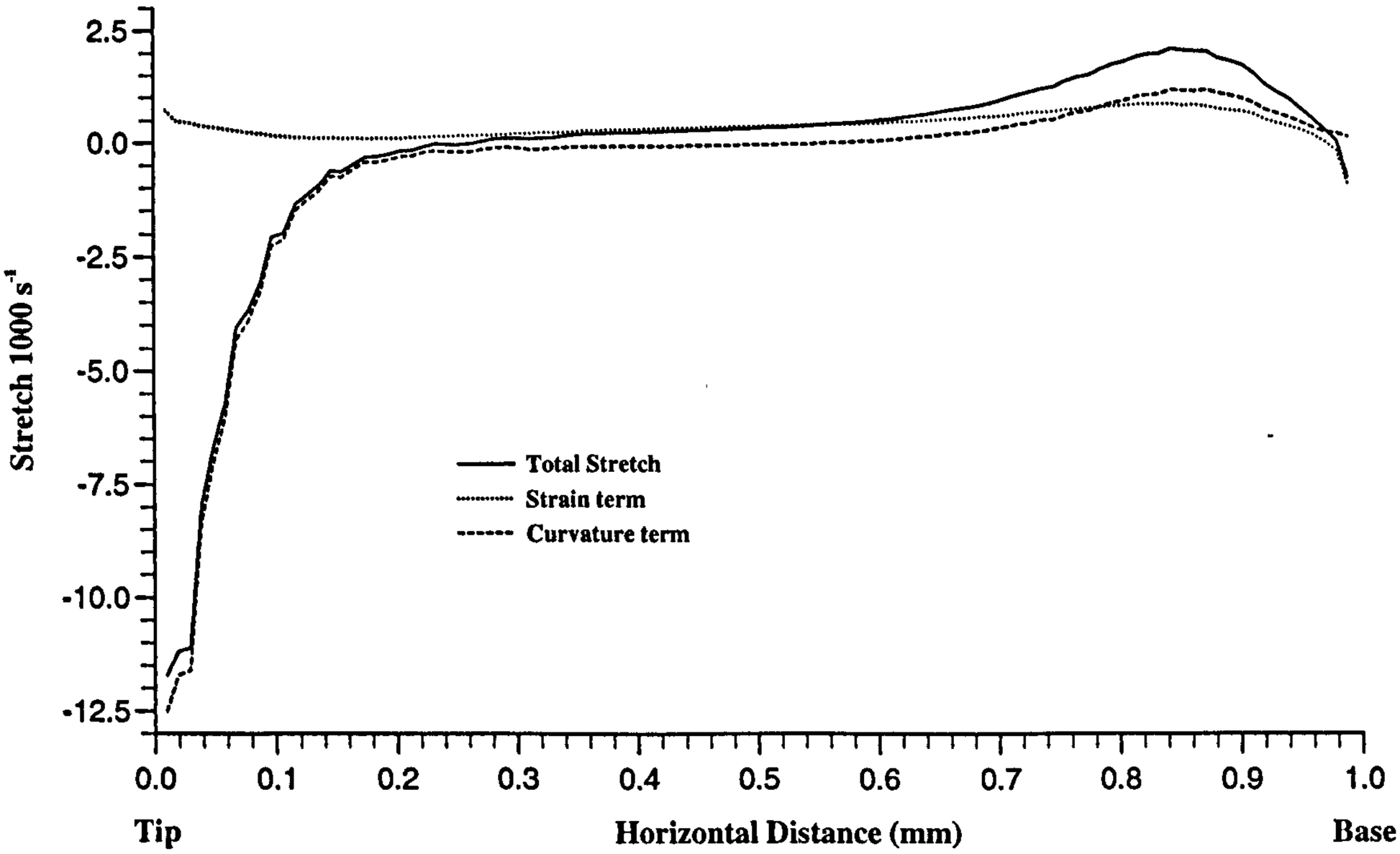

Fig. 7.4 Distribution of total stretch and its components in an asymmetric flame with mean inlet velocity v_m = 1.0 m/s and ϕ = 0.84.

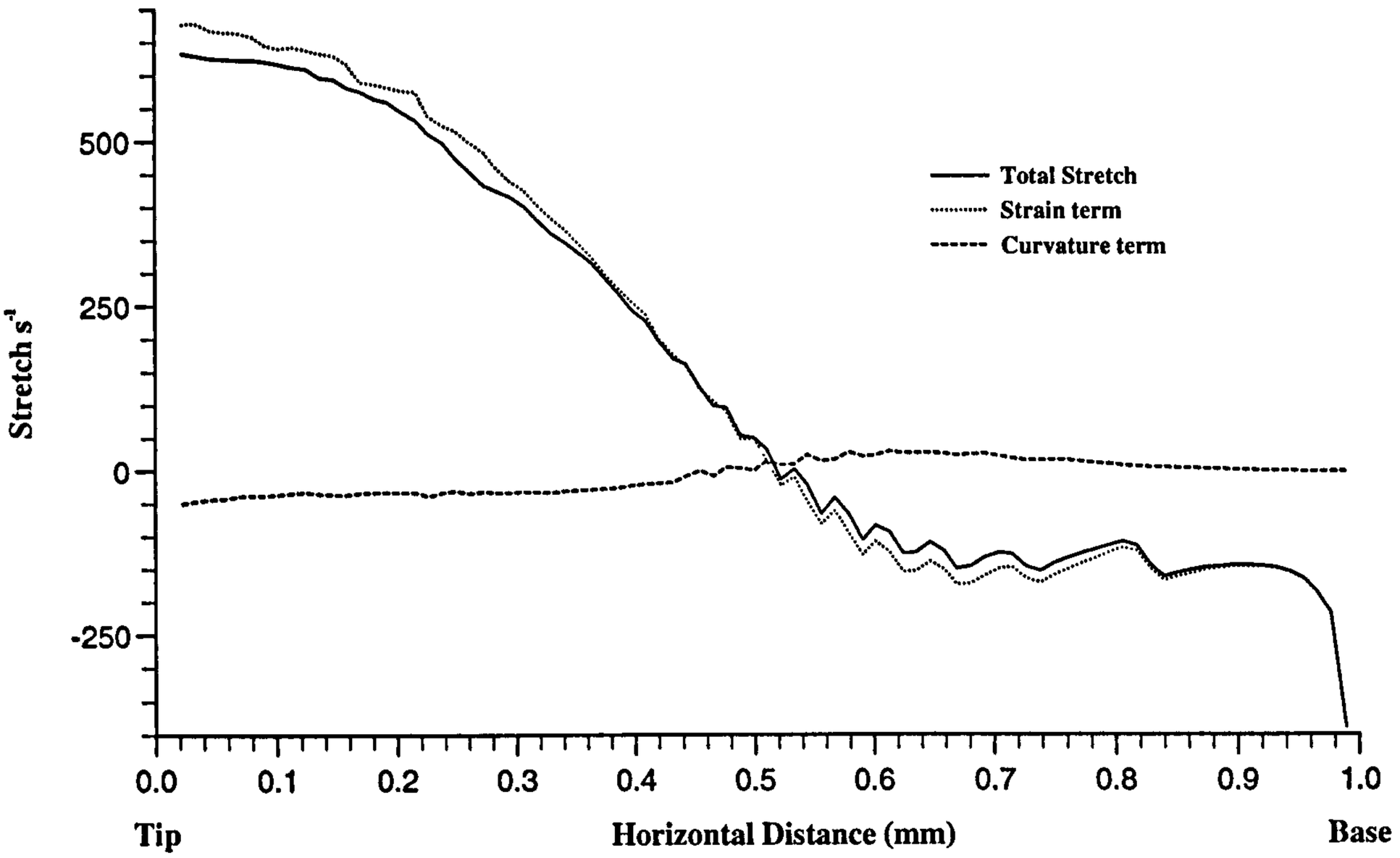

Fig. 7.5 Distribution of total stretch and its components in an axisymmetric flame with mean inlet velocity $v_m = 0.4$ m/s and $\phi = 0.84$.

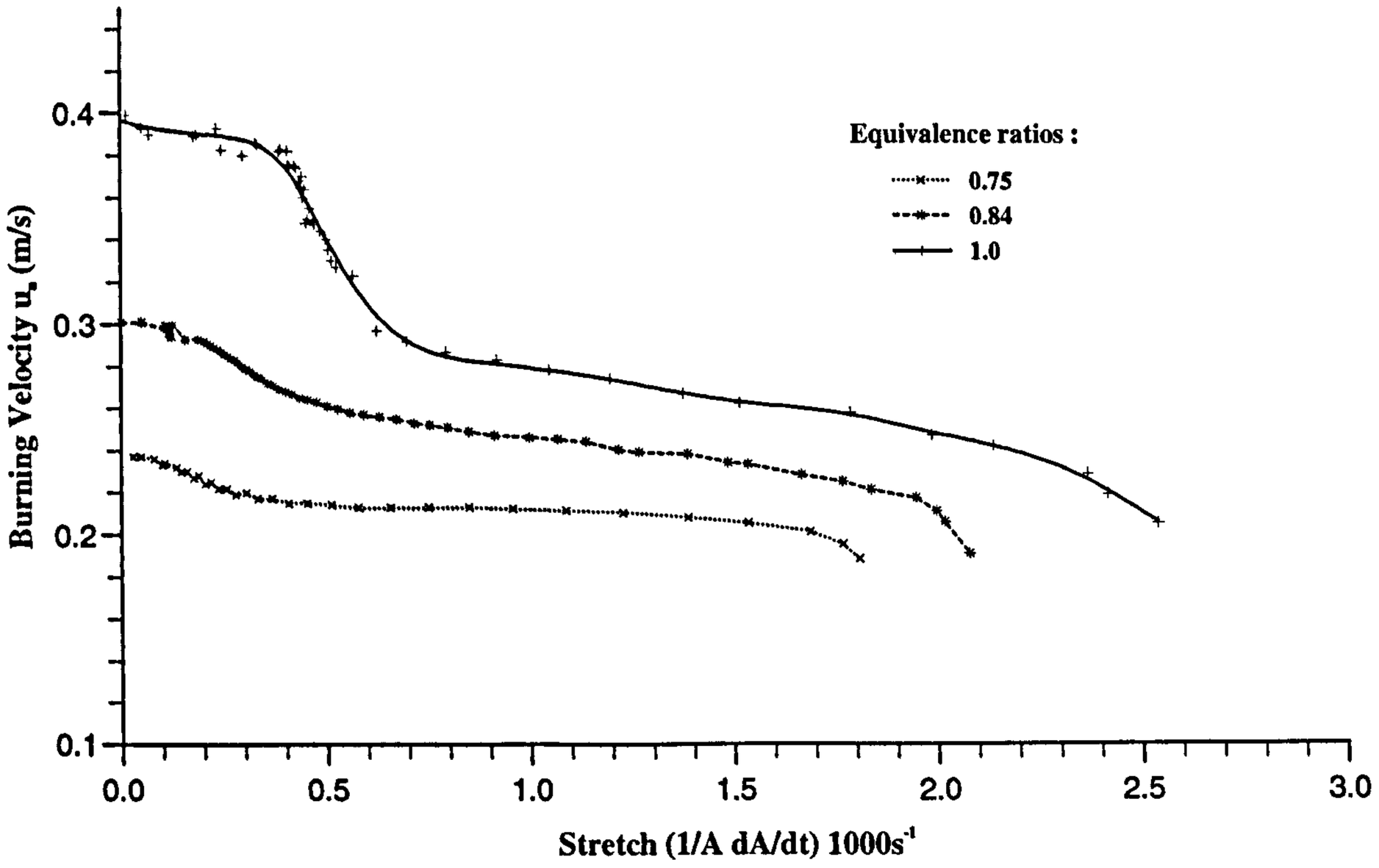

Fig. 7.6 Variation of burning velocity in the positively stretched region of an axisymmetric flame.

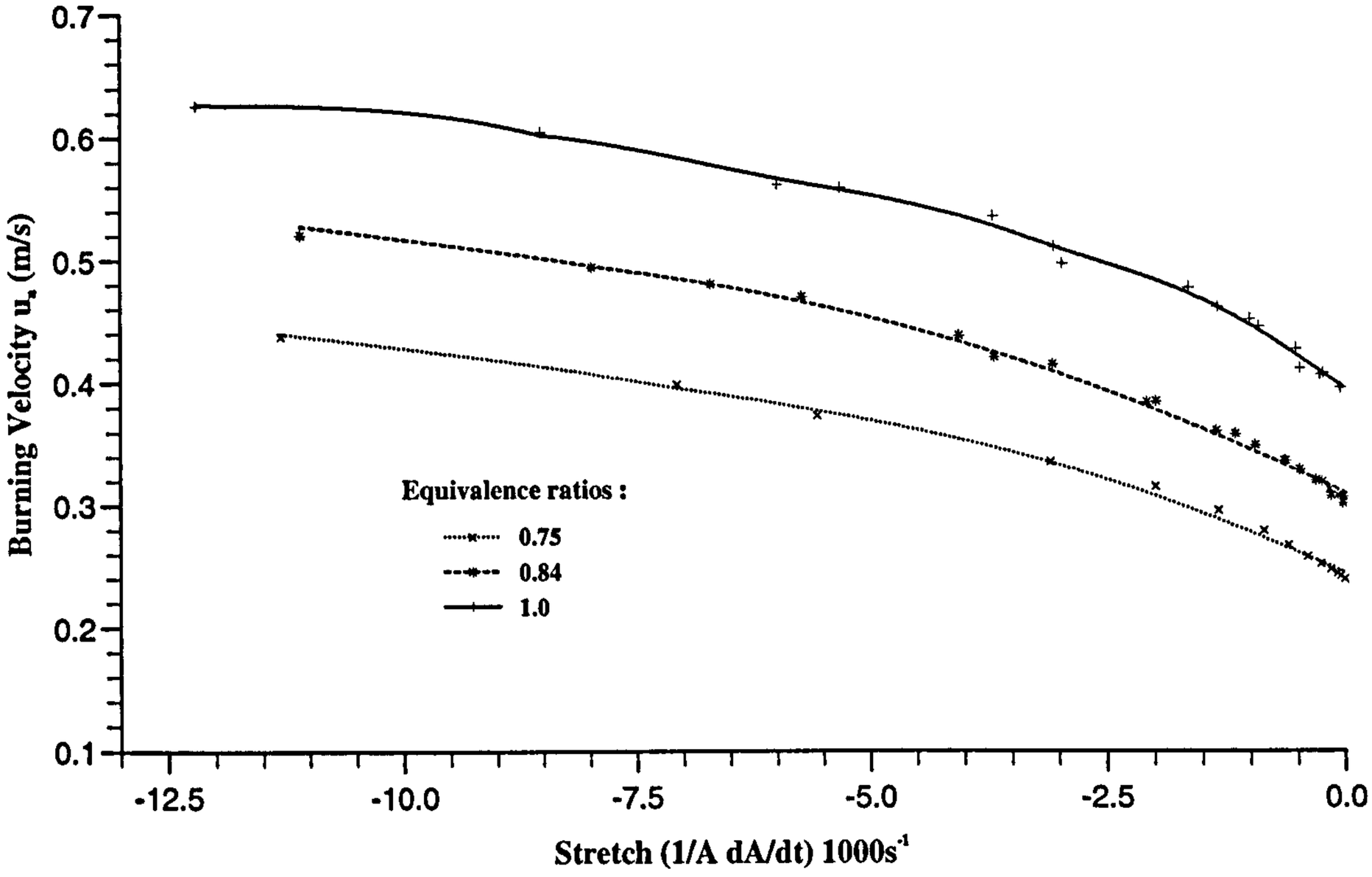

Fig. 7.7 Variation of burning velocity in the negatively stretched region of an axisymmetric flame.

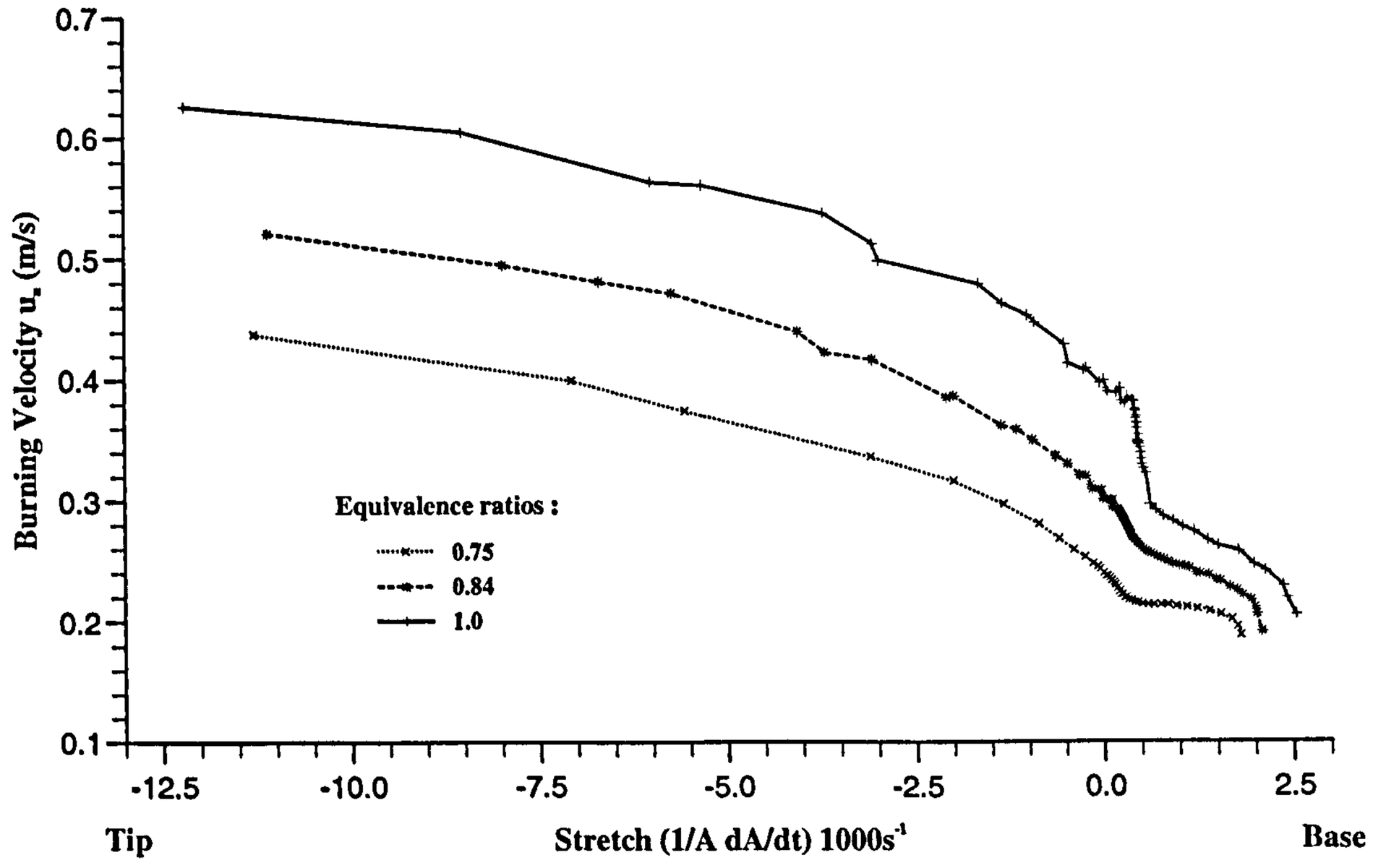

Fig. 7.8 Variation of burning velocity in an axisymmetric flame for various equivalence ratios.

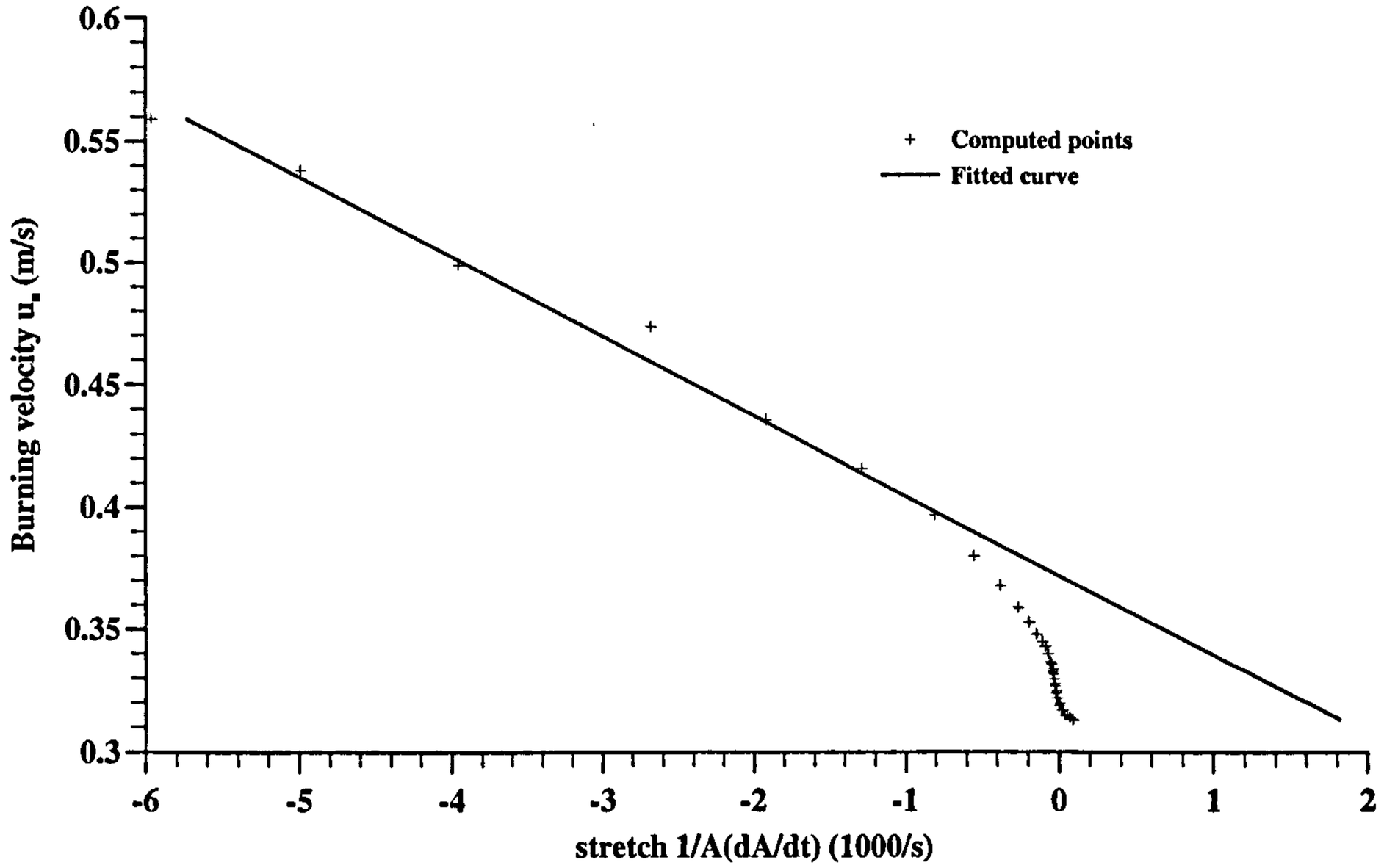

Fig. 7.9 Determination of Markstein length for curvature stretch from an axisymmetric flame with $v_m = 0.7$ m/s and $\phi = 0.75$.

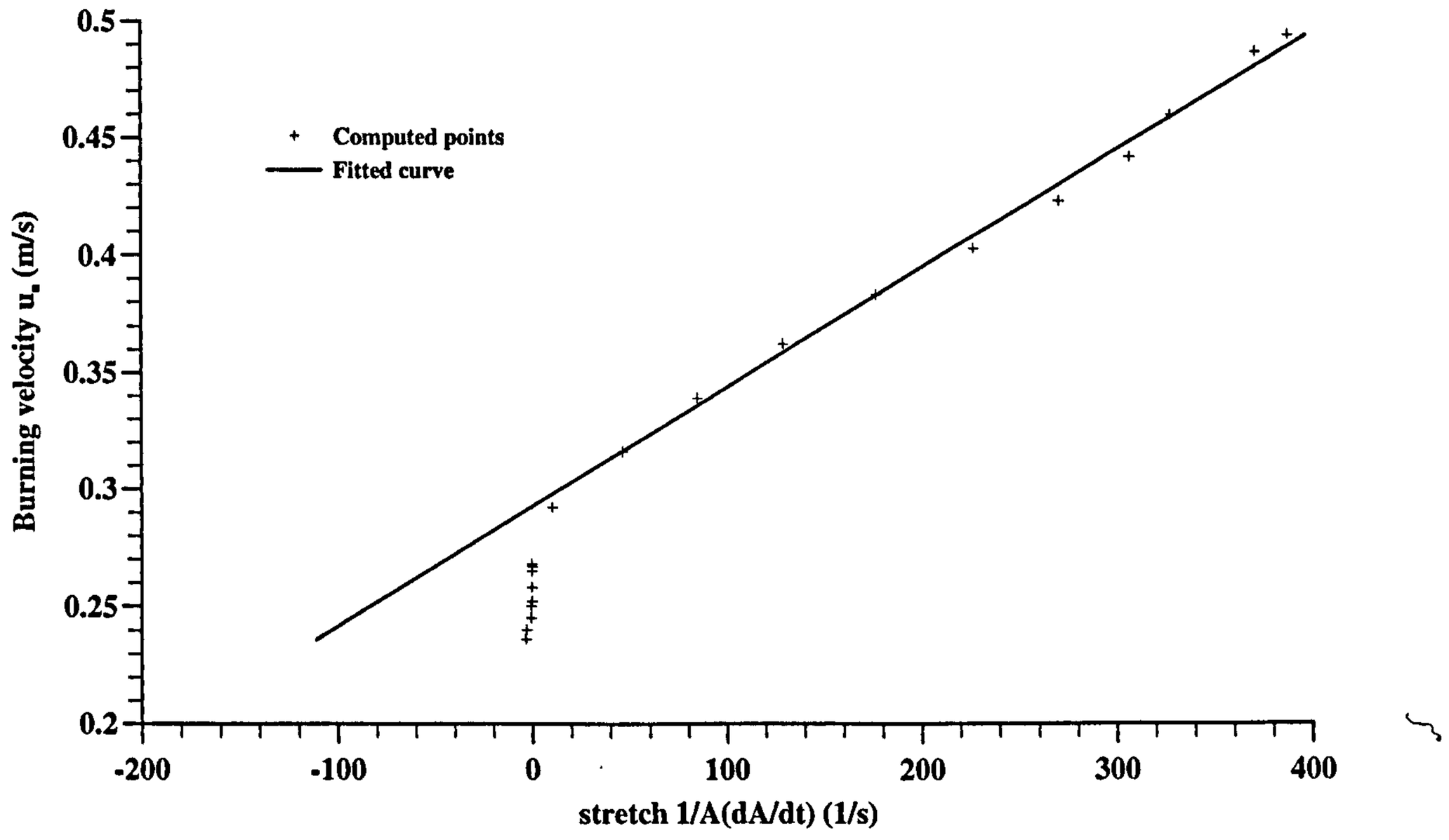

Fig. 7.10 Determination of Markstein length for aerodynamic strainning from an axisymmetric flame with $v_m = 0.3$ m/s and $\phi = 0.75$.

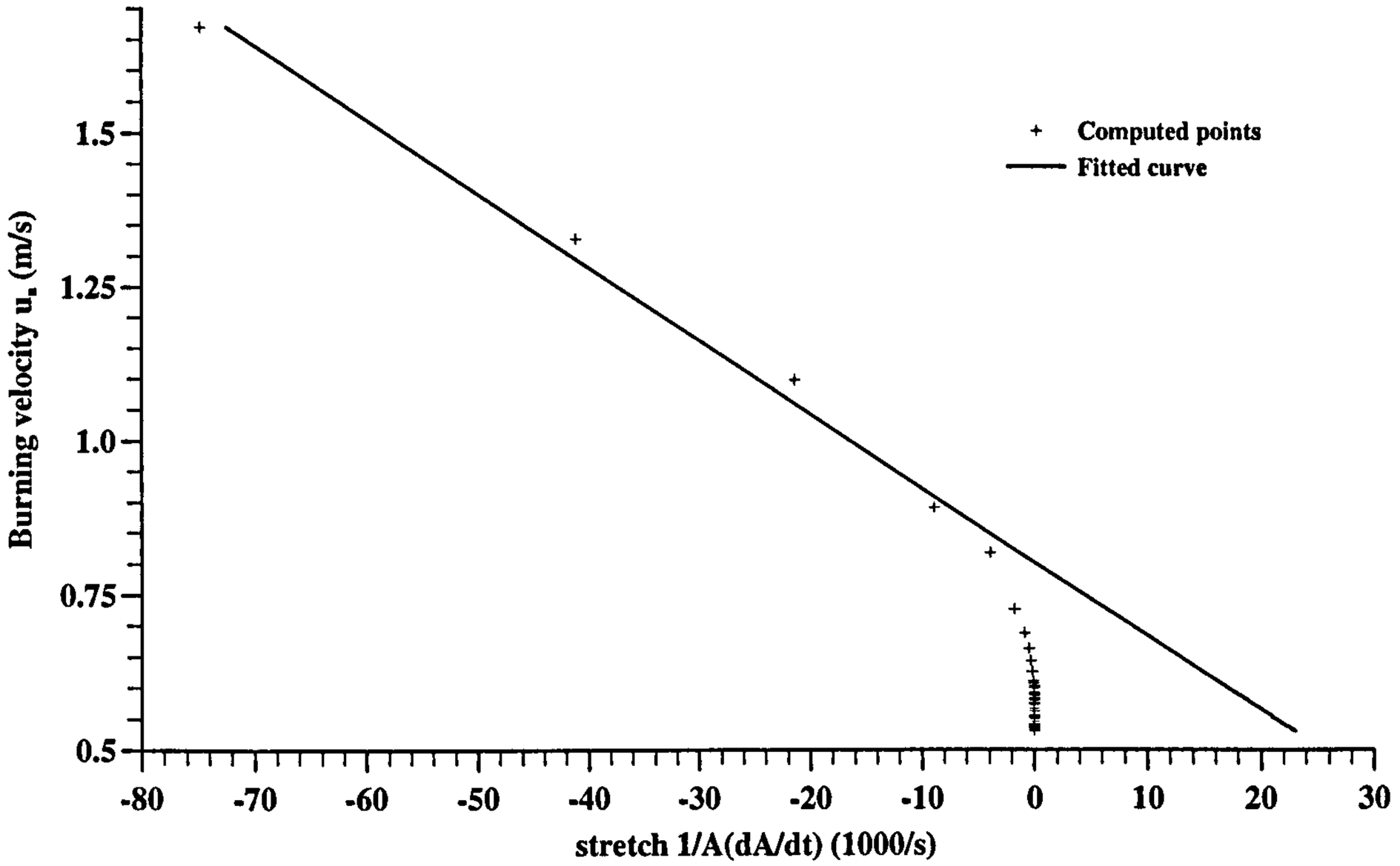

Fig. 7.11 Determination of Markstein length for curvature stretch from an axisymmetric flame with v_m = 1.0 m/s and ϕ = 0.84.

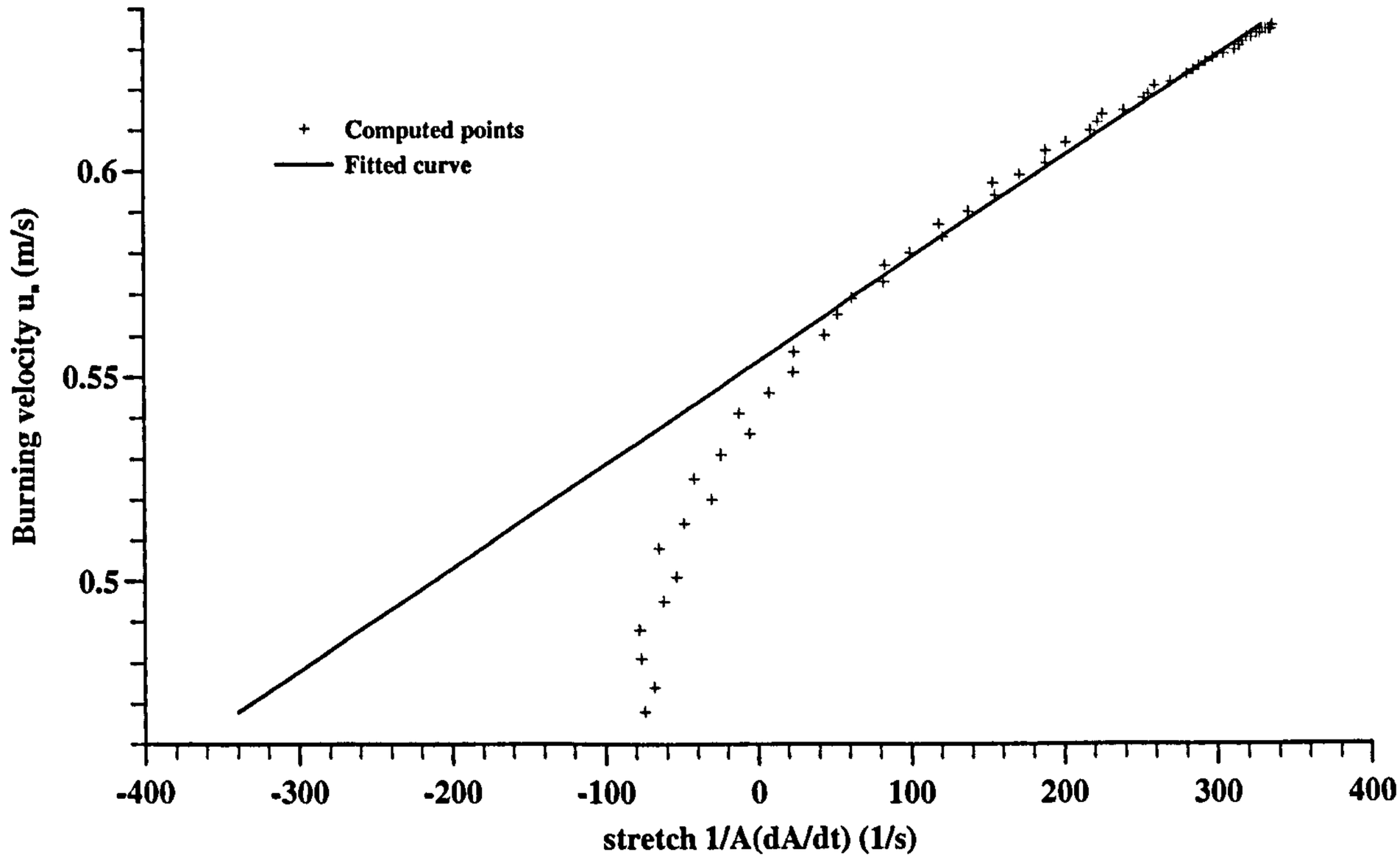

Fig. 7.12 Determination of Markstein length for aerodynamic straining from an axisymmetric flame with v_m = 0.4 m/s and ϕ = 0.84.

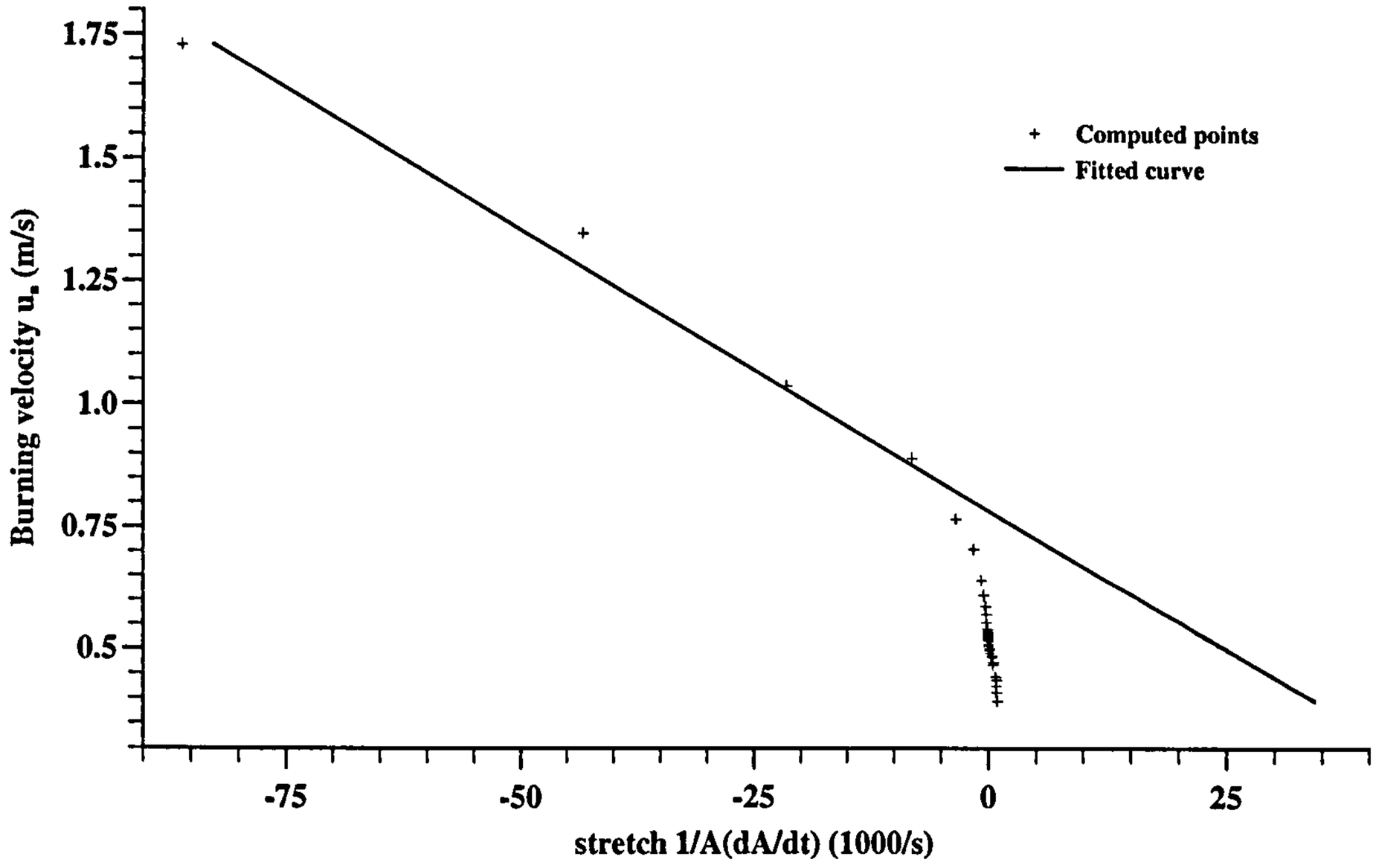

Fig. 7.13 Determination of Markstein length for curvature stretch from an axisymmetric flame with v_m = 1.0 m/s and ϕ = 1.0.

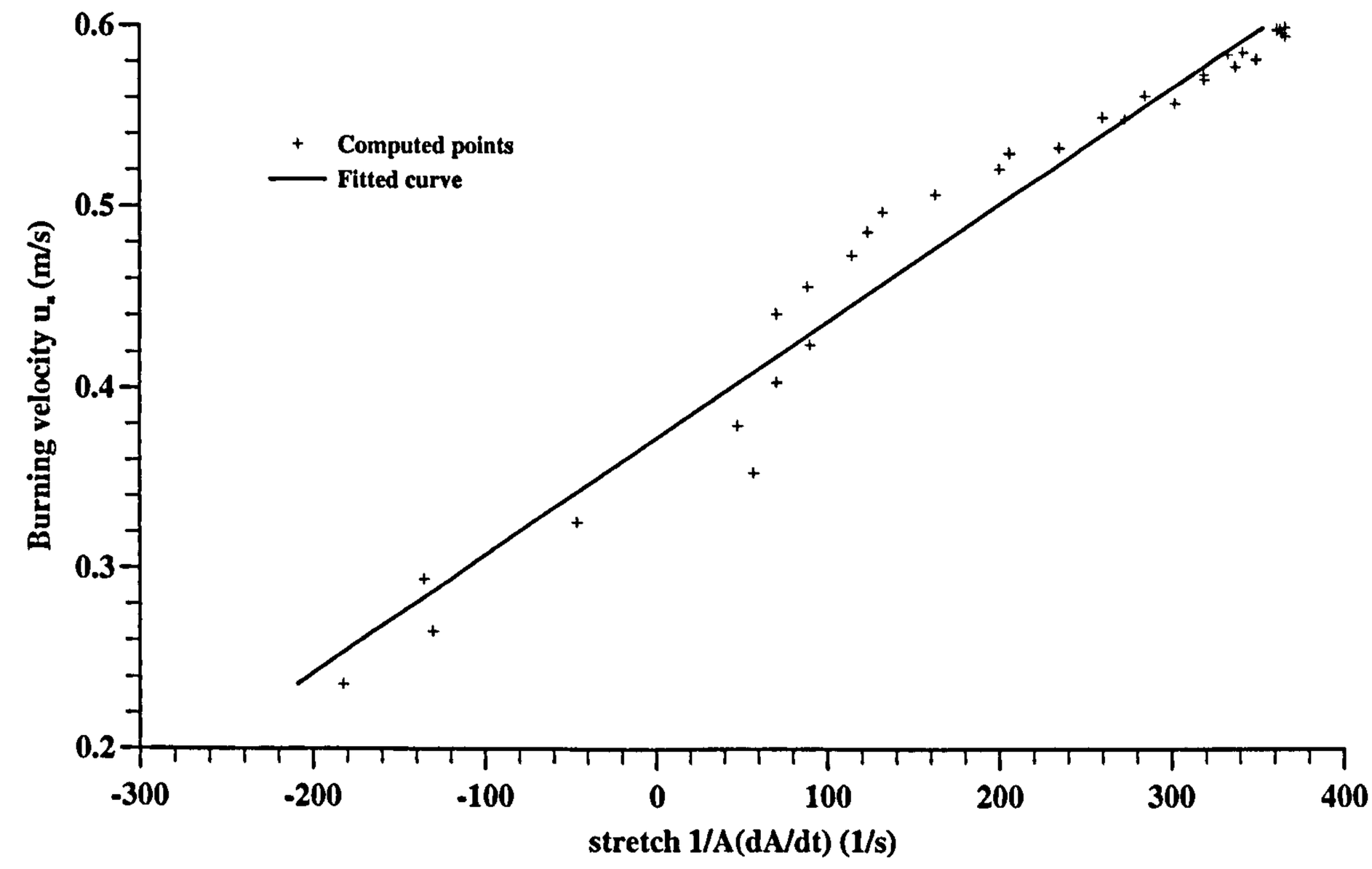

Fig. 7.14 Determination of Markstein length for aerodynamic straining from an axisymmetric flame with v_m = 0.4 m/s and ϕ = 1.0.

CHAPTER EIGHT
Conclusions and Suggestions for Future work

8.1 Conclusions

The major objective of the research was to develop efficient and robust mathematical models for the analysis of two-dimensional methane-air premixed axisymmetric flames. The chemical source terms present major computational demands. They were minimised with reduced schemes. These were the heat release rate scheme and the reduced chemical kinetic schemes. As partial validation of the model, CARS temperatures were measured on a multiple slot burner supplied by British Gas plc. The overall conclusions which emerged now are summarised.

1. A computer program based on the heat release rate approximation for a two-dimensional axisymmetric flame analysis has been developed. This heat release model was less satisfactory at higher flow rates. It could neither predict the effect of negative strain rate nor predict the effects of curvature flame stretch and aerodynamic straining separately. In general, its main use was to obtain initial estimates for use in the reduced model.

2. Efforts were therefore directed at the development of a reduced chemical kinetic scheme. The P1 scheme has been successfully developed and the predictions from it showed good agreement with the "full" scheme of Dixon-Lewis and also experimental results. The computed results demonstrated grid independence in a number of tests. Very good initial estimates, however, were required for the reduced

model, particularly at high flow rates, and the solutions could take as long as three weeks to obtained.

3. The implementation of the more recent reduced kinetic (MP) scheme, to the two-dimensional, axisymmetric flame, proved to be more difficult. The main reason lay in the complex relations introduced by the additional steady state species. Indeed, the improvements associated with this scheme, which include more steady state species, are still to be tested in two-dimensional models. Numerical convergence is relatively slow compared to that in the P1 scheme.

4. Temperature profiles have been measured using the CARS technique on the centre slot of the multi-slot burner. Three mixtures with different flow rates were examined in the experiments. Overall, the measured temperature profiles validated the P1 model, but the heat loss to the burner tube seemed to be underestimated by the model.

5. Complete profiles of flame structure were obtained with the model for a stoichiometric mixture over a range of flow rates. The height of the flame is well predicted by the model. Heat loss to the burner tube is important and can range between 5 and 32 % of the chemical energy in the initial mixture.

6. The computations revealed the importance of the flame stretch variations in the flow field. At low flow rates the base of the flame has a negative stretch rate, while the flame tip is positively stretched. At high flow rates the stretch rates are completely opposite to this state of affairs. Because of stability problems no computations could be completed close to lift off or flash back. Further work is necessary here on the role of stretch rate at these limit conditions.

7. The computations also revealed some fundamental aspects of the influences of stretch rates upon burning velocities. In particular, the effects of stretch on burning velocity

were, probably for the first time, comprehensively investigated in a two-dimensional field. The computed results showed burning velocity to be substantially affected by flame stretch, and burning velocities to be significantly increased by negative stretch. The effects of stretch are embodied in the Markstein lengths and values of these are found for different values of equivalence ratio. These are compared with values obtained experimentally by other researchers. There is good agreement between the present values and those of others, despite the large scatter in the experimental values.

8. The results further showed that the importance of the two contributions to flame stretch, namely flame curvature and aerodynamic straining. Their separate effects on burning velocities are very different. It is found to be appropriate to introduce two Markstein lengths to correlate the separate effects of the two components of stretch. Values of Markstein lengths for flame curvature and aerodynamic straining are presented. The effect of the latter on the burning velocity is more important than that of the former.

8.2 Suggestions for Future Work

1. Chemical kinetic schemes

This thesis has demonstrated the implementation of realistic chemical kinetic schemes, included the C_1-chain only, in a two-dimensional premixed flame model. Extension to diffusion flames would appear to require the C_2 and C_3 chains to be included in the reduced scheme. The work of Mauss and Peters (1993), who have demonstrated that C_2 and C_3 chains can be included in their reduced scheme, provides a good introduction to this subject.

This is the basis for the introduction of "complete" schemes with more chemical species and elementary reactions, in two-dimensional flames, in the future. Indeed, with the dramatic increases of computing power over recent years, the introduction of "complete" kinetic schemes in two-dimensional or even three-dimensional flames very soon becomes a possibility.

2. **Burner heat loss, mixture preheat and flame stability**

This is an important area of flame stability analysis and is a natural extension of the present researches. As indicated by the CARS measurements in the present work, there was an indication of significant heat loss to the burner walls. In practice, the heat loss can result in some preheating of the fresh mixture. A full consideration of the heat loss and mixture preheat is necessary for realistic predictions of flame stability. At high flow rates, it would be valuable to examine the detailed conditions for blow-off at the flame base and tip. It also would be beneficial if parametric studies are performed to investigate the effects of heat loss and mixture preheat on flame stability.

3. **Numerical techniques**

For any curved flame surfaces, an indiscriminate, rectangular, refinement is computationally inefficient. A better strategy is that of local grid refinement, either by enrichment or by adaptation of the available grid. To apply the proposed models to practical devices, non-orthogonal grid algorithms should be introduced. Although higher order discretisation schemes give good accuracy of solutions, these can be further improved by grid refinement together with multi-grid acceleration.

4. **Correlation of burning velocity and stretch**

This research has demonstrated the non-linear relationship of burning velocity and stretch, and proposed an appropriate correlation with two Markstein lengths. This proposal, however, requires the support of separate computational, or preferably, experimental data.

Appendix A Stretch of Some Specific Flame Configurations

Consider the general expression for flame stretch as given in Eq. 2.38. For a two-dimensional flow field, the unit normal vector n, the differential operator ∇ and the fluid velocity v are given by:

$$n = n_i\, i + n_j\, j \tag{A.1}$$

$$\nabla = \frac{\partial}{\partial x}\, i + \frac{\partial}{\partial y}\, j \tag{A.2}$$

and

$$v = u_x\, i + u_y\, j \tag{A.3}$$

thus,

$$n.\nabla = (n_i\, i + n_j\, j)\left(\frac{\partial}{\partial x}\, i + \frac{\partial}{\partial y}\, j\right)$$

$$= n_i \frac{\partial}{\partial x} + n_j \frac{\partial}{\partial y} \tag{A.4}$$

$$n.\nabla v = \left(n_i \frac{\partial}{\partial x} + n_j \frac{\partial}{\partial y}\right)\left(u_x\, i + u_y\, j\right)$$

$$= \left(n_i \frac{\partial u_x}{\partial x} + n_j \frac{\partial u_x}{\partial y}\right) i + \left(n_i \frac{\partial u_y}{\partial x} + n_j \frac{\partial u_y}{\partial y}\right) j \tag{A.5}$$

$$nn:\nabla v = \left(n_i\, i + n_j\, j\right)\left[\left(n_i \frac{\partial u_x}{\partial x} + n_j \frac{\partial u_x}{\partial y}\right) i + \left(n_i \frac{\partial u_y}{\partial x} + n_j \frac{\partial u_y}{\partial y}\right) j\right]$$

$$= n_i^2 \frac{\partial u_x}{\partial x} + n_i n_j \frac{\partial u_x}{\partial y} + n_i n_j \frac{\partial u_y}{\partial x} + n_j^2 \frac{\partial u_y}{\partial y}$$

$$= n_i^2 \frac{\partial u_x}{\partial x} + n_i n_j \left(\frac{\partial u_x}{\partial y} + \frac{\partial u_y}{\partial x}\right) + n_j^2 \frac{\partial u_y}{\partial y} \tag{A.6}$$

$$\nabla.v = \left(\frac{\partial}{\partial x}\, i + \frac{\partial}{\partial y}\, j\right)\left(u_x\, i + u_y\, j\right)$$

$$= \frac{\partial u_x}{\partial x} + \frac{\partial u_y}{\partial y} \tag{A.7}$$

$$\nabla.n = \left(\frac{\partial}{\partial x} i + \frac{\partial}{\partial y} j \right)\left(n_i i + n_j j \right)$$
$$= \frac{\partial n_i}{\partial x} + \frac{\partial n_j}{\partial y} \qquad \text{(A.8)}$$

therefore, the general expression for flame stretch becomes :

$$\frac{1}{A}\frac{dA}{dt} = -\left[n_i^2 \frac{\partial u_x}{\partial x} + n_i n_j \left(\frac{\partial u_x}{\partial y} + \frac{\partial u_y}{\partial x} \right) + n_j^2 \frac{\partial u_y}{\partial y} \right] + \frac{\partial u_x}{\partial x} + \frac{\partial u_y}{\partial y} + u_n \left(\frac{\partial n_i}{\partial x} + \frac{\partial n_j}{\partial y} \right)$$
$$= \left(1 - n_i^2 \right) \frac{\partial u_x}{\partial x} - n_i n_j \left(\frac{\partial u_x}{\partial y} + \frac{\partial u_y}{\partial x} \right) + \left(1 - n_j^2 \right) \frac{\partial u_y}{\partial y} + u_n \left(\frac{\partial n_i}{\partial x} + \frac{\partial n_j}{\partial y} \right) \qquad \text{(A.9)}$$

Stationary Two-Dimensional Flames

For a steady-state two-dimensional curved flame with two-dimensional flow field, the normal unit vector and velocity vector are given by :

$$n = \left(- \sin\alpha \, i - \cos\alpha \, j \right) \qquad \text{(A.10)}$$

$$u = \left(u i + v j \right) \qquad \text{(A.11)}$$

i.e.

$$n_i = - \sin\alpha, \; n_j = - \cos\alpha \text{; and } u_x = u, \; u_y = v. \qquad \text{(A.12)}$$

thus,

$$\frac{1}{A}\frac{dA}{dt} = \left(1 - \sin^2\alpha \right) \frac{\partial u}{\partial x} - \sin\alpha \cos\alpha \left(\frac{\partial u}{\partial y} + \frac{\partial v}{\partial x} \right)$$
$$+ \left(1 - \cos^2\alpha \right) \frac{\partial v}{\partial y} + u_n \left(\sin\alpha \frac{\partial \alpha}{\partial y} - \cos\alpha \frac{\partial \alpha}{\partial x} \right)$$
$$= \cos^2\alpha \frac{\partial u}{\partial x} - \sin\alpha \cos\alpha \left(\frac{\partial u}{\partial y} + \frac{\partial v}{\partial x} \right)$$
$$+ \sin^2\alpha \frac{\partial v}{\partial y} + u_n \left(\sin\alpha \frac{\partial \alpha}{\partial y} - \cos\alpha \frac{\partial \alpha}{\partial x} \right) \qquad \text{(A.13)}$$

with unidirectional shear flow, $v = u(y) \, i$, Eq. A.13 becomes :

$$\frac{1}{A}\frac{dA}{dt} = - \sin\alpha \cos\alpha \frac{\partial u}{\partial y} + u_n \frac{\partial \alpha}{\partial x} \qquad \text{(A.14)}$$

which is identical to that of Matalon (1983).

Cylindrical and Spherical Flames

For expanding cylindrical and spherical flames, $n = \left(-\cos\theta\, i - \sin\theta\, j\right)$, $v = \left(u\cos\theta\, i + u\sin\theta\, j\right)$, as shown in Fig. 2.2. Substituting in Eq. A.13 gives :

$$\frac{1}{A}\frac{dA}{dt} = \left(1 - \cos^2\theta\right)\frac{\partial u\cos\theta}{\partial x} - \sin\theta\cos\theta\left(\frac{\partial u\cos\theta}{\partial y} + \frac{\partial u\sin\theta}{\partial x}\right)$$

$$+ \left(1 - \sin^2\theta\right)\frac{\partial u\sin\theta}{\partial y} + u_n\left(\frac{\partial -\cos\theta}{\partial x} + \frac{\partial -\sin\theta}{\partial y}\right)$$

$$= -u\sin^3\theta\frac{\partial\theta}{\partial x} + u\sin^2\theta\cos\theta\frac{\partial\theta}{\partial y} - u\sin\theta\cos^2\theta\frac{\partial\theta}{\partial x}$$

$$+ u\cos^3\theta\frac{\partial\theta}{\partial y} + u_n\left(\sin\theta\frac{\partial\theta}{\partial x} - \cos\theta\frac{\partial\theta}{\partial y}\right)$$

$$= -u\sin\theta\left(\sin^2\theta + \cos^2\theta\right)\frac{\partial\theta}{\partial x} + u\cos\theta\left(\sin^2\theta + \cos^2\theta\right)\frac{\partial\theta}{\partial y}$$

$$+ u_n\left(\sin\theta\frac{\partial\theta}{\partial x} - \cos\theta\frac{\partial\theta}{\partial y}\right)$$

$$= -u\left(\sin\theta\frac{\partial\theta}{\partial x} - \cos\theta\frac{\partial\theta}{\partial y}\right) + u_n\left(\sin\theta\frac{\partial\theta}{\partial x} - \cos\theta\frac{\partial\theta}{\partial y}\right)$$

$$= \left(u_n - u\right)\left(\sin\theta\frac{\partial\theta}{\partial x} - \cos\theta\frac{\partial\theta}{\partial y}\right) \qquad \text{(A.15)}$$

Appendix B Computational Results with P1 Scheme

Table B.1

Computed results for lean ($\phi = 0.75$) methane-air flames with reduced mechanism (2 mm slot width).

Flow Rate ($X10^{-4}$ m^2/s)	Δ_S (mm)	Δ_H (mm)	Flame Height (mm)	Lift Off Height (mm)	Heat Loss to Base (W/slot)
0.80	0.493	0.334	2.207	0.888	222
0.90	0.505	0.363	2.526	0.926	229
1.00	0.519	0.373	2.863	0.947	232
1.10	0.519	0.389	3.158	0.953	234
1.20	0.511	0.426	3.368	0.946	235
1.40	0.529	0.459	3.908	0.962	237
1.57	0.551	0.434	4.409	1.001	213
1.70	0.566	0.508	4.632	1.043	243
2.00	0.680	0.494	5.489	1.080	225
2.40	0.797	0.607	6.316	1.146	257
2.80	0.860	0.625	7.303	1.182	260
3.20	0.964	0.712	8.289	1.205	265
3.40	0.976	0.691	9.032	1.238	271
3.60	1.029	0.718	9.484	1.278	276
3.80	1.023	0.771	9.871	1.282	278
4.00	1.047	0.776	10.46	1.303	279

Table B.2

Computed results for lean ($\phi = 0.84$) methane-air flames with reduced mechanism (2 mm slot width).

Flow Rate ($X10^{-4}$ m^2/s)	Δ_S (mm)	Δ_H (mm)	Flame Height (mm)	Lift Off Height (mm)	Heat Loss to Base (W/slot)
0.80	0.423	0.388	1.411	0.605	410
1.00	0.472	0.373	1.879	0.603	349
1.40	0.542	0.486	3.132	0.729	325
2.00	0.697	0.544	3.574	0.783	303
2.40	0.856	0.673	5.211	0.851	291
2.80	0.980	0.775	5.968	0.977	295
3.20	1.154	0.758	6.926	1.006	293
3.60	1.289	0.845	7.579	1.024	302
3.70	1.294	0.851	7.789	1.030	302
3.80	1.287	0.899	8.167	1.030	306
4.00	1.340	0.987	8.481	1.045	308

Table B.3

Computed results for lean ($\phi = 0.84$) methane-air flames with reduced mechanism (3 mm slot width).

Flow Rate ($X10^{-4}$ m^2/s)	Δ_S (mm)	Δ_H (mm)	Flame Height (mm)	Lift Off Height (mm)	Heat Loss to Base (W/slot)
1.20	0.436	0.420	1.895	0.570	445
1.50	0.468	0.448	2.684	0.606	444
1.80	0.521	0.460	3.408	0.640	428
2.10	0.629	0.584	4.737	0.772	415
2.40	0.711	0.587	4.605	0.769	398
2.55	0.776	0.610	5.066	0.820	402
2.70	0.917	0.608	5.474	0.855	403
2.85	0.899	0.701	5.645	0.852	401
3.00	0.945	0.714	6.158	0.966	386
3.15	0.913	0.719	6.329	0.978	385
3.30	0.970	0.760	6.632	1.045	380
3.60	1.048	0.796	7.303	1.126	375
3.90	1.195	0.866	7.829	1.167	380
4.20	1.384	0.917	8.421	1.204	382
4.50	1.314	0.948	8.974	1.251	376
4.80	1.444	1.004	9.263	1.327	375
5.10	1.411	0.946	10.39	1.315	370
5.40	1.378	0.979	11.06	1.316	371
5.70	1.344	0.991	11.52	1.319	372
6.00	1.371	0.989	12.19	1.326	374
6.30	1.435	0.934	12.87	1.331	375

Table B.4

Computed results for stoichiometric methane-air flames with reduced mechanism (2 mm slot width).

Flow Rate ($X10^{-4}$ m^2/s)	Δ_S (mm)	Δ_H (mm)	Flame Height (mm)	Lift Off Height (mm)	Heat Loss to Base (W/slot)
0.80	0.356	0.423	0.782	0.373	481
1.00	0.365	0.442	1.263	0.414	395
1.20	0.357	0.488	1.842	0.471	373
1.60	0.377	0.563	2.681	0.532	348
2.00	0.385	0.605	3.447	0.595	354
2.40	0.443	0.705	4.145	0.672	346
2.80	0.498	0.729	4.921	0.713	344
3.20	0.538	0.794	5.526	0.756	341
3.60	0.602	0.865	6.263	0.857	340
3.80	0.613	0.929	6.447	0.873	339
4.09	0.635	0.992	6.724	0.891	338
4.20	0.681	1.010	7.092	0.914	338
4.40	0.687	1.019	7.295	0.923	338

Table B.5

Computed results for stoichiometric methane-air flames with reduced mechanism (3 mm slot width).

Flow Rate ($X10^{-4}$ m^2/s)	Δ_S (mm)	Δ_H (mm)	Flame Height (mm)	Lift Off Height (mm)	Heat Loss to Base (W/slot)
1.20	0.361	0.477	1.061	0.366	653
1.50	0.353	0.471	1.895	0.413	608
1.80	0.347	0.522	2.487	0.410	605
2.40	0.358	0.583	3.579	0.480	576
2.49	0.361	0.579	3.704	0.482	544
3.00	0.394	0.645	4.547	0.616	541
3.60	0.487	0.728	5.684	0.747	494
4.20	0.601	0.772	6.816	0.800	462
4.80	0.709	0.887	7.368	0.904	472
5.40	0.719	0.952	8.526	0.929	440
6.00	0.785	1.003	9.474	1.008	426
6.60	0.955	1.036	10.59	1.108	418
7.20	0.992	1.079	11.68	1.211	406
7.80	0.996	1.136	12.32	1.292	410
8.10	1.010	1.208	12.43	1.301	406
8.25	1.075	1.194	12.97	1.354	408

Appendix C Raw Experimental Data

The experimental data presented here were measured with the CARS technique described in Chapter 6. In the following tables, x denotes the horizontal distance and y denotes the height above burner. These two parameters have been defined in Fig. 6.6. T_{mean} is the calculated mean temperature in K, while T_{max} and T_{min} were the maximum and minimum temperature in K, obtained from the accepted CARS spectra. δ is the standard derviation of the temperature readings, and were obtained via :

$$\delta = \sqrt{\frac{1}{N_a}\sum_{i=1}^{N_a}(T_i - T_{mean})^2} \qquad \text{(C1)}$$

where N_a is the number of accepted spectra readings, and N_T is the number of total spectra obtained in the experiment.

Table C1

Raw experimental data for methane-air mixture of equivalence ratio 0.75 and mean inlet velocity of 1.2 m/s.

x (mm)	y (mm)	T_{mean}	T_{max}	T_{min}	δ	N_T	N_a
0.00	0.00	360.87	487.64	280.67	40.070	100	56
0.00	8.60	393.80	518.23	298.18	67.587	100	26
0.00	9.20	478.43	578.38	371.68	52.029	100	31
0.00	9.60	474.82	583.61	376.33	56.734	100	20
0.00	10.00	483.07	618.15	385.62	56.996	100	26
0.00	10.40	484.23	1044.78	386.55	122.495	100	25
0.00	10.80	490.07	624.11	383.82	58.715	100	24
0.00	11.20	498.79	607.39	397.47	53.986	100	33
0.00	11.60	584.28	836.87	405.95	72.924	100	53
0.00	11.80	641.04	819.07	434.05	79.852	100	44
0.00	12.00	640.54	925.48	449.85	83.621	100	45
0.00	12.20	626.90	768.38	397.58	70.860	100	58
0.00	12.40	694.76	845.66	528.80	75.350	100	53
0.00	12.60	770.54	1243.32	542.26	115.002	100	62
0.00	12.80	894.85	1241.17	529.96	139.248	100	58
0.00	13.00	937.15	1383.10	680.42	148.172	100	70

Table C1 Raw experimental data ($\phi = 0.75$, $u = 1.2$ m/s) (continued)

x (mm)	y (mm)	T_{mean}	T_{max}	T_{min}	δ	N_T	N_a
0.00	13.20	1034.92	1553.23	684.17	156.330	100	73
0.00	13.40	1234.93	1599.51	875.64	197.585	100	74
0.00	13.60	1451.81	1771.63	931.55	168.621	100	85
0.00	13.80	1449.61	1653.18	992.51	136.130	100	75
0.00	14.00	1541.36	1714.17	1255.69	99.071	100	86
0.20	6.00	387.79	1981.37	274.68	248.338	100	43
0.20	7.00	392.04	477.76	300.84	44.033	100	22
0.20	7.80	451.09	538.70	414.81	34.360	100	12
0.20	8.40	462.25	539.08	327.12	52.892	100	11
0.20	9.00	428.69	509.31	291.39	52.507	100	15
0.20	9.40	470.90	562.16	393.23	55.955	100	15
0.20	9.80	446.26	536.69	344.81	49.488	100	24
0.20	10.20	489.95	623.64	414.12	58.652	100	15
0.20	10.60	517.54	600.99	377.29	58.107	100	23
0.20	11.00	546.78	761.16	422.25	87.318	100	33
0.20	11.40	603.58	760.35	403.69	77.228	100	40
0.20	11.60	678.05	807.14	497.87	68.521	100	48
0.20	11.80	643.38	739.18	494.27	63.379	100	38
0.20	12.00	692.69	893.31	511.26	81.237	100	44
0.20	12.20	875.61	1123.50	679.36	89.211	100	56
0.20	12.40	885.40	1250.55	734.77	108.733	100	42
0.20	12.60	950.59	1371.79	719.75	134.718	100	62
0.20	12.80	1014.99	1471.71	623.37	155.171	100	60
0.20	13.00	1187.83	1625.07	869.78	205.062	100	73
0.20	13.20	1308.52	1596.51	676.66	209.059	100	74
0.20	13.40	1410.38	1666.78	927.19	170.381	100	77
0.20	13.60	1537.92	1721.65	1094.91	115.227	100	83
0.20	14.00	1629.91	1810.40	1429.97	79.525	100	87
0.40	4.00	345.48	447.87	270.33	40.488	100	68
0.40	5.00	366.19	470.19	261.65	46.107	100	52
0.40	6.00	349.73	447.89	273.28	44.102	100	16
0.40	7.00	358.35	444.45	269.66	39.867	100	32
0.40	7.60	373.32	446.43	290.57	40.379	100	15
0.40	8.00	391.67	516.34	317.27	41.819	100	36
0.40	8.40	424.88	511.09	346.84	31.492	100	39
0.40	8.80	464.23	792.37	356.96	86.545	100	37
0.40	9.20	487.02	596.61	381.45	53.682	100	44
0.40	9.60	564.48	707.78	333.47	63.608	100	50
0.40	10.00	556.33	679.73	441.30	67.966	100	38
0.40	10.40	667.24	857.45	445.07	87.231	100	45
0.40	10.60	696.12	898.70	527.82	74.761	100	49
0.40	10.80	677.41	858.60	489.05	75.112	100	47
0.40	11.00	709.61	928.80	490.07	108.491	100	44
0.40	11.20	770.71	993.73	547.41	103.733	100	63
0.40	11.40	823.60	1110.62	523.48	121.049	100	56
0.40	11.60	1031.64	1505.12	693.00	161.298	100	64

Table C1 Raw experimental data ($\phi = 0.75$, $u = 1.2$ m/s) (continued)

x (mm)	y (mm)	T_{mean}	T_{max}	T_{min}	δ	N_T	N_a
0.40	11.80	1116.50	1458.09	834.27	135.172	100	67
0.40	12.00	959.00	1283.81	676.02	122.017	100	61
0.40	12.00	988.02	1365.11	568.14	135.535	100	64
0.40	12.20	1070.22	1418.67	724.57	153.836	100	71
0.40	12.40	1196.71	1632.49	816.15	161.794	100	75
0.40	12.60	1173.23	1644.83	898.03	170.148	100	73
0.40	12.80	1372.86	1696.66	1027.44	139.707	100	78
0.40	13.00	1446.44	1713.62	1138.04	122.277	100	79
0.40	13.40	1562.95	1752.20	1312.21	96.102	100	84
0.40	14.00	1582.61	1752.23	1283.31	95.374	100	81
0.60	3.40	360.49	454.44	268.02	41.211	100	75
0.60	4.40	377.02	515.09	291.68	54.376	100	21
0.60	5.40	368.51	474.33	286.43	44.809	100	43
0.60	6.00	388.67	479.13	310.88	42.293	100	39
0.60	6.40	406.83	476.71	307.56	37.967	100	39
0.60	7.00	462.90	544.95	365.53	39.961	100	40
0.60	7.40	457.37	712.15	340.38	67.025	100	46
0.60	7.80	507.41	652.59	341.66	72.568	100	41
0.60	8.00	535.90	725.76	401.35	66.784	100	50
0.60	8.20	605.23	832.13	440.28	69.934	100	51
0.60	8.40	639.41	808.08	499.53	73.078	100	48
0.60	8.60	612.93	792.22	423.56	85.646	100	47
0.60	8.80	686.67	826.72	565.01	65.657	100	60
0.60	9.00	661.21	745.05	478.11	53.474	100	51
0.60	9.20	710.80	894.41	538.84	80.653	100	47
0.60	9.40	807.33	999.12	624.22	90.107	100	59
0.60	9.60	877.42	1108.40	628.79	120.963	100	53
0.60	9.80	769.81	935.54	622.32	67.779	100	59
0.60	10.00	838.79	1206.15	642.11	117.376	100	49
0.60	10.20	915.73	1176.61	665.34	110.792	100	55
0.60	10.60	1036.80	1316.18	795.99	119.803	100	69
0.60	11.00	1068.41	1394.55	824.91	130.176	100	77
0.60	12.00	1428.41	1696.00	1047.51	129.582	100	84
0.60	13.00	1554.88	1791.38	1249.58	102.051	100	81
0.80	2.40	361.87	458.52	275.13	40.033	100	68
0.80	3.40	443.18	1727.91	274.20	298.419	100	20
0.80	4.40	376.23	472.72	263.01	44.648	100	47
0.80	5.40	415.38	493.50	333.61	41.371	100	39
0.80	5.80	437.52	550.73	290.44	54.909	100	45
0.80	6.20	535.69	666.83	420.10	57.464	100	50
0.80	6.60	566.79	682.49	282.91	70.104	100	47
0.80	6.80	527.50	643.72	427.00	58.224	100	43
0.80	7.00	581.90	691.32	456.49	47.720	100	53
0.80	7.20	623.63	769.92	499.43	63.770	100	51
0.80	7.40	653.11	769.39	501.98	56.846	100	52
0.80	7.60	681.15	826.16	546.43	60.893	100	56

Table C1 Raw experimental data ($\phi = 0.75$, $u = 1.2$ m/s) (continued)

x (mm)	y (mm)	T_{mean}	T_{max}	T_{min}	δ	N_T	N_a
0.80	7.80	718.51	905.69	558.92	70.401	100	52
0.80	8.00	769.73	1007.28	578.54	86.541	100	58
0.80	8.20	754.45	883.43	570.12	65.580	100	59
0.80	8.40	744.80	867.19	607.61	64.383	100	52
0.80	8.60	857.15	1107.68	655.84	100.971	100	49
0.80	8.80	861.94	1050.86	643.75	88.447	100	45
0.80	9.20	943.48	1127.33	743.53	86.064	100	56
0.80	9.60	1053.49	1314.63	822.63	93.852	100	54
0.80	9.80	1033.27	1320.36	791.25	126.485	100	50
0.80	10.00	1309.16	1635.67	956.21	125.955	100	72
1.00	1.00	370.00	462.97	288.88	35.724	100	73
1.00	1.40	376.44	503.74	296.68	35.892	100	64
1.00	2.40	348.88	408.87	272.07	33.888	100	37
1.00	3.40	385.94	487.11	283.35	45.288	100	40
1.00	3.80	417.67	505.72	306.82	45.584	100	45
1.00	4.20	450.78	552.28	324.23	45.949	100	47
1.00	4.60	503.30	619.93	324.69	68.858	100	40
1.00	5.00	532.30	619.20	417.98	46.826	100	56
1.00	5.40	612.95	747.60	425.53	60.438	100	61
1.00	5.80	690.96	830.22	497.45	62.832	100	61
1.00	6.00	720.25	829.68	572.38	55.390	100	49
1.00	6.20	794.59	909.98	648.88	59.707	100	54
1.00	6.40	823.54	916.90	695.69	57.826	100	37
1.00	6.60	796.07	958.27	654.99	69.296	100	57
1.00	6.80	856.72	1085.38	682.54	77.064	100	48
1.00	7.00	846.10	1026.35	674.32	79.352	100	45
1.00	7.20	938.21	1104.18	807.53	72.811	100	45
1.00	7.40	952.27	1201.13	805.19	82.360	100	55
1.00	7.60	1069.16	1270.82	798.02	102.562	100	48
1.00	7.80	1081.24	1261.50	843.00	89.396	100	43
1.00	8.00	1035.18	1217.25	783.64	87.241	100	65
1.00	8.20	1153.64	1384.87	919.47	107.719	100	59
1.00	8.40	1147.27	1298.36	997.57	78.842	100	66
1.00	8.60	1253.99	1490.95	1043.76	108.652	100	51
1.00	9.00	1251.94	1451.89	1018.77	89.399	100	71
1.00	10.00	1486.29	1723.70	1212.17	104.868	100	84
1.20	6.00	1018.62	1319.70	752.31	92.288	100	48
1.20	7.00	1472.42	1711.93	1255.58	90.844	100	81
1.20	8.00	1472.37	1642.03	1248.39	84.689	100	81
1.20	9.00	1534.24	1767.84	1274.37	89.619	100	88

Table C2

Raw experimental data for methane-air mixture of equivalence ratio 0.84 and mean inlet velocity of 0.6 m/s.

x (mm)	y (mm)	T_{mean}	T_{max}	T_{min}	δ	N_T	N_a
0.00	0.00	318.04	431.25	253.06	34.576	200	147
0.00	3.00	371.57	473.44	287.29	35.356	200	207
0.00	3.50	375.72	450.84	282.86	37.702	200	104
0.00	4.00	352.06	443.78	267.08	34.410	200	59
0.00	4.50	400.09	502.14	295.18	47.070	200	89
0.00	4.75	452.03	672.19	307.37	72.867	200	108
0.00	4.90	501.84	1206.79	320.68	103.330	200	126
0.00	5.00	492.96	790.79	347.38	83.321	200	119
0.00	5.10	615.44	1455.94	367.22	170.944	200	118
0.00	5.25	738.15	1548.96	334.36	222.652	200	138
0.00	5.40	1051.03	1833.48	501.21	338.359	200	103
0.00	5.50	1199.79	1728.14	612.40	304.349	200	88
0.00	5.60	1560.70	1900.56	608.76	197.565	200	135
0.00	5.70	1628.33	1900.61	1038.40	132.901	200	137
0.00	6.00	1672.50	1883.23	1476.48	89.618	200	151
0.20	0.00	320.27	424.42	254.90	35.965	200	147
0.20	4.00	381.36	447.89	271.09	38.572	200	102
0.20	4.70	541.15	919.79	324.98	101.944	200	124
0.20	4.75	544.79	919.79	324.98	103.485	200	129
0.20	4.80	535.10	862.08	331.08	99.920	200	112
0.20	4.80	537.00	862.08	331.08	97.476	200	121
0.20	4.90	636.25	1197.17	416.57	132.408	200	108
0.20	4.90	647.83	1197.17	416.57	140.310	200	125
0.20	5.00	637.55	1215.52	411.96	150.586	200	135
0.20	5.10	720.81	1519.80	431.90	203.614	200	89
0.20	5.10	748.82	1519.80	388.13	213.871	200	114
0.20	5.20	887.30	1666.20	476.87	301.745	200	67
0.20	5.20	895.93	1666.20	476.87	297.376	200	91
0.20	5.30	1104.50	1807.00	499.52	355.639	200	70
0.20	5.30	1103.96	1807.00	499.52	353.798	200	86
0.20	5.40	1293.44	1777.84	617.55	314.228	200	82
0.20	5.40	1268.23	1777.84	617.55	319.227	200	96
0.20	5.50	1551.53	1836.89	782.04	199.316	200	110
0.20	5.50	1537.90	1836.89	782.04	214.893	200	123

Table C2 Raw experimental data ($\phi = 0.84$, $u = 0.6$ m/s) (continued)

x (mm)	y (mm)	T_{mean}	T_{max}	T_{min}	δ	N_T	N_a
0.40	0.00	321.48	418.91	253.40	35.148	200	147
0.40	0.00	331.46	1798.10	253.40	125.936	200	148
0.40	4.10	500.61	663.97	371.34	64.159	200	150
0.40	4.10	501.02	663.97	371.34	63.518	200	156
0.40	4.20	566.74	841.14	383.54	95.858	200	131
0.40	4.20	570.35	841.14	383.54	95.092	200	139
0.40	4.30	584.01	839.57	420.14	85.463	200	138
0.40	4.30	588.76	839.57	420.14	87.808	200	150
0.40	4.40	625.89	881.78	414.07	81.825	200	119
0.40	4.40	630.95	889.25	414.07	85.043	200	128
0.40	4.50	682.41	948.60	412.21	105.172	200	111
0.40	4.50	692.43	1136.63	412.21	113.736	200	123
0.40	4.60	586.87	875.86	329.41	122.727	200	105
0.40	4.60	608.63	1130.11	329.41	139.256	200	123
0.40	4.70	730.72	1180.07	456.07	159.925	200	66
0.40	4.70	751.66	1270.64	456.07	163.710	200	88
0.40	4.80	620.94	1297.59	306.32	162.095	200	125
0.40	4.80	632.70	1297.59	306.32	166.087	200	136
0.40	4.90	717.07	1424.60	396.42	191.269	200	89
0.40	4.90	730.67	1424.60	396.42	197.056	200	103
0.40	5.00	969.45	1534.18	602.89	255.788	200	57
0.40	5.00	975.83	1534.18	602.89	242.355	200	72
0.40	5.10	1310.36	1801.50	499.44	295.813	200	68
0.40	5.10	1294.61	1801.50	499.44	311.651	200	88
0.40	5.20	1254.71	1704.52	595.71	262.626	200	79
0.40	5.20	1244.89	1756.23	595.71	267.701	200	90
0.60	0.00	365.49	1787.06	261.95	158.387	200	172
0.60	0.00	348.86	477.93	261.95	39.825	200	170
0.60	3.40	470.65	632.82	343.11	53.475	200	172
0.60	3.40	469.36	632.82	343.11	53.402	200	164
0.60	3.50	499.57	678.43	372.19	56.298	200	160
0.60	3.50	499.47	678.43	372.19	56.566	200	151
0.60	3.60	543.74	737.16	390.08	64.932	200	158
0.60	3.60	540.79	721.37	390.08	61.579	200	141
0.60	3.70	544.00	743.68	373.27	68.538	200	154
0.60	3.70	539.45	743.68	373.27	68.388	200	138

Table C2 Raw experimental data ($\phi = 0.84$, $u = 0.6$ m/s) (continued)

x (mm)	y (mm)	T_{mean}	T_{max}	T_{min}	δ	N_T	N_a
0.60	3.80	583.31	809.57	427.71	79.548	200	137
0.60	3.80	581.62	809.57	427.71	79.749	200	152
0.60	3.90	643.43	1119.64	457.29	98.812	200	112
0.60	3.90	636.71	1119.64	457.29	95.868	200	91
0.60	4.00	707.92	1349.29	536.99	140.054	200	65
0.60	4.00	714.62	1349.29	536.99	151.078	200	45
0.60	4.10	649.98	969.35	439.27	112.202	200	72
0.60	4.10	636.77	886.29	439.27	109.105	200	49
0.60	4.20	797.50	1177.22	493.44	145.441	200	50
0.60	4.20	784.47	1107.12	493.44	127.777	200	36
0.60	4.30	727.87	1165.56	453.24	153.575	200	78
0.60	4.30	696.60	1165.56	453.24	158.920	200	53
0.60	4.40	857.01	1288.92	516.86	147.289	200	55
0.60	4.40	841.18	1288.92	516.86	145.342	200	31
0.60	4.50	1099.30	1504.61	724.39	158.124	200	52
0.60	4.50	1118.54	1504.61	848.56	154.832	200	27
0.80	0.00	393.12	538.51	307.34	42.671	200	188
0.80	0.00	393.12	538.51	307.34	42.671	200	188
0.80	2.80	489.26	1699.96	371.53	111.239	200	158
0.80	2.90	468.36	625.17	355.32	50.939	200	160
0.80	3.00	499.06	639.50	372.22	60.184	200	157
0.80	3.10	548.34	714.27	406.24	62.227	200	117
0.80	3.20	552.67	722.83	401.45	67.076	200	137
0.80	3.30	558.37	801.43	417.14	71.857	200	131
0.80	3.40	601.12	845.26	435.50	83.203	200	109
0.80	3.50	730.78	1183.65	433.85	141.392	200	47
0.80	3.60	648.50	1065.06	426.12	124.563	200	83
0.80	3.70	843.19	1300.55	529.28	198.205	200	43
0.80	3.80	823.94	1221.47	579.80	159.731	200	45
0.80	3.90	974.75	1259.22	596.95	161.415	200	35
0.80	4.00	1192.28	1535.28	959.03	180.164	200	14
0.80	4.00	1192.28	1535.28	678.61	194.422	200	29
0.80	4.10	1074.19	1550.63	547.04	241.701	200	29
0.80	4.20	1312.76	1607.19	840.66	192.903	200	37
1.00	0.00	334.88	396.82	263.57	30.718	200	66
1.00	2.30	447.76	592.87	337.71	51.677	200	156

Table C2 Raw experimental data ($\phi = 0.84$, $u = 0.6$ m/s) (continued)

x (mm)	y (mm)	T_{mean}	T_{max}	T_{min}	δ	N_T	N_a
1.00	2.40	489.14	1828.12	360.04	124.114	200	147
1.00	2.50	493.41	633.45	380.59	51.688	200	146
1.00	2.60	559.25	732.00	399.79	64.684	200	126
1.00	2.70	570.22	759.39	424.94	68.866	200	115
1.00	2.80	621.04	863.36	442.85	71.658	200	81
1.00	2.90	643.46	955.70	388.20	109.752	200	62
1.00	3.00	754.23	1076.92	489.55	123.705	200	43
1.00	3.10	891.12	1249.27	651.51	141.335	200	40
1.00	3.20	739.21	1085.71	399.75	149.249	200	48
1.00	3.30	924.82	1242.87	575.01	176.119	200	39
1.00	3.40	945.21	1236.22	671.76	144.624	200	36
1.00	3.50	1266.23	1580.55	904.67	167.343	200	26
1.20	1.80	447.34	599.00	317.70	49.472	200	146
1.20	1.90	465.40	584.76	337.03	47.290	200	139
1.20	2.00	504.04	644.58	375.03	52.765	200	134
1.20	2.10	551.17	730.18	384.43	76.089	200	111
1.20	2.20	571.57	697.64	431.50	60.097	200	96
1.20	2.30	613.08	898.66	450.55	86.516	200	76
1.20	2.40	641.48	938.70	494.62	73.964	200	71
1.20	2.50	750.21	1076.69	619.91	95.784	200	36
1.20	2.60	793.50	1055.50	554.75	138.184	200	21
1.20	2.70	905.20	1193.76	617.58	156.635	200	28
1.20	2.80	951.28	1249.88	760.21	147.223	200	25
1.20	2.90	1162.10	1416.81	951.15	104.398	200	42
1.40	1.50	504.00	617.64	370.73	54.589	200	124
1.40	1.60	528.31	641.13	390.37	52.931	200	120
1.40	1.70	573.29	707.60	425.46	61.791	200	116
1.40	1.80	630.41	800.88	452.72	67.809	200	81
1.40	1.90	675.65	955.84	420.91	100.903	200	55
1.40	2.00	713.26	899.48	593.02	69.828	200	46
1.40	2.10	726.93	998.42	445.20	124.068	200	59
1.40	2.20	835.18	1135.29	500.53	148.021	200	22
1.40	2.30	1003.85	1385.09	766.34	118.227	200	30
1.40	2.40	1014.70	1392.31	853.53	126.293	200	24
1.40	2.50	1082.33	1299.94	762.76	145.906	200	27
1.60	0.80	452.92	1786.53	307.89	137.977	200	112

Table C2 Raw experimental data ($\phi = 0.84$, $u = 0.6$ m/s) (continued)

x (mm)	y (mm)	T_{mean}	T_{max}	T_{min}	δ	N_T	N_a
1.60	0.90	470.75	579.10	279.43	53.788	200	124
1.60	1.00	490.52	621.59	347.67	53.900	200	132
1.60	1.10	519.47	647.25	374.78	52.193	200	119
1.60	1.20	553.42	693.04	391.90	56.055	200	127
1.60	1.30	575.91	727.86	397.34	64.912	200	117
1.60	1.40	630.11	776.36	360.14	73.954	200	90
1.60	1.60	730.84	855.97	492.73	77.273	200	51
1.60	1.80	922.25	1249.08	645.59	114.234	200	33
1.60	1.90	979.19	1145.41	817.25	82.724	200	29
1.60	2.00	1083.41	1231.04	878.33	79.648	200	32
1.60	2.10	1144.48	1350.79	890.30	137.128	200	19
1.60	2.20	1309.60	1636.33	1002.12	136.297	200	45
1.80	0.60	479.66	634.18	353.31	58.002	200	141
1.80	0.70	545.03	1771.36	350.51	117.483	200	137
1.80	0.80	577.15	683.31	433.96	50.344	200	108
1.80	0.90	611.44	717.48	432.06	61.862	200	108
1.80	1.00	636.21	779.56	449.20	59.921	200	97
1.80	1.10	685.70	813.16	527.80	56.701	200	71
1.80	1.20	749.11	949.35	522.98	86.435	200	49
1.80	1.30	805.19	956.96	658.15	74.075	200	49
1.80	1.40	872.04	1126.23	728.69	93.226	200	32
1.80	1.50	964.57	1121.22	680.60	104.558	200	31
2.00	0.70	659.86	825.09	513.57	63.688	200	100
2.00	0.80	708.91	887.32	517.22	61.259	200	65
2.00	0.90	771.43	919.18	648.07	62.783	200	66
2.00	1.00	837.55	972.42	678.81	74.191	200	52
2.00	1.10	911.01	1023.58	729.34	62.000	200	35
2.00	1.20	1007.15	1145.84	830.38	77.486	200	38
2.20	0.80	855.66	1018.14	676.81	77.552	200	49
2.20	0.90	959.91	1184.60	797.23	87.224	200	55
2.20	1.00	1050.53	1217.17	918.13	73.332	200	73
2.20	1.10	1111.57	1284.34	918.81	86.351	200	54
2.40	0.80	991.11	1149.50	797.96	78.755	200	62
2.40	0.90	1062.77	1349.72	853.12	85.936	200	90
2.40	1.00	1166.68	1393.42	975.33	80.294	200	108
2.60	0.90	1182.04	1456.16	985.24	86.358	200	115
2.80	0.90	1263.30	1489.55	1019.77	89.621	200	139
3.00	0.90	1284.84	1558.91	1062.90	90.762	200	131

Table C3

Raw experimental data for methane-air mixture of equivalence ratio 0.84 and mean inlet velocity of 1.2 m/s.

x (mm)	y (mm)	T_{mean}	T_{max}	T_{min}	δ	N_T	N_a
0.00	0.00	289.62	356.58	262.01	23.093	200	71
0.00	5.00	309.29	417.32	250.57	31.073	200	117
0.00	7.00	771.97	949.31	426.88	73.038	200	120
0.00	7.90	502.38	877.64	363.37	73.354	200	67
0.00	8.00	480.29	654.35	334.09	57.373	200	112
0.00	8.10	531.94	726.01	379.38	72.042	200	82
0.00	8.20	605.05	1040.88	407.90	117.037	200	76
0.00	8.30	573.95	901.80	448.26	69.297	200	78
0.00	8.40	737.94	1471.19	525.68	177.381	200	73
0.00	8.50	610.00	871.88	395.48	78.064	200	121
0.00	8.60	667.96	957.64	492.87	69.230	200	121
0.00	8.70	697.95	908.08	514.00	71.478	200	121
0.00	8.80	518.67	806.00	406.93	61.053	200	103
0.00	10.00	1753.77	2024.00	1487.83	93.742	200	114
0.20	7.50	457.72	552.43	367.86	41.928	200	106
0.20	7.60	478.33	830.21	307.77	64.870	200	105
0.20	7.70	470.24	586.14	343.06	48.792	200	107
0.20	7.80	503.46	949.95	385.86	71.541	200	109
0.20	7.90	556.32	1002.77	427.87	90.187	200	112
0.20	8.00	601.71	1097.12	423.20	119.381	200	97
0.20	8.10	650.67	1116.97	461.63	128.116	200	107
0.20	8.20	679.42	1099.64	429.94	148.585	200	96
0.20	8.30	807.20	1093.42	484.14	150.576	200	96
0.20	8.40	812.42	1237.82	519.45	170.836	200	78
0.20	8.50	952.41	1590.28	559.29	217.287	200	98
0.20	8.60	945.56	1500.55	615.47	197.532	200	81
0.40	6.70	1295.81	2029.21	955.85	129.102	200	154
0.40	6.80	503.42	642.60	356.53	51.903	200	121
0.40	6.90	495.76	615.84	347.63	65.191	200	101
0.40	7.00	575.09	1052.08	399.74	114.943	200	127
0.40	7.10	678.05	1120.78	442.58	153.930	200	112
0.40	7.20	694.32	1113.98	418.40	161.272	200	124
0.40	7.30	733.38	1318.10	474.41	183.349	200	100
0.40	7.40	882.94	1345.73	426.89	207.597	200	115
0.40	7.50	860.64	1273.74	514.85	212.589	200	111
0.40	7.60	920.17	1287.15	530.71	209.513	200	107
0.40	7.70	1021.38	1348.89	499.36	183.235	200	100
0.40	7.80	978.66	1343.63	577.78	203.506	200	109
0.40	7.90	1065.21	1866.66	631.01	188.693	200	112
0.40	8.00	1121.11	1539.25	644.90	153.816	200	89
0.40	8.10	1140.29	1512.60	721.35	152.523	200	103
0.40	8.20	1149.33	1706.55	821.34	138.699	200	109
0.60	5.30	883.93	1132.62	665.58	85.733	200	139

Table C3 Raw experimental data ($\phi = 0.84$, $u = 1.2$ m/s) (continued)

x (mm)	y (mm)	T_{mean}	T_{max}	T_{min}	δ	N_T	N_a
0.60	5.40	1111.60	1456.19	870.86	94.519	200	156
0.60	5.50	470.94	793.39	326.43	57.539	200	118
0.60	5.60	512.54	680.59	379.59	59.299	200	93
0.60	5.70	516.66	643.24	407.28	54.217	200	74
0.60	5.80	537.57	860.67	387.02	75.268	200	111
0.60	5.90	571.37	898.19	360.05	78.448	200	120
0.60	6.00	582.25	898.24	405.70	70.263	200	114
0.60	6.10	599.16	893.26	416.54	76.828	200	112
0.60	6.20	638.08	916.66	418.21	83.991	200	113
0.60	6.30	674.32	936.13	480.57	85.254	200	109
0.60	6.40	697.83	888.92	522.98	82.001	200	109
0.60	6.50	743.47	955.34	526.19	92.430	200	105
0.60	6.90	788.55	1001.15	519.51	92.095	200	116
0.60	7.00	338.59	446.65	269.63	40.136	200	112
0.60	7.10	1000.00	1268.92	728.19	108.026	200	105
0.60	7.20	923.54	1198.84	725.15	100.258	200	125
0.60	7.30	1080.35	1449.43	821.36	120.926	200	151
0.60	7.40	1050.28	1395.21	792.68	106.237	200	148
0.60	7.50	1137.82	1411.08	810.58	109.984	200	136
0.80	4.20	703.50	886.20	471.56	69.798	200	107
0.80	4.30	888.67	1112.82	583.21	95.435	200	120
0.80	4.40	455.11	570.66	327.18	45.807	200	103
0.80	4.50	463.55	635.13	340.02	50.589	200	104
0.80	4.60	502.18	649.64	335.43	53.379	200	119
0.80	4.70	541.50	818.38	315.89	78.389	200	107
0.80	4.80	559.37	850.04	317.15	72.552	200	113
0.80	4.90	632.99	897.65	495.58	70.472	200	113
0.80	5.00	758.80	925.96	565.49	63.616	200	102
0.80	5.10	793.28	1018.23	607.86	76.585	200	103
0.80	5.20	661.50	873.12	479.12	75.290	200	122
0.80	5.30	880.64	1461.32	592.81	195.960	200	93
0.80	5.50	713.02	931.82	535.38	75.708	200	134
0.80	6.00	698.07	903.81	489.17	76.085	200	114
1.00	2.50	1108.32	1657.93	635.69	261.421	200	78
1.00	3.30	881.75	1056.12	685.61	76.780	200	114
1.00	3.40	362.26	516.39	270.49	41.523	200	121
1.00	3.50	473.04	619.73	354.84	54.248	200	106
1.00	3.60	512.04	748.06	363.23	66.534	200	102
1.00	3.70	549.82	949.10	328.51	93.028	200	119
1.00	3.80	583.99	870.02	400.06	71.067	200	126
1.00	3.90	624.18	926.97	470.25	80.653	200	117
1.00	4.00	853.56	1272.59	525.78	172.954	200	88
1.00	4.10	776.73	990.89	591.11	75.117	200	103
1.00	4.20	654.56	986.78	483.85	94.342	200	117
1.00	4.50	744.57	907.33	529.50	68.635	200	129

Table C3 Raw experimental data ($\phi = 0.84$, $u = 1.2$ m/s) (continued)

x (mm)	y (mm)	T_{mean}	T_{max}	T_{min}	δ	N_T	N_a
1.20	1.50	570.88	718.82	412.45	58.362	200	95
1.20	2.30	540.18	665.29	422.93	53.715	200	86
1.20	2.40	570.14	844.45	421.42	65.545	200	102
1.20	2.50	1415.63	1974.56	645.53	265.813	200	96
1.20	2.60	446.00	565.31	359.78	39.801	200	114
1.20	2.70	469.32	576.18	368.16	45.731	200	104
1.20	2.80	496.10	648.60	366.23	55.783	200	102
1.20	2.90	518.57	665.21	381.87	49.922	200	89
1.20	3.00	787.28	970.87	568.15	63.373	200	107
1.20	3.10	599.62	800.75	444.21	69.897	200	96
1.20	3.20	562.64	820.83	396.43	71.483	200	100
1.20	3.50	576.26	688.21	417.58	56.612	200	160
1.40	1.00	705.75	810.26	489.25	59.061	200	85
1.40	1.70	895.19	1085.49	766.26	73.473	200	101
1.40	1.80	668.40	820.97	471.87	63.242	200	97
1.40	1.90	398.12	513.24	295.52	43.179	200	109
1.40	2.00	493.90	756.74	354.67	55.514	200	110
1.40	2.40	611.91	857.04	471.00	59.839	200	95
1.40	2.50	896.01	1114.21	663.15	81.186	200	120
1.40	2.60	1128.68	1291.21	956.97	81.772	200	81
1.40	2.70	640.68	791.18	496.68	63.835	200	95
1.40	3.00	1038.10	1274.69	854.37	80.349	200	70
1.60	0.60	950.88	1173.61	754.50	71.693	200	120
1.60	0.70	753.78	906.09	589.50	67.924	200	103
1.60	0.80	709.27	901.22	547.41	67.923	200	89
1.60	0.90	433.74	564.79	312.33	45.257	200	125
1.60	1.00	448.56	623.53	304.29	55.768	200	110
1.60	1.10	476.14	706.33	358.24	51.620	200	97
1.60	1.20	492.96	610.16	334.93	55.241	200	95
1.60	1.30	524.08	699.02	369.89	52.978	200	112
1.60	1.40	554.34	691.68	414.65	51.272	200	98
1.60	1.50	745.52	905.92	621.20	61.929	200	95
1.60	1.60	368.50	517.50	264.04	44.402	200	139
1.60	1.70	631.18	787.93	448.02	60.864	200	83
1.60	1.80	599.83	804.37	458.68	54.485	200	87
1.60	2.00	791.25	1017.31	646.19	67.279	200	95
1.80	0.70	1233.09	1435.54	991.36	86.837	200	82
1.80	0.80	1045.72	1283.38	800.73	80.230	200	151
1.80	0.90	926.82	1070.21	809.07	67.772	200	107
1.80	1.00	1251.29	1489.36	991.56	112.035	200	92
1.80	1.10	611.06	744.71	453.80	63.000	200	98
1.80	1.20	635.40	755.28	492.36	58.335	200	100
1.80	1.30	676.03	806.22	521.03	60.986	200	102
1.80	1.40	750.95	917.23	583.00	64.933	200	95
1.80	1.50	839.04	1010.85	573.21	75.243	200	117
1.80	2.00	797.37	1041.95	644.50	69.512	200	109

Table C3 Raw experimental data ($\phi = 0.84$, $u = 1.2$ m/s) (continued)

x (mm)	y (mm)	T_{mean}	T_{max}	T_{min}	δ	N_T	N_a
2.00	0.70	1021.85	1203.70	837.15	84.375	200	64
2.00	0.80	1148.30	1411.82	967.49	89.604	200	66
2.00	0.90	1092.55	1302.85	965.39	83.464	200	70
2.00	1.00	990.32	1195.92	830.34	81.212	200	79
2.00	1.10	797.99	988.83	588.54	74.244	200	104
2.00	1.20	765.51	940.74	516.32	74.354	200	106
2.00	1.50	853.25	1000.36	670.25	72.591	200	95
2.20	0.70	1041.58	1229.35	845.61	78.736	200	86
2.20	0.80	1199.03	1389.44	1046.57	80.906	200	52
2.20	0.90	876.88	1050.54	728.56	67.461	200	81
2.20	1.00	954.55	1084.05	770.52	66.159	200	67
2.20	1.10	806.31	1006.18	673.09	68.806	200	109
2.40	0.70	1125.20	1335.27	933.16	77.500	200	84
2.40	0.80	1226.70	1424.39	1030.93	92.847	200	54
2.40	0.90	1276.80	1463.60	1126.35	78.921	200	70
2.40	1.00	962.44	1110.96	749.93	80.451	200	57
2.60	0.80	694.16	852.87	537.21	56.597	200	113
2.60	0.90	719.21	915.27	509.30	68.990	200	108
2.60	1.00	851.57	1090.14	677.75	76.682	200	107

Table C4

Raw experimental data for methane-air mixture of equivalence ratio 0.84 and mean inlet velocity of 2.0 m/s.

x (mm)	y (mm)	T_{mean}	T_{max}	T_{min}	δ	N_T	N_a
-0.20	4.00	344.33	463.91	262.61	37.256	150	106
-0.20	4.40	393.32	492.57	267.63	45.130	150	111
-0.20	4.80	418.49	688.98	308.97	67.552	150	94
-0.20	5.20	582.57	805.38	436.83	87.959	150	56
-0.20	5.60	997.42	1257.31	820.37	104.179	150	29
-0.20	6.00	1322.30	1606.66	1046.04	143.264	150	34
-0.20	6.40	1591.44	1834.15	1338.09	103.456	150	65
-0.20	6.80	1686.87	1900.50	1465.24	80.046	150	134
-0.20	7.00	1699.54	1930.78	1444.55	93.095	150	137
-0.20	8.00	1787.06	1996.84	1548.17	82.291	150	114
-0.20	9.00	1817.10	2017.48	1595.44	87.928	150	122
-0.20	10.00	1851.15	2022.27	1516.60	86.448	150	122
-0.20	11.00	1860.10	2049.71	1674.94	74.482	150	108
-0.20	12.00	1896.49	2036.89	1739.88	61.412	150	105
-0.20	13.00	1910.39	2058.64	1683.44	76.287	150	97
0.00	0.00	336.25	454.40	264.25	36.672	150	134
0.00	7.80	489.43	601.79	358.52	48.346	150	132
0.00	8.20	522.32	1832.36	349.06	135.520	150	109
0.00	8.60	493.01	587.67	362.94	46.292	150	80
0.00	9.00	554.72	725.80	401.62	58.314	150	90
0.00	9.20	561.99	719.01	435.69	62.856	150	83
0.00	9.40	604.73	772.93	458.01	65.833	150	67
0.00	9.60	644.90	766.44	539.53	62.085	150	48
0.00	9.80	690.39	804.02	545.29	64.822	150	21
0.00	10.00	786.44	993.21	575.14	92.278	150	21
0.00	10.20	925.76	1155.61	783.79	102.599	150	18
0.00	10.40	906.94	1012.90	734.97	70.698	150	27
0.00	10.60	996.20	1167.36	812.93	95.580	150	29
0.00	10.80	1065.15	1368.10	839.62	105.347	150	39
0.00	11.00	1247.01	1643.44	1023.97	122.077	150	50
0.00	11.20	1420.41	1714.25	1125.75	147.019	150	84
0.00	11.40	1562.56	1880.24	1226.78	127.730	150	89
0.00	11.60	1662.28	1890.08	1466.89	87.076	150	117
0.00	11.80	1708.92	1937.92	1456.40	107.561	150	110
0.00	12.00	1738.60	1954.42	1482.34	95.235	150	87
0.00	12.40	1790.94	2005.71	1463.91	97.264	150	95
0.00	12.80	1827.27	2080.43	1646.21	85.259	150	98
0.00	13.00	1862.18	1998.61	1603.75	77.805	150	88
0.00	14.00	1886.11	2128.29	1697.47	77.687	150	108
0.00	15.00	1905.75	2067.25	1623.27	77.075	150	109
0.20	9.20	404.37	489.98	317.07	39.616	150	70
0.20	9.60	408.70	488.02	284.25	44.286	150	63

Table C4 Raw experimental data ($\phi = 0.84$, $u = 2.0$ m/s) (continued)

x (mm)	y (mm)	T_{mean}	T_{max}	T_{min}	δ	N_T	N_a
0.20	10.00	443.24	528.31	347.55	40.029	150	55
0.20	10.40	459.76	577.99	381.35	42.827	150	47
0.20	10.80	527.48	637.79	428.35	48.185	150	48
0.20	11.20	581.28	772.51	438.66	59.756	150	67
0.20	11.60	676.04	904.92	516.04	78.410	150	68
0.20	11.80	776.99	956.39	539.73	88.033	150	56
0.20	12.00	905.62	1145.34	705.95	107.806	150	46
0.20	12.20	1083.29	1744.80	775.06	215.350	150	78
0.20	12.40	1376.17	1823.00	819.74	225.176	150	73
0.20	12.60	1610.93	1846.54	983.80	144.243	150	98
0.20	12.80	1701.72	1926.71	1305.84	104.030	150	108
0.20	13.00	1773.51	1966.67	1501.87	88.458	150	89
0.20	13.40	1794.95	1981.71	1513.21	88.205	150	99
0.20	13.80	1841.05	2061.80	1546.14	91.070	150	101
0.20	14.20	1860.75	2091.51	1669.81	82.345	150	111
0.20	14.60	1858.02	2065.23	1659.47	77.923	150	116
0.20	15.00	1891.44	2077.56	1517.52	92.297	150	114
0.40	6.00	310.00	426.39	255.48	33.439	150	85
0.40	6.80	347.13	422.40	258.36	45.709	150	38
0.40	7.20	405.38	494.77	265.47	48.656	150	24
0.40	7.60	454.82	572.66	369.53	48.983	150	42
0.40	8.00	446.73	626.77	336.82	59.183	150	61
0.40	8.40	464.83	683.73	372.30	53.729	150	68
0.40	8.80	551.02	753.98	373.58	87.112	150	52
0.40	9.20	609.26	726.15	425.13	82.617	150	44
0.40	9.60	574.51	766.39	402.63	85.435	150	41
0.40	10.00	619.54	868.46	335.92	87.339	150	39
0.40	10.40	677.18	824.81	576.27	64.212	150	49
0.40	10.80	753.87	1013.71	601.93	81.212	150	72
0.40	11.00	866.02	1458.40	634.82	129.826	150	83
0.40	11.20	1105.05	1614.08	723.32	202.587	150	92
0.40	11.40	1219.58	1813.41	797.26	229.562	150	94
0.40	11.60	1447.67	1847.01	859.18	192.837	150	84
0.40	11.80	1723.50	1924.22	1361.76	93.851	150	91
0.40	12.00	1772.44	1942.40	1515.68	91.305	150	91
0.40	12.40	1804.42	2048.53	1585.52	84.267	150	92
0.40	12.80	1829.75	2049.47	1555.14	83.783	150	98
0.40	13.60	1867.39	2064.94	1659.51	76.940	150	97
0.40	14.00	1878.58	2045.09	1686.94	76.200	150	116
0.60	4.00	314.67	393.85	262.84	28.174	150	99
0.60	5.00	380.27	446.69	274.01	41.397	150	16
0.60	6.00	378.73	420.62	293.42	34.010	150	14
0.60	6.80	376.93	454.74	280.22	40.986	150	41
0.60	7.20	397.64	512.70	325.30	37.013	150	54
0.60	7.60	443.46	567.20	347.74	51.218	150	61
0.60	8.00	476.65	571.06	338.81	47.423	150	73

Table C4 Raw experimental data ($\phi = 0.84$, $u = 2.0$ m/s) (continued)

x (mm)	y (mm)	T_{mean}	T_{max}	T_{min}	δ	N_T	N_a
0.60	8.40	519.73	702.06	324.79	64.680	150	75
0.60	8.60	571.95	719.32	384.39	65.535	150	89
0.60	8.80	626.00	837.18	435.00	70.030	150	98
0.60	9.00	639.57	965.14	408.85	99.504	150	95
0.60	9.20	690.69	939.17	495.21	81.149	150	76
0.60	9.40	752.11	964.38	605.50	79.832	150	69
0.60	9.60	783.63	1008.88	652.15	80.314	150	58
0.60	9.80	824.58	1058.39	656.04	103.081	150	51
0.60	10.00	806.37	1018.98	606.90	87.081	150	60
0.60	10.20	872.94	1035.13	666.71	91.176	150	41
0.60	10.40	966.72	1205.38	767.96	113.694	150	38
0.60	10.60	1024.51	1213.43	824.97	92.462	150	46
0.60	10.80	1149.11	1418.00	856.36	120.236	150	80
0.60	11.00	1183.86	1469.32	974.05	113.412	150	84
0.60	11.40	1590.88	1848.08	1186.96	133.190	150	108
0.60	11.80	1737.94	1950.46	1360.11	103.820	150	100
0.60	12.00	1714.52	1941.53	1436.11	100.682	150	97
0.60	12.50	1807.05	1998.19	1512.99	90.306	150	108
0.60	13.00	1849.16	2021.47	1599.71	78.669	150	102
0.80	2.00	313.85	403.36	254.20	30.533	150	96
0.80	3.00	325.14	465.79	253.94	38.464	150	85
0.80	4.00	396.32	453.14	353.76	32.531	150	16
0.80	4.60	392.02	453.23	328.96	34.415	150	34
0.80	5.20	393.05	467.53	324.00	35.830	150	36
0.80	5.60	398.43	505.79	306.25	44.991	150	55
0.80	6.00	446.86	539.33	364.64	39.465	150	82
0.80	6.40	539.30	717.31	399.16	65.197	150	103
0.80	6.80	580.05	776.84	361.17	67.498	150	81
0.80	7.00	623.37	791.20	412.48	68.989	150	63
0.80	7.20	637.16	816.48	434.79	61.569	150	61
0.80	7.40	650.74	778.37	481.09	66.223	150	54
0.80	7.60	672.30	812.01	411.04	63.561	150	43
0.80	7.80	719.34	856.88	576.47	62.804	150	40
0.80	8.00	770.20	917.72	658.74	71.676	150	25
0.80	8.20	803.72	1003.50	640.24	88.111	150	24
0.80	8.60	1005.75	1200.57	638.91	114.784	150	19
0.80	9.00	1156.53	1400.05	866.51	126.843	150	31
0.80	9.20	1309.49	1489.79	1140.49	89.336	150	67
0.80	9.60	1420.18	1617.59	1239.69	87.916	150	95
0.80	10.00	1483.35	1690.26	1230.55	91.801	150	105
0.80	11.00	1647.76	1838.68	1454.91	75.311	150	89
1.00	1.00	322.63	422.93	259.24	34.032	150	119
1.00	2.00	383.82	451.27	296.95	49.037	150	15
1.00	3.00	380.14	452.43	328.03	35.353	150	21
1.00	3.60	378.06	440.43	290.55	38.954	150	39
1.00	4.00	402.61	491.16	279.89	46.489	150	77

Table C4 Raw experimental data ($\phi = 0.84$, $u = 2.0$ m/s) (continued)

x (mm)	y (mm)	T_{mean}	T_{max}	T_{min}	δ	N_T	N_a
1.00	4.40	449.43	584.25	312.81	47.280	150	91
1.00	4.80	511.63	662.62	380.62	59.255	150	91
1.00	5.00	541.62	646.35	392.98	48.981	150	81
1.00	5.20	576.26	688.21	417.58	56.612	150	80
1.00	5.40	619.76	807.82	467.40	67.866	150	66
1.00	5.60	631.49	801.33	293.91	81.962	150	51
1.00	6.00	757.31	887.27	606.95	72.732	150	31
1.00	6.20	761.05	947.13	619.54	78.128	150	17
1.00	6.40	855.25	1031.99	713.39	105.416	150	13
1.00	6.60	947.41	1093.62	788.89	84.660	150	19
1.00	7.00	1049.51	1190.51	823.89	93.229	150	21
1.00	7.40	1277.87	1475.91	1003.19	89.246	150	47
1.00	8.00	1456.45	1736.96	1227.24	97.006	150	92
1.20	0.80	393.08	454.06	331.72	35.780	150	22
1.20	1.00	395.20	472.11	302.71	41.165	150	19
1.20	2.00	375.43	446.87	280.86	37.327	150	41
1.20	3.00	423.59	520.83	335.32	41.650	150	78
1.20	3.20	453.01	577.73	301.11	46.526	150	79
1.20	3.40	497.69	628.58	365.25	56.929	150	85
1.20	3.60	534.27	686.65	409.55	56.405	150	84
1.20	3.80	569.50	684.09	394.78	55.512	150	70
1.20	4.00	600.75	732.59	418.19	61.411	150	43
1.20	4.20	644.86	783.43	337.84	71.625	150	45
1.20	4.40	709.65	853.72	532.28	66.877	150	30
1.20	4.60	764.79	914.08	605.27	76.188	150	28
1.20	5.00	965.33	1116.57	709.04	88.692	150	28
1.20	5.40	1127.81	1264.40	956.14	88.651	150	30
1.20	5.80	1290.85	1468.55	1158.11	67.871	150	56
1.20	6.00	1371.41	1576.18	1170.56	100.319	150	65
1.20	7.00	1608.77	1895.75	1394.53	89.435	150	119
1.40	0.80	375.72	465.22	292.37	40.322	150	42
1.40	1.20	387.03	478.99	299.07	39.845	150	73
1.40	1.60	415.35	536.59	304.89	44.814	150	76
1.40	2.00	467.90	660.53	328.04	54.414	150	89
1.40	2.20	522.56	659.90	404.80	47.374	150	85
1.40	2.40	547.69	683.73	432.00	50.286	150	88
1.40	2.60	583.60	734.16	422.38	56.508	150	72
1.40	2.80	634.94	785.92	433.97	76.746	150	41
1.40	3.00	681.92	787.48	527.41	61.990	150	29
1.40	3.20	810.29	955.66	652.63	66.077	150	36
1.40	3.40	878.78	1018.74	717.55	78.647	150	23
1.40	3.60	976.54	1137.53	858.93	73.505	150	20
1.40	3.80	1052.14	1230.62	822.65	81.422	150	31
1.40	4.00	1190.64	1350.11	1016.03	84.887	150	56
1.40	5.00	1547.41	1791.04	1284.00	87.298	150	136
1.60	0.80	473.05	567.10	366.09	45.663	150	84

Table C4 Raw experimental data ($\phi = 0.84$, $u = 2.0$ m/s) (continued)

x (mm)	y (mm)	T_{mean}	T_{max}	T_{min}	δ	N_T	N_e
1.60	1.00	502.95	599.23	385.06	43.421	150	98
1.60	1.40	569.69	721.64	439.79	51.322	150	74
1.60	1.60	614.74	754.27	459.09	62.729	150	63
1.60	1.80	667.56	856.09	531.83	74.481	150	55
1.60	2.00	752.85	891.42	647.21	57.221	150	40
1.60	2.20	820.86	1018.27	699.72	78.389	150	32
1.60	2.40	912.95	1080.45	741.24	83.479	150	24
1.60	2.60	1035.82	1151.88	762.60	81.552	150	37
1.60	3.00	1267.58	1450.02	1046.84	82.660	150	76
1.60	3.40	1436.34	1692.77	1206.85	101.518	150	121
1.60	4.00	1607.07	1826.73	1346.00	78.404	150	137
1.80	0.80	1066.49	1210.67	927.66	68.118	150	43
1.80	1.00	1172.29	1347.62	1000.64	85.557	150	71
1.80	1.20	1300.19	1455.64	1095.08	70.108	150	94
1.80	1.60	1489.14	1681.92	1287.90	85.801	150	115
1.80	2.00	1186.99	1389.61	995.39	78.721	150	48
1.80	2.40	1396.97	1587.83	1158.68	87.070	150	121
1.80	3.00	1593.71	1758.68	1370.81	77.859	150	123
2.00	0.80	855.03	1025.17	711.74	62.729	150	61
2.00	1.00	956.38	1078.84	839.77	56.538	150	45
2.00	1.20	1065.95	1237.17	893.66	65.795	150	88
2.00	1.40	1176.07	1358.02	1043.06	80.145	150	84
2.00	1.60	1328.11	1552.19	1122.51	77.906	150	103
2.00	2.00	1508.27	1752.14	1251.50	91.243	150	133
2.20	0.80	1023.49	1197.08	852.60	71.611	150	92
2.20	1.00	1168.60	1378.31	946.78	82.233	150	121
2.20	1.40	1435.35	1599.40	1188.46	75.387	150	124
2.20	2.00	1599.60	1761.79	1329.06	82.895	150	129
2.40	0.80	1169.50	1344.15	979.40	72.738	150	99
2.40	1.00	1321.91	1531.62	1088.37	79.976	150	114
2.40	1.40	1508.96	1799.07	1257.97	90.121	150	138
2.40	2.00	1632.77	1868.53	1402.66	88.809	150	138
2.40	3.00	1720.09	1890.90	1511.51	74.171	150	125
2.60	0.80	1267.39	1509.52	1058.64	81.021	150	118
2.60	1.40	1543.52	1739.68	1397.39	81.555	150	127
2.60	2.00	1670.81	1873.47	1432.97	84.067	150	136
2.80	0.80	1304.93	1467.96	1104.99	73.825	150	120
2.80	1.40	1557.68	1741.06	1281.89	85.557	150	144
2.80	2.00	1668.64	1838.63	1384.65	73.323	150	133
3.00	0.80	1314.14	1627.52	1126.33	89.662	150	120
3.00	1.40	1561.86	1776.27	1270.33	95.094	150	131
3.00	2.00	1671.87	1865.54	1437.09	81.576	150	129

Table C5

Raw experimental data for stoichiometric methane-air mixture and mean inlet velocity of 1.2 m/s.

x (mm)	y (mm)	T_{mean}	T_{max}	T_{min}	δ	N_T	N_a
0.00	0.00	307.55	372.57	261.07	28.447	200	105
0.00	4.00	346.93	444.42	265.70	32.239	200	125
0.00	5.00	334.20	424.36	265.36	33.768	200	128
0.00	6.00	489.11	639.94	313.55	56.331	200	133
0.00	6.20	690.32	1378.72	455.58	155.219	200	132
0.00	6.60	1650.09	1914.76	998.09	147.511	200	175
0.00	6.80	1776.79	1994.30	1591.63	84.233	200	175
0.00	7.00	1795.51	1965.57	1439.95	77.664	200	156
0.00	8.00	1913.21	2056.30	1725.72	65.150	200	142
0.00	9.00	1848.80	2098.48	1487.43	104.693	200	154
0.20	0.00	323.90	422.14	261.51	33.794	200	99
0.20	3.00	356.17	451.70	263.56	38.624	200	148
0.20	3.00	355.62	469.31	265.70	36.675	200	109
0.20	4.00	332.56	438.45	265.22	32.593	200	131
0.20	4.60	357.74	438.09	267.89	34.925	200	143
0.20	4.80	391.95	1799.52	286.42	127.034	200	137
0.20	5.00	414.85	552.21	273.31	52.172	200	127
0.20	5.20	490.88	635.68	364.62	58.307	200	123
0.20	5.40	612.86	870.33	398.96	83.179	200	117
0.20	5.40	612.97	798.46	425.72	78.481	200	78
0.20	5.60	750.84	1044.15	401.92	120.249	200	126
0.20	5.80	822.16	1119.90	565.92	120.000	200	124
0.20	6.00	1030.12	1402.04	571.87	153.848	200	135
0.20	6.20	1278.22	1738.54	809.12	193.333	200	145
0.20	6.40	1625.84	1949.39	965.11	146.731	200	164
0.20	7.00	1839.04	2049.76	1579.28	74.685	200	170
0.20	8.00	1933.83	2119.72	1712.46	70.757	200	148
0.40	3.00	339.54	456.46	262.49	37.259	200	118
0.40	4.00	385.17	1791.86	272.81	131.173	200	128
0.40	4.20	432.06	547.03	298.61	48.253	200	131
0.40	4.40	497.86	636.00	373.90	56.131	200	124
0.40	4.80	792.01	994.64	620.30	82.515	200	49
0.40	5.00	930.55	1231.94	712.08	111.945	200	39
0.40	5.20	1003.02	1528.17	709.61	183.499	200	31
0.40	5.40	1295.39	1588.63	1084.67	126.801	200	27
0.40	5.60	1447.22	1707.93	1099.47	132.811	200	57
0.40	5.80	1655.65	1850.55	1346.24	115.312	200	66
0.40	6.00	1719.58	1942.43	1552.58	85.592	200	96
0.40	6.20	1761.42	1913.02	1558.84	73.356	200	129
0.40	6.40	1778.90	1962.23	1507.09	72.406	200	182
0.40	7.00	1841.45	2068.22	1599.56	67.483	200	171
0.60	3.00	359.53	1878.08	264.78	139.728	200	128

Table C5 Raw experimental data ($\phi = 1.0$, $u = 1.2$ m/s) (continued)

x (mm)	y (mm)	T_{mean}	T_{max}	T_{min}	δ	N_T	N_a
0.60	3.40	382.42	542.75	289.29	40.698	200	137
0.60	3.60	438.92	575.05	308.73	48.888	200	135
0.60	3.80	527.48	642.23	363.28	55.456	200	112
0.60	4.00	638.64	799.25	458.95	74.950	200	57
0.60	4.20	763.89	898.72	531.32	84.965	200	27
0.60	4.40	940.91	1133.76	705.51	116.343	200	25
0.60	4.60	1126.40	1360.92	893.92	101.134	200	25
0.60	4.80	1329.14	1663.35	1068.37	124.230	200	37
0.60	5.00	1506.60	1757.95	1186.85	122.208	200	48
0.60	5.20	1630.91	1872.57	1420.63	98.905	200	71
0.60	5.40	1697.00	1913.40	1330.82	99.817	200	67
0.60	5.60	1768.08	1952.06	1540.38	77.309	200	94
0.60	5.80	1744.85	1946.35	1562.14	71.126	200	113
0.60	6.00	1712.68	1953.08	1492.41	80.688	200	151
0.60	6.20	1740.61	1914.13	1460.50	82.695	200	160
0.60	7.00	1824.90	1997.78	1558.64	75.789	200	175
0.80	2.40	366.81	483.98	263.61	40.297	200	113
0.80	2.60	394.35	522.17	277.88	44.429	200	122
0.80	2.80	462.21	637.40	325.65	54.521	200	107
0.80	3.00	486.73	626.16	333.88	55.847	200	117
0.80	3.20	660.57	880.23	465.50	86.920	200	53
0.80	3.40	828.19	1171.50	646.79	109.821	200	33
0.80	3.60	989.33	1232.58	610.91	122.639	200	30
0.80	3.80	1260.46	1606.23	988.50	128.009	200	35
0.80	4.00	1478.07	1713.30	1152.29	121.285	200	67
0.80	4.20	1621.50	1906.32	1183.24	118.681	200	75
1.00	1.80	375.70	498.88	272.98	41.360	200	124
1.00	2.00	401.71	519.41	276.17	47.761	200	121
1.00	2.20	441.34	554.05	305.09	54.665	200	104
1.00	2.40	545.28	697.94	386.56	67.369	200	82
1.00	2.60	701.20	839.65	570.06	71.274	200	43
1.00	2.80	912.19	1115.37	609.77	100.317	200	27
1.00	3.00	1130.30	1366.96	623.54	163.881	200	34
1.00	3.20	1306.03	1670.31	1014.47	128.898	200	47
1.00	3.40	1548.92	1762.16	1300.93	108.822	200	53
1.00	4.00	1747.57	1956.76	1396.42	98.634	200	166
1.40	2.20	1490.71	1699.08	1155.12	102.625	200	81
1.40	2.20	1490.51	1704.36	1191.58	98.202	200	99
1.40	2.40	1634.67	1911.14	1386.51	91.037	200	136
1.60	0.80	594.58	716.52	479.70	54.619	200	70
1.60	1.00	722.72	821.38	594.61	56.612	200	51
1.60	1.20	824.62	1054.33	687.57	83.052	200	32
1.60	1.40	1073.62	1272.40	842.53	113.041	200	33
1.60	1.60	1320.55	1517.92	1033.98	101.287	200	66
1.60	1.80	1540.88	1772.58	1270.31	99.648	200	166
1.60	2.00	1648.71	1871.65	1319.44	98.445	200	174

Table C5 Raw experimental data ($\phi = 1.0$, $u = 1.2$ m/s) (continued)

x (mm)	y (mm)	T_{mean}	T_{max}	T_{min}	δ	N_T	N_a
1.60	2.20	1697.67	1876.96	1397.83	80.985	200	164
1.60	2.40	1721.33	1938.58	1484.81	95.518	200	143
1.80	0.80	823.71	1184.90	601.08	83.023	200	67
1.80	1.00	993.89	1202.72	799.67	83.269	200	85
1.80	1.00	994.03	1226.27	487.50	101.545	200	86
1.80	1.20	1190.14	1402.58	850.70	102.345	200	152
1.80	1.40	1417.85	1668.00	1170.42	99.445	200	114
1.80	1.60	1562.71	1862.28	1325.11	94.291	200	76
1.80	1.80	1562.01	1958.37	1242.73	127.090	200	85
1.80	2.00	1595.90	1835.19	1334.26	92.547	200	77
1.80	2.20	1609.04	1948.48	1272.40	111.261	200	85
2.00	1.00	1219.64	1433.40	937.68	90.873	200	150
2.00	1.20	1410.18	1685.15	1053.97	108.110	200	94
2.00	1.40	1539.72	1771.48	1231.02	109.170	200	78
2.00	1.60	1569.87	1783.53	1321.38	92.765	200	92
2.00	1.80	1580.96	1943.04	1276.55	110.391	200	101
2.20	0.80	1153.00	1385.05	820.81	98.834	200	128
2.20	1.00	1349.52	1572.47	1037.32	100.466	200	96
2.20	1.20	1421.52	1633.52	1199.29	94.800	200	85
2.20	1.40	1503.32	1718.64	1195.50	85.923	200	81
2.20	1.80	1544.62	1705.77	1234.09	96.621	200	95
2.40	1.00	1370.45	1592.50	1066.91	97.442	200	89
2.40	1.20	1425.40	1656.52	1221.29	91.326	200	74
2.40	1.40	1463.93	1676.42	1197.65	101.077	200	103
2.40	1.60	1484.18	1656.17	1222.42	102.161	200	90
2.60	1.00	1341.45	1560.50	1105.05	91.983	200	82
2.60	1.20	1393.60	1576.48	1200.45	91.810	200	83
2.60	1.40	1455.74	1677.22	1110.05	98.306	200	92
2.80	1.00	1309.90	1480.81	1138.96	82.832	200	95
2.80	1.20	1399.31	1647.07	1109.61	103.456	200	110
2.80	1.40	1442.43	1610.98	1137.29	97.248	200	86
3.00	1.00	1302.64	1517.15	1057.09	98.841	200	86
3.00	1.20	1373.25	1700.27	1114.11	104.360	200	93
3.00	1.40	1417.13	1628.25	1041.70	104.515	200	97
3.00	3.00	1657.04	1879.42	1288.36	105.466	200	87

Table C6

Raw experimental data for stoichiometric methane-air mixture and mean inlet velocity of 2.0 m/s.

x (mm)	y (mm)	T_{mean}	T_{max}	T_{min}	δ	N_T	N_a
-0.20	2.40	341.39	444.25	258.21	42.005	100	71
-0.20	2.80	344.00	431.61	261.65	38.522	100	64
-0.20	3.20	381.57	459.53	268.35	47.637	100	47
-0.20	3.60	365.96	468.79	288.09	39.088	100	32
-0.20	4.00	526.92	1825.15	369.01	254.491	100	29
-0.20	4.40	1021.04	1340.93	810.05	136.384	100	17
-0.20	4.80	1407.76	1684.69	1059.56	135.497	100	36
-0.20	5.20	1770.51	1979.13	1530.32	88.776	100	89
-0.20	5.60	1857.36	2041.98	1578.81	70.446	100	94
-0.20	6.00	1879.00	2096.88	1734.51	73.640	100	86
-0.20	7.20	1923.74	2106.50	1668.07	88.713	100	80
-0.20	7.60	1945.68	2112.37	1526.15	84.844	100	84
-0.20	8.00	1953.62	2110.20	1683.84	77.473	100	90
0.00	0.00	383.39	1647.75	268.02	140.210	100	90
0.00	4.40	493.34	573.39	314.42	45.126	100	81
0.00	4.80	406.89	543.98	296.86	52.497	100	60
0.00	5.20	402.86	581.06	276.13	54.404	100	52
0.00	5.60	482.20	661.36	352.65	56.803	100	46
0.00	6.00	760.67	1806.62	535.87	214.031	100	30
0.00	6.40	788.83	882.98	631.70	64.400	100	38
0.00	6.80	835.54	1004.91	735.65	63.275	100	31
0.00	7.00	891.92	1045.14	831.40	62.850	100	12
0.00	7.20	1075.37	1212.85	907.41	95.165	100	12
0.00	7.40	1268.60	1673.58	1029.11	171.140	100	31
0.00	7.60	1466.15	1688.52	1186.56	142.612	100	33
0.00	7.80	1597.18	1825.88	1289.13	112.969	100	58
0.00	8.00	1744.39	1927.83	1549.92	87.898	100	67
0.00	8.20	1779.85	1988.61	1491.41	102.160	100	67
0.00	8.60	1420.97	1683.15	1153.79	127.828	100	34
0.00	9.00	1739.07	1996.78	1476.42	120.405	100	74
0.00	9.40	1825.29	2091.52	1654.89	76.563	100	70
0.00	10.00	1915.19	2125.40	1739.04	78.430	100	62
0.00	11.00	2000.49	2212.55	1740.43	83.262	100	61
0.00	13.00	2071.27	2225.73	1882.45	76.803	100	73
0.00	15.00	2072.37	2251.70	1802.55	88.682	100	85
0.20	6.80	466.51	1717.35	328.43	140.574	100	89
0.20	7.20	511.40	620.05	396.86	52.431	100	76
0.20	7.60	578.10	1733.09	464.73	157.674	100	59
0.20	8.00	578.41	703.08	439.50	63.402	100	55
0.20	8.00	571.85	711.93	403.55	60.076	100	59
0.20	8.20	663.09	810.41	483.57	76.568	100	46
0.20	8.40	762.42	1031.81	598.54	96.163	100	44

Table C6 Raw experimental data ($\phi = 1.0$, $u = 2.0$ m/s) (continued)

x (mm)	y (mm)	T_{mean}	T_{max}	T_{min}	δ	N_r	N_a
0.20	8.60	884.22	1043.33	761.66	79.751	100	36
0.20	8.80	1173.99	1612.43	920.71	177.882	100	36
0.20	9.00	1448.02	1869.98	1098.03	198.574	100	56
0.20	9.20	1681.33	1931.24	1062.14	164.182	100	72
0.20	9.40	1823.67	2043.51	1571.90	85.187	100	69
0.20	9.60	1853.43	2047.85	1657.55	76.448	100	75
0.20	10.00	1950.34	2142.09	1727.69	83.741	100	57
0.20	11.00	2009.00	2155.60	1820.07	73.936	100	67
0.40	5.80	372.21	486.51	281.42	45.130	100	92
0.40	6.20	393.01	1675.33	267.04	190.460	100	50
0.40	6.60	418.54	496.78	336.32	41.501	100	25
0.40	7.00	498.31	571.13	422.20	42.337	100	36
0.40	7.40	537.36	635.54	461.27	45.853	100	21
0.40	7.80	566.95	701.32	504.19	47.527	100	15
0.40	8.00	539.30	620.71	363.68	53.196	100	36
0.40	8.20	570.01	690.67	450.31	51.599	100	26
0.40	8.40	593.23	769.20	483.11	56.641	100	44
0.40	8.60	666.10	986.76	491.62	81.859	100	56
0.40	8.80	802.47	1198.63	544.47	142.709	100	53
0.40	9.00	1215.54	1833.68	716.23	342.622	100	50
0.40	9.20	1628.80	1943.10	902.51	207.259	100	77
0.40	9.40	1812.30	1972.75	1224.56	107.069	100	82
0.40	10.00	1916.88	2074.66	1610.16	75.303	100	77
0.40	11.00	1981.00	2192.12	1732.85	87.728	100	77
0.60	4.40	329.31	456.28	259.53	38.208	100	84
0.60	4.80	392.87	540.80	315.48	44.407	100	67
0.60	5.20	451.57	539.89	367.54	51.752	100	10
0.60	5.60	364.24	476.47	266.64	39.755	100	31
0.60	6.00	370.57	475.30	294.31	42.468	100	57
0.60	6.40	377.83	460.28	303.68	42.367	100	63
0.60	7.00	470.15	571.14	358.06	48.443	100	77
0.60	7.20	555.54	708.69	391.83	72.779	100	72
0.60	7.40	611.41	790.68	477.95	81.989	100	56
0.60	7.60	672.01	816.56	530.95	61.400	100	47
0.60	7.80	720.72	912.78	571.41	83.507	100	44
0.60	8.00	739.29	930.40	488.77	87.420	100	33
0.60	8.20	783.58	928.75	611.80	90.262	100	37
0.60	8.40	873.48	1124.46	709.94	91.048	100	43
0.60	8.60	1000.85	1323.60	750.88	125.989	100	62
0.60	8.80	1159.34	1593.31	738.35	205.643	100	68
0.60	9.00	1487.60	1876.41	995.47	220.426	100	81
0.60	9.40	1871.42	2041.66	1653.38	78.671	100	81
0.60	10.00	1930.85	2194.62	1673.91	84.820	100	72
0.80	3.00	347.66	470.17	260.42	41.965	100	86
0.80	3.60	386.50	464.80	337.03	38.843	100	16
0.80	4.00	354.19	423.77	279.52	37.994	100	22

Table C6 Raw experimental data ($\phi = 1.0$, $u = 2.0$ m/s) (continued)

x (mm)	y (mm)	T_{mean}	T_{max}	T_{min}	δ	N_T	N_o
0.80	4.40	363.97	462.30	283.64	41.249	100	55
0.80	4.80	361.72	499.77	278.43	39.596	100	70
0.80	5.20	379.11	557.65	296.17	49.236	100	57
0.80	5.60	452.88	613.49	335.44	52.912	100	71
0.80	6.00	568.44	750.53	416.91	76.098	100	63
0.80	6.20	629.02	776.46	466.15	66.486	100	58
0.80	6.40	693.30	893.19	552.44	60.086	100	40
0.80	6.60	727.74	889.44	571.58	74.749	100	22
0.80	6.80	724.29	854.59	594.89	66.350	100	19
0.80	7.00	801.93	946.71	594.59	93.683	100	22
0.80	7.20	879.77	1030.10	712.17	72.082	100	18
0.80	7.40	976.68	1337.84	776.42	144.840	100	12
0.80	7.80	1277.90	1487.78	997.30	126.522	100	50
0.80	8.00	1325.24	1681.18	1047.69	144.703	100	41
0.80	9.00	1762.18	2098.38	1488.51	107.517	100	84
1.00	1.00	365.52	450.12	272.96	39.755	100	81
1.00	2.00	371.16	476.54	287.06	40.171	100	86
1.00	2.60	361.89	472.01	265.08	46.741	100	35
1.00	3.00	342.04	449.39	272.81	37.889	100	53
1.00	3.20	353.67	437.15	273.53	35.399	100	63
1.00	3.60	361.97	455.35	272.39	38.599	100	61
1.00	4.00	397.86	494.23	284.04	42.467	100	64
1.00	4.40	477.28	618.57	287.95	55.021	100	68
1.00	4.60	538.94	687.53	405.91	55.616	100	55
1.00	4.80	611.71	761.17	504.30	57.562	100	47
1.00	5.00	667.92	799.35	560.88	51.162	100	33
1.00	5.20	685.74	861.45	540.13	70.189	100	27
1.00	5.40	702.70	909.70	574.03	78.408	100	16
1.00	5.60	815.01	903.66	680.22	64.972	100	15
1.00	5.80	868.68	995.55	737.69	80.884	100	16
1.00	6.00	942.97	1171.94	771.80	113.021	100	12
1.00	6.40	1230.15	1513.88	1053.72	105.474	100	58
1.00	6.60	1394.53	1707.70	1171.17	126.136	100	80
1.00	6.80	1447.44	1693.68	1092.37	103.688	100	90
1.00	7.00	1540.18	1759.89	1344.33	98.114	100	97
1.00	7.60	1702.98	1917.22	1489.64	83.596	100	92
1.00	8.00	1784.81	1969.02	1532.63	83.591	100	93
1.20	1.00	414.58	1668.19	281.36	138.751	100	90
1.20	1.60	368.89	1641.12	265.39	168.372	100	62
1.20	2.00	346.32	461.89	262.65	40.451	100	63
1.20	2.40	355.15	452.11	273.84	44.852	100	69
1.20	2.80	378.52	478.21	270.28	46.072	100	64
1.20	3.20	461.58	583.01	370.67	49.590	100	56
1.20	3.40	526.45	662.49	399.50	54.632	100	58
1.20	3.60	571.81	725.06	430.91	63.028	100	45
1.20	3.80	651.32	763.79	515.13	70.025	100	29

Table C6 Raw experimental data ($\phi = 1.0$, $u = 2.0$ m/s) (continued)

x (mm)	y (mm)	T_{mean}	T_{max}	T_{min}	δ	N_T	N_a
1.20	4.00	699.77	813.81	521.07	66.098	100	24
1.20	4.20	780.60	948.06	692.78	82.911	100	14
1.20	4.40	878.55	961.99	801.68	52.533	100	11
1.20	4.60	980.62	1200.82	859.24	99.509	100	19
1.20	4.80	1124.58	1352.33	864.51	113.550	100	35
1.20	5.00	1203.61	1446.04	939.21	115.574	100	44
1.20	5.20	1390.82	1690.48	1123.31	111.421	100	94
1.20	5.60	1592.73	1873.01	1275.10	119.597	100	97
1.20	6.00	1722.05	1949.98	1465.45	90.399	100	96
1.20	6.20	1733.07	1951.67	1553.03	82.204	100	98
1.20	6.60	1762.02	1925.74	1502.42	84.202	100	94
1.20	7.00	1792.39	1946.20	1537.03	71.871	100	90
1.40	0.80	384.44	485.54	259.92	42.919	100	62
1.40	1.00	369.46	476.90	280.21	44.230	100	62
1.40	1.40	381.66	448.99	290.85	35.292	100	55
1.40	1.80	406.92	509.42	308.18	43.089	100	57
1.40	2.20	447.21	585.57	307.97	52.442	100	59
1.40	2.40	514.17	667.05	342.60	61.567	100	60
1.40	2.60	551.22	686.80	416.56	63.276	100	34
1.40	2.80	658.70	809.72	584.65	55.792	100	18
1.40	3.00	723.22	900.07	612.78	73.354	100	18
1.40	3.20	799.83	854.36	744.68	34.533	100	10
1.40	3.40	963.88	1053.60	813.91	65.331	100	15
1.40	3.60	1069.11	1220.59	955.26	81.891	100	23
1.40	3.80	1211.51	1439.95	964.50	105.766	100	60
1.40	4.00	1412.52	1833.04	1113.67	109.807	100	88
1.40	4.20	1498.21	1738.61	1208.91	114.737	100	94
1.40	4.60	1689.21	1923.03	1427.92	92.122	100	97
1.40	5.00	1744.69	1911.71	1547.51	76.379	100	96
1.60	0.80	404.89	513.85	302.65	40.932	100	58
1.60	1.00	443.82	538.33	324.69	50.508	100	64
1.60	1.20	461.64	566.15	374.66	44.237	100	66
1.60	1.40	499.75	619.79	387.33	48.567	100	66
1.60	1.60	529.16	651.70	388.83	51.848	100	63
1.60	1.80	593.53	747.94	473.89	52.366	100	41
1.60	2.00	689.20	1006.71	532.98	97.062	100	41
1.60	2.20	823.34	1832.29	626.60	246.755	100	19
1.60	2.40	886.04	1052.56	694.64	85.094	100	16
1.60	2.60	1011.92	1137.58	785.22	91.104	100	14
1.60	2.80	1146.64	1327.98	991.04	82.195	100	50
1.60	3.00	1294.36	1492.56	1066.82	78.549	100	68
1.60	4.00	1693.49	1869.09	1496.46	74.852	100	92
1.80	0.80	555.50	699.09	457.28	49.951	100	51
1.80	1.00	618.16	737.09	497.11	59.193	100	37
1.80	1.20	670.73	866.18	514.65	65.671	100	31
1.80	1.40	746.43	970.56	641.46	66.682	100	29

Table C6 Raw experimental data ($\phi = 1.0$, $u = 2.0$ m/s) (continued)

x (mm)	y (mm)	T_{mean}	T_{max}	T_{min}	δ	N_T	N_a
1.80	1.60	873.37	1133.50	765.67	79.114	100	23
1.80	1.80	1007.99	1175.05	842.97	78.777	100	29
1.80	2.00	1170.69	1331.71	1020.73	70.272	100	57
1.80	2.20	1306.43	1486.11	1117.27	84.818	100	66
1.80	2.60	1561.57	1741.00	1314.41	89.869	100	82
1.80	3.00	1714.94	1882.20	1471.93	82.738	100	92
2.00	0.80	766.97	876.99	568.01	69.518	100	44
2.00	1.00	872.42	1035.09	688.28	68.003	100	37
2.00	1.20	983.43	1132.77	822.94	68.248	100	48
2.00	1.40	1150.64	1316.02	999.16	76.856	100	56
2.00	1.60	1312.94	1503.88	1128.01	83.368	100	75
2.00	2.00	1590.54	1830.98	1405.65	88.186	100	91
2.20	0.80	930.09	1115.41	756.07	72.236	100	86
2.20	1.00	1138.16	1328.97	944.30	81.510	100	79
2.20	1.20	1314.14	1519.14	1150.05	81.967	100	86
2.20	1.40	1466.25	1629.43	1283.94	89.291	100	86
2.20	2.00	1698.33	1937.29	1527.71	75.971	100	96
2.40	0.80	1060.93	1288.61	905.78	74.827	100	92
2.40	1.00	1347.33	1599.06	1139.87	92.358	100	82
2.40	1.40	1605.69	1791.45	1441.47	81.291	100	95
2.40	2.00	1730.52	1891.89	1475.50	88.458	100	93
2.60	0.80	1109.07	1284.63	891.38	91.451	100	83
2.60	1.00	1403.46	1617.90	1203.05	72.607	100	85
2.60	1.40	1610.61	1756.27	1389.38	73.606	100	93
2.80	0.80	1123.45	1860.10	890.79	122.002	100	90
2.80	1.00	1427.69	1670.19	1205.70	85.563	100	89
2.80	1.40	1594.87	1735.06	1339.31	78.070	100	93
3.00	0.80	1128.73	1371.63	955.56	87.562	100	85
3.00	1.00	1451.27	1647.21	1254.75	76.804	100	84
3.00	1.40	1610.88	1874.15	1394.42	81.752	100	93
3.20	1.00	1413.28	1656.11	1210.09	79.082	100	84
3.20	1.40	1626.26	1853.66	1435.79	87.040	100	89
3.20	2.00	1755.72	1997.49	1572.76	82.014	100	85

References

Abd Al-Masseeh, W. A., Bradley, D., Gaskell, P. H. and Lau, A. K. C., *Twenty-third Symposium (International) on Combustion.* The Combustion Institute, Pittsburgh, 1990, 825.

Abd Al-Masseeh, W. A., Bradley, D., Gaskell, P. H. and Lau, A. K. C., *Eurotech Direct '91 London.* The Institution of Mechanical Engineers, 1991, **C413/043**.

Adams, G. K., and Cook, G. B.,, *Combust. and Flame,* 1960, 4.9.

Ali, Y., Bradley, D, Lawes, M. and Mushi, E. M. J., *Joint meeting of the British and German Sections,* British Sections of the Combustion Institute, Cambridge, 1993, 404.

Andrews, G. E. and Bradley, D., *Combust. and Flame,* 1972, **18**,133.

Andrews, G. E. and Bradley, D., *Fourteenth Symposium (International) on Combustion.* The Combustion Institute, Pittsburgh, 1973, 1119.

Bilger, R. W., Starner, S. H., and Kee, R. J., *Combustion and Flame,* 1990, 80:135

Bradley, D., Gaskell, P. H., Lau, A. K. C., Missaghi, M. and Chin, S. B., *International Conference on Computers in Engine Technology.* The Institution of Mechanical Engineers, 1987, **C35/87**, 315.

Bradley, D., Kwa, L. K., Lau, A. K. C., and Missaghi, M.,
Combust. and Flame, 1988, **71**:109.

Bradley, D. and Lau, A. K. C., *Pure and Appl. Chem.*, 1990, **62**(5), 803.

Bradley, D., Gaskell, H. and Lau, A. K. C., *Twenty-Third Symposium (International) on Combustion.* The Combustion Institute, Pittsburgh, 1990, 685.

Bradley, D., Lau, A. K. C. and Lawes, M., *Phil. Trans. R. Soc. Lond.*, 1992, **A338**, 359.

Bradley, D., Laws, M., Scott, M. J., Sheppard, G. W., Greenhalgh, D. A. and Porter, F. M., *Twenty-Fourth Symposium (International) on Combustion.* The Combustion Institute, Pittsburgh, 1992, 527.

Bray, K. N. C., *Seventeenth Symposium (International) on Combustion.* The Combustion Institute, Pittsburgh, 1979, 223.

Bray, K. N. C., *Chapter 4.* In Turbulent Reacting Flows, (Eds. Libby, P. A. and Williams, F. A.), 1980, (Springer-Verlag Berlin-Heidelberg New York).

Bray, K. N. C., Libby, P. A., Masuya, G. and Moss, J. B., *Combust. Sci. Tech.*, 1981, **25**, 127.

Bray, K. N. C., Libby, P. A. and Moss, J. B., *Combust. and Flame*, 1985, **61**, 87.

Bray, K. N. C., *Proc. R. Soc. London*, 1990, **A431**, 315.

Buckmaster, J., *Combust. Sci. Tech.*, 1979, **20**, 33.

Buddenberg, J. W., and Wilke, C. R., *Ind. Eng. Chem.*, 1949, **41**, 1435.

Burke, S. P., and Schumann, T. E. W., *Diffusion Flames, Indust. Eng. Chem.*, 1928 **29**, 998

Candel, S. M., and Poinsot, T. J., *Combust. Sci. and Tech.*, 1990, **70**, 1.

Chapman, S. and Cowling, T. G., *The Mathematical Theory of Non-Uniform Gases,* 3rd edition, 1970, (The University Press, Cambrige).

Chung, S. H. and Law, C. K., *Combust. and Flame*, 1984, **55**, 123.

Clavin, and Joulin, G., *J. Phys. Lett.*, 1983, **44**, L-1.

Clavin, P., *Prog. in Energy Combust. Sci.*, 1985, **11**, 1.

Clavin, P., and Joulin, G., Turbulent Reactive Flows. In Lecture Notes in Engineering. 1989, **40**, 213, (Spring-Verlag).

Clifford, A. A., Gray, P., Mason, R. S., and Waddicor, J. I., *Proc. Roy. Soc. Lond.*, 1982, **A380**, 241.

Coelho, P. J., and Pereira, J. C. F., *Combust. Sci. and Tech.*, 1993, **92**, 243.

Coffee, T. P., and Heimerl, J. M., *Combust. and Flame*, 1981, **43**, 273.

Coffee, T., Kotlar, A. J., and Miller, M. S., *Combust. and Flame*, 1983, **54**, 155.

Courant, R., Isaacson, E. and Rees, M., *Comm. Pure Appl. Math.*, 1952, **5**, 242.

Daniell, J., *Proc. Roy. Soc. London*, 1930, **A126**, 393.

Darrieus, G., Propagation d'un front de flamme. Essai de theorie des vitesses anomales de deflagration par developpement spontane de la turbulence. Unpublished manuscript, 1938; 6th International Congress of Applied Mechanics, Paris, 1946.

Deshaies, B., and Cambray, P., 1990, *Combust and Flame,* **82**:361.

Dixon-Lewis, G. and Williams, A. *Ninth Symposium (International) on Combustion.* The Combustion Institute, Pittsburgh, 1963, 576.

Dixon-Lewis, G., *First Specialists Meeting* (International) *of the Combustion Institute.* Section Francaise du Combustion Institute, 1981, 284.

Dixon-Lewis, G. and Islam, S. M., *Nineteenth Symposium (International) on Combustion.* The Combustion Institute, Pittsburgh, 1982, 283.

Dixon-Lewis, G., *Computer Modeling of Combustion Reactions in Flowing Systems with Transport.* In Combustion Chemistry, (Eds. William C., and Gardiner Jr.), 1984, 21, (Springer-Verlag, New York).

Dixon-Lewis, G., David, T., Gaskell, H., Fukutani, S., Jinno, H., Miller, J. A., Kee, R. J., Smooke, M. D., Peters, N., Effelsberg, E., Warnatz, J., and Behrendt, F., *Twentieth Symposium (International) on Combustion.* The Combustion Institute, Pittsburgh, 1984, 1893.

Dixon-Lewis, G., Proc. of Workshops on Gas Flame Structure: Part 2, 3, USSR Academy of Sciences, Novosibirsk, 1988.

Dixon-Lewis, G., *Twenty-Third Symposium* (*International*) *on Combustion.* The Combustion Institute, Pittsburgh, 1990, 305.

Dixon-Lewis, G., "Aspects of Laminar Premixed Flame Extinction Limits", to appear in *Twenty-Fifth Symposium* (*International*) *on Combustion.* The Combustion Institute, Pittsburgh, 1995.

Dowdy, D. R., Smith, D. B., Taylor, S. C. and Williams, A., *Twenty-Third Symposium (International) on Combustion.* The Combustion Institute, Pittsburgh, 1990, 325.

Draper, M. S., *Mathematical Modelling of a Jet Stirred Combustor*, Ph.D. Thesis, Department of Mechanical Engineering, The University of Leeds, 1977.

El-Sherif, S., *The Role of Gas Phase Chemical Kinetics in The Combustion of Liquids and Solids*, Ph.D. Thesis, Department of Mechanical Engineering, The University of Leeds, 1990.

Finlayson, B. A. *The method of Weighted Residuals and Variational Principles*, 1972, (Academic, New York).

Frenklach, M., *Progress in Astronautics and Aeronautics*, 1991, **135**, 129.

Garcia-Ybarra, P., Nicoli, C. and Clavin, P., *Combust. Sci. Tech.*, 1984, **42**, 87.

Gaskell, P. H. and Lau, A. K. C., *Report No. T40,* Deparment of Mechanical Engineering, The University of Leeds, 1986.

Gaskell, P. H. and Lau, A. K. C., *International Journal For Numerical Methods in Fluids*, 1988, **8**, 617.

Gaskell, P. H. and Lau, A. K. C., *AIAA/ASME/SIAM/APS 1st National Fluid Dynamics Congress*, Cincinnati, Ohio, Part 1, 1988b, 272.

Gaskell, P. H. and Wright, N. G., *AIAA/ASME/SIAM/APS 1st National Fluid Dynamics Congress*, Cincinnati, Ohio, Part 1, 1988, 264.

Gaydon, A. G., and Wolfhard, H. G., *Flames - Their Structure, Radiation and Temperature*, 1953, (Chapman and Hall, London).

Gentry, R. A., Martin, R. E. and Daly, B. J., *J. Comp. Phys.*, 1966, **1**, 87.

Glarborg, P., Miller, J. A., and Kee, R. J., *Combust. and Flame*, 1986, **65**:177.

Gosman, A. B., Pun, W. M., Runchal, A. K., Spalding, D. B. and Wolfshtein, M., *Heat and Mass Transfer in Recirculating Flows,* (Academic, New York).

Gu, X. Z., private communication, 1994.

Han, T., Humphrey, J. A. C. and Launder B. E., Comp. Meth. Appl. Mech. Engng. 1981, **29**, 81.

Harlow, F. H. and Welch, J. E., *Phys. Fluids*, 1965, **8**, 2182.

Hecht, E., *Theory and Problems of Optics*, Schaum's Outline Series, 1975, (Mcgraw-Hill Book Company).

Heywood, J. B., *Internal Combustion Engine Fundamentals*, McGraw-Hill Book Company, 1988.

Hill, C. G., Jr., *An introduction to Chemical Engineering Kinetics and Reactor Design*, 1977, 92, (Wiley, New York).

Hirschfelder, J. O., Curtiss, C. F. and Campbell, D. E., *Fourth Symposium (International) on Combustion.* 1953, 190, (Williams and Wilkins, Baltimore, Maryland).

Hirschfelder, J. O., Curtiss, C. F., and Bird, R. B., *Molecular Theory of Gases and Liquids,* 1954, (John Wiley & Sons, New York).

Karlovitz, B., Denniston, J. R., Knapschaefer, D. H. and Wells, F. E., *Fourth Symposium on Combustion.* The Combustion Institute, Pittsburgh, 1953, 613.

Kee, R. J., Grcar, J. F., Smooke, M. D. and Miller, J. A., *A Fortran Program for Modelling Steady Laminar One-Dimensional Premixed Flames.* Sandia National Laboratories Report SAND85-8240, 1985.

Kee, R. J., Miller, J. A., Evans, G. H. and Dixon-Lewis G., *Twenty-Second Symposium (International) on Combustion.* The Combustion Institute, Pittsburgh, 1988, 1479.

Klimov, A. M., *Zh. prikl. Mech. tekh. Fiz,* 1963, **3**, 49.

Kuo, J. C. W. and Wei, J., *Industrial and Engineering Chemistry Fundamentals,* 1969, **8**, 124.

Kuo, K. K., *Principles of Combustion.* 1986, (John Wiley & Sons).

Kwan, K. C., *Numerical results of two-dimensional, laminar, premixed, axisymmetric methane-air flames with reduced kinetic mechanism*, Departmental report, Department of Mechanical Engineering, The University of Leeds, 1994.

Kwon, S., Wu, M. S., Driscoll, J. F., and Faeth, G. M., *Combust. Sci. Tech.* 1992, **88**, 221.

Kwon, S., and Faeth, G. M., *Twenty-Fourth Symposium (International) on Combustion.* The Combustion Institute, Pittsburgh, 1992, 451.

Kwon, S., Tseng, L. K., and Faeth, G. M., *Combust. and Flame.* 1992, **90**, 230.

Landau, L., *Acta Physicochim*, URSS, 1944, **19**, 77.

Law, C. K., Ishizuka, S. and Cho, P. *Combust. Sci. and Tech.*, 1982, **28**, 89.

Law, C. K., *Prog. Energy Combust. Sci.* 1984, **10**, 295.

Law, C. K., Zhu, D. L. and Yu, G., *Twenty-First Symposium (International) on Combustion.* The Combustion Institute, Pittsburgh, 1986, 1426.

Law, C. K., *Twenty-Second Symposium (International) on Combustion.* The Combustion Institute, Pittsburgh, 1988, 1381.

Leonard, B. P., *ASME Appl. Mech. Div*, 1979a, **34**.

Leonard, B. P., *AIAA*, 1979b, **226**, 1469.

Leonard, B. P., *Comp. Meth. App. Mech. Eng.*, 1979c, **19**, 59.

Leonard, B. P., In *Computer Method in Fluids.* (Eds. Morgan, K., Taylor, C. and Brebbia, C. A.), 1980, 159, (Pentech Press).

Lewis, B. and von Elbe, G., *Combustion Flames and Explosion of Gases,* 1961, 220, (Academic, New York).

Linan, A. and Clavin, P., *Combust. and Flame,* 1987, **70**, 137-160.

Linnett, J. W., *Fourth Symposium (International) on Combustion.* The Combustion Institute, Pittsburgh, 1953, 20.

Maas, U. and Pope, S. B., *Combust. and Flame*, 1992, **88**, 239.

Mallard, E. and LeChatelier, H. L., *Ann. Mines*, 1883, **4**, 379.

Markstein, G. H., *J. Aero. Sci.*, 1951, **18**, 199.

Markstein, G. H., *Nonsteady Flame Propagation*, 1964, 5, (MacMillan, New York).

Mason, E.A., and Monchick, L., *J. Chem. Phys.*, 1962, **36**, 1622.

Matalon, M., *Combust. Sci. and Tech.*, 1983, **31**,169.

Matalon, M. and Matkowsky, B. J., *Combust. Sci. Tech.*, 1983, **34**, 295.

Mauss, F. and Peters, N., *Reduced Kinetic Mechanisms for Premixed Methane-Air Flames* (Eds. N. Peters, and B. Rogg), Lecture Notes in Physics, 1993, **M15**, 58, Springer-Verlag.

Mendes-Lopes, J. M. C., and Daneshyar, H., *Combust. and Flame*, 1985, **60**, 29.

Miller, J. A., Kee, R. J., Smooke, M. D. and Grcar, J. F., Paper WSS/CI 84-10, Western States Section of the Combustion Institute, Spring Meeting 1984.

Mizomoto, M., Asaka, Y., Ikai, S., and Law, C.K., *Twentieth Symposium (International) on Combustion/ The Combustion Institute,* 1984, 1933.

Monchick, L., Pereira, A. N. G., and Mason, E. A. J. *Chem. Phys.*, 1965, **42,** 3241.

Oran, E. S., and Boris, J. P., 1981, *Progr. in Energy and Combustion Science,* **7,** 1.

Patankar, S. V. and Spalding, D. B., *Heat and Mass Transfer in Boundary Layers* (2nd. edition), 1970, (Intertext Books).

Patankar, S. V. and Spalding, D. B., *Int. J. Heat Mass Transfer*, 1972, **15,** 1787.

Patankar, S. V., *Numerical Heat Transfer*, 1980, (Mc Graw-Hill, New York).

Peters, N. and Warnatz, J. (Eds.), *Numerical Methods in Laminar Flame Propagation*, 1982, (Vieweg, Braunschweig).

Peters, N., *Progr. Energy Combust. Sci.*, 1984, **10,** 319.

Peters, N., *Twenty-First Symposium (International) on Combustion.* The Combustion Institute, Pittsburgh, 1986, 1231.

Peters, N., *Prog. in Energy and Combust. Sci.*, 1984, **10,** 319.

Peters, N., *Numerical and Asymptotic Analysis of Systematically Reduced Reaction Schemes for Hydrocarbon Flames* (Eds. Glowinski R., Larrouturou B., and Temam R.), Lecture Notes in Physics, 1985, **241,** 90, (Springer-Verlag).

Peters, N., *Twenty-First Symposium (International) on Combustion.* The Combustion Institute, Pittsburgh, 1986, 1231.

Peters, N. and Kee, R. J., *Combust. and Flame,* 1987, **68,** 17.

Peters, N. and Williams, F. A., *Combust. and Flame,* 1987, **68,** 185.

Peters, N., Reducing Mechanisms. In *Reduced Kinetic Mechanisms and Asymptotic Approximations for Methane-Air Flames* (Ed. Smooke M. D.), Lecture Notes in Physics, 1991, **384,** (Springer-Verlag).

Peters, N., *Flames Calculation with Reduced Mechanisms — An Outline* (Eds. N. Peters, and B. Rogg), Lecture Notes in Physics, 1993, **M15,** 3, Springer-Verlag.

Phillips, O. M., *J. Fluid Mech.*, 1972, **51,** 97.

Powling, J., *Fuel,* 1949, **28,** 25.

Prasad, K., and Price, E. W., *Combust. Flame*, 1992, **90,** 155.

Rakestraw, D. J., Lucht, R. P. & Dreier, T., *Appl. Opt.*, 1989, **28**(19), 4116.

Reitz, R. D., and Bracco, F. V., *Combust. Flame*, 1983, **53**, 141.

Rhie, C. M. and Chow, W. L., *AIAA J.*, 1983, **21**, 1525.

Richtmyer, R. D. and Morton, K. W., *Difference Methods for Initial value Problems*, 2nd. edition, 1967, (Interscience Publishers).

Rogg, B., *Combust. and Flame,* 1988, 73:45.

Rogg, B. and Peters, N., *Combust. and Flame*, 1990, **79**, 402.

Roache, P. J., *Computational Fluid Dynamics*, Hermosa Publishers, Albuquerque, 1972.

Scott, M. J., *Distributions of Strain Rate and Temperature in Turbulent Combustion*, Ph.D. Thesis, Department of Mechanical Engineering, The University of Leeds, 1992.

Searby, G. and Quinard, J., *Combust. and Flame*, 1990, **82**, 298.

Seshadri, K. and Peters, N., *Combust. and Flame*, 1988, **73**, 23.

Seshadri, K. and Peters, N., *Combust. and Flame*, 1990, **81**, 96.

Shifrin, A. S., *Teploenergetik*, **6**, 22.

Sivashinsky, G. I., *Ann. Rev. Fluid Mech.*, 1983, **15**, 179.

Smith, D. B., Taylor, S. C., and Williams, A., Problems with Defining and Measuring Burning Velocity, paper presented at the joint meeting of the British and French sections of the Combustion Institute, Rouen, France, 1989.

Smooke, M. D., Mitchell, R. E., and Keyes, D. E., *Combust. Sci. and Tech.*, 1989, **67**, 85.

Smooke, M. D., Lin,, Lam, J. K., and Long, M. B., *Twenty-third Symposium (International) on Combustion,* The Combustion Institute, Pittsburgh, 1990, 575.

Smooke, M. D. and Giovangigli, V., Chapters 1 & 2, *Reduced Kinetic Mechanisms and Asymptotic Approximations for Methane-Air Flames*, (Ed. Smooke, M. D.), Lecture Notes in Physics, 1991, **384,** (Springer-Verlag).

Smooke, M. D., (Ed.), *Reduced Kinetic Mechanisms and Asymptotic Approximations for Methane-Air Flames*, Lecture Notes in Physics, 1991, **384,** (Springer-Verlag).

Smoot, L. D., Hecker, W. C. and Williams, G. A., *Combust. and Flame*,

1976, **26**, 323.

Spalding, D. B., *Some Fundamentals of Combustion,* London, 1955.

Spalding, D. B., *Phil. Trans. R. Soc. Lond.,* 1956, **A249**, 1.

Spalding, D. B., *Combust. and Flame*, 1957, **1**, 287.

Spalding, D. B., Stephenson, L. and Taylor, R. G., *Combust. and Flame,* 1971, **17**, 55.

Spalding, D. B., *Int. J. Num. Meth. Eng.,* 1972, **4**, 551.

Strehlow, R. A., *Combustion Fundamentals,* 1985, (McGraw-Hill).

Strehlow, R. A. and Savage, L. D., *Combust. Flame*, 1978, **31**, 209.

Svehla, R. A., Technical Report R-132, NASA, Washington, D. C., 1962.

Taffanel, M., *Compt. Rend.,* 1913, **157**, 714.

Taffanel, M., *Compt. Rend.,* 1913, **158**, 42.

Taylor, S. C., PhD. thesis, *Department of Fuel and Energy,* University of Leeds, 1991.

Tien, J. H. and Matalon, M., *Combust. and Flame*, 1991, **84**, 238.

Troe, J., *Seventeenth Symposium (International) on Combustion.* The Combustion Institute, Pittsburgh, 1979, 535.

Tsatsaronis, G., *Combust. and Flame*, 1978, **33**, 217.

Tseng, L. K., Ismail, M. A. and Faeth, G. M., *Combust. and Flame*, 1993, **95**, 410.

Van Doormall, J. P.and Raithby, G. D., *Num. Heat Transfer*, 1984, **7**, 147.

Warnatz, J., *Eighteenth Symposium (International) on Combustion.* The Combustion Institute, Pittsburgh, 1981, 369.

Warnatz, J., *Combustion Chemistry,* (Ed. W. C. Gardiner, Jr.), 1984, 197, (Springer-Verlag, New York).

Warnatz, J., *Twenty-Fourth Symposium (International) on Combustion.* The Combustion Institute, Pittsburgh, 1992.

Watson, J. T. R., *Viscosity of Gases in Metric Units*, H. M. S. O., London, 1972.

Wei, J. and Prater, C. D., The Structure and Analysis of Complex Reaction Systems. *Advances in Catalysis*, 1962, **13**, 203.

Wei, J. and Kuo, J. C. W., *Industrial and Engineering Chemistry Fundamentals,* 1969, **8**, 114.

Westbrook, C. K., and Dryer, F. L., *Combust. Sci. Tech.,* 1981, **27**, 31.

Westbrook, C. K., and Dryer, F. L., *Progr. Energy Combust. Sci.,* 1984, **10**, 1.

Wilde, K. A., *Combust. Flame,* 1972, **18**, 43.

William, C., and Gardiner, Jr., (Eds.), *Table of Coefficient Sets for NASA Polynomials,* Appendix C, Combustion Chemistry, 1984, (Springer-Verlag, New York).

Williams, F. A., A review of some theoretical considerations of turbulent flame structure. *Agard Conference Proceedings,* **164**.

Williams, F. A., *Combustion Theory,* 1985, (Benjamin-Cummings, Menlo Park, CA).

Wilson, J. and Hawkes, J. F. B., *Lasers : Principles and Applications,* Prentice Hall International Series in Optoelectronics, 1987.

Wong, H. H., and Raithby, B. D., *Num. Heat Transfer,* 1979, **2**, 131.

Wright, N. G., *Multigrid Solutions of Elliptic Fluid Flow Problems.* Ph.D. Thesis, Department of Mechanical Engineering, The University of Leeds, 1988.

Wu, C. K., and Law, C. K., *Twentieth Symposium (International) on Combustion,* The Combustion Institute, Pittsburgh, 1985, 1941.

Wu, M. S., Kwon, S., Driscoll, J. F., and Faeth, G. M., *Combust. Sci. Technol.,* 1991, **78**, 69.

Yamaoka, I., and Tsuji, H., *Twentieth Symposium (International) on Combustion.* The Combustion Institute, Pittsburgh, 1985, 1883.

Zeldovich, Y. B., and Frank-Kamenetskii, D. A., *Dokl. Akad. Nauk ussr,* 1938a, **19**, 693.

Zeldovich, Y. B., and Frank-Kamenetskii, D. A. *Zh. Fiz. Khim,* 1938b, **12**, 100.

Zeldovich, Y. B., *The Theory of Combustion and Detonation,* Publ. Academy of Sciences, USSR, 1944 (in Russian).

Zeldovich, Y. B., *Combust. and Flame,* 1981, **40**, 225.